CHEMIA

S T U D I A

UNIVERSITATIS BABEŞ-BOLYAI

CHEMIA

1

CUPRINS – CONTENT – SOMMAIRE – INHALT

Studia Universitatis Babes-Bolyai Chemia has been selected for coverage in Thomson Reuters products and custom information services. Beginning with V. 53 (1) 2008, this publication will be indexed and abstracted in the following:

- Science Citation Index Expanded (also known as SciSearch®)
- Chemistry Citation Index®
- Journal Citation Reports/Science Edition

PROFESSOR ENG. LIVIU LITERAT PHD

Professor Liviu Literat has been over 58 years in the service of chemistry and chemical engineering education at two reference Universities of Cluj-Napoca – the **Polytechnic Institute** (1953-1974) and **"Babeş-Bolyai" University** (1974 -). He graduated the chemical-physics (1951) in Cluj at "V. Babeş" University, the chemical engineering (1961) at Polytechnic Institute of Bucharest and became PhD in chemistry (1966). He got scientific research training (post doctoral schooling) in: Reactions in solid state (1966) – University Bucharest, Faculty of Chemistry, Department of physical-chemistry (acad. Ilie Murgulescu); Magnetic Nuclear Resonance (RMN) in Organic Chemistry (1967) – Romanian Academy Bucharest (acad. Prof. Costin D. Neniţescu) and UNESCO international training course in Scientific Research Management (Balkan Union of Mathematicians), Bucharest (1977). He also performed training in academic management, such as the Educational Management (1982) training – UBB, Cluj-Napoca, the Ministry of Education and European Foundation "J. C. Drăgan" and became coordinator of TEMPUS programs (1991-1996). Professor Literat was the **initiator and organizer of the chemical engineering education in the Cluj-Napoca University Center** by establishing the specializations: the Technology of Building Materials (1971), Organic and Inorganic Technology (1977) and the Science and Engineering of Oxide Materials (1990). He was founder and head of the Department of Chemical Engineering (1990) and founder of the Science of Oxide Materials (1992) specialization. He was also the promoter of the post-university (master) specializations (1994, 1995) and PhD advisor (1991) in chemical engineering and Science of Oxide Materials. Professor Literat was the Head of the Organic Chemistry and Technology Department (1977-1985) and of the Chemical Engineering and Science of Oxide Materials (1992-1995) chair, while he was also PhD supervisor in chemical engineering. He is author of 15 books (university manuals, treatises, monographs, history of sciences and education) and of over 130 scientific articles published in specialized journals in Romania and in foreign countries or in volumes of some international scientific events. Professor Literat is the author of over 300 scientific communications at national and international Congresses and Symposiums, of 75 applied research reports (contracts, grants, projects). He was member of the Commission of the National Council for Inventions of Engineers and Technicians (CNIT) Cluj (1985-1989). He served as active member of the editorial boards of Scientific Bulletin of Polytechnic Institute Cluj, Studia Universitatis Babeş-Bolyai, Seria Chemia and Romanian Journal of Materials (Bucharest). He is member of the Association of Scientists (AOS) of the Romanian Academy – Transylvania subsidiary (1986). He is also founding member (1995), president (1995-2000) and honorary
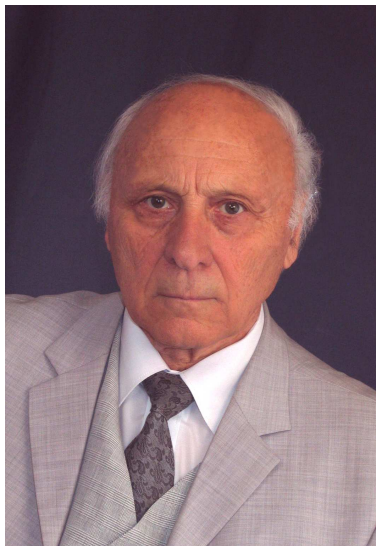
president (2000) of the Romanian Chemical Engineering Society (SICR) – Cluj branch. As recognition of his outstanding scientific merits he became honorary member of the Romanian Academy of Technical Sciences (2004) and member of the European Federation of Chemical Engineering (1999). He was proposed and accepted to be honorary citizen of Făgăraş Municipality (2005). Professor Literat is mentioned in numerous Romanian and foreign biographical compendiums (who's who) as scientist, culture and successful man, as teacher and mentor for over 50 series of graduate chemical, mechanical, civil engineers and university chemists and as adviser of master and PhD students. This would be, in short, the visiting card of professor dr. eng. Liviu Literat.

Born on 9 September 1928 in Vinţul de Jos, Alba County, professor Liviu Literat is a descendant of an old (scholar) family promoting knowledge and national traditions (rustics, priests, teachers, professors) with deep roots in the history of Făgăraş Country, strongly attached to the culture and national traditions.

Grown up in the cult of work and of the moral precepts respect of honesty, truth and justice, he always rigorously followed these principles.

High school studies have been performed at Braşov ("Andrei Şaguna" College), 1939-1945, Făgăraş ("Radu Negru" Lyceum), 1945/46 and Cluj ("Simion Ştefan" Lyceum), 1946/47, and baccalaureate at "George Bariţiu" Lyceum (1947).

He got a thorough College education at "Victor Babeş" University from Cluj, Faculty of Chemistry (1947-1951), graduated in chemical-physics (1951) and at Polytechnic Institute of Bucharest, Faculty of Industrial Chemistry (1961), became a chemical engineer, specialized in the Technology of Inorganic Substances (1963).

From the professional-scientific training perspective, Professor Liviu Literat is the product of the Chemistry School of Cluj and of the Chemical Engineering one, of Bucharest. This synthesis proved beneficial in his activity as member of the professorial staff and on a larger plan in organizing the chemical engineering education in Cluj-Napoca, a desideratum for which Professor Liviu Literat has pleaded for and has consistently acted in favor of and with which he has entirely identified himself.

In 1966 he obtained the scientific title of doctor in chemistry (PhD) with an ample research works in the field of non-stoichiometry of refractory oxides (a physical-chemistry study of some reducing alumina) performed under the guidance of academician Raluca Ripan.

The university career started as soon as his student's years, as a teaching assistant, (Department of Mineralogy, "V. Babeş" University) then he ascended all the steps of the higher education hierarchy and since 1972 he has become full professor.

Within the **Polytechnic Institute** (1953-1974) he was the titular of the General Chemistry, Inorganic and Physical-chemistry, Analytical chemistry and Technical Analysis, Building Materials and Building materials on polymer compounds disciplines.

At the Babes-Bolyai University he thought disciplines of chemical engineering including: Operations and Equipments in the Building Material Industry (1974-1991), Processes and Equipments in the Chemical Technology (1976-1991), Transfer Phenomena and Equipments in the Chemical Engineering (1980-1993), Heterogeneous catalysis (1977-1980), Operations and Equipments in the Oxide Materials Industry (1990-1995), Engineering of Interface Processes (1994-2001).

For these disciplines, he elaborated courses (5) and applications (7), appreciated for their content, modern approach and high level of analysis for the involved problems. Among these are the book on General Chemistry (1975) recommended by the Ministry of Education and EDP House (in 1973) as textbook for all higher technical education Institutes; Transfer Phenomena and Equipments in the Chemical Industry; Transport Processes (1985) – where the concept of Property Transport has been first introduced; Operations and Equipments in the Oxide Material Industry-Applications (1994) – example of applied theory, or in a reversed sense, inferred from the experiment and extended to the design; Technical Ceramics; Calculus and Designing Principles (2001) –synthesis of subjects and problems of theory, technology, research and designing in the ceramics domain.

Besides the didactic activity, Professor Liviu Literat has carried out a sustained and varied **scientific activity** in the fields of **physical-chemistry**, **chemical engineering** and **materials science**.

His formation as engineer and chemist offered to professor Literat the possibility to perform fundamental and applied research in the field of the materials science and chemical engineering, both considered as based on physical and chemical processes or phenomena.

Interested on the problems specific to each of these fields, Professor Liviu Literat and the school set up around him, have developed studies, with priority, in the competition area of these domains, situated at the border between the materials science and process engineering, at the interface between the "phenomenological" and "structural" aspects.

In the Materials Science domain, Professor Literat has essentials contributions to the discovery and research of a new class of refractory oxides (alumina) with deviation from stoichiometry, in the synthesis and characterization of some oxide-nano-systems and materials with pre-set destination aim, properties and characteristics (oxide refractory, metallic and composite matters with controlled porosity, ceramic membranes, catalysts, selective adsorbents, powders and sintered matters).

As concerns the alumina non-stoichiometry (reducing alumina with oxygen deficit, paramagnetic properties, n-type semiconductor behaviour and catalytic activity in electron-change processes), the PhD thesis (1964) and the publications on this subject, had a particular interests and were favorable commented in literature (reviewed by Chemical Abstract, Referativnîi Zhurnal), professor Literat being considered as pioneer in this field that, later, will be called nano materials compounds and also, in the non conventional synthesis methods (organic-inorganic precursors, in special conditions).

He has developed a new technique of punctual quantitative chemical analysis of the oxide and composite micro-phases systems using the methods of the electronic microscopy (electron microprobe). A non-conventional granular analysis method of analogy based on physical metallurgy (Epiquant) has been developed, by which the dimension, shape, volume, specific surface and the distribution function of the powders size fractions are estimated automatically.

In the field of chemical engineering, professor Literat's interests are connected to the concept of property transport and transfer phenomena, to the dimensional analysis applied to the phenomenological study of the interface processes (sorbtion, catalysis, extraction), to separation processes, to thermodynamics

and kinetics in solid state reactions and catalysis, to modeling and simulation, to scale up and design of the research equipments and industrial installations.

In the transfer theory, he has determined (12) new similitude criteria and criterion equations for stationary and transitory conductive-convective processes with electric load carriers.

In the field of the separations processes, he has developed a graph-analytical procedure for the discrimination of the movement of dispersed particles in the sedimentation process, has established some news recurrence equations and nomographic charts between the sedimentation speed and the size of particles. As well, he has drawn up an experimental computerized method and technique for recording of settling curves and of the size distribution functions. In the separation of the fluid micro-dispersions by filtering, there were also studied the phenomenology of the micro and ultra filtering processes, and the separation techniques.

He brought original contributions at the gas-solid sorption processes such as theory, experiment, apparatus, computation programs and applications in gas separations and to the porous solids and powders characterization.

In professor's Liviu Literat activity as a whole, an important part is **played** by his constant interest and concern for **the development** of the technical higher education in Cluj-Napoca, in general, and especially for **the chemical engineering**. For this desiderate he developed a prodigious didactic and scientific – theoretical, applicative and managerial activity, with special effects.

The name of the professor Liviu Literat has been inseparably linked with the actions and initiatives of setting up, developments and advances of the chemical engineering education in Cluj-Napoca University Center for over four decades, being considered one of the founder of the fourth Romanian Chemical Engineering School (1971) after Iaşi (1937), Bucharest (1938) and Timişoara (1948).

Therefore, Professor Liviu Literat does not belong only to the Babeş-Bolyai University and Polytechnic Institute of Cluj, he is a prominent personality of the Romanian School of Chemical Engineering and of the Oxide Material Science, as he is, in these domains, a founder of school, and representative of the higher education, considered as a whole. In the same time, professor Liviu Literat is a personality of high morality, with a grand spirit and a great availability, always involved in the activities that he put love all along his life. Professor Liviu Literat has always been a dynamic, active and dedicated person; he has presented to the higher education with everything he has to give, with responsibility and competence.

At the age of 80, Professor Liviu LITERAT is an active person in the academic life as he still has many projects to work on. The group of his former and present colleagues and co-workers from the Faculty of Chemistry and Chemical Engineering addresses to Professor Literat the best wishes for a long life, full with further achievements.

Volume Editors,
Mircea-Vasile Cristea
Adina Lucreţia Ghirişan

LIST OF PUBLICATIONS

BOOKS

A. Scientific and Technical books

1. **Liviu Literat**, Lucia Gagea, Firuţa Goga, Eugenia Mirică, Ecaterina Olariu, Ceramică tehnică. Principii de calcul şi proiectare, Ed. Casa Cărţii de Ştiinţă, Cluj-Napoca, ISBN 973-686-194-5, 334 pag., 2001

2. **Liviu Literat**, Învăţământul şi cercetarea în chimie în perioada postbelică. Istoria României, Transilvania-vol II, cap V, Ed. Fundaţiei "George Bariţiu", Cluj-Napoca, ISBN 973-97902-0-8, p. 1167-1162, 1999

3. **Liviu Literat**, Operaţii şi utilaje în industria materialelor oxidice, Ed. Universităţii Babeş-Bolyai, Cluj-Napoca, 425 pag., 1995

4. **Liviu Literat**, Fenomene de transfer şi utilaje în industria chimică. Procese de transport, Ed. Universităţii Babeş-Bolyai, Cluj-Napoca, 177 pag., 1985

5. **Liviu Literat**, Chimie generală, Ed. Didactica şi Pedagogică, Bucureşti, 412 pag., 1975

6. **Liviu Literat**, Studiu fizico-chimic asupra unor alumine reducătoare nestoechiometrice. Teza de doctorat, Univ. Babeş-Bolyai, Cluj-Napoca, 1964

B. University Text Books

1. **Liviu Literat**, Operaţii şi utilaje in industria materialelor oxidice, Ed. Universităţii Babeş-Bolyai, Cluj-Napoca, vol. I, 297 pag., vol II, 129 pag., 1995

2. **Liviu Literat**, Operaţii şi utilaje in industria materialelor oxidice. Aplicaţii, Ed. Universităţii Babeş-Bolyai, Cluj-Napoca, 207 pag., 1994

3. **L. Literat**, R. Mişca, A. Ozunu, S. Drăgan, Fenomene de transfer şi utilaje în industria chimică, Ed. Universităţii Babeş-Bolyai, Cluj-Napoca, 110 pag., 1993

4. **L. Literat**, R. Mişca, A. Ghirişan, Fenomene de transfer şi utilaje in industria chimică. Îndrumar de lucrări practice, Ed. Universităţii Babeş-Bolyai, Cluj-Napoca, 107 pag., 1991

5. T. Bereczky, **L. Literat,** Lucrări practice de chimie generală, Ed. Institutului Politehnic din Cluj-Napoca, 110 pag., 1970

6. **Liviu Literat**, Chimie generală, Ed. Institutului Politehnic din Cluj-Napoca, 375 pag., 1966

7. T. Bereczky, **L. Literat**, E. Felszeghy, Chimie generală. Lucrări practice, Ed. Institutului Politehnic din Cluj-Napoca, 97 pag., 1958

8. T. Bereczky, A. Iacob, **L. Literat,** Chimie Generală (note de curs). Litografia Învăţământului Cluj, 400 pag., 1955

C. **Miscellaneea (Books, chapters and articles on various subjects in books and volumes, monographs)**

1. **Liviu Literat**, Învăţământul tehnic superior la Universitatea Daciei Superioare în concepţia profesorului Vasile Parvan, Lucrările celei de a 3-a Conferinţe Naţionale a Academiei de Ştiinţe Tehnice din România (ASTR), Ed. MEDIAMIRA Cluj-Napoca, Editori: R. Munteanu şi D. Banabic, ISBN 978-973-713-223-9, p. 171-176, 2008

2. **Liviu Literat**, La zi aniversară în Universitatea POLITEHNICA Bucureşti "Catedra de Ştiinţa şi Ingineria Materialelor Oxidice şi Nanomateriale la 60 de ani", Ed. POLITEHNICA Press, 2008

3. D. Fornade, Personalităţi clujene (1800-2007). Dicţionar ilustrat. 678 pag. Ed. Casa Cărţii de Ştiinţă, Cluj-Napoca, ISBN 98-973-133-101-0, (**L. Literat** colaborator), 2007

4. **Liviu Literat**, Alexandra Rus, Virgil Fulicea – Întoarcere în timp, Ed. Casa Cărţii de Ştiinţă, Cluj-Napoca, ISBN 978-973-133165-7, 115 pag., 2007

5. **Liviu Literat**, Şcoala clujeană de inginerie chimică la a 35-a aniversare. Simpozionul Naţional de Inginerie chimică. LUCRĂRI ŞTIINŢIFICE, Ed. ACCENT, Cluj-Napoca, ISBN (13) 978-973-8915-18-3 (autor şi editor), 118 pag., 2006

6. **Liviu Literat**, Rezonanţe ale personalităţii profesorului Şerban Solacolu în învăţământul superior clujean, Academia de Ştiinţe Tehnice din România (colectiv de autori). Ed. AGIR, Bucureşti, p. 43-47, 2005

7. Valeriu Literat, AMINTIRI. Ed. Casa Cărţii de Ştiinţă, Cluj-Napoca, ISBN 973-686-719-6. (**L. Literat**, editor), 177 pag., 2005

8. **Liviu Literat**, A hault on the centenary of an illustrious scientist and school founder, Romanian Journal of Materials, Bucureşti, vol. 35, nr. 3, p. 186-188, 2005

9. **Liviu Literat**, Professor Emilian A. Bratu centenary, Romanian Journal of Materials, vol. 35, nr. 1, p. 84-86, 2005

10. **Liviu Literat**, Învăţământul românesc de inginerie chimică ctitorie a profesorului Emilian A. Bratu, Sesiune omagială "Centenar E. A. Bratu" Bucureşti, p. 20-22, 2004

11. **Liviu Literat**, La centenarul profesorului Emilian A. Bratu. Sesiune omagială "Centenar Emilian A. Bratu", ASTR Bucureşti, p. 23-30, 2004

12. **Liviu Literat**, Homage Paid to associate Professor dr. ing. Lucia Gagea. Romanian Journal of Materials, Bucharest, vol. 34, nr. 2, p. 150-152, 2004

13. **Liviu Literat**, The Chemical Engineering School of Cluj at the 30-th Anniversary, Studia Univ. Babeş-Bolyai, Chemia, vol. XLVI, nr. 1-2, p. 3-4, 2001

14. **Liviu Literat**, The Chemical Engineering Education at Cluj-Napoca in Data and Achive Documents, CD-ROM, Ed. ACCENT, Cluj-Napoca, ISBN 973-99821-8-2 Symposium "30-th years of Chemical Engineering Education at Cluj-Napoca", 2001

15. **Liviu Literat,** Becoming steps. Three Quarters Century of Romanian Chemical Education at the Alma Mater Napocensis, Journal of Building Materials, vol. 26, nr. 2, p. 160-170, 1995

16. **Liviu Literat**, 75 de ani de învăţământ chimic românesc la Alma Mater Napocensis, Rev. Chim., vol. 45, nr. 7, p. 542, 1994

17. **Liviu Literat**, 20 de ani de învăţământ de Inginerie Chimică la Cluj-Napoca, Studia Univ. Babeş-Bolyai, Chemia, vol. XXXVI, nr. 1-2, p. 59-60, 1991

18. **Liviu Literat** (autor şi editor), Breviar Monografic (1971-1991). Facultatea de Chimie şi Chimie Industrială. "Din istoricul învăţământului de inginerie chimică la Cluj-Napoca", Ed. Universităţii Babeş-Bolyai, Cluj-Napoca, p. 14-92, 1991

SCIENTIFIC PUBLICATIONS. ARTICLES

1. **L. Literat**, Modelling of some processes with mass variation. Applications to the separation, classification and characterization of ceramic microdispersions through sedimentation, Romanian Journal of Materials, Bucharest, vol. 38, nr. 4, p. 321-330, 2008

2. L. Szell, **L. Literat**, A. Toth, L. Gagea, Pigmenţi ceramici purpurii cu structură tip fluorină, Simpozion Naţional de Inginerie Chimică, Cluj-Napoca, Ed. ACCENT, Cluj-Napoca, ISBN (13)- 978-973-8915-18-3, p. 63-66, 2006

3. A. Orban, **L. Literat**, Consideraţii privind presarea axială a pulberilor ceramice, Simpozion Naţional de Inginerie Chimică, Cluj-Napoca, Ed. ACCENT, p. 67-71, 2006

4. C. Voica, L. Gagea, **L. Literat**, Glazuri ceramice cu efecte speciale pentru porţelan fosfatic, Simpozion Naţional de Inginerie Chimică, Cluj-Napoca, Ed. ACCENT, p. 78-84, 2006

5. F. Goga, **L. Literat**, C. Suciu, Glasses in the SiO_2-B_2O_3-Bi_2O_3 system, Reliability of Ceramics ECERS, Polish Ceramic Society, Cracow, (P.E 01), 2006

6. F. Goga, **L. Literat**, M. Gorea, C. Suciu, Immiscibility in the SiO_2-B_2O_3-Bi_2O_3 system, The 32-th Conference SSCHE, Tatranske Matliare (SK), Proceedings CD-ROM, p. 241-246, 2005

7. F. Goga, **L. Literat**, C. Suciu, M. Mocean, PbO free frits for ceramic colorants, Romanian International Conference on Chemistry and Chemical Engineering RICCCE XIV, Science and Engineering of Oxide Materials, Proceedings vol. 1, p. S08-71-78, 2005

8. F. Goga, **L. Literat**, M. Gorea, C. Suciu, The immiscibility in the SiO_2-B_2O_3-Bi_2O_3 system, Romanian International Conference on Chemistry and Chemical Engineering RICCCE XIV, Proceedings vol. 1, p. S08-202-210, 2005

9. A. Toth, C. Dardai, L. Szell, L. Gagea, **L. Literat**, Structure of thin porous layers obtained from reactive powders, Romanian Journal of Materials, vol. 34, nr. 2, p. 90-98, 2004

10. A. Toth, **L. Literat**, R. Mişca, V. Dumbraveanu, C. Neagu, Asimetrical membranes with application for wine clearing and stabilizing, Romanian Journal of Materials, vol. 34, nr. 3, p. 196-205, 2004

11. L. Szell, **L. Literat**, L. Gagea, Cr. Dardai, A. Toth, Study on the synthesis and properties of the ceramic pigments in the CeO_2-PrO_2 system, Romanian Journal of Materials, vol. 34, nr. 3, p. 183-189, 2004

12. A. Orban, M. Turos, **L. Literat**, Considerations about the axial pressing moulding method for grinding parts, Romanian Journal of Materials, vol. 34, nr. 4, p. 183-189, 2004

13. A. Toth, **L. Literat**, R. Mişca, R. Dumbraveanu, C. Neagu, Asymetric ceramic membranes with application in wine clarification and stabilisation, CONSILOX IX, Ceramics, Sighişoara, p. 185-196, 2004

14. L. Szell, Cr. Dardai, A.Toth, **L. Literat**, L. Gagea, Stady on the synthesis and properties of the ceramic pigments in the CeO_2-PrO_2 system, CONSILOX IX, Ceramics, Sighişoara, p. 89-94, 2004

15. **L. Literat**, A. Orban, A study of the behaviour of some superaluminous powders at the shaping by isostatic and axial pressing, CONSILOX IX, Ceramics, Sighişoara, p. 159-170, 2004

16. A. Orban, **L. Literat**, M. Turos, Grinding parts shaped by axial pressing, CONSILOX IX, Ceramics, Sighişoara, p. 171-184, 2004

17. A. Toth, **L. Literat**, R. Mişca, Hydraulic strenght of the oxide membranes and gel layer, at convective transport of the aqueous dispersions, Romanian Journal of Materials, vol. 33, nr. 3, p. 234-241, 2003

18. **L. Literat**, A. Orban, The behaviour of some superaluminous ceramic powders atomised in the process of isostatic pressing, Romanian Journal of Materials, vol. 33, nr. 4, p. 270-277, 2003

19. A. Toth, R. Mişca, L. Gagea, A. Ozunu, **L. Literat**, Cross-flow separation of some heterogeneous systems through filtering on ceramic membranes, The 29-th Conference SSCHE, Tatranske Matliare (Sk) CD-ROM, p. 27-31, 2002

20. **L. Literat**, L. C. Bodizs, The influence of humidity on the rheological behaviour of ceramic powders in the pressing process, Romanian Journal of Materials, vol. 32, nr.1, p. 54-59, 2002

21. **L. Literat**, Recording device and exploring procedure of the settling curves. Applications to the Symptotic classifying of powdery systems, Studia Univ. Babeş-Bolyai, Chemia, vol. XLVI, nr. 1-2, p. 5-10, 2001

22. A. Toth, **L. Literat**, L. Gagea, Pore structure stability of alumina bazed membranes, Studia Univ. Babeş-Bolyai, Chemia, vol. XLVI, nr. 1-2, p. 11-16, 2001

23. **L. Literat**, Procedure of computerized recording of the settling curves. Application at the symptotic classifying of powdery systems, "30 years of Chemical Engineering Education at Cluj-Napoca", Ed.ACCENT Cluj-Napoca, CD ROM, 2001

24. A. Toth, **L. Literat**, L. Gagea, Pore structure stability of alumina based membrane, "30 years of Chemical Engineering Education at Cluj-Napoca", Ed. ACCENT Cluj-Napoca, CD ROM, ISBN-973-99821-8-2, 2001

25. **L. Literat**, Considerations on some mathematics models with application to the press-forming of ceramic powders, Ed. ACCENT Cluj-Napoca, CD ROM, 2001

26. A. Toth, I. Kotsis, K. Belofine-Bako, **L. Literat**, L. Gagea, Oxide membranes with selective layer organic-mineral, CONSILOX VIII, Alba-Iulia, vol. 1, p. 203-208, 2000

27. **L. Literat**, A. Ghirişan, The rheological behaviour of some silicate sol-gel systems, CONSILOX VIII, Alba-Iulia, vol. 1, p. 20-26, 2000

28. **L. Literat**, M. Cristea, L. Gagea, C. Pavel-Voica, Shaping by pressing of some ceramic powders. Diagrams and computing equations, CONSILOX VIII, Alba-Iulia, vol. 1, p. 290-295, 2000

29. C. Vasile, **L. Literat**, L. Gagea, L. Szell, Ceramic mass with ZrO_2 content and thermo-mechanics properties, CONSILOX VIII, Alba-Iulia, vol. 1, p. 27-32, 2000

30. **L. Literat**, A. Toth, M. Lascu, L. Gagea, Application of the ceramic membranes on the selective separation processes, Papers of the 2-nd International Symposium on Chemical Engineering Bucharest, SICHEM 2000, p. 49-56, 2000

31. **L. Literat**, A. Toth, M. Lascu, L. Gagea, Application of the ceramic membranes on the selective separation processes. Papers of the 2-nd International Symposium on Chemical Engineering Bucharest, SICHEM 2000, p. 49-56, 2000

32. **L. Literat**, I. Mureşan, P. Mureşan, Automatic determination of vapors adsorption isotherms on porous solids, Acta Technica Napocensis Section Constr. Machines and Materials, vol. 2, p. 139-146, 1999

33. A. Ozunu, **L. Literat**, L. Ghergari, L. Gagea, Kinetic models for gypsum dehydration, Journal of Building Materials, vol. 28, nr. 1, 1999

34. C. Pavel, L. Gagea, **L. Literat**, Glazuri mate pentru porţelan fosfatic, Analele Univ. Oradea, Chimie, p. 11-19, 1999

35. F. Goga, L. Gagea, **L. Literat**, M. Moceanu, Matrici vitoase cu fusibilitate ridicată, Analele Univ. Oradea, Chimie, p. 39-45, 1999

36. A. Ghirişan, **L. Literat**, Rheologic evolution of some sol-gel systems, International Conference on Chemistry and Chemical Engineering, POLITECHNICA University Bucharest, CD-ROM, p. 203-208, 1999

37. A. Ozunu, **L. Literat**, R. Mişca, Investigation of Gypsum Dehydration, The 1-st International Conference of the Chemical Societies of the South-East European Countries. Chemical Sciences and Industry, Greece, vol. 1, p. 103-105, 1998

38. A. Ozunu, **L. Literat**, R. Mişca, The materials moving in the drum rotary equipments. The influence of operational variables on the hold-up time distribution, Journal of Building Materials, vol.3, p. 197-203, 1998

39. **L. Literat**, F. Bele, L. Gagea, E. Koncz, Frite ceramice fusibile fără conţinut de metale toxice, Analele Univ. Oradea, Chimie, p. 113-119, 1998

40. R. Mişca, **L. Literat**, A. Ozunu, Appreciation of the rate determinant stage at non stationary extraction from porous medium through the general dimensional analysis, Chem. Bull. „Politechnica" Univ. Timişoara, vol. 43(57), p. 321-325, 1998

41. R. Mişca, **L. Literat**, A. Ozunu, Heat transfer in non steady state in liquid medium, Chem. Bull. „Politechnica" Univ. Timişoara, vol. 43(57), p. 326-332, 1998

42. A. Ozunu, **L. Literat**, R. Mişca, S. Drăgan, Parametric investigation of gypsum dehydration in a rotary drum reactor. Conference on Materials and Manufacturing Technologies (II), MACHTEHN '98, Polytechnic University Cluj-Napoca, p. 215-220, 1998

43. R. Mişca, **L. Literat**, A. Ozunu, S. Drăgan, General dimensional analysis applied to the unsteady dissolution of pure solids, Papers of the 1-st International Chemical Engineering Symposium SICHEM. '98, Bucharest, p. 134-141, 1998

44. R. Mişca, **L. Literat**, A. Ozunu, S. Drăgan, General dimensional analysis applied to the unsteady extraction from porous solid medium under the ultra sound action, Papers of the 1-st International Chemical Engineering Symposium SICHEM '98, Bucharest, p. 178-183, 1998

14

45. A. Ozunu, **L. Literat**, R. Mişca, S. Drăgan, Scale-up of the rotary drum reactors. Applications to the non catalytic gas-solid processes devolving at low temperatures, Papers of the 1-st International Chemical Engineering Symposium SICHEM '98, Bucharest, p. 192-201, 1998

46. A. Ozunu, **L. Literat**, R. Mişca, S. Drăgan, Comparative study on the macro kinetic and mathematics modeling of the sodium bicarbonate thermal decomposition and of the natural gypsum dehydration, Papers of the 1-st International Chemical Engineering Symposium SICHEM '98, Bucharest, p. 202-211, 1998

47. **L. Literat**, A. Toth, L. Gagea, A. Sintoma, Structural and functional characteristics of some micro filtering oxide membranes, Papers of the 1-st International Chemical Engineering Symposium SICHEM '98, Bucharest, p. 394-401, 1998

48. **L. Literat**, C. Voica, L. Gagea, Study on the crystallization process in matte glazes for the phosphate porcelain, STICLOCERAM '98, Technical University Cluj-Napoca, p. 112-116, 1998

49. A. Ozunu, R. Mişca, **L. Literat,** Parametric investigation of sodium bicarbonate decomposition in a rotary drum reactor, Studia Univ. Babeş-Bolyai, Chemia, vol. XLII, nr. 2, p. 255-262, 1997

50. A. Ozunu, R. Mişca, **L. Literat,** Experimental aspects on the thermal decomposition of sodium bicarbonate in a rotary drum reactor, National Conference of Chemistry and Chemical Engineering, Politechnica University Bucharest, vol. 1, pag. 540-545, 1997

51. A. Ozunu, **L. Literat**, R. Mişca, M. Ozunu, Pulverous materials motion in the rotary drum equipments, National Conference of Chemistry and Chemical Engineering, Politechnica University Bucharest, vol. 1, p. 583-588, 1997

52. R. Mişca, A. Ghirişan, **L. Literat**, A. Ozunu, S. Drăgan, The kinetic of solid-liquid extraction. Hypophae fructus oil, Studia Univ. Babeş-Bolyai, Chemia, vol. XLI, nr. 1, p. 55-60, 1996

53. **L. Literat**, L. Gagea, E. Mirică, J. Ţipan, Alternative proceeding for granulometric analysis of powdery dispersions, Journal of Building Materials, vol. 24, nr. 2, p. 132-137, 1995

54. T. Klainhempel, F. Atanasiu, **L. Literat,** Dimensionarea tehnologică a instalaţiilor PSA. Model de echilibru pentru dimensionarea coloanelor PSA, Rev. Chim, vol. 46, nr. 8, p. 756-764, 1995

55. **L. Literat**, A. Ozunu, R. Mişca, A. Ghirişan, Discrimination method for sedimentation regimes with application in the symptotyc classification, Proceedings Academic Days Timişoara, Section Chemical Sciences, vol. 2, p. 27-30, 1995

56. A. Ozunu, **L. Literat,** Considerations about fluid catalytic cracking. Modeling and control, Selected topics on Chemical Reaction Engineering, Bratislava, Slovakia, p. 202, 1994

57. R. Mişca, **L. Literat,** Hypophae fructus oil separation, Selected topics on Chemical Reaction Engineering, Bratislava, Slovakia, p. 203, 1994

58. **L. Literat,** Corelări privind regimul, viteza şi dimensiunile particulelor în analiza sedimentometrică, Rev. Chim., vol. 45, nr. 10, p. 921-922, 1994

59. **L. Literat**, E. Mirica, L. Gagea, F. Bele, Proprietăţile filmelor subţiri de titanat de bariu obţinute prin metoda sol-gel, Simpozionul de Ştiinţe Moderne şi Energie, Universitatea Tehnică Cluj-Napoca, p. 39-41, 1993

60. **L. Literat,** Korindonische unterlagen fur maleische Anhydrid Katalyzatoren, Studia Univ. Babeş-Bolyai, Chemia, vol. XXXVII, nr. 1, p. 99-104, 1992

61. **L. Literat,** Relaţii criteriale privind transportul difuziv-convectiv în procese staţionare şi nestaţionare, Comunicări ştiinţifice, Aparate şi automatizări în industria chimică, Timişoara, vol. II, p. 5-12, 1991

62. **L. Literat,** Neue kriterielle Abfassungen im stationaren konvektiv-molekularen Eigenschafts Transport, Studia Univ. Babeş-Bolyai, Chemia, vol. XXXV, nr.2, p. 51-54, 1990

63. **L. Literat,** Uber einige kriterielle Beziehungen in nichtstationaren konductiv-konvektiven Eigenschafts transport, Studia Univ. Babeş-Bolyai, Chemia, vol. XXXV, nr. 1, p. 99-103, 1990

64. **L. Literat,** Electro-corindonul poros, suport pentru catalizatori, Revista Materiale de Construcţii, vol.19, nr. 4, p. 246-249, 1989

65. **L. Literat**, D. Vasilescu, Suporturi catalitice pentru anhidrida ftalică, Revista Materiale de Construcţii, vol.18, nr. 3, p. 204-207, 1988

66. N. Almaşi, J. Mureşan, **L. Literat**, E. Cîmpan, F. Kakso, C. Viragh, I. Batiu, Structura şi morfologia unor pulberi de carbonat de nichel, Conferinţa Naţională de Metalurgie a Pulberilor (III), Institutul Politehnic Cluj-Napoca, vol. 2, p. 25-30, 1988

67. **L. Literat**, T. Farcaş, N. Farbas, D. Literat, E. Cîmpean, F. Kacso, N. Almaşi, V. Corbeanu, Investigaţii de microscopie electronică asupra unor dispersii de carbonat de nichel, Conferinţa Naţională de Metalurgie a Pulberilor (III), Institutul Politehnic Cluj-Napoca, vol. 2, p. 31-36, 1988

68. **L. Literat**, N. Farbas, M. Lazar, D. Literat, E. Bodis, Forma disribuţiei particulelor pulberilor de carbonat de nichel, Conferinţa Naţională de Metalurgie a Pulberilor (III), Institutul Politehnic Cluj-Napoca, vol. 3, p. 15-18, 1988

69. **L. Literat,** Electronenmikroscopische Untersuchung einiger Feuerfestmassen die als katalytische Trager Wirken, Keramische Zeitschrift, 6, p. 378-381, 1987

70. **L. Literat**, D. Vasilescu, Mase ceramice superaluminoase cu liant mulitic şi porozitate controlată ca suport catalitic, Revista Materiale de Construcţii, vol.16, nr. 1, p. 47-50, 1986

71. **L. Literat**, N. Farbas, Investigaţii asupra silicaţilor prin intermediul analizei microelectronice, Revista Materiale de Construcţii, vol.16, nr. 2, p. 140-142, 1986

72. **L. Literat,** Microstructura, compoziţia şi textura unor cimenturi uşoare cu granulit, Revista Materiale de Construcţii, vol.16, nr. 2, p. 89-94, 1986

73. **L. Literat,** Studiul microscopiei electronice asupra unor suporturi catalitice refractare, Revista Materiale de Construcţii, vol. 15, nr. 2, p. 89-91, 1985

74. **L. Literat**, S. Gocan, E. Ursu, Caracteristici de suprafaţă şi cromatografice ale silicagelului RIE, Studia Univ. Babeş-Bolyai, Chemia, vol. XXVIII, nr. 1, p. 52-55, 1983

75. **L. Literat**, V. Cuciurean, I. Dragomir, Investigaţii reologice a unor dispersii ceramice în câmp ultrasonic, Studia Univ. Babeş-Bolyai, Chemia, vol. XXVIII, nr. 1, p. 56-59, 1983

76. **L. Literat**, N. Farbas, Investigaţii ale microscopiei electronice asupra unor depuneri metalice pe suporţi silico-aluminoşi, Conferinţa Naţională de Metalurgie a Pulberilor (II), Institutul Politehnic Cluj-Napoca, vol. 3, p. 135-140, 1983

77. **L. Literat**, A. Motiu, N. Farbas, Microstructura, compoziţia şi textura unor ceramici sinterizate, Conferinţa Naţională de Metalurgie a Pulberilor (II), Institutul Politehnic Cluj-Napoca, vol. 3, p. 141-146, 1983

78. **L. Literat,** Studiul unor zeoliţi naturali indigeni, Simpozionul Naţional - Zeoliţii în Tehnologia Modernă, Iaşi, p. 417-423, 1983

79. **L. Literat**, A. Barbat, E. Baditoiu, Indigene volcanic tuffs as anti agglomerating agents for nitrogenous fertilizer, Conference Permanente des Ingineurs de Sud-Est de l' Europe COPISEE (II), Section 3, p. 343-350, Cluj-Napoca, Romania, 1983

80. **L. Literat**, A. Barbat, I. Batiu, Zeolite antiagglomerating agents for mineral fertilizer. Protection mechanisms, Conference Permanente des Ingineurs de Sud-Est de l'Europe COPISEE (II), Sec. 3, p. 551-561, Cluj Napoca, Romania, 1983

81. **L. Literat**, T. Farcaş, C. Dasoveanu, M. Stanciu, Metoda analizei microscopiei electronice asupra structurii şi compoziţiei unor catalizatori pentru procese petrochimice, Lucrările ştiinţifice ale ICITPR Ploieşti, p. 4-10, 1983

82. **L. Literat**, J. Gros, Răşini schimbătoare de ioni cu structură de stiren şi divinil benzen, Contribuţii în Chimie, Simpozionul Naţional Cluj-Napoca, p. 65-68, 1982

83. **L. Literat**, A. Moţiu, T. Farcaş, Catalizatori pentru etilen oxid. Investigaţii microstructurale. Contribuţii în Chimie, Simpozionul Naţional Cluj-Napoca, p. 69-71, 1982

84. **L. Literat,** Procedee de sorbţie aplicate pentru investigarea caracteristicilor de suprafaţă şi texturale ale solidelor, Academia Română, Series 4, nr. 2, p. 67-89, tome 4, 1981 (prezentare acad. Emilian A. Bratu)

85. **L. Literat**, S. Gocan, E. Ursu, Caracteristici de suprafaţă ale silicagelului cromatografic R tratat termic şi chimic, Studia Univ. Babeş-Bolyai Cluj, Chemia, vol. XXV, nr. 1, p. 67-71, 1980

86. **L. Literat**, L. Marta, Cercetări asupra pietrei de ciment din betoanele uşoare cu granulit, Schimb experimental cu Laboratoarele de Inginerie Civilă Tg. Mureş, vol. 1, p. 110-116, 1979

87. **L. Literat**, M. Langa, Cercetări experimentale privind posibilităţile de caracterizare structurală a unor solide poroase şi pulverulente utilizând date cinetice, Schimb experimental cu Laboratoarele de Inginerie Civilă Tg. Mureş, vol. 1, p. 215-220, 1979

88. **L. Literat**, J. Gros, Schimbători de ioni macroporoşi indigeni. Caracteristici texturale, Studia Univ. Babeş-Bolyai, Chemia, vol. XXIII, nr. 1, p. 58-60, 1978

89. **L. Literat**, O. Negru, Procedeu de calcul şi reprezentare programată a distribuţiei volumului porilor în solide poroase şi pulverulente, Studia Univ. Babeş-Bolyai Cluj, Chemia, vol. XXIII, nr. 2, p. 47-51, 1977

90. **L. Literat,** Caracteristici fizice şi structurale ale unor cimenturi expandate, Lucrările ştiinţifice ale I.P.C., C1, p. 375-379, 1978

91. **L. Literat**, V. Cuciurean, Reziduuri ale fabricării acetilenei din carbit utilizate ca materiale de construcţii, Lucrările ştiinţifice ale I.P.C., p. 390-393, 1978

92. **L. Literat**, J. Gros, Caracteristici superficiale şi de structură ale unor răşini schimbătoare de ioni indigene, Studia Univ. Babeş-Bolyai Cluj, Chemia, vol. XXII, 1, p. 3-7, 1977

93. **L. Literat,** Modificări de stoechiometrie induse de sorptţia amoniacului gazos pe alumine, Studia Univ. Babeş-Bolyai Cluj, Chemia, vol. XXII, nr. 1, p. 8-10, 1977

94. **L. Literat**, O. Negru, Procedeu de calcul pentru determinarea ariei specifice şi a distribuţiei porilor în solide poroase şi pulberi, Studia Univ. Babeş-Bolyai Cluj, Chemia, vol. XXII, nr. 1, p. 61-64, 1977

95. **L. Literat**, V. Cuciurean, Studiul fizico-chimic al unor argile coloidale montmorillonitice. Bentonita de la Săndulești-Turda, Studia Univ. Babeş-Bolyai, Cluj, Chemia, vol. XXII, nr. 2, p. 43-46, 1977

96. **L. Literat**, O. Negru, Procedeu de calcul pentru caracterizarea unor pulberi texturate, Conferința Națională de Metalurgice a Pulberilor (I), Cluj-Napoca, Comunicări ştiințifice, vol. 1, p. 45-50, 1975

97. **L. Literat,** Considerații asupra unor metode cinetice de sorbție pentru solide poroase şi pulberi, Conferința Națională de Metalurgie a Pulberilor (I), Cluj-Napoca, Comunicări ştiințifice, vol. 1, p. 51-55, 1975

98. **L. Literat**, V. Cuciurean, Studii termoanalitice privind oxidarea unor aliaje de Ag-Cd alloys, Conferința Națională de Metalurgie a Pulberilor (I), Cluj-Napoca, Comunicări ştiințifice, vol. 3, p. 19-22, 1975

99. **L. Literat,** Investigations des solids poreux par mesurages cinetiques de sorbtion, Comte Rendu du Colloque International RILEM/IUPAC - Structure des pores et proprietees des materiaux, C, p. 129-138, Prague, Czekoslovakia, 1973

100. **L. Literat,** Proprietăți electrice ale unor catalizatori montmorillonitici, Buletinul Ştiințific al I.P.C., nr.13 bis, p. 75-78, 1971

101. **L. Literat**, V. Cuciurean, Studii privind aplicarea unor metode simple pentru determinarea suprafețelor specifice ale cimenturilor, Buletinul Ştiințific al I.P.C., nr.13 bis, p. 79-83, 1971

102. **L. Literat,** Suprafața acidă a unor alumine sărace în oxigen, Lucrările ştiințifice ale I.P.C., p. 145-148, 1971

103. **L. Literat**, V. Cuciurean, Studii termo-analitice ale unor pulberi pe bază de aliaje de Ag-Cd, Lucrările ştiințifice ale I.P.C., p. 149-152, 1971

104. **L. Literat**, V. Cuciurean, Studiul cinetic al oxidării unor pulberi pe bază de aliaje de Ag-Cd, Lucrările ştiințifice ale I.P.C., p. 153-156, 1971

105. **L. Literat**, V. Cuciureanu, Criteres cinetiques dans l'etude d'oxidation des alliages d'Ag-Cd pulverulents, 39-eme Congres International de Chimie Industrielle, Bucharest, 3, p. 71-75, 1970

106. **L. Literat,** Studiul termo-analitic şi cinetic al descompunerii metil-aluminelor, Buletinul Ştiințific al I.P.C., nr.12, p. .111-1184, 1969

107. E. Stoicovici, E. Felszeghy, **L. Literat**, P. Krobl, E. Vermesan, L. Nagy, Contribuții la studiul argilelor coloidale din R.S.R. (IX). Argila de la Sindominic-Ciuc, Studia Univ. Babeş-Bolyai Cluj, Chemia, vol. XIII, nr. 2, p. 111-118, 1968

108. **L. Literat,** Deviations from stoichiometry and structural modifications of some aluminae, Revue Roumaine de Chemie, nr. 13, p. 1161-1167, 1968

109. E. Felszeghy, M. Ilies, P. Krobl, **L. Literat**, L. Nagy, E. Stoicovici, Contribuţii la studiul argilelor coloidale din R.P.R. (VIII). Bentonite din Ciugud, Alba, Studia Univ. Babeş-Bolyai Cluj, Chemia, vol. XIII, nr. 1, p. 9-17, 1968

110. **L. Literat,** Donnees thermoanalytiques sur la nonstoechimetrie de quelques alumines noires reductrices, Revue Roumaine de Chimie, nr. 13, p. 731-737, 1968

111. **L. Literat,** Activitatea catalitică şi structura suprafeţei unor alumino-silicaţi, Buletinul Ştiinţific al I.P.C., nr.11(1), p. 117-123, 1968

112. **L. Literat,** Activitatea catalitică a unor alumine nestoechiometrice reducătoare, Buletinul Ştiinţific al Institutului Politehnic Bucureşti, tome 29, nr. 3, p. 65-75, 1967

113. E. Felszeghy, M. Ilies, P. Krobl, **L. Literat**, L. Nagy, E. Stoicovici, Contribuţii la studiul argilelor coloidale din R.P.R. (VII). Bentonita de la Gura-Sada – Hunedoara, Studia Univ. Babeş-Bolyai Cluj, Chemia, vol. XII, nr. 2, p. 43-48, 1967

114. **L. Literat,** L'activitee catalytique des certaines alumines nonstoechio-metriques, Revue Roumaine de Chemie, nr. 12, p. 1213-1222, 1967

115. **L. Literat,** Studii de resonanţă magnetică şi a conductivităţii electrice cu variaţia presiunii de oxigen a unor alumine reducătoare nestoechimetrice, Analele Universităţii Bucureşti, Seria Ştiinţele Naturii, nr. 1, p. 49-63, 1965

116. E. Felszeghy, **L. Literat**, A. Covaci, Un aparat simplu pentru dozarea carbonatului. Note de laborator, Studia Univ. Babeş-Bolyai Cluj, Chemia, vol. X, nr. 1, p. 145-146, 1965

117. **L. Literat,** Contribuţii la problema nestoechiometriei oxizilor refractari. Studii asupra caracteristicilor magnetoelectrice ale unor alumine nestoechiometrice reducătoare, Rev. Chim, vol. 16, nr.5, p. 262-268, 1965

118. **L. Literat,** Noi date privind nestoechiometria aluminelor. Variaţia izotermală a conductivităţii electrice cu persiunea oxigenului, Lucrările ştiinţifice ale Institutului Politehnic Cluj (I.P.C.), nr. 7, p. 87-94, 1964

119. **L. Literat,** Studiul aluminelor nestoechiometrice reducătoare prin rezonanţă electro-magnetică, Lucrările ştiinţifice ale I.P.C., nr. 7, p. 95-101, 1964

120. E. Felszeghy, M. Ilies, P. Krobl, **L. Literat**, L. Nagy, E. Stoicovici, Contribuţii la studiul unor argile coloidale din R.P.R. (VI). Bentonita de la Oraşul Nou, Studia Univ. Babeş-Bolyai Cluj, Chemia, vol. VIII, nr. 1-2, p. 93-103, 1963

121. **L. Literat,** Studiul fizico-chimic al aluminei nestoechiometrice, Lucrările ştiinţifice ale I.P.C., nr. 6, p. 119-126, 1963

122. E. Felszeghy, M. Ilies, **L. Literat**, L. Naghy, E. Stoicovici, I. Soos, Contribuţii la studiul unor argile coloidale din R.P.R. (V). Bentonita de la Ocna Mureş, Studia Univ. Babeş-Bolyai Cluj, Chemia, vol. VII, nr. 1-2, p. 87-98, 1962

123. **L. Literat,** Contribuţii la studiul aluminei nestoechiometrice (II). Studiul proprietăţilor electrice, Buletinul Ştiinţific al I.P.C., nr.5, p. 95-105, 1962

124. **L. Literat,** Contribuţii la studiul aluminei nestoechiometrice (I). Condiţii de obţinere a aluminei reducătoare, Buletinul Ştiinţific al I.P.C., nr. 5, p. 81-93, 1962

125. **L. Literat,** Descompunerea acidului formic cu alumine reducătoare nestoechiometrice, Buletinul Ştiinţific al I.P.C., nr. 5, p. 107-118, 1962

126. **L. Literat,** Consideraţii la determinarea ariei specifice a cimentului, Buletinul Ştiinţific al I.P.C., nr. 4, p. 103-111, 1961

127. T. Bereczky, **L. Literat,** O nouă metodă de studiu aplicată nisipurilor pentru turnare, Lucrările ştiinţifice ale Institutului Politehnic Cluj, nr. 3, p. 69-79, 1960

128. E. Felszeghy, **L. Literat**, E. Stoicovici, M. Ilies, M. Kulcsar, L. Nagy, Contribuţii la studiul argilelor coloidale din R.P.R. (IV), Noi date despre bentonita de la Cugir, Studia Univ. Babeş-Bolyai Cluj, Chemia, vol. IV, nr. 1-2, p. 175-192, 1959

129. E. Felszeghy, **L. Literat**, E. Stoicovici M. Ilies, M. Kulcsar, L. Nagy, Contribuţii la studiul argilelor coloidale din Republica Populară Română (III). Bentonitele de la Tg. Lăpuş şi Izvorul Oltului, Lucrările ştiinţifice ale I.P.C., nr. 2, p. 159-169, 1959

130. E. Felszeghy, M. Ilies, M. Kulcsar, **L. Literat**, L. Nagy, E. Stoicovici, Contribuţii la studiul argilelor coloidale din R.P.R. (II). Lucrările ştiinţifice ale I.P.C., nr. 2, p. 145-157, Romania, 1959

130. E. Felszeghy, **L. Literat,** Izotermele de adsorbţie ale vaporilor de metanol pe argile coloidale, Lucrările ştiinţifice ale I.P.C., nr. 2, p. 171-179, 1959

132. **L. Literat,** Contribuţii la metodologia adsorbţiei vaporilor şi gazelor, Lucrările ştiinţifice ale I. P.C., nr.2, p. 181-189, 1959

133. E. Felszeghy, M. Ilies, M. Kulcsar, **L. Literat**, L. Nagy, E. Stoicovici, Contribuţii la studiul argilelor coloidale din R.P.R. (I), Lucrările ştiinţifice ale I.P.C., nr. 1, p. 31-46, 1958.

Dedicated to Professor Liviu Literat, at his 80th anniversary

PROCAINE EFFECTS ON SURFACE TOPOGRAPHY OF SPREAD DIPALMITOYL PHOSPHATIDYLCHOLINE MONOLAYERS

PETRE T. FRANGOPOL[a], D. ALLAN CADENHEAD[b], MARIA TOMOAIA-COTIŞEL[c*] AND AURORA MOCANU[c]

ABSTRACT. The surface topography of dipalmitoyl phosphatidylcholine (DPPC) monolayers, spread at the air/water interface, in the absence and the presence of procaine, has been investigated by self-assembly Langmuir-Blodgett (LB) technique and atomic force microscopy (AFM), operating in tapping mode. The LB monolayers were transferred on mica, at a controlled surface pressure, characteristic for the liquid expanded to liquid condensed phase transition of pure DPPC monolayers. Our data indicate that procaine penetrates into and specifically interacts with DPPC monolayers stabilizing the phospholipid membrane interface.

Keywords: DPPC, procaine, monolayers, AFM, LBT, phase transition

INTRODUCTION

Changes in physical and chemical properties of lipid membranes due to the distribution of local anesthetics within these membranes are of a major importance [1-4] for understanding the molecular mechanism of anesthesia. In spite of numerous investigations, the molecular mechanism of anesthesia and the involved interfacial phenomena in anesthetics action are still not well understood [5]. As a first step, the anesthetics action presumes that the anesthetic molecules modify the lipid membrane structure and thus, they change the biological membrane properties [5].

---

[a] *Institutul Național de Fizică şi Inginerie Nucleară Horia Hulubei, Str. Atomiştilor, Nr. 407, Măgurele-Bucureşti, Romania*
[b] *State University of New York at Buffalo, Department of Chemistry, 410 NSC, Buffalo, NY 14260-3000, USA*
[c] *Universitatea Babeş-Bolyai, Facultatea de Chimie şi Inginerie Chimică, Str. Kogălmiceanu, Nr. 1, RO-400084 Cluj-Napoca, Romania, mcotisel@chem.ubbcluj.ro*

Previously, we have reported that the local anesthetics, like procaine, expand the lipid monolayers spread at the air/water interface, at low and intermediate surface pressures, depending on the pH's, ionic strengths and surface characteristics of the chosen lipid [6-24].

The interfacial characteristics of the mixed lipid and procaine monolayers results from the adsorption on and the penetration of procaine into lipid membrane models in substantial agreement with other related published data [1-5, 22-29].

The objective of the present work is to analyse the effects of procaine on the structural and topographical characteristics of lipid monolayers using atomic force microscopy (AFM) and Langmuir-Blodgett technique (LBT). We have chosen a synthetic phospholipid, namely L-α dipalmitoyl phosphatidyl choline (1, 2-dipalmitoyl -sn- glycero-3-phospho-choline: DPPC), which forms stable monolayers at fluid interfaces [30-32]. Here, we investigate the structure and surface topography of the DPPC monolayers spread on aqueous solution in the absence and the presence of procaine and the formation of liquid condensed domains is evidenced.

RESULTS AND DISCUSSION

The surface pressure versus mean molecular area isotherms were recorded for pure DPPC monolayers, spread at the air/water (pH 5.6) interface, and for mixed DPPC and procaine monolayers, obtained by spreading DPPC monolayers on procaine (10^{-3} M) aqueous phase (pH 5.2), at 20 ^{o}C. For pure DPPC monolayer, the compression isotherm shows a phase transition at a lateral surface pressure of about 8 mN/m, from liquid expanded (LE) to liquid condensed (LC) state [30]. The mixed DPPC and procaine monolayer also presents a LE/LC phase transition, evidenced on compression isotherm, at around 15 mN/m.

In addition, the compression isotherms show a collapse phenomenon at very high surface pressures, characterized by collapse area (A_c) and collapse pressure (π_c). The collapse characteristics and the limiting molecular areas (A_0), characterizing the LC phase of DPPC monolayers, are given in Table 1.

Table 1. Surface characteristics of DPPC monolayers spread at the air/water interface both in the absence and in the presence of procaine (P) in aqueous phase.

Monolayer	P (M)	A_0 (Å^2)	A_c (Å^2)	π_c (mN/m)
DPPC	0	54	42	55
DPPC and P	10^{-3}	78	42	63

From Table 1, it is observed the expanded effect of procaine, namely the limiting molecular area (A_0) for LC state and the collapse pressure (π_c) are much higher in the presence of procaine than for pure DPPC monolayers. These data indicate that procaine has a notable effect both on the DPPC phase transition and on the collapse of DPPC monolayers, at the air/water interface. Due to the same collapse areas, (A_c), it is found that the procaine is excluded from DPPC monolayers at collapse, but still remains adsorbed on DPPC monolayer surface thus, increasing the monolayer collapse pressure and stability. This effect might correspond to pressure-driven exclusion of procaine from zwitterionic DPPC monolayers.

Similar expansion effects were previously reported for octadecanoic acid [22, 24] and for tetradecanoic acid [23] spread on procaine aqueous phase. The magnitude of the effect increased with increasing procaine concentration in the aqueous phase.

The surface topography of pure DPPC monolayers, transferred at 8 mN/m on mica surface, is given in the AFM images, Figs. 1 and 2. The 2D topographies show a heterogeneous DPPC monolayer with characteristic features and the domains formation is clearly evidenced.

Brighter areas (Figs. 1 and 2) are assigned for high domains of the DPPC in LC state, but darker areas correspond to lower domains characteristic for LE phase. The boundaries of DPPC domains are typically observed and are thought to be the borders between various DPPC areas with different tilt of molecular orientations [19, 30, 32]. We suggest that the lighter domains correspond to well organized probably almost vertically oriented DPPC molecules, while the darker areas correspond to less orderly DPPC molecules. The LC domains are distributed within the LE matrix of DPPC monolayers.

The analysis of surface topographies, Figs. 1 and 2, clearly indicate the phase separation between LC and LE phases, which is consistent with the two surface phase transition recorded at the lateral surface pressure of 8 mN/m, as it is evidenced on compression isotherms. The AFM images of DPPC monolayers show nano island LC domains (with long axis of isolated 20 nm up to 100 nm domains, Fig. 1B). The large LC domains are observed in Figs. 1A and 2 (with long axis from 500 nm up to 2 and 3 µm). Also, micro islands of LC phase are identified particularly at big scanned areas (e.g., 25 µm x 25 µm) with major axis up to 3 or even 8 µm.

The large LC domains are almost circular or elongated (Fig. 1A and Fig. 2A). The nano LC domains are predominantly circulars, square or elongated associated as asymmetric clusters, like windmill shape (Fig. 1B and 2) as previously observed by fluorescence microscopy [23], by direct compression of DPPC monolayer at the air/water interface. The large LC domains are higher with 0.8, 1.5 or 2 nm than the LE phase. It is to be noted that the large LC domains show almost the same height as the surrounding nano LC domains.

Ultimately, near the DPPC monolayer collapse a homogeneous structure results from the close packed DPPC molecules, well oriented vertically at the air/water interface, as a consequence of strong molecular interactions.

(A)　　　　　　　　　　　(B)
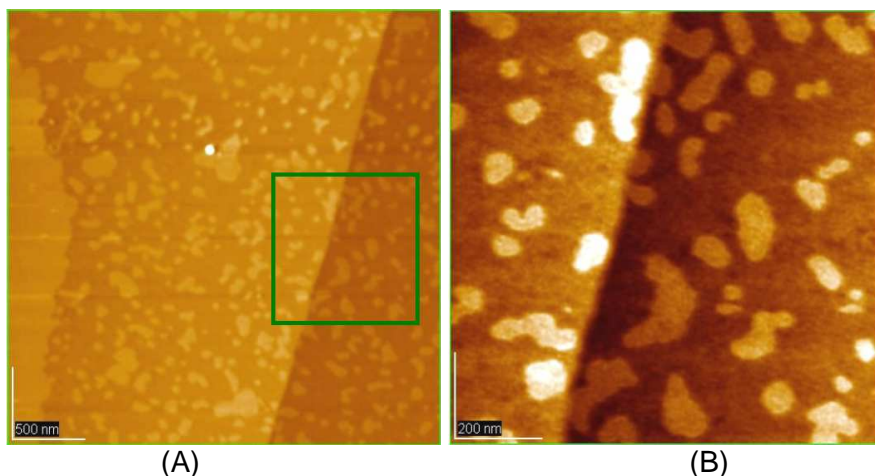
Figure 1. AFM topography images of DPPC monolayers, for 3 μm x 3 μm (A) and 1 μm x 1 μm (B) scanned areas. Monolayers were transferred by Langmuir-Blodgett technique on mica surface, at 8 mN/m, for the liquid expanded (LE) to liquid condensed (LC) phase transition. The z-scale is 5 nm for image A and 3 nm for image B. Image B was recorded by scanning on small area marked in image A.

(A)　　　　　　　　　　　(B)
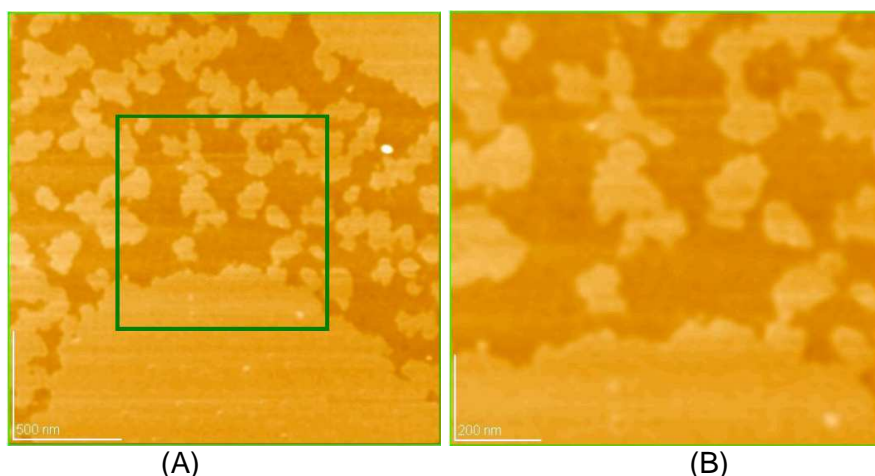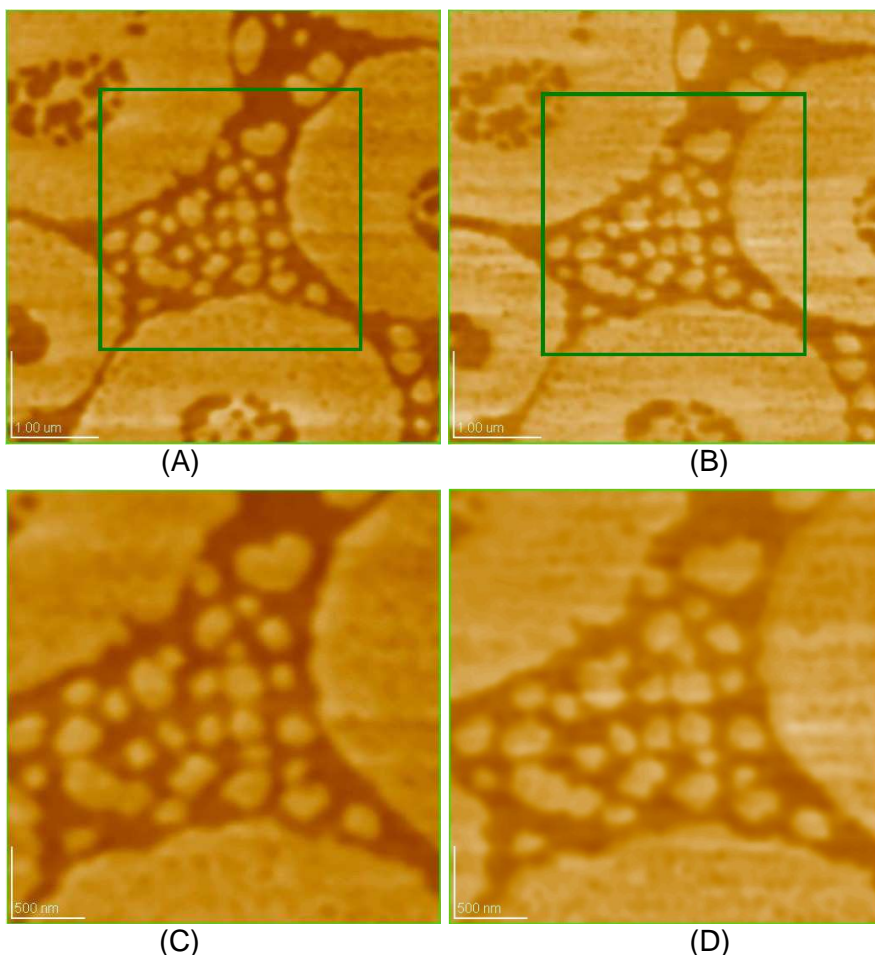
Figure 2. AFM topography images of DPPC monolayers, for 2 μm x 2 μm (A) and 1 μm x 1 μm (B) scanned areas. Monolayers were transferred at the phase transition (8 mN/m) on mica surface. The z-scale is 5 nm for image A and 3 nm for image B. Image B was recorded by scanning on small area marked in image A.

26

The presence of procaine (0.001 M in aqueous phase, pH 5.2) causes changes in surface properties of DPPC monolayers as determined on compression isotherms and in the structure of DPPC layers as observed on AFM images.

The LE/LC phase transition is evidenced on compression isotherms for mixed DPPC and procaine monolayers, at 15 mN/m. Thus, a substantial increase in transition lateral surface pressure is recorded for mixed monolayers as compared with pure DPPC monolayers (i.e., 8 mN/m) on water.

(A)

(B)

(C)

(D)

Figure 3. Topographies (A and C) and phase images (B and D) of DPPC monolayers spread on aqueous phases of 0.001 M procaine, transferred on mica at 8 mN/m. A and B: scanned area 5 μm x 5 μm; C and D: 3 μm x 3 μm. AFM images (C and D) were recorded by scanning on small areas marked in images A and B, respectively. The z-scale is 5 nm for A and C topographies.

27

For the beginning, the AFM images for mixed DPPC and procaine monolayers, transferred on mica at the lateral surface pressure of 8 mN/m, are examined (Fig. 3) and compared with AFM images of pure DPPC monolayers (Figs. 1 and 2). A phase separation is also found and visualized in AFM images for mixed DPPC and procaine monolayers (Fig. 3) in a similar way with the situation for pure DPPC monolayers (Figs 1 and 2). Thus, the LC domains within mixed DPPC and procaine monolayers are detected at low value of lateral surface pressure (about 8 mN/m). The LC domains in mixed monolayers are smaller (Fig. 3) than those observed in DPPC monolayers on a pure water substrate (Fig. 1A), at the lateral pressure of 8 mN/m, which is characteristic for the phase transition within the pure DPPC monolayers.

As the compression of mixed DPPC and procaine monolayers continued, the LC domains increased in size and number (Fig. 4, for 14 mN/m).

Furthermore, for mixed DPPC and procaine monolayers at the LE/LC phase transition (about 15 mN/m) recorded on compression isotherm, it was observed a continuous increase in the LC domains, which carry various interesting shapes. In other words, at 10^{-3} M procaine concentration, the LE/LC phase transition of mixed monolayers was observed by AFM images (Fig. 5, at the transition lateral surface pressure of about 15 mN/m), while the formation of LC phase was detected at much lower pressures, like 8 mN/m (Fig. 3) and at 14 mN/m (Fig. 4).

Clearly, procaine induces nucleation of liquid condensed domains before the phase transition recorded on compression isotherms for mixed DPPC and procaine monolayers. It appears that the onset of the LE/LC phase transition starts before the transition lateral surface pressure for mixed monolayers.

At lateral pressures above the phase transition, e.g. 20 mN/m, still some very large LC domains are visualized in AFM images. Near the collapse, the mixed DPPC and procaine monolayers are well ordered as in the case of pure DPPC monolayers showing a very low roughness (rms about 0.2 nm).

Undoubtedly, the presence of procaine in aqueous phase brings strong modifications on the structure and morphology of DPPC monolayers, even at low lateral surface pressure of 8 mN/m, which is characteristic for LE/LC phase transition of pure DPPC monolayers.

We suggest that procaine coexists with less ordered DPPC molecules and is preferentially located at the domain boundaries. This would indicate that the lighter domains correspond to almost highly oriented DPPC molecules. The dark domains probably correspond to less organized DPPC molecules mixed with procaine. Thus, AFM images reveal a phase separation between DPPC condensed phase (high areas) and DPPC expanded phase enriched in procaine (low areas).

28
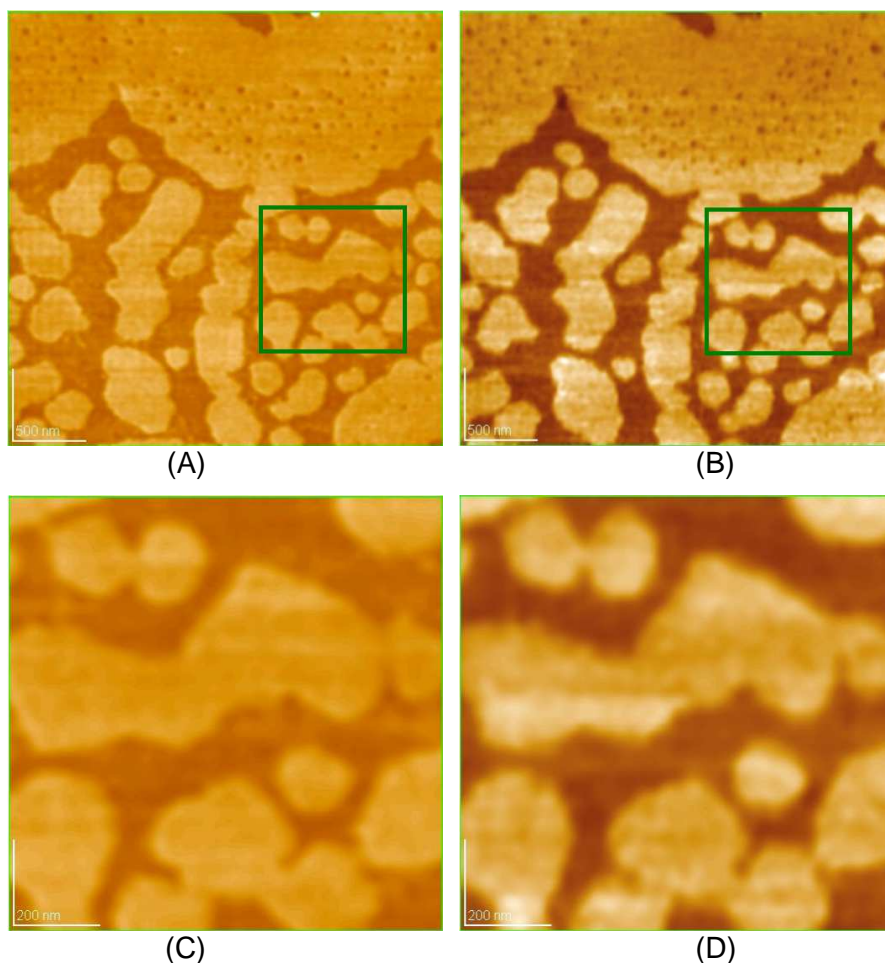
Figure 4. Topographies (A and C) and phase images (B and D) of DPPC monolayers spread on aqueous phases of 0.001 M procaine, compressed to 14 mN/m and transferred on mica surface. A and B: scanned area 3 µm x 3 µm; C and D: 1 µm x 1 µm. AFM images (C and D) were recorded by scanning on small areas marked in images A and B, respectively. The *z*-scale is 5 nm for A and C topographies.

The mixed DPPC and procaine monolayers present LC nano domains co-existing with small round LE procaine rich phase in the center of the LC large micro domains (Fig. 3A and B), where the LC nano domains form a network of filament unique structure. Also, the LC nano domains are situated at the edges of the large LC domains forming larger aggregates (Fig. 3C and D), belts (Fig. 4A and B) or stripes (Fig. 4C and D).

By increasing the surface pressure (Fig. 4, at 14 mN/m), the stripes are formed by the alignment of many smaller LC domains, that have almost the same height with the large LC domains of DPPC monolayers.

The phase images (Figs. 3B, 3D, 4B and 4D) show the morphological character more clearly than the corresponding topography (Figs. 3A, 3C, 4A and 4C) due to the difference in the surface physical and chemical properties between the condensed and expanded DPPC monolayers.

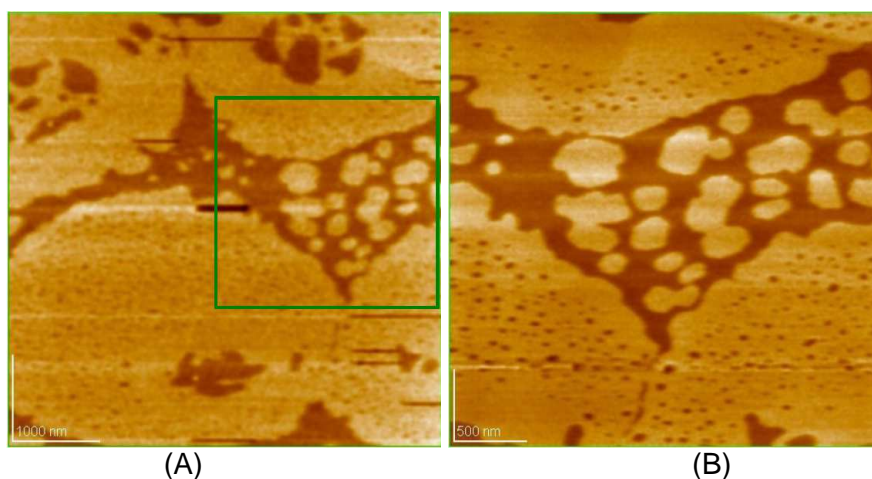(A)   (B)

Figure 5. Topographies (A and B) of DPPC monolayers spread on aqueous phases of 0.001 M procaine, compressed at about 15 mN/m and transferred on mica surface by LB technique. A: scanned area of 5 μm x 5 μm. (B): 3 μm x 3 μm were recorded by scanning on small areas marked in image A. The z-scale is 5 nm.

Thus, almost in the center of the large LC domains, many nano LC domains are observed (with axis of 50 to 150 nm), particularly in small scale images (Figs. 3 and 5). The large LC domains have the same height as the edges of the aligned stripes.

The large LC domains are about 2 nm higher than the fluid LE phase and are surrounded by a mixture of LE phase and LC nano domains, in which LC domains are aligned in a striped pattern (Fig. 5). The large LC domains are rather well packed at high lateral surface pressure (15 mN/m) that corresponds to the phase transition of mixed DPPC:P monolayers evidenced on compression isotherm.

Thus, a unique morphology of mixed DPPC and procaine monolayers is observed, showing large LC domains, which contain a network of filaments of LC domains surrounded by LE procaine rich phase, where the

procaine is adsorbed preferentially at the edge of the LC domains. At the transition surface pressure (15 mN/m), numerous filaments in the center of the large LC domains are formed (Fig. 5A) and larger patches at their edges appears (Fig. 5B).

The differing shapes of LC phase within the mixed DPPC and procaine monolayers reflect a different structure of DPPC monolayers under the action of procaine. These data suggest that procaine affects DPPC morphology in the LC phase. Nevertheless, the morphological changes within mixed DPPC and procaine monolayers support the participation of procaine in anesthesia.

Higher amounts of procaine in aqueous phase give numerous filaments in the center of the LC micro domains and evidently larger LC patches at their edges.

Qualitatively, the same effects were observed at lower procaine concentrations. However, the magnitude of the procaine effects was smaller and was diminished with decreasing of procaine concentrations.

This situation might be related to the fact that the procaine adsorbs and penetrates preferably at the boundaries between LC domains, with a different tilt direction, and in the expanded DPPC phase, as also found by epifluorescent microscopy [23]. However, the binding of procaine molecules to the surface of the DPPC condensed domains could also perturb the lipid chains organization. In this regard, the maximum height in mixed monolayers is about 3.6 nm as determined in Fig. 3. This height corresponds to the mixed DPPC and procaine condensed domains, and is decreased as compared to the height of the condensed domains existing in pure DPPC layers (Fig. 1A, where maximum height of 4.3 nm was found). The phase contrast images, given in Figs. 3 and 4, show also clearly the morphological character corresponding to the given surface topography.

The tertiary amine procaine is an amphiphilic molecule which exists in the charged form [13] at the working pH of about 5.6. The hydrophilic amine moiety is responsible for water solubility and DPPC membrane surface binding and the hydrophobic moiety appears to control the organization within the DPPC membrane model. The interaction of procaine molecules with zwitterionic DPPC molecules may lead to an ordering effect on the DPPC monolayer interface and to a disordering effect on the hydrocarbon interior of DPPC monolayers, in substantial agreement with AFM observations.

In order to explain the mode of action of procaine, positively charged under the working conditions, on the zwitterionic phospholipids monolayers, we assume that positively charged procaine molecules adsorb onto the lipid membrane surface. This will allow the hydrophobic portion of procaine molecule to be embedded into the hydrocarbon part of the expanded liquid phase and at the domain boundaries of lipid monolayers.

The positively charged amine group of procaine molecules can interact electrostatically, at the monolayer/water interface, with the negatively charged group of the zwitterionic DPPC molecules. The electrostatic interaction will appear in both the condensed and the expanded liquid state of DPPC monolayers increasing the stability of the lipid membrane.

The findings in this study suggest that procaine accumulates in the lipid phase of cell membranes, and thus might change the physical properties of the membrane lipid and consequently, procaine molecules influence the protein conformation. The effect of procaine and other local anesthetics on DPPC membrane structuration at various lateral surface pressures is under further investigation in our laboratories.

CONCLUSIONS

Combined surface chemistry, Langmuir-Blodgett (LB) self-assembly technique, and atomic force microscopy have been used to determine the spreading, structure and topography of DPPC monolayers at the air/water interface.

During compression at the air/water interface, DPPC monolayers present a structural transition at a lateral surface pressure of about 8 mN/m, from liquid expanded (LE) to liquid condensed (LC) structures, showing LC domains with heterogeneous structures. Finally, near the DPPC monolayer collapse a homogeneous structure results from the close packed DPPC molecules, well oriented in a matrix at the air/water interface, which is a consequence of the strong molecular interactions.

The LB self-assembled monolayers were transferred from Langmuir films onto mica, at controlled surface pressures characteristic for the phase transition in DPPC monolayers by using vertical transfer method. In the presence of procaine (10^{-3} M) in aqueous phase, the stability of DPPC films is highly increased as it is reflected by the increased collapse and phase transition pressures of DPPC monolayers.

The DPPC monolayer structure is influenced by the presence of procaine in aqueous phase and a more expanded monolayer structure is observed for 10^{-3} M procaine. AFM images confirm, at the microscopic and nanoscopic levels, almost the same type of structural changes deduced from the compression isotherms for DPPC monolayers as a function of surface pressure.

Structural characteristics and the surface topography of DPPC monolayers are highly dependent on the lateral surface pressure for a particular concentration of procaine in the aqueous phase. In addition, the appearance of a new liquid condensed (LC) phase is strongly evidenced in the mixed DPPC and procaine monolayers.

The results reveal some specific molecular interactions between DPPC and procaine in substantial agreement with molecular interactions and with molecular structure of these biocompounds.

32

EXPERIMENTAL SECTION

Materials

Synthetic 1,2-dipalmitoyl-*sn*-glycero-3-phosphocholine: DPPC, and procaine, 2-(diethylamine)ethyl-*para*-(amine) benzoate, hydrochloride (P- HCl), were purchased from Sigma Chemical Co., and used without further purification. For the study of the procaine effect, P- HCl was first dissolved in two-distilled water, giving a chosen procaine concentration, e.g., 10^{-3} M procaine, in the aqueous solution.

Langmuir-Blodgett (LB) film

DPPC was dissolved in a mixture of chloroform: ethanol (9:1, v/v), giving a 1 mM phospholipid in organic solution. The DPPC solution was spread at the air/water interface with a microsyringe both in the absence and the presence of procaine in aqueous solutions. After spreading, the system was allowed to stand for 10 min, without causing the surface disturbance. Then, the compression isotherms in terms of surface pressure versus mean molecular area of DPPC were recorded. All measurements were performed with KSV equipment. The speed of the compression was 10 mm min^{-1} (i.e., 8 Å^2/(molecule x min). For AFM observations, a single layer (LB film) was transferred on freshly cleaved mica surface, using a vertical dipping method at different surface pressures maintained constant (e.g., 8 mN/m). The LB film transfer took place at a rate of about 5 mm/min.

AFM observations

Atomic force microscopy (AFM) is a surface imaging technique with a nanometer-scale resolution [32-35]. AFM studies were performed using the AFM JEOL 4210. The cantilevers with a resonance frequency of 250 – 350 kHz were used. Triplicate samples were prepared for each monolayer composition and at least four separate areas were imaged for each sample. Through this study, AFM images were obtained at several constant surface pressures in order to examine the effect of procaine on the phase behaviour of DPPC monolayers spread at the air/water interface.

REFERENCES

1. H. Tsuchiya, M. Mizogami, T. Ueno, K. Takakura, *Inflammopharmacol.*, **2007**, *15*, 164.
2. T. Hata, H. Matsuki, S. Kaneshina, *Colloids Surf. B*, **2000**, *18*, 41.
3. Z. Leonenko, E. Finot, D. Cramb, *Biochim. Biophys. Acta,* **2006**, *1758*, 487.
4. H. Matsuki, S. Kaneshina, H. Kamaya, I. Ueda, J. *Phys. Chem. B,* **1998**, *102*, 3295.

5. Z. V. Leonenko, D. T. Cramb, *Can. J. Chem.,* **2004**, *82*, 1128.

6. M. Tomoaia-Cotisel, E. Chifu, A. Mocanu, J. Zsakó, M. Salajan, P.T. Frangopol, *Rev. Rroum. Biochim.,* **1988**, *25(3)*, 227.

7. M. Tomoaia-Cotisel, J. Zsakó, E. Chifu, P. T. Frangopol, W. A. P. Luck, E. Osawa, *Rev. roum. Biochim.,* **1989**, *26(4)*, 305.

8. J. Zsakó, M. Tomoaia-Cotisel, E. Chifu, A. Mocanu, P. T. Frangopol, *Biochim. Biophys. Acta,* **1990**, *1024*, 227.

9. J. Zsakó, M. Tomoaia-Cotisel, E. Chifu, I. Albu, A. Mocanu, P. T. Frangopol, *Rev. Roum. Chim.,* **1990**, *35(7-9)*, 867.

10. E. Chifu, M. Tomoaia-Cotisel, J. Zsakó, I. Albu, A. Mocanu, P.T. Frangopol, *Rev. Roum. Chim.,* **1990**, *35(7-9)*, 879.

11. M. Tomoaia-Cotisel, E. Chifu, S. Jitian, I. Bratu, S. Bran, P. T. Frangopol, A. Mocanu, *Stud. Univ. Babes-Bolyai, Chem.,* **1990**, *35(2)*, 17.

12. E. Chifu, M. Tomoaia-Cotisel, J. Zsakó, A. Mocanu, M. Salajan, M. Neag, P. T. Frangopol, *Seminars in Biophysics, Vol. 6,* Editors: P. T. Frangopol, V. V. Morariu, IAP Press, Bucharest, **1990**, 117.

13. J. Zsakó, M. Tomoaia-Cotisel, I. Albu, A. Mocanu, E. Chifu, P. T. Frangopol, *Rev. roum. Biochim.,* **1991**, *28(1-2)*, 33.

14. M. Tomoaia-Cotisel, E. Chifu, J. Zsakó, P. T. Frangopol, P. J. Quinn, A. Mocanu, *Stud. Univ. Babes-Bolyai, Chem.,* **1993**, *38(1-2)*, 81.

15. J. Zsakó, M. Tomoaia-Cotisel, E. Chifu, A. Mocanu, P. T. Frangopol, *Gazz. Chim. Ital.,* **1994**, *124*, 5.

16. J. Zsakó, E. Chifu, M. Tomoaia-Cotisel, A. Mocanu, P. T. Frangopol, *Rev. Roum. Chim.,* **1994**, *37(7)*, 777.

17. M. Tomoaia-Cotisel, J. Zsakó, E. Chifu, A. Mocanu, P. T. Frangopol, P. J. Quinn, *J. Romanian Colloid and Surface Chem. Assoc.,* **1997**, *2(3-4)*, 30.

18. M. Tomoaia-Cotisel, T. Oproiu, J. Zsako, A. Mocanu, P. T. Frangopol, P. J. Quinn, *Rev. Roum. Chim.,* **2000**, *45(9)*, 851.

19. M. Tomoaia-Cotisel, A. Mocanu, *Rev. Chim. (Bucharest),* **2008,** *59(11)*, 1230.

20. P. T. Frangopol, D. Mihailescu, *Colloids Surf. B,* **2001**, *22*, 3.

21. T. Hianik, M. Fajkus, B. Tarus, P. T. Frangopol, V. S. Markin, D. F. Landers, *Bioelectrochem. Bioenergetics,* **1998**, *46*, 1.

22. M. Tomoaia-Cotisel, D. A. Cadenhead, *Langmuir,* **1991**, *7*, 964.

23. B. Asgharian, D. A. Cadenhead, M. Tomoaia-Cotisel, *Langmuir,* **1993**, *9*, 228.

24. M. Tomoaia-Cotisel, *Progr. Colloid Polym. Sci.,* **1990**, *83*, 155.

25. H. Matsuki, K. Shimada, S. Kaneshina, M. Yamanaka, H. Kamaya, I. Ueda, *Langmuir,* **1997**, *13*, 6115.

26. S.-Y. Choi, S.-G. Oh, J.-S. Lee, *Colloids Surf. B,* **2001**, 20, 239.

27. A. Cavalli, G. Borissevitch, M. Tabak, O. N. Oliveira, Jr., *Thin Solid Films,* **1996**, *284*, 731.

28. D. M. Goodman, E. M. Nemoto, R. W. Evans, P. M. Winter, *Chemistry and Physics of Lipids,* **1996**, *84*, 57.

29. S.-Y. Choi, S.-G. Oh, J.-S. Lee, *Colloids Surf. B,* **2000**, *17*, 255.

30. M. Tomoaia-Cotisel, J. Zsako, E. Chifu, *Ann. Chim. (Rome),* **1981**, *71(3)*, 189.

31. G. Chimote, R. Banerjee, *Colloids Surf. B,* **2008**, *65*, 120.

32. S. Yokoyama, Y. Ohta, H. Sakai, M. Abe, *Colloids Surf. B,* **2004**, *34*, 65.

33. M. Tomoaia-Cotisel, Convergence of Micro-Nano-Biotechnologies, Series in Micro and Nanoengineering, Vol. *9,* Editors: M. Zaharescu, E. Burzo, L. Dumitru, I. Kleps, D. Dascalu, Romanian Academy Press, Bucharest, **2006**, 147.
34. K. Hoda, Y. Ikeda, H. Kawasaki, K. Yamada, R. Higuchi, O. Shibata, *Colloids Surf*. B, **2006**, *52*, 57.
35. Gh. Tomoaia, M.Tomoaia-Cotisel, A. Mocanu, O. Horovitz, L.-D. Bobos, M. Crisan, I. Petean, *J. Optoelectron. Adv. Materials*, **2008**, *10(4)*, 961.

Dedicated to Professor Liviu Literat, at his 80th anniversary

SOME ASPECTS REGARDING MICROWAVE DRYING OF MATERIALS

BARBU RADU HORAȚIU MIȘCA[a], DORIN MANCIULA[b]

ABSTRACT. The paper presents the experimental results of microwave drying for a granular material (siliceous sand). Drying kinetics and effective power absorbed by the material for two cases: compact volume (bulk) and extended volume (layer) were determined and analyzed.

Keywords: microwaves, drying, thermal properties, heat transfer, power transport.

INTRODUCTION

Traditionally, drying of solid materials is carried out by convective heating, transferring the thermal energy from the heater to the heated material. The penetration of this energy into material depends on the thermal conductivity of the material. While the material dries, the thermal and mass conductivity decrease. As a result, the penetration of the delivered heat is reduced progressively, and water is slower transferred to surface layers, where evaporation occurs. Consequently, the surface layers become overheated and it may even produce a crust, which will need to be mechanically broken up to transfer the dried material to shipping containers.

To increase the effectiveness of the drying process it is necessary to employ various tricks, such as stirring the substance, drying in fluidized bed etc. Normally this requires high power consumption.

Drying under microwave irradiation presents several advantages comparative to convective drying. The main advantages consist on high conversion of microwave energy into thermal energy, independence on thermal conductivity and selectivity [1]. In the same time, the influence of the resistance of the boundary layer between the material and drying air, as well as the thermal conductive transport through the material are eliminated, under microwave irradiation heating occurring simultaneously in whole volume of the heated material.

---

[a] *Universitatea Babeş-Bolyai, Facultatea de Chimie şi Inginerie Chimică, Str. Kogălniceanu Nr. 1, RO-400084 Cluj-Napoca, Romania, miscar@chem.ubbcluj.ro;*
[b] *Universitatea Babeş-Bolyai, Facultatea de Ştiinţa Mediului, Str. Kogălniceanu Nr. 1, RO-400084 Cluj-Napoca, Romania, dimro21@gmail.com*

Equipments used in microwave drying are relatively simple and can be easily adapted to the variable conditions; have no thermal inertia, therefore can quickly reach natural regime of operation; the volume of all installation is small and that for needs no large space.

The disadvantages of the method are: high exploitation costs and limited using field.

Depending on the type of radiation and material nature, when one irradiates solids with microwaves, the microwaves can be reflected, absorbed, or simply pass through the sample with no absorption occurring [2, 3]. Through vibration, elongation and successive contraction of bounds and atoms, the radiant energy is transformed into heat which propagates from the warmest zones towards the coldest zones through convection and conduction mechanisms.

During the microwave drying process in many cases the material being dried does not absorb or absorb a low level of microwave irradiation but the water molecules associated with it do. Thus the microwave drying process is caused by the property of water to absorb microwave irradiation. Consequently, removing of the water molecules from the drying materials eliminates the heating effect. In such a way the microwave drying appears to be self-regulative process.

Microwave irradiation consists in electromagnetic wave in the range 300 MHz to 300 GHz that corresponds to wavelengths of 1 cm to 1 m, and frequency between 2450 kHz - 434, 915 MHz, being defined by international regulations. The microwave region of the electromagnetic spectrum lies between infrared and radio frequencies [4].

In order to avoid local heating if the material is keeping static, shifting of material into irradiated space is necessary to be applied [5].

RESULTS AND DISCUSSION

Preliminary results obtained by the heating of water under microwave irradiation in two situations: compact volume (beakers) and extended volume (trays), at different power levels of the microwave oven are shown in Table 1 and Table 2.

Table1. Water temperature in beaker during microwave heating

Time [minutes]	L Level [^{0}C]	ML Level [^{0}C]	M Level [^{0}C]	MH Level [^{0}C]	H Level [^{0}C]
0	20	20	21	20	21
1	28	27	54	77	96
0	20	20	20	21	20
2	35	60	88	94	-
0	20	20	20	20	20
3	41	77	-	-	-
0	20	21	20	20	20
4	45	90			

Table1. Water temperature in beaker during microwave heating (continuation)

Time [minutes]	L Level [^{0}C]	ML Level [^{0}C]	M Level [^{0}C]	MH Level [^{0}C]	H Level [^{0}C]
0	20	20	20	20	20
5	50	-	-	-	-
0	20	20	20	20	20
6	60	-	-	-	-

L = low level; ML = medium - low level; M = medium level; MH = medium - high level; H = high level.

Table 2. Water temperature in tray during microwave heating

Time [minutes]	L Level [^{0}C]	ML Level [^{0}C]	M Level [^{0}C]	MH Level [^{0}C]
0	20	20	20	20
1	35	42	55	70
0	20	20	20	20
2	37	55	69	77
0	21	21	21	21
3	43	63	77	-
0	21	21	21	21
4	47	64	75	-
0	21	21	21	21
5	50	68	-	-
0	21	21	21	21
6	56	-	-	-

Each temperature is the average of at least three measurements carried out in the same conditions.

Considering the difference of temperature between initial moment and final moment of each heating experiment, the effective power absorbed by water can be determined by the relation [4]:

$$P_{ef} = (m_{water} \, c_{p \, water} \cdot \Delta T_{water} / \tau),$$

where: m_{water} is the mass of heated water, 100 [g] = 0.1 [kg]; $c_{p \, water}$ - specific heat of water 4,185 [J/kg ^{0}K]; ΔT_{water} - difference of temperature between the initial moment and the final moment of the heating process [^{0}K]; and τ - irradiation time [s].

The resulted values are presented in Table 3 and Table 4.

**Table 3.** The effective power absorbed by water during microwave heating in beaker

Heating time [min]	L Level [W]	ML Level [W]	M Level [W]	MH Level [W]	H Level [W]
1	55.8	128.825	230.175	397.575	523.125
2	48.825	129.5	237.16	372.025	-
3	48.825	123.212	-	-	-
4	43.594	120.319			
5	43.245	-	-	-	-
6	46.5	-	-	-	-
$P_{ef \, av}$	47.798	125.464	233.667	384.480	523.125

Table 4. The effective power absorbed by water during microwave heating in tray

Heating time [min]	L Level [W]	ML Level [W]	M Level [W]	H Level [W]
1	140.625	153.450	244.125	348.75
2	59.287	122.0625	170.8875	198.7875
3	51.15	97.650	-	-
4	45.3375	74.98125	-	-
5	40.455	-	-	-
6	40.6875	-	-	-
$P_{ef\,av}$	62.923	112.0575	207.5	273.76875

It is easy to see that calculated values of effective power increase with the increase of power level of the microwave oven and generally, the effective absorbed power is higher for compact volume (in backer) that for extended volume (in tray).
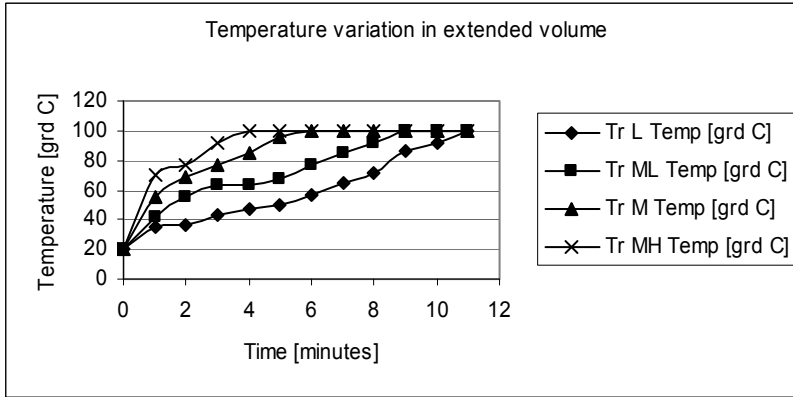
Temperature variation during microwave irradiation of siliceous sand (tested material) in both cases analyzed earlier (compact and extended volume) are shown in Figure 1 and Figure 2.
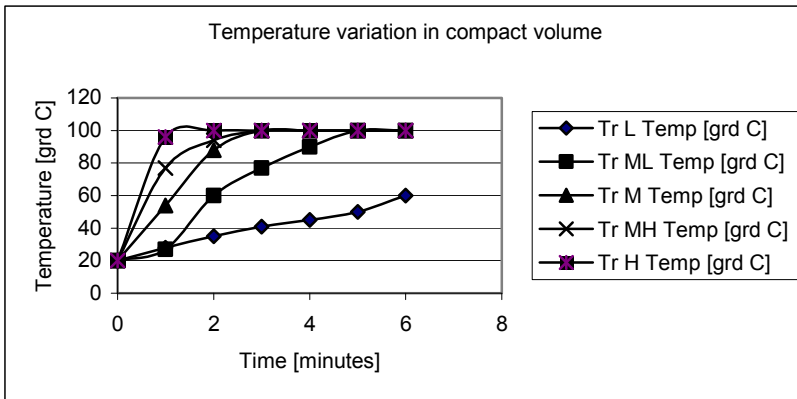
**Figure 1.** Temperature variation during microwave drying of sand in compact volume.

It can be seen that the temperature curves increase continuously, with a faster rhythm for higher power level of the microwave oven and with a slower rhythm for lower power level. In the same time the temperature increase slower in the case of extended volume comparative to compact volume. This phenomenon can be attributed to the higher heat lost into the chamber environment, which remains cold and does not increase its temperature, surface area exposed by tray was 181.366 cm^2, comparative to surface area exposed by backer, 28.6 cm^2.

Figure 2. Temperature variation during microwave drying of sand in extended volume.

Regarding the effective power absorbed by siliceous sand, it was measured an almost constant power in the case of compact volume. The effective power absorbed by the sand decreases progressively with a tendency of stabilization in the case of extended volume (Figure 3). An explanation for such behavior of the system could not be found.
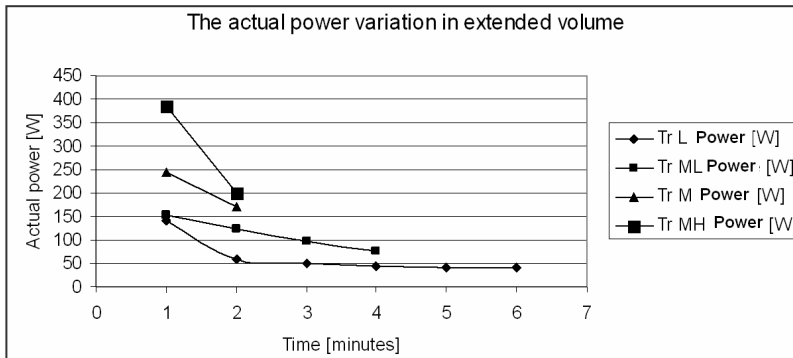
Figure 3. The effective power absorbed by the sand in extended volume.

Kinetic curves of drying for compact volume and for extended volume samples at lower power level of the microwave oven are shown in Figure 4 and 5. These curves present the variation in time of several characteristics of the system: weight, temperature and humidity.

During the microwave irradiation the sand temperature follows a tendency similar to the heating of water alone; the weight of the samples diminishes similarly in both situations.
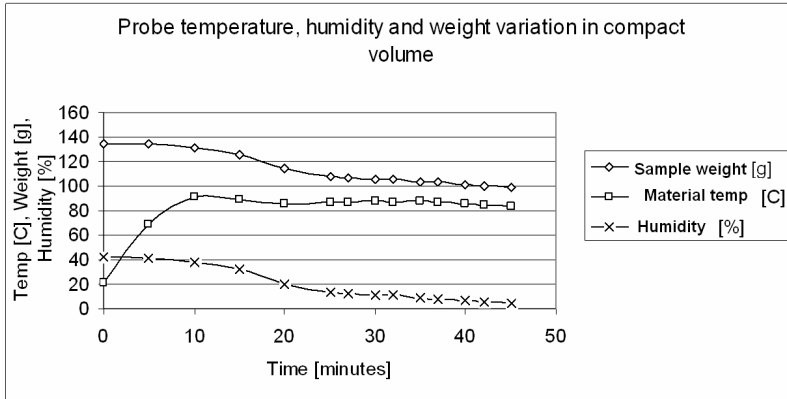
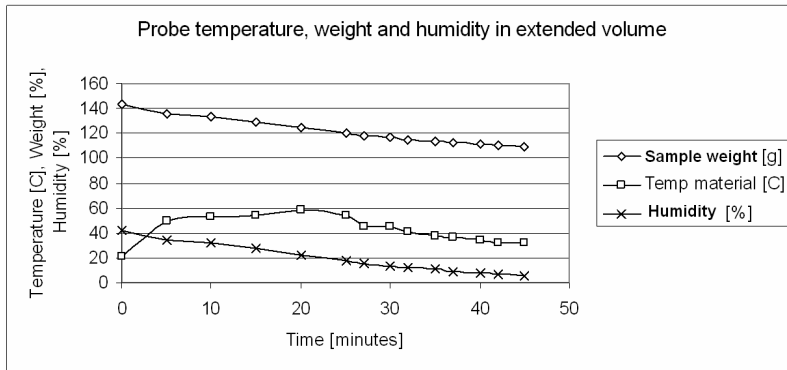**Figure 4.** Drying curves for sand in compact volume.

Figure 5. Drying curves for sand in extended volume.

To compare the results of microwave drying of sand in compact and extended volume, Figures 6, 7 and 8 are plotted.
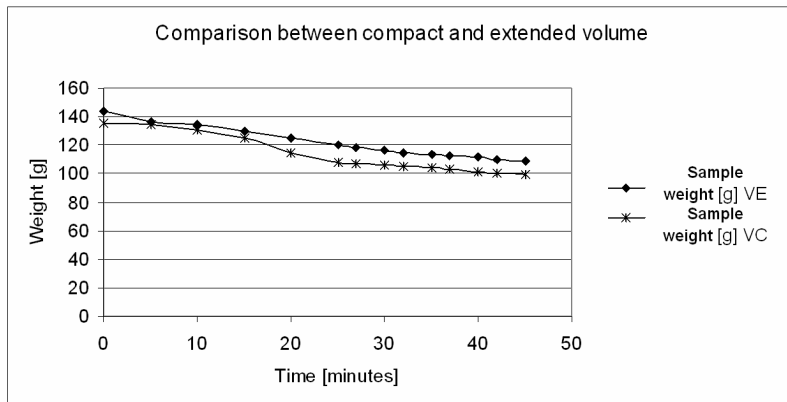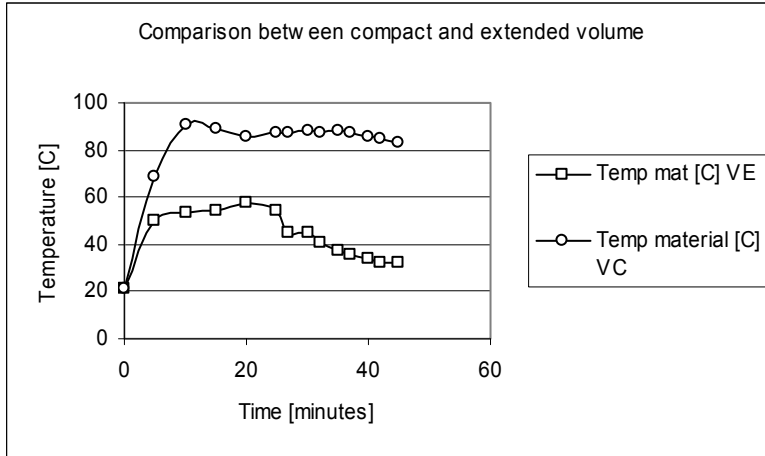

**Figure 6.** Weight variation for compact and extended volume.

Figure 6 shows a decrease of the weight almost linear in both cases. The detected difference between the curves can be attributed to the weight difference of the containers: 2, 4 g for beaker and 7, 7 g for tray, which means that the weight of containers can influence the drying process; containers heat up only by conduction.

Figure 7. Temperature variation for compact and extended volume.

The evolution in time of temperature plotted in Figure 7 shows for extended volume a lower increase than in the case of compact volume. In both cases, at the end of the process, the temperature decrease more slowly, due to the decrease of the water quantity in the material.

The slope of the curves suggests the idea of using extended volumes in case of temperature-sensitive materials. In this way, these materials are less affected by the temperature and due to the higher heat lost, the material cooling occurs more rapidly.
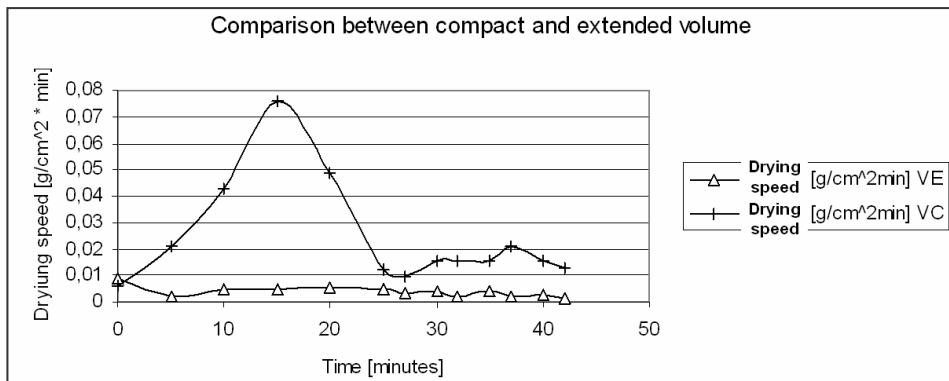
Figure 8. Drying kinetics for sand in compact and extended volume.

The drying rate, in terms of water amount eliminated per unit of time and surface, [g/cm^2·min] or in international system IS [kg/m^2·s], shows the rhythm of humidity elimination (Figure 8). It can be seen a relatively constant loss of humidity in the case of extended volume. In the case of compact volume, the drying rate presents higher variation. The following observations were made: in the first stage, the drying rate is reduced because of the heat lost by convection in the cold environment; at the end, the diminution of the rate is due to a decrease of the humidity amount.

This behavior was explained by the followings facts:

- during the first stage, the material is intensely heated and the losses to the external environment are diminished due to the smaller contact surface of the material to the cold environment;

- the heat of the material mass is near to the water boiling point value and this generates an intense evaporation and also water boiling. The generation of a larger amount of vapors indicates a higher drying rate, associated to material splash because of energetic formation and evacuation of steams (this phenomenon was experimentally observed);

- reaching of a minimum drying rate was explained by the formation of a "coating" of relatively dry material, which is difficult to be penetrated by the generated water vapors;

- the barrier penetration determines a growth of the released vapor amount, specifically an increase of the drying rate, but since the vapor amount is smaller, a maximum rate due to vaporization cannot be reached. In addition, the material temperature decrease contributes to this phenomenon;

- the decrease of the drying rate is attributed to the decrease of the material humidity amount in a relatively constant rhythm (Figure 9).
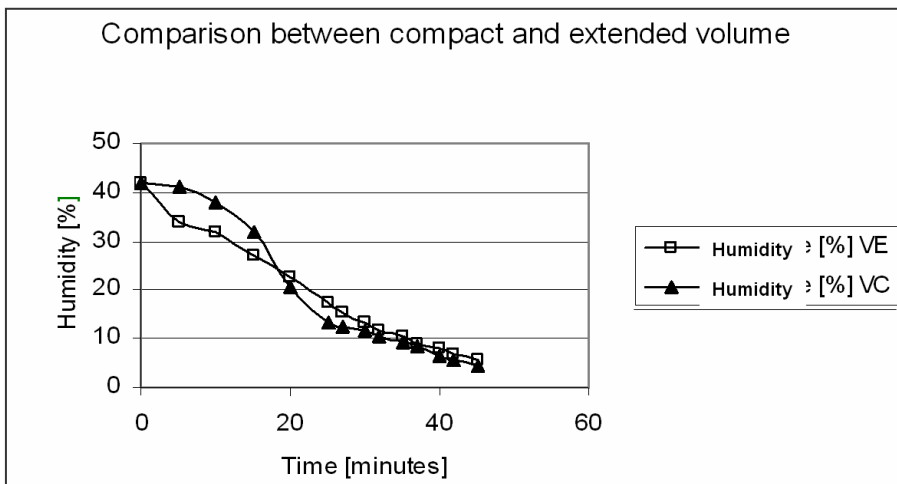

Figure 9. Comparison of humidity losses.

CONCLUSIONS

Microwave heating was experimentally studied using a household microwave oven, type CANDY-CMG-2180-M, in order to obtain useful experimental information, special for improving the process of the drying operation.

Effective emitted power of the generator and the power absorbed by the material were determined. Effective absorbed power was constant in the case of compact volume, while in the case of extended volume the effective absorbed power was progressively decreased, showing a stabilization tendency. An explanation for such system behavior was not found.

During microwave drying the temperature of the tested material has shown a continuous increase. The smaller increase of the temperature in the case of extended volume was attributed to the heat lost in the chamber environment. In the same time, the obtained results suggest the idea of using extended volumes in case of temperature-sensitive materials.

The humidity was reduced with relatively constant rate in the case of extended volume and with variable rate, in the case of compact volume.

EXPERIMENTAL SECTION

The drying process under microwave field was monitored in order to obtain valid experimental data that may be useful for the drying process improvement. The experimental measurements were focused on:

1. Determination of the technical characteristics of the equipment and

2. Determination of drying kinetics and effective absorbed energy.

In order to determine technical characteristics of the equipment, a household microwave oven, type CANDY CMG 2180 M was used. The technical features presented by the manufacturer in the technical book are:

Supply voltage	220 - 230 V;
Network Frequency	50 Hz;
Generator working frequency	2450 Hz;
Absorbed power from the network	1300 W;
Emission power	800 W;
Chamber sizes	300 x 295 x 205 mm;
Useful volume	21 dm^3;
Turntable diameter	270 mm;
5 power levels	

Preliminary measurements were made in order to determine the "active" power emitted by the generator of the microwave oven and absorbed by water.

The working method: 100 ml of water were introduced in the shock-absorbing polystyrene container. Two types of containers are used: backers for compact volume experiment and trays for extended volume. Parameters of containers at microwave heating tests were:

- beaker: truncated cone shape, small base (at the bottom), diameter $\varnothing$ 45 mm; large base (up) diameter $\varnothing$ 60 mm; and height 50 mm,
- tray: cylinder of negligible height, and diameter $\varnothing$ 152 mm.

Simple shock-absorbing polystyrene beakers and trays were chosen due to the following reasons: they are compatible with the microwave radiations and their effects; the shock-absorbing polystyrene does not warm up under the microwave action; they have a reduced weight and their mass is negligible in thermal subsequent calculations; the subsequent error entered is minor (the beaker mass is 2.4 g, and the tray mass is 7.7 g); it provides two significant forms for the drying process: compact volume and extended volume with a larger exposed surface to microwaves.

The initial water temperature was measured and then the container was introduced in the chamber of the oven. A power level was selected and then the material was irradiated for a determined period of time. The water temperature was measured at the end of the established time. Each experiment was repeated at least 3 times. This condition is necessary because of the special structure of the device, which has a power limiter mechanism that interrupts the microwave generation process when the generator is overheated. Therefore, the microwaves generation is not continuous; the limiter has the purpose of protecting the equipment against overheating.

In order to determine the drying kinetics, direct measurements were carried out using a synthetic blend consisting of siliceous sand and water. This blend was introduced in: beaker for compact volume experiment, and tray for extended volume experiment.

The working procedure was as follows: 95 g of siliceous sand were introduced in the container; the sand was considered as "perfectly dried" due to the drying in the oven at 105 ^{0}C for 8 hours. 35 ml of water were added to the sand. This amount is sufficient to cover all the sand in the container. Thus, it is possible to detect a phenomenon similar to that observed during the period I of the convective drying in constant conditions.

The material was irradiated with microwaves; e.g. "low level, L", and the temperature and weight of material were regularly measured.

REFERENCES

1. O. Floarea, Gh. Jinescu, "Procedee intensive în operaţiile unitare de transfer"; Ed. Tehnică, Bucureşti, **1975**, 139.
2. A. J. B. Fuller, "Microwaves: an Introduction to Microwave Theory and Technology", Pergamon Press, Inc., Oxford, **1994**.
3. B. R. H. Mişca, A. Ozunu, "Introducere in ingineria mediului", Ed. Presa Universitara Clujeană, **2006**, 111.
4. H. M. Silaghi, "Tehnologii cu microunde"; Ed. Teora, Bucureşti, **2001**, 28.
5. A. Badea, H. Necula, M. Stan, L. Ionescu, P. Blaga, G. Darie, "Echipamente şi instalaţii termice, Ed. Tehnică, Bucureşti, **2003**, 530.

Dedicated to Professor Liviu Literat, at his 80th anniversary

CHEMICAL RISK AREA ESTIMATION AS A TOOL FOR EFFICIENT EMERGENCY PLANNING

ZOLTÁN TÖRÖK[a], NICOLAE AJTAI, ALEXANDRU OZUNU

ABSTRACT. Chemical disaster management has two essential components: Chemical Risk Management (CRM) and Emergency Situations Management (ESM). The connection between these two major elements is represented by the risk area estimations. Risk area estimations are an important tool in the process of Risk Assessment. It provides the authorities responsible with intervention in case of a major chemical accident, accurate and detailed information on the site, weather conditions, hazardous chemicals involved, and their dispersion patterns aiding in the development of Emergency Response Plans. The paper presents an overview of the Chemical Disaster Management process and a comparative case study of a possible chemical accident involving chlorine.

Keywords: chemical risk assessment, risk analysis, consequence maps, chlorine

INTRODUCTION

The technological processes that involve dangerous substances are known to have high risk levels, due to their capability to produce major accidents. These accidents can occur during the process, storage and transportation, releasing a large quantity of energy or substance which can harm humans or the environment, and lead to technological disasters.

Therefore the need for strict regulations arises, in order to prevent these disasters form occurring with the active participation of the industry, the authorities and the general public. The regulatory organism in the field of major industrial accidents involving dangerous substances is the European Union by the 2003/105/CE Directive, also called the Seveso III Directive [1].

Chemical disaster management has two essential components: Chemical Risk Management (CRM) and Emergency Situations Management (ESM), Figure 1.

---

[a] *Universitatea Babeş-Bolyai, Facultatea de Ştiinţa Mediului,Str. Kogălniceanu, Nr. 1, RO-400084, Cluj-Napoca, Romania, torokzoltan@yahoo.com*

CRM can be considered as a combination of all the processes necessary to control chemical risk: risk analysis, risk evaluation, cost-benefit analysis, and change management. On the other hand ESM focuses on managing these events once they have occurred. ESM includes: internal and external emergency plans, emergency response, and post-emergency recovery.
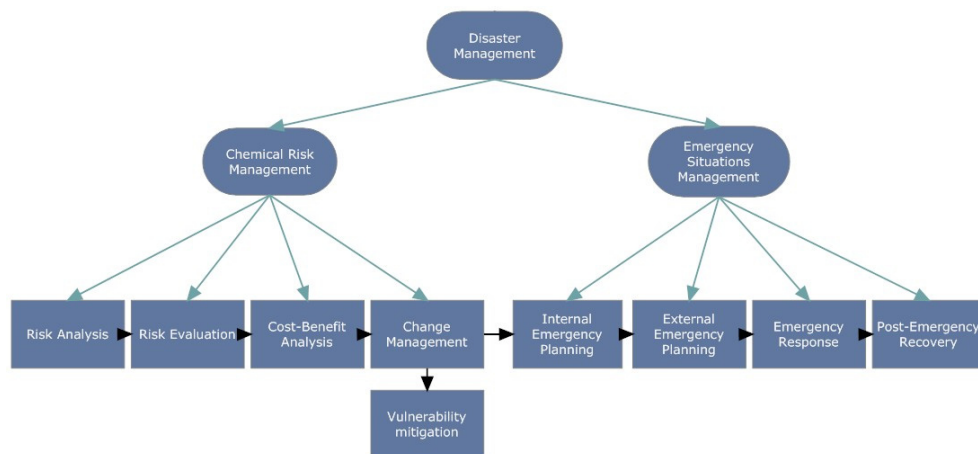
Figure 1. Disaster Management Scheme.

Risk analysis starts with the identification of the hazards present or likely to be formed in the process, dangerous conditions that are present or could be generated failures of certain parts of the process or process control system, and human errors. After the identification of the hazards and estimation of the likelihood of these hazardous events and an evaluation of the effects and possible consequences to humans, environment and for structures is needed.

In risk analysis certain questions need to be addressed:
- What weaknesses could occur in the security management system?
- What preventive measures can be taken in order to control the risk factor?
- How are these actions monitored?

The qualitative part of risk analysis focuses on identifying the risks, possible failure cases, using methods like:
- Preliminary Hazard Analysis (PHA), was developed according to military standards in this field, and can be applied in the preliminary project phases. It focuses on the main areas that might contain dangerous substances, and on the main equipments, and monitors the possible failure points where dangerous substances or energies could be released.

- "What If?" method, poses a series of questions in order to determine unexpected events in the system.
- Checklists identify known and predictable risks using standards. Some of the more relevant techniques are: DSF – Diagnosis Safety Form, DCT – Diagnostique et Conditions de Travail, SDQ – Safety Diagnosis Questionnaire.
- Hazard and Operability studies (HAZOP), is designed to identify safety and operability problems using a systematic and structured approach by a multidisciplinary team. Using brainstorming and certain keywords deviations in the process from the normal functioning are identified, their causes and consequences on the process, humans and environment are evaluated qualitatively. HAZOP is one of the most used methods in technological hazard evaluation.
- Failure Modes and Effects Analysis (FMEA) determines how the failures of certain system components affect the optimum system performance. This ensures that proper safety measures are taken and safety systems are installed. The FMEA is a complementary analysis of Layer Of Protection Analysis (LOPA).

The qualitative methods focus mainly on identifying the possible hazards and are usually followed by a more thorough quantitative analysis (QRA).

In order to quantify the risk historical data or mathematical algorithms can be used to estimate probabilities of failures and frequencies of accidental scenarios. Proper safety measures can be applied efficiently only after a thorough quantitative risk analysis. QRA is the starting point for more complex processes like Land-use Planning, and Emergency Planning. High quality data also provides decision-makers with accurate information about the situation.

Vulnerability (V [-]) should be introduced in the risk formula shown below:

$$R = F \times C \times V \text{ [loss/year]}$$

where F [event/year] is the frequency of the event and C [loss/event] represents the magnitude of the consequences [2].

Consequence analysis relies on theoretical models to simulate events like release, dispersion, fire and explosion of different hazardous materials. Generally, risk assessment methods begin with the identification of hazards and vulnerabilities. Consequence based risk analysis has an approach that starts with the identification of the major consequences by analyzing the potential accident scenarios and the effects of the accidents upon the environment, human factor and structures. Then the process searches for combinations of hazard and vulnerability that could result in the most serious consequences.

The advantage of the consequence based risk analysis is that it will show how qualitative threat, vulnerability and consequence information can be combined to derive a qualitative value for risk and offer an easy-to-understand graphical way to present risk assessment results [3].

Assessment of vulnerability

Vulnerability can be defined as the proneness to experience adverse impacts or failures, or as the characteristics of a person or a group to anticipate, cope, resist and recover after a hazardous impact. Vulnerability involves a combination of factors which determine the level of the hazard for health, life, and damage of property following an incident.

Quantitatively the vulnerability can be expressed as a number between 0-1 or 0%-100%.

The vulnerability depends on the infrastructure and socio-economical conditions of the area. With reducing the hazards we are reducing the vulnerability, too. In many cases the increased number of victims is not due to bigger hazards, but the amplification of vulnerability of population. Some social groups are more vulnerable than others, in function of sex, age, corporeal condition etc.

A major component of a risk assessment is assessing the area's vulnerability to hazards. Regional vulnerability is determined by evaluating hazard exposure and coping capacity. For determining the vulnerability it can be selected a set of indicators. In case of technological disasters these indicators can differ from one case to another, depending on the possible accident consequences [4].

Mitigation of vulnerability is strongly correlated with socioeconomic development, and with social stability. Therefore it can be used to reduce the causes of environmental vulnerability, not only the consequences in terms of disastrous casualties and losses [5].

The modeling and simulation of chemical accidents

In general, models can be used to measure and represent; describe structure, behavior and pattern; reconstruct past or predict future behavior; generate and test theories and hypotheses [6].

Consequence assessment and modeling is based on models for source-term definition, dispersion calculations, fire and explosion, and finally vulnerability estimation of health effects [1].

The most important issue in simulation of chemical accidents is to find the right model which fits to the purpose of the study. For example, different models should be used in case of a toxic dispersion simulation for

flat and complex terrain. Two dimensional models can be applied for short distances where the topography of the terrain is not significant. 3D dispersion models are very useful for major releases above complex topography terrain. One of these 3D modeling systems is the SEVEX (SEVeso EXPert) system, which is built from three different parts:

- The *SEVEX-Meso* is a complex 3D terrain and meteorological model which solves the Navier-Stokes equations, considering the terrain roughness (the topography of the terrain), the land use of the terrain (five categories: water, forest, urban, grass-land and the mixture of the previous four) and the solar radiation and heat transfer between the ground and the atmosphere.
- The *SEVEX-Toxic* module is a Lagrangian 3D dispersion model that simulates the passive transport and dispersion of toxic and flammable material.
- The *SEVEX-Source* module simulates different types of releases and the effects of accidents. These three modules combined in SEVEX View software compute the worst-case realistic conditions of an accident. SEVEX View is the only software that considers both the SEVESO directives of the European Commission, and U.S. EPA guidelines. The software was built to simulate major industrial accidents, so the model is designed for impact zones from 1 to 18 km. The software was developed by the *Lakes Environmental Software* from Canada, in collaboration with ATM-Pro, Belgium [7].

A very popular model is the SLAB atmospheric dispersion model for denser-then-air releases over flat terrain. This model does not calculate source emission rates. It assumes that all source input conditions have been determined before. The current version of the *SLAB* model treats the following situations: instantaneous releases, finite and continuous releases from different sources like evaporating pools on land, horizontal or vertical jets, and instantaneous or short-duration evaporating pool on ground level.

The atmospheric dispersion of the released gas is calculated by solving the mass, heat and momentum flux conservation equations. The mathematical model is based on the theory of the superficial layer. The description of the variation that occurs in the gas plume is given by a differential equation system based on the total mass conservation and for the components, on the heat and impulse conservation for the three directions. The model is completed with the equations which describe the shape of the vapor cloud and physical equations [8]. The SLAB View software is the windows interface for the SLAB model and it was created by the Lakes Environmental Software in Canada.

Comparative analysis of a possible accident

In the followings are presented simulations of a chemical accident involving major liquefied chlorine release from storage vessel, a comparison between results obtained with 2D SLAB dispersion model and 3D SEVEX model.

The selected site is located at a height of 150 m above sea level, at 10 km from the city of Ramnicu-Valcea, Romania, on the right side of the Olt River on an alluvial terrace 7 meters above Govora Lake. The facility is 2 km long and 1,5 km wide. The site is surrounded by hills with a maximum altitude of 450 m, and the mean absolute altitude is 150 m.

With the building of the dams on the Olt valley, the surface covered by water increased, resulting in an increase of the relative humidity in the site's area, with a mean of 76%. The total annual precipitation in the area is 710,5 mm.

The wind circulation, both direction and speed, are influenced by the area's landscape. The Olt Valley has an obvious funneling effect, the highest wind frequencies occurring from the North (10,2%) and South (13%). The atmospheric calm situation has the highest occurrence rate (37,4%). The mean wind speed varies between 0.8 and 2 m/s. The dominant atmospheric stability conditions are class D (neutral), E (slightly stable) and F (stable) [9].

Simulations of the accident have been performed considering the meteorological "worst case scenario", for daytime, with a complete cloud cover, a 70% relative humidity, stability class D, ambient temperature of 20^oC, and for nighttime with no cloud cover, a 90% relative humidity, stability class F, ambient temperature of 10^oC.

The storage vessel has the following technical characteristics: length, L = 11 m, diameter d = 3 m, maximum capacity of storage equal to 90 tons of chlorine at 20^oC storage temperature, 80% filling level at 10 bar service pressure.

The SEVEX simulation considers the complex topography (GTOPO 30 database) and the land use of the terrain (CORIN database), calculating the wind direction and velocity for every 1 km x 1 km square using a 2 m/s synoptic wind [7]. The wind speeds for 36 directions were computed, for every multiples of 10°, from 0° to 350°. For this reason, the overall area of danger is estimated based on a discrete set of results, generating the so called plume fingers.

RESULTS AND DISCUSSION

In the followings are presented the consequence maps obtained from SEVEX and SLAB simulations, for the daytime scenario considering the wind direction form S-SW and for the nighttime scenario from N-NE. These wind directions can be found most frequently in the area.
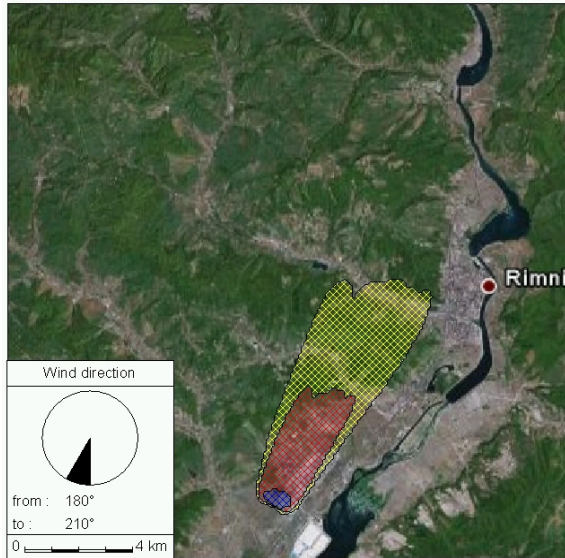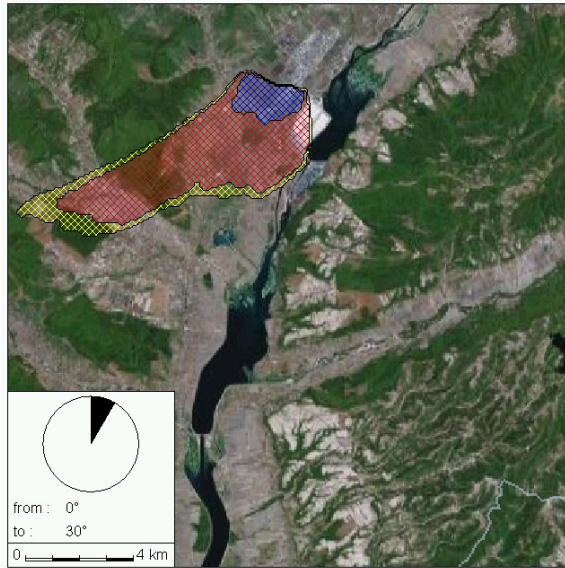
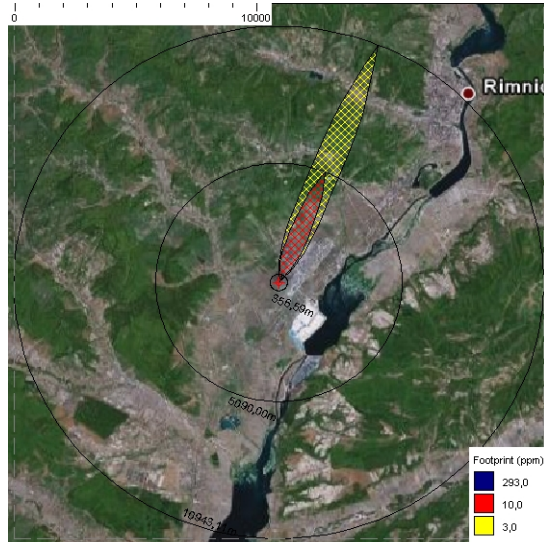**Figure 2.** SEVEX View simulation for daytime scenario.

| Risk	Orders	Criteria
None	No change in behaviour	C < 3,0 ppm p < 20 mbar
Temporary diseases Superficial injuries	Avoiding exposure advised	3,0 < C < 10,0 ppm 20 < p < 45 mbar
Permanent injuries out door	Self-confinement exclusion	10,0 < C < 293,0 ppm 45 < p < 100 mbar
Danger indoor	Evacuation	293,0 < C ppm 100 < p mbar

Figure 3. SEVEX View simulation for nighttime scenario.

55

In the SLAB View simulations we used the source emission rates calculated by the SEVEX model.

The distances obtained for the following typical concentration levels after one hour exposure: LC50 (Lethal Concentration 50%) = 293 ppm, IDLH (Immediately Dangerous to Life or Health concentration) = 10 pmm and EEGL (Emergency and Continuous Exposure Guidance Level) [10], are presented in Table 1:

Figure 4. SLAB View simulation for daytime scenario.
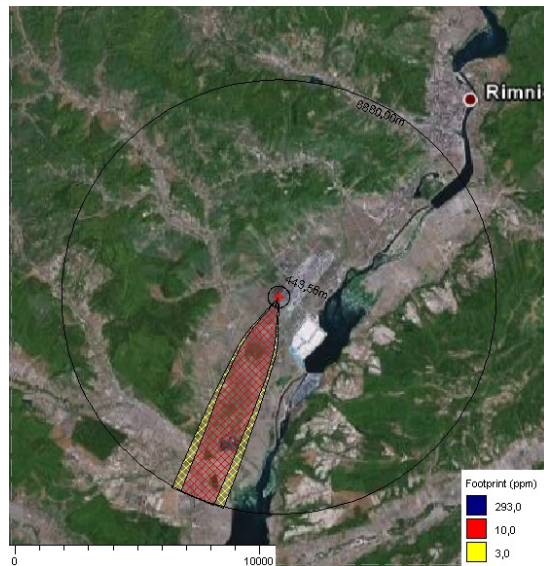
Figure 5. SLAB View simulation for nighttime scenario.

Table 1. Distances for the concentration levels of concern

SEVEX	Concentration level	Daytime scenario	Nighttime scenario
	LC50	651,9 m	1632,5 m
	IDLH	5042,3 m	6630,6 m
	EEGL	9780,8 m	9527,1 m
SLAB	Concentration level	Daytime scenario	Nighttime scenario
	LC50	357 m	443 m
	IDLH	5000 m	8880 m
	EEGL	10943 m	> 15000 m

The SEVEX model considers a possible fluctuation of 30 degrees in the wind direction and the results are presented considering this wind sector. The distances obtained in SEVEX, shown in Table 1, are the highest values from this 30 degrees wind sector. The SLAB simulation considers only one wind direction.

As seen, the daytime simulation results regarding the maximum distances are showing pretty close values in both cases. There are major differences in the nighttime simulation results; the distances obtained with the SLAB model are overestimated. The SLAB model does not take into account the topography of the terrain; it assumes that the dispersion is over a flat terrain with a specific roughness. This can lead to over or underestimation of danger zones for major releases, where the dispersion process can reach large distances.

CONCLUSIONS

The Chemical Risk Assessment is an important tool in the development of Safety Reports and Emergency Plans. The combination of qualitative and quantitative analysis methods can offer a good solution for the estimation of risk zones.

The aim of the Risk Analysis process is to reduce uncertainties by increasing safety levels by developing more efficient Emergency Plans for the restriction of insulation perimeters, offering immediate decisions, detailed, accurate and steady instructions.

Simulations of a possible chemical accident involving liquefied chlorine at a large storage facility have been preformed, and obtained dispersion results using two commercial software packages, SLAB View and SEVEX View.

The simulations show that the situation could become extremely dangerous to the nearby inhabitants, therefore an efficient external emergency plan must be developed and according to the Seveso III directive, the population should be informed about the hazards involved, emergency individual and collective measures, warning and evacuation plans.

In order to achieve this, high quality data is required, following the principle: "good quality data leads to good decisions". With the use of high performance software like SEVEX, we can aid the Romanian stakeholders and decision makers with information in order to develop efficient plans and policies.

REFERENCES

1. C. Kirchsteiger, M. D. Christou, G. A. Papadakis, *Risk Asessment and management in the context of Seveso II Directive*, Industrial Safety Series, Volume 6, Elsevier, **1998**, chapter 2-4.
2. Al. Ozunu, C. Anghel, "Evaluarea riscului tehnologic şi securitatea mediului", Editura Accent, Cluj-Napoca, **2007**.
3. Z. Török, N. Ajtai, Al. Ozunu, Proceedings of the 35th International Conference of SSCHE, Publisher Slovak University of Technology, **2008**.
4. Al. Ozunu, Z. Török, V. Coşara, E. Cordoş, A. Dutrieux - *Vulnerability Mitigation and Risk Assessment of Technological Disaster*, NATO Security through Science Series, IOS Pres, Chisinau**, 2007**.
5. P. Blaikie, T. Cannon, I. Davis, and B. Wisner, "At Risk: Natural Hazards, People's Vulnerability and Disasters", London: Routledge, **1994**, 320.
6. A. J. Jakeman, A. A. Voinov, A. E. Rizzoli, S. H. Chen, "Environmental Modeling, Software And Decision Support", Elsevier, The Netherlands, 2008, chapter 2.
7. SEVEX View:
   http://www.atmpro.be/product.php?item=sevex_view&onglet=general
8. D. L. Ermak, "User's manual for slab: an atmospheric dispersion model for denser-than-air releases", Livermore, California, USA, **1990**.
9. *Ramnicu Valcea Extremal Emergency Plan*, Romania, **2005**.
   http://enviro.ubbcluj.ro/cercetare/ccpaim/Apell/pdf/Oltchim.pdf
10. The National Institute for Occupational Safety and Health:
    http://www.cdc.gov/niosh/idlh/7782505.html

Dedicated to Professor Liviu Literat, at his 80th anniversary

POWER PLANTS ASHES RECOVERY IN ECO-FRIENDLY MORTAR COMPOSITIONS

LÁSZLÓ SZÉLL[a], VALENTINA CETEAN[b], TÓTH ANIKÓ[a], GAGEA LUCIA[c], ROMAN CECILIA[d], ROMAN MARIUS[d], GOG ADRIANA[d]

ABSTRACT. The paper treats the possibilities to recover the wastes resulted by coal combustion in power plants. This issue is in the researchers attention because the power plant's ashes represents the main waste in almost all European countries and the coal combustion will remain the most important source of energy. The greenhouse gas and the ashes have a huge impact on environment and the living species. In the experimental work the properties of five different mortars, realized with different proportion of ash were compared.

Keywords: *fly ash, concrete, mortar*

INTRODUCTION

The main reason for the ash use is not only the low price, but also the technical and qualitative benefits brought to the products. Due to its puzzolanic activity the ash combine with calcium hydroxide resulted from cement hydration giving birth in this way to cementitious materials which harden in time and have similar properties with the cement hydration products [1-3]. Through this activity is reduced the calcium hydroxide quantity in concrete which can leach in time by water providing cracks and voids. Thereby, the porosity and permeability of the concrete are reduced and the freeze-thaw resistance is increased, with other words the concrete is more durable.

[a] *S.C. Procema Cercetare S.R.L., Punct de lucru Cluj-Napoca, Str. Beiuşului, Nr. 1, RO-400394 Cluj-Napoca, Romania, procema.cluj@clicknet.ro*

[b] *S.C. Procema Geologi S.R.L., B-dul Preciziei, Nr.6, RO-062203 Bucureşti, Romania, procema.geologi@clicknet.ro*

[c] *Universitatea Babeş-Bolyai, Facultatea de Chimie şi Inginerie Chimică, Str. Kogălniceanu, Nr. 1, RO-400084 Cluj-Napoca,Romania, gagea@chem.ubbcluj.ro*

[d] *INCDO-INOE2000 filiala ICIA, str Donath, Nr. 67, RO-400293 Cluj-Napoca, Romania, icia@icia.ro*

Ashes fill in the minute voids that no other part of the mix can fill, thus creating a denser and less absorptive concrete with improved mechanical features. On short term mechanical strengths are lower than plain concrete, after 28 days they equalized and after a long period of hydration products with ashes present 15-20% higher mechanical strength than classic concrete [4-6].

Ashes use – recovered wastes – reduces the natural resources use. They also reduces the energy-intensive production of other concrete ingredients, leading to energy saving and "greenhouse gas" emission decrease. Replacing one tone of cement with fly ash it would save enough electricity to power an average home for 24 days, and reduce carbon dioxide emissions equal to a two months use of an automobile.

RESULTS AND DISCUSSIONS

The setting time (SR EN 196-3:2006) and the workability (SR EN 1015-9:2002) were determined on the fresh mortar. The results are presented in Figures 1 and 2.
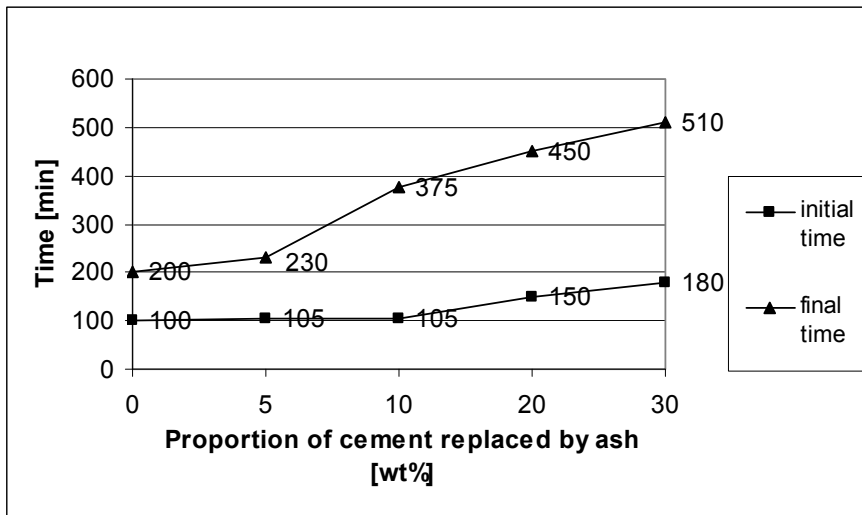
**Figure 1.** Variation of setting time in function of proportion of cement replaced by ash.

After 28 days of hardening in standard conditions (5 days in moulds at 20°C and 90% humidity; 2 days without moulds at 20°C and 90% humidity; 21 days without moulds at 20°C and 65% humidity) the density and water absorption of the mortars were determined using the methods indicated in SR EN 1015-10:2002 and SR EN 1015-18:2003.
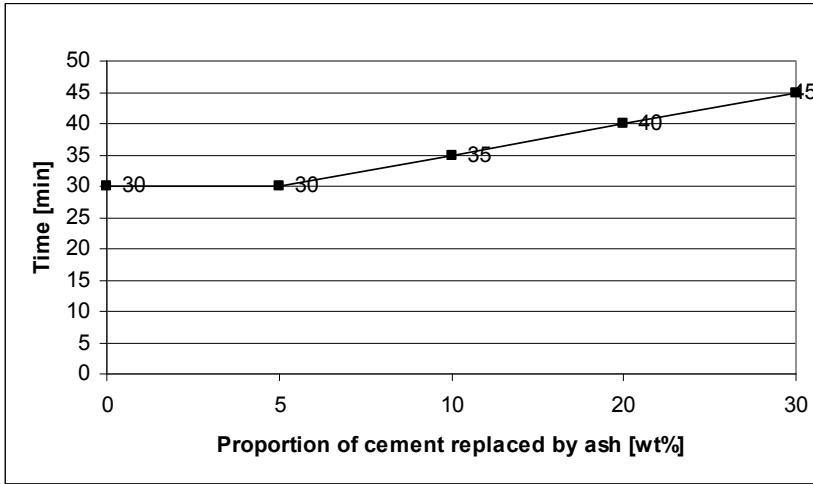
Figure 2. Variation of workability in function of proportion of cement replaced by ash.

The results are shown in the Figures 3 and 4.
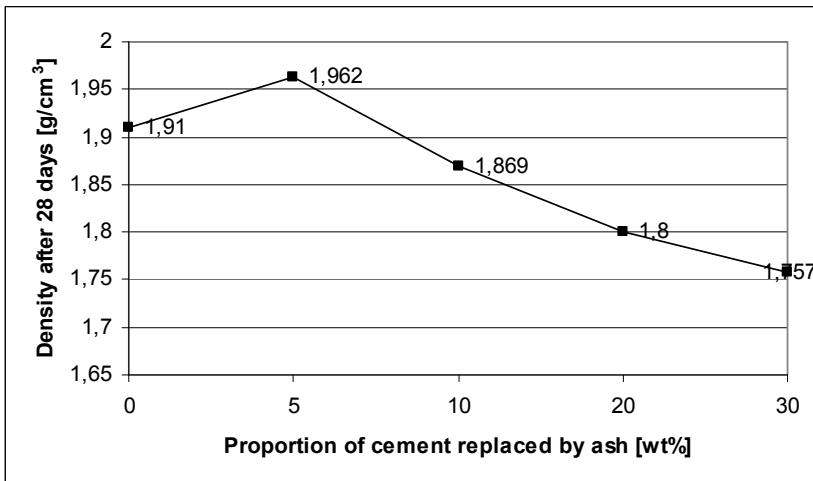
Figure 3. Density variation in function of cement replaced by ash.

The flexural and compressive strength of the compositions were determined after 28 days of hardening using the method indicated in SR EN 196-1:2006. In Figure 5 is presented the evolution of the strength in function of proportion of cement replaced by ash.
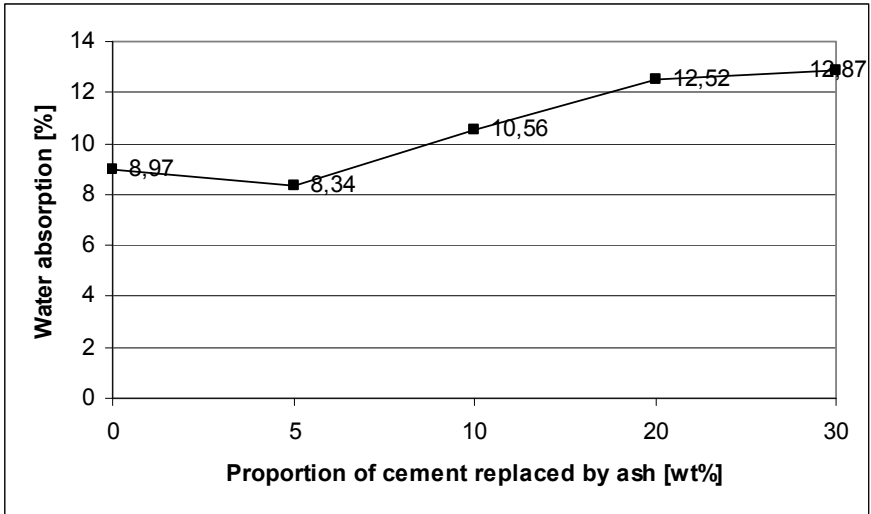
Figure 4. Water absorption variation in function of cement replaced by ash.

Figure 5. Flexural strength variation in function of proportion of cement replaced by ash.

Figure 6. Compressive strength variation in function of proportion of cement replaced by ash.

It is a known fact that the mechanical strength of the mortars and concretes with ash content is lower after 28 days and a beneficial effect it is observed only after 56 or 91 days. To demonstrate the evolution of the strength, mechanical tests were repeated after 56 days (Figure 7 and 8).

Figure 7. Flexural strength variation in function of proportion of cement replaced by ash.
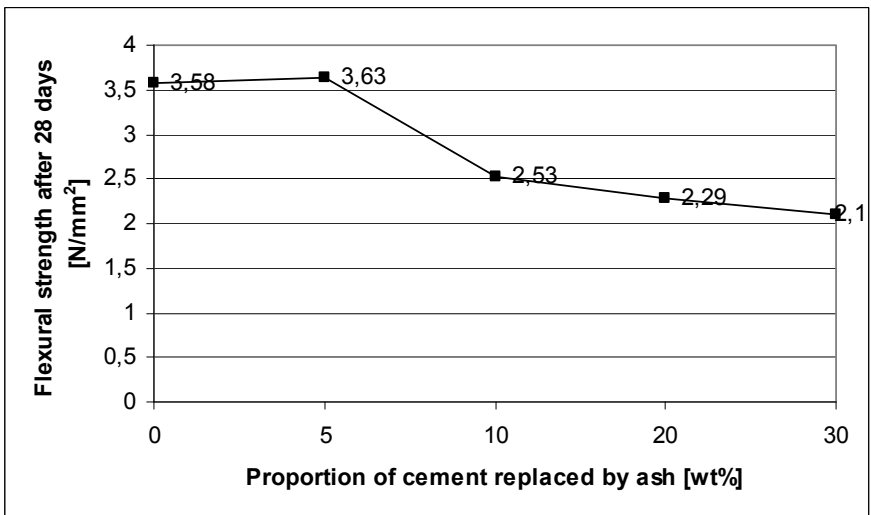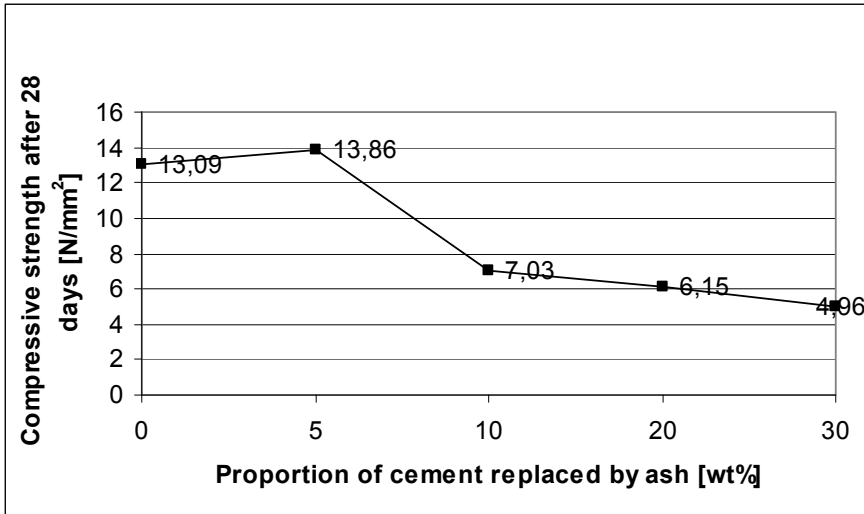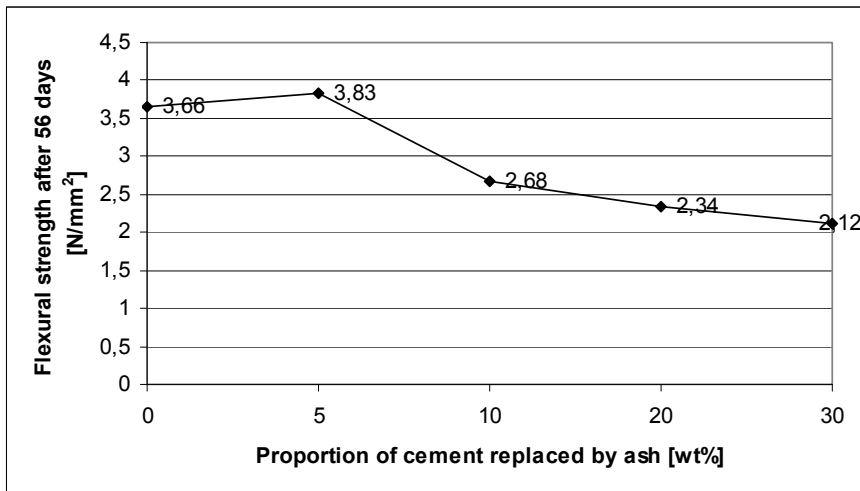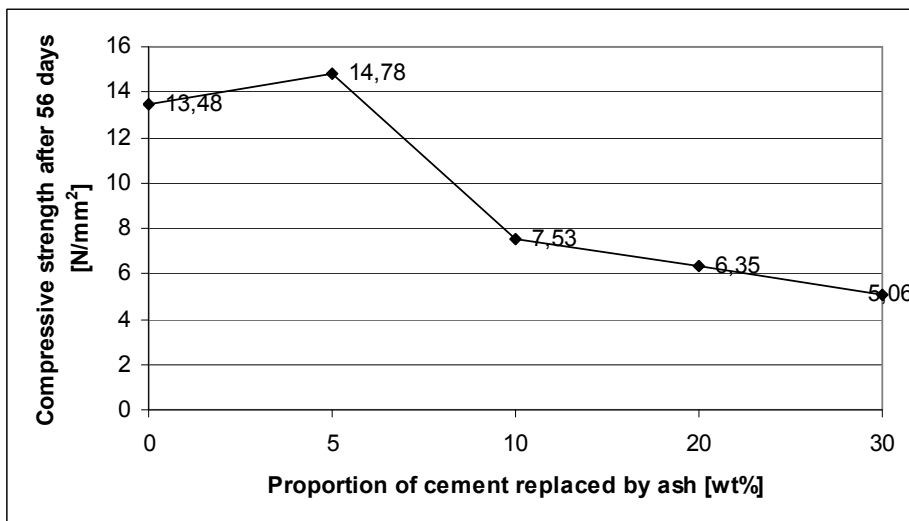
Figure 8. Compressive strength variation in function of proportion of cement replaced by ash.

From the figures presented above it can be concluded that it is possible to use ashes in mortar compositions, respectively a part of the cement can be replaced by ashes. The replacement of cement in proportion of 5, 10, 20 and 30 wt% was experimented (composition 2, 3, 4 and 5).

By replacing the cement with ash, the setting times of the mortars increases. The difference between the initial setting time of the composition without ash and the composition in which 5 wt% of cement was replaced by ash is only 5 minutes. The differences are bigger for higher ash content; it reaches 80 minutes for composition 5 in which 30 wt% of cement was replaced by ash.

The differences are more evident in the case of the final time of setting, where replacement of 5 wt% cement lead to a 30 minutes longer final setting time and replacement of 30 wt% cement with ash a 310 minutes longer time, which means an increase of 1,5 times.

In the case of mortars workability no differences were observed between the composition with no ash and the composition in which 5 wt% of cement were replaced, after that every 10wt% of cement replaced by ash brings 5 minutes in plus.

The density increases slowly by replacing 5% of cement, after that a decrease is observed, every sample densities being under the density of the standard composition. The water absorption is in agreement with the results obtained for the densities. The water absorption decrease from 8,96 % for the standard composition to 8,34 % for composition 2 with 5 wt% ash.

For the other compositions the value of absorption increases to 12,87 %, while the ash proportion was increased to 30 wt%.

The values for the mechanical strength state the observations at the density and absorption determination. Thus an increase in strength, both flexural and compressive, was observed for the composition 2 with 5 wt% ash. While the ash content was increased the mechanical strength decreased and it is situated below the standard composition strength.

The mechanical test after 56 day of hardening shows that the strength increase is higher for the compositions with ash. In the figure 9 are presented the proportions of the strength increase from 28 to 56 days.
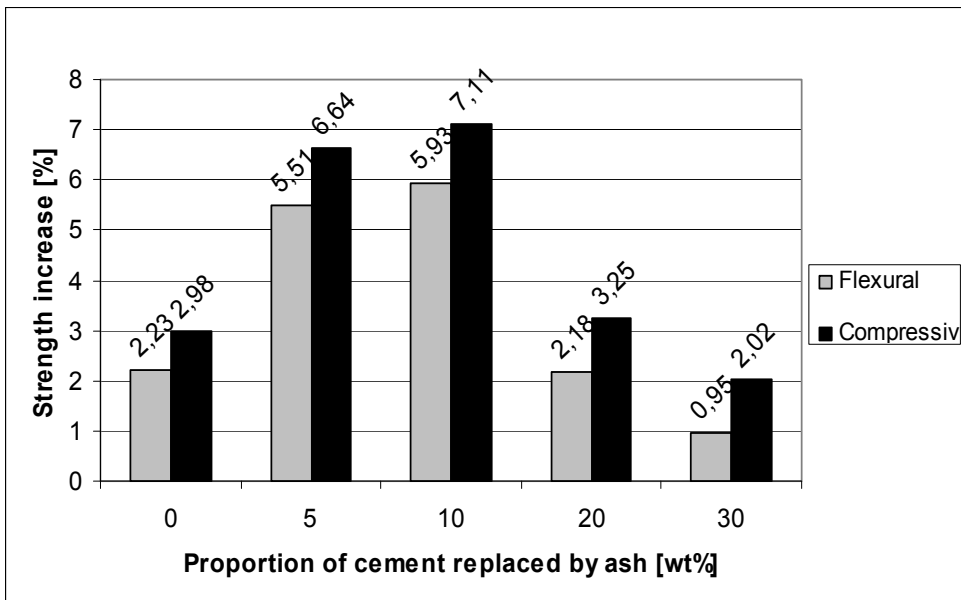
Figure 9. The increasing strength from 28 to 56 days in function of proportion of cement replaced by ash.

CONCLUSIONS

It can be concluded that the Zalău power plant ash can be used in mortar compositions. Replacement of 5 wt% cement by ash brings both economical and qualitative benefits.

Using power plants ash presents some advantages: ash is a cheap unconventional raw material, which introduce in mortar composition determine the decrease of production cost with 10-20%, without any quality compromises; the mechanical strength and durability of the product can be improved.

EXPERIMENTAL SECTION

In this experimental works 5 compositions of masonry mortars were prepared replacing the cement with different amounts of ash. The fresh and hardened mortars characteristics were investigated. The compositions were prepared by forced mixing using a laboratory mixer. The fresh mortar was cast in metallic moulds obtaining 160x40x40 mm prisms which were subjected to testing in hardened state.

In the table 1 are presented the proportions of the raw materials used in the compositions. The first composition, without ash is the standard composition.

Table 1. Mortar compositions

	1	2	3	4	5
CEM II/A-S 32,5 R %	25	23,75	22,5	20	17,5
Ash %	0	1,25	2,5	5	7,5
Sand 0-4 %	75	75	75	75	75
+ Water %	17,70	17,90	18,10	19,40	20,80

Three types of raw materials were used for the experimentation.

a) Cement - CEM II/A-S 32,5 R

►Chemical and physical–mechanical characteristics:
Initial setting time   Min 75 min.
Soundness   Max 10 mm.
Compression strength:
After 2 days: Min 10 N/mm^2
After 28 days: Min 32.5 N/mm^2
                                          Max 52.5 N/mm^2
Sulphate content (SO_3)   Max 3.5%
Chloride content   Maxim 0.10%

b) The chemical composition and the grain size distribution **of the power plant ash from Zalău** are given in Table 2 and 3.

Table 2. Chemical composition of the ash.

Oxides [wt %]								
SiO_2	Al_2O_3	TiO_2	Fe_2O_3	CaO	MgO	Na_2O	K_2O	L.O.I.
59,71	21,62	0,62	7,10	4,48	1,02	0,60	2,60	1,31

Table 3. Grain size distribution.

Fraction	Percent [wt %]
> 2mm	6,33
> 1mm	5,58
> 500µm	12,00
> 200µm	42,52
> 100µm	25,29
< 100µm	8,28

c) SAND 0-4 mm in conformity with SR EN 13139:2003 (Aggregates for mortar)

Table 4. Determination of particle size distribution of the sand – Sieving method SR EN 933-1/2002.

Sieve [mm]	Rest on sieve (R_i) kg	Refuse percent (R_i//M1) 100 [wt %]	Cumulated percents of refuse 100-(R_i//M1 100) [wt %]
8	0	0	100
4	0	0	100
2	0.019	9.5	90.5
1	0.0384	19.2	71.3
0.25	0.1144	57.2	14.1
0.1	0.023	11.5	2.6
0.063	0.0044	2.2	0.4
<0.063	0.0008	0.4	0

Table 5. Sand characteristics.

No	Characteristics	M.U.	Obtained value	Determination methods
1	Fine particle content	%	0,40	SR EN 933-1:2002
2	Sand equivalent (SE_4)	%	74	SR EN 933-8:2001
3	Impurities content - -humus	-	Light yellow	SR EN 1744-1:2004
5	Loose bulk density	Mg/m^3	1,50	SR EN 1097-3:2002
6	Voids	%	44,3	SR EN 1097-3:2002
7	Absolute density	Mg/m^3	2,71	SR EN 1097-6:2000
8	Oven dried real density	Mg/m^3	2,57	SR EN 1097-6:2000
9	Saturated dried surface real density	Mg/m^3	2,62	SR EN 1097-6:2000
10	Water absorption in 24 h	%	1,98	SR EN 1097-6:2000
11	Composition, content - chlorides - carbonates - total sulphur - sulphates	%	- 1,26 0,56 0,42	SR EN 1744-1:2004

REFERENCES

1. Gao Pei-wei, Lu Xiao-lin, Lin Hui, Li Xiaoyan, Hou Jie, *Fuel*, **2007,** *86*, 1208.
2. Sarat Kumar Das Yudhbir, *Cement and Concrete Research*, **2006**, *36*, 1827.
3. N. P. Rajamane, J. Annie Peter, P.S. Ambily, *Cement & Concrete Composites*, **2007,** *29*, 218.
4. Tsong Yen, Tsao-Hua Hsu, Yu-Wen Liu, Shin-Ho Chen, *Construction and Building Materials*, **2007,** *21*, 458.
5. Takeshi Yamamoto, Tsutomu Kanazu, Masateru Nambu, Takao Tanosaki, *Fuel*, **2006**, *85*, 2345.
6. Serdar Aydın, Halit Yazıcı, Hüseyin Yigiter, Bülent Baradan, *Building and Environment*, **2007,** *42,* 717.

Dedicated to Professor Liviu Literat, at his 80th anniversary

HEAT INTEGRATION OF AN INDUSTRIAL FLUID CATALYTIC CRACKING PLANT

ELIANA JARA-MORANTE[a], MIHAELA-HILDA MORAR[a], PAUL ŞERBAN AGACHI[a]

ABSTRACT. The fluid catalytic cracking process represents the main conversion process in a refinery. The successful operation of the FCC unit determines the position on the market of the refinery. The objective of this work is to analyze the actual heat exchanger network (HEN) of an industrial fluid catalytic cracking plant (FCC) and, using real data provided by a refinery from Romania and Pinch technique, to improve it. ASPEN Plus was used to simulate the process. ASPEN HX-Net was used to generate the retrofitted designs of the HEN. The obtained results present the possibility to improve the actual heat exchanger distribution in the heat exchanger network and to save energy. Adding heat exchangers, re-piping, and improving the performance of some heat exchangers, it is possible to save energy from the actual heat exchanger network and to improve the process operation.

Keywords: fluid catalytic cracking, heat exchanger network, optimization

INTRODUCTION

The fluid catalytic cracking process (FCC) is the process most common used in any modern oil refinery. The FCC unit consists of three distinct sections: the reactor-regenerator unit section including air blower and waste heat boiler, the main fractionator section including wet gas compressor and unsaturated gas plant section (Gascon). In order to improve its operation and to recover a certain quantity of energy, the FCC process must go through some structural changes (retrofitting). Retrofitting represents changes (new heat transfer area, re-piping, changing the heat exchangers place, etc) in the actual structure of the HEN in order to reduce the operation cost and in this way to increase the capital cost, indicating that there is a trade-off between the operational and capital costs.

---

[a] *Universitatea Babeş-Bolyai, Facultatea de Chimie şi Inginerie Chimică, Str. Kogălniceanu, Nr. 1, RO-400084 Cluj-Napoca, Romania, mmorar@chem.ubbcluj.ro*

The method most used for energy integration is Pinch Analysis. This technique is the simplest, easy to use, with immediate results and demonstrates its efficiency and applicability in many industrial saving energy problems. In addition, heat integration reduces site utility costs and capital costs. The savings made applying this technique came up to the 20-30% comparative with classical process design (B. Linnhoff, 1997).

A rigorous analysis of a FCC plant for energy saving was made by B. A. Al-Riyami et al., 2001. The HEN included the feed preheating, main fractionation and gas concentration section. The system was simulated using HySys.

The aims of our research were to analyze the actual heat exchanger network (HEN) of an FCC industrial plant using real process data (ex. flow streams, temperatures, transfer areas etc.) and to improve its operation from the economical point of view, using Pinch Analysis.

The FCC plant was already integrated in the past, during the time there were some changes in its operation (different raw materials, no production of heavy gasoline, different flow streams etc.). Constrained by the new type of operation and changes appeared in the design, a retrofit was realized trying not to affect the conversion process.

RESULTS AND DISCUSSION

Analyzing the existing HEN

The investigation of the actual HEN and the determination of the minimum duty of heating and cooling utilities have been done. The system was simulated in ASPEN Plus with the real process data collected from a Romanian refinery (UOP Fluid Catalytic Cracking process).

The scheme of the FCC unit which was implemented in Aspen Plus may be seen in the Figure 1.
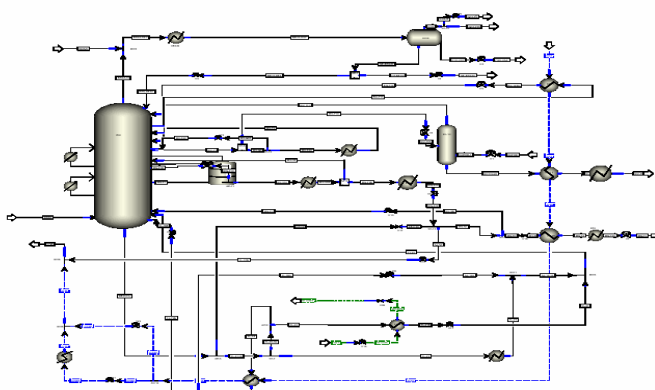
Figure 1. Flow diagram of FCC process.

In this study was realized the inventory of the heating and cooling sources. The data extracted from the simulation results using ASPEN HX-Net may be seen in Table 1. The table comprises 10 hot streams and 4 cold streams.

Table 1. Hot and Cold Streams Extracted from Simulation

| Streams	Type	Supply Temp. [C]	Target Temp. [C]	CP [kW/C]	HTC [kW/C-m2]	Enthalpy [kW]
SL-20-21	Hot	393.6	254	35.95	0.15	5018.0
SL-22-23	Hot	393.6	238	74.94	0.12	11660.3
SL-18-19:23	Hot	393.6	234.4	37.41	0.12	5956.1
MG-9:MG-10	Hot	334.7	60	17.89	0.15	4914.8
MG-41A:MG-41B	Hot	250.4	224	102.39	0.15	2703.0
MG-42B:MG-42D	Hot	224	177	5.85	0.12	275.1
MU-86A:MU-72	Hot	205.5	108.9	79.31	0.12	7661.8
MOT-USO:MU-83	Hot	177.2	60	9.64	0.2	1129.3
BG-111:BG-129	Hot	145.4	98	61.74	0.2	2926.7
BU-207:BENZ-OUT	Hot	66	43	342.60	0.15	7879.9
C-31:C-32	Cold	80	110.2	96.91	0.15	2926.7
C-32:C-33	Cold	110.2	114.5	96.86	0.15	416.5
C-33:C-34	Cold	114.5	143.2	96.94	0.15	2782.3
C-34:C-35	Cold	143.2	204.7	96.85	0.15	5956.1
C-35:C-36	Cold	204.7	293.8	96.82	0.15	8626.6
B1-GE12:B2GE12	Cold	172	187.6	747.46	0.25	11660.3
B1-GE11:B2GE11	Cold	172	176.1	659.27	0.2	2703.0
B1-GE9:B2GE9	Cold	105	112.7	995.04	0.2	7661.8
WFE3-FE23	Cold	100	200.7	49.83	0.5	5018.0

The raw material stream of the FCC process, mainly the heavy vacuum distillate stream from the vacuum distillation unit, is a cold stream that is been heated up to a temperature around 290 ^{0}C in 4 heat exchangers (streams: C-31:C-32, C-32:C-33, C-33:C-34, C-34:C-35 and 1 fire heater (stream C-35:C36).

The products stream from the riser is fractionated in the main column in the following streams: heavy diesel oil, light diesel oil, heavy gasoline, light gasoline and slurry.

The slurry stream separated on the bottom of the column has the highest temperature (393.6 ^{0}C). It provides energy to produce superheated steam (WFE3-FE23) and to heat up other process streams: the gasoline from Gascon and the raw material. The steam generation stream was considered as a process stream in order to keep the existing production of steam the same both before and after the retrofit. The steam is needed for the other processes from the refinery. In the Aspen Plus simulation slurry stream is splited in: SL-20-21, SL-22-23 and SL-18-19:23.

The cold gasoline streams from Gascon plant (B1-GE12:B2GE12, B1-GE11:B2GE11, B1-GE9:B2GE9) were considered to be process streams trying not to modify the process behavior and the consumption of cold utility of the FCC process. The light (MU-86A:MU-72, MOT-USO: MU-83) and heavy (MG-41A:MG-41B, MG-42B:MG-42D) diesel oil streams help to increase the temperature of the raw material and are cooled and sent to storage. Heavy diesel oil (BG-111: BG-129) in the actual operation of the FCC process it's not considered anymore as one of the main products. It is used only to heat up the raw material stream and then is reintroduced in the main column. The gasoline and gases stream from the top of the column (BU-207: BENZ-OUT) is sent to Gascon unit after a part of the gases are separated to the furnace.

Based on the data provided by the simulation and that have been presented in Table 1, the composite curves (Figure 2) and Grand composite curve (Figure 3) were generated.
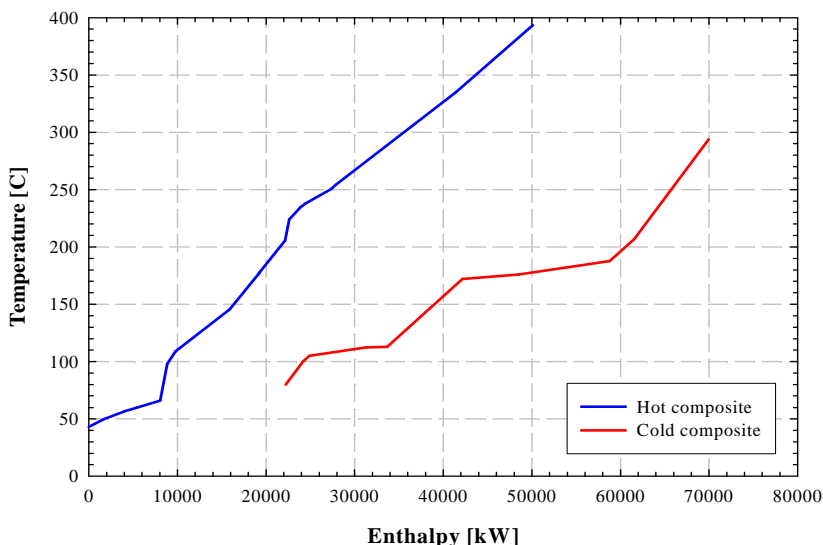
Figure 2. Composite Curves of the existing HEN.
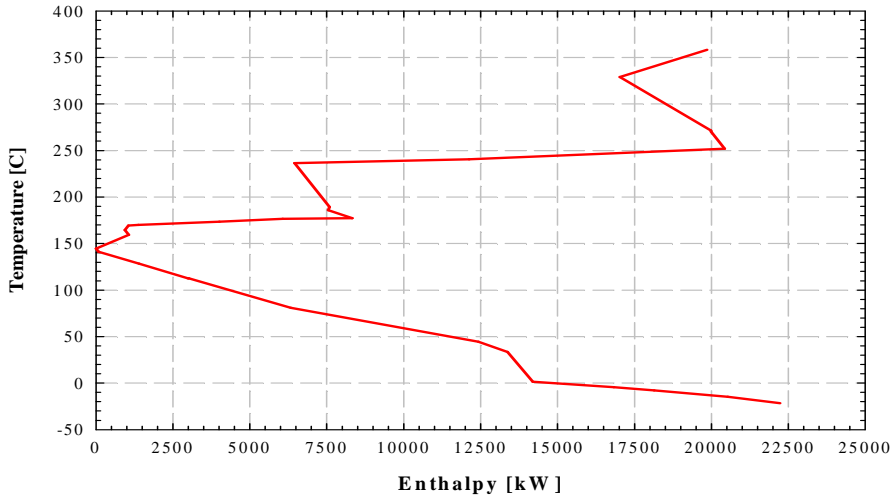
Figure 3. Grand Composite of the existing HEN.

The Grand composite curve shows that the pinch temperature of the process is 144.5^0C and from the composite curves it was discovered that the ΔT_{min} for the process is 129^0C and the duty of hot utility is 19858 kW and of cold utility is 22234.79 kW.

Table 2. Heat exchangers from the industrial process

Heat exchanger	Cost [$]	Simulation area [m2]	Real area [m2]	Duty [kW]
FE-21	271525.74	941.91	324	2926.69
FE-18	62073.63	81.15	113	2782.33
FE-9	0.00	0.00	18777	0.00
FE-4	52865.53	50.28	120	2132.50
FE-22	38003.33	8.44	7	275.09
FE-17	48050.00	35.39	248	416.46
FE-3	83867.74	163.15	76	4766.40
FE-23	39939.71	13.04	12.3	251.60
FE-6	106258.59	256.77	894	7879.95
GE-12	366717.43	1678.59	-	11660.34
FE-2	130758.34	367.28	111	5956.05
FE-10	73604.16	123.20	2776	712.84
GE-9	462658.57	1657.14	-	7661.77
GE-11	197879.39	596.48	-	2702.99

The simulation of industrial process provided 15 heat transfer units (excepting the fire heater) that are summarized in Table 2. The cold utilities used are cooling water (94%) and air (6%) with a total cooling need of 11000.38 kW. The only hot utility considered is the fuel (8626.6 kW).

73

The heat exchanger FE-9 present in the real process it is used only for cooling down the temperature of the gasoline stream (top of the column) when it increases above a fixed value. The heat exchangers GE-9, GE-11 and GE-12 are located in the Gascon plant and they have to remain unmodified.

Besides the heat exchangers summarized in Table 2, preheating train of the raw material contain another heat exchanger, FE-24, that is out of order and it wasn't considered in the simulation. It was designed to cool the heavy gasoline stream that goes to the storage but this product is not produced anymore.

The existing heat exchanger network design was generated by Aspen HX-Net (Figure 4). The heat transfer marked with blue dots represents the heat exchangers with cold utilities, the red dots represent a heat exchanger with hot utility and the grey dots represent process to process heat exchangers.
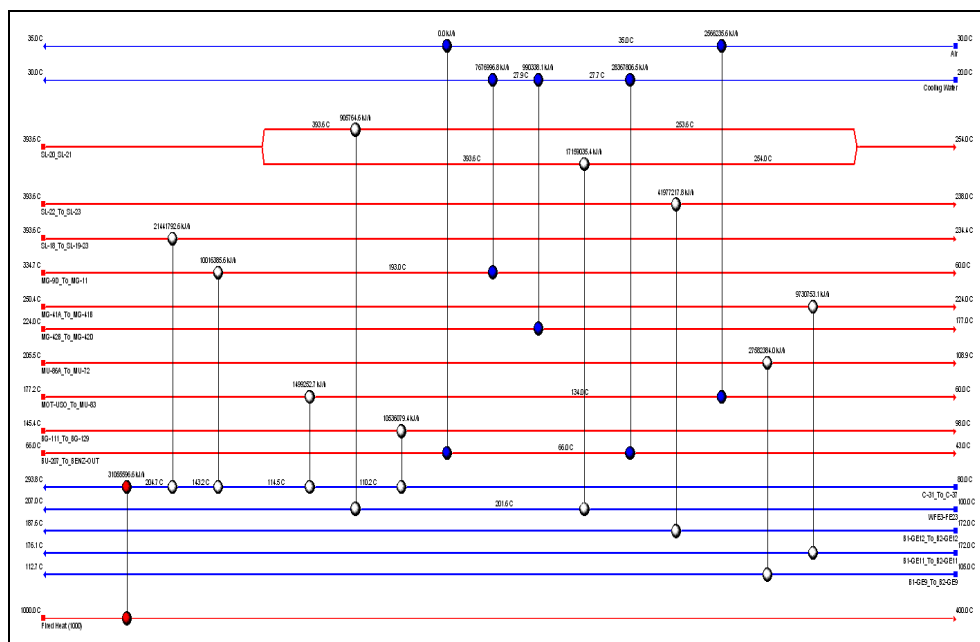

Figure 4. Existing Heat Exchanger Network.

Improving the existing HEN

In order to improve the real heat exchanger network the optimization of the total cost of FCC process was done. The total cost as a function of ΔT_{min} is represented in Figure 5. It can be seen that the minimum cost is achieved in a range of $\Delta T_{min}=8.5$ to 12^0C; and as a conservative approach the optimum minimum approach temperature for the retrofit target is $\Delta T_{min}=12^0C$ because operating with a ΔT_{min} less than $10\ ^0C$ should be avoided [4].
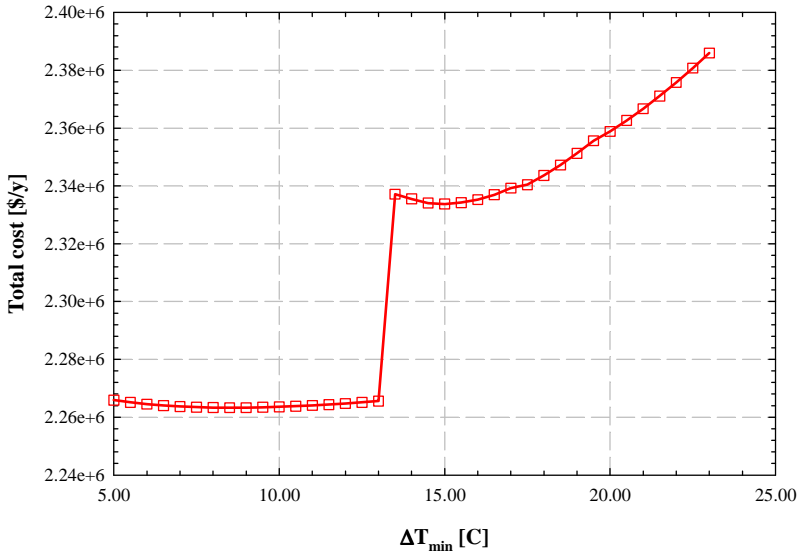
Figure 5. Total cost vs. minimum ΔT.

Considering that the actual HEN is operated with $\Delta T_{min}=129^0$C, decreasing it to 12^0C it is possible to improve the actual heat exchanger distribution for saving energy of 13553 kW.
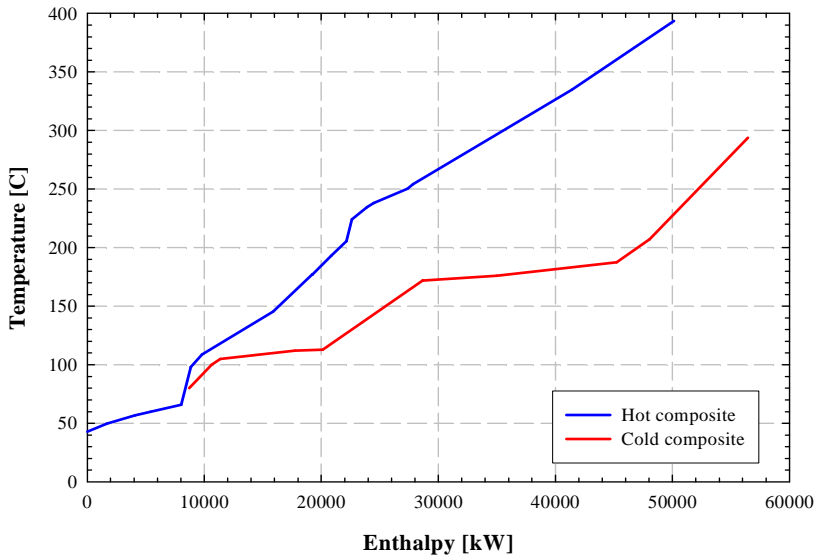
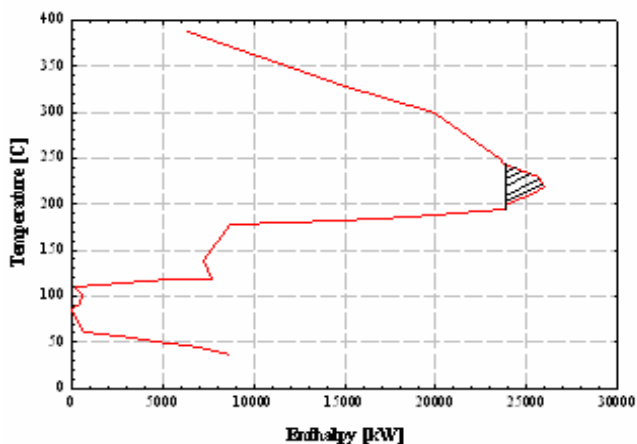**Figure 6.** Composite curves with $\Delta T_{min}=12^0$C.

Figure 7. Grand Composite curve with $\Delta T_{min}=12^0C$

The new composite curves, generated in Figure 6 and Figure7, show that the pinch temperature has been reduced from 144.5 ^{0}C to 88 ^{0}C and the minimum need of heating and cooling is reduced to 6325.92 kW and 8701.28 kW respectively. In conclusion, reducing the ΔT_{min} reduces the heating and cooling needs approximately with 32% and 39% respectively. Also it can be observed in Grand Composite curve that there are some pockets of extra energy that may be saved.

Table 3 presents the comparison of the necessary of cooling and heating needs in those two cases considered: $\Delta T_{min}=129$ ^{0}C and $\Delta T_{min}=12$ ^{0}C. These results were compared against the Grand Composite curve (Figure 8).

Table 3. Saving energy through reduction of ΔT_{min}

		ΔT_{min} [^{0}C]		Reduce
		129	12	[%]
Heating	[kW]	19859.00	6325.92	68.15
Cooling	[kW]	22234.36	8701.28	60.87

In the new HEN, generated with Aspen HX-Net, there is not process-to-process heat exchange that crosses the pinch temperature. This is an improvement compared to the initial design extracted from the simulation.

In order to improve the HEN other designs were generated and analyzed. The only change considered in those designs is the distribution of the heat exchangers. The designs were compared in terms of their operation costs and efficiency. In all the designs the stream corresponding to steam generation was consider as a process stream. Five designs were proposed and have been used the economic model recommended in [1] and by ASPEN HX-Net.
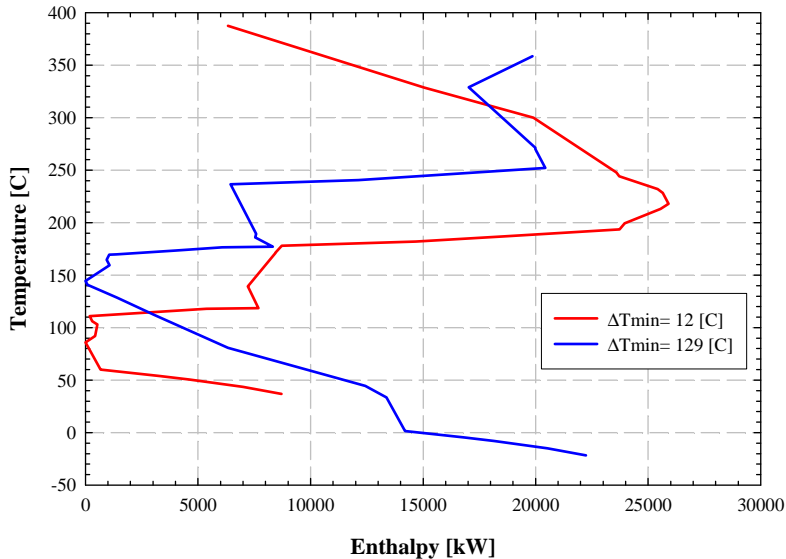
Figure 8. Grand Composite curves comparison.

The designs used present the following conditions:

Design A:
- The order of the heat exchangers are changed optimizing the production of steam;
- The total area of the HEN was increased;
- The operating cost was reduced.

Design B:
- Addition of a fire heater to heat the cold stream;
- The heating and cooling needs are decreased;
- The operating cost and the total cost are reduced.

Design C:
- The split of slurry stream was taken out;
- The number of heat exchangers was reduced;
- The operation and the capital costs have been increased;
- The cooling need was the same as in the base case;

The total area was increased.

Design D:
- The number of heat exchangers that are used to heat up the raw material were increased;
- The total area of the heat exchangers was increased;
- The operating cost and the total cost increased.

77

Design E:

- A part of the hot stream "heavy diesel oil" was re-piped to produce steam;
- The heating and cooling needs were decreased;
- The operating, capital, and total costs were reduced.

The characteristics (total cost, transfer area, etc.) of the designs obtained are compared in the Table 4.

Table 4. Comparison among designs evaluated

	Total cost	Area	Heating	Cooling	Operating cost
	[$/y]	[m2]	[kW]	[kW]	[$/y]
SimulationBaseCase	2569201.45	6238.39	8626.55	11000.38	1049460.81
Design A	2707323.90	8443.29	8621.23	11000.38	998785.53
Design B	2430791.22	8542.85	8309.79	10689.08	947392.96
Design C	2695805.34	8441.96	8621.23	11000.38	998785.53
Design D	2377950.54	8581.62	8033.84	10413.99	915249.06
Design E	2335706.83	6350.65	7325.39	9701.64	897860.72

The performance of the considered designs, with respect to the ideal target, was evaluated through the alpha plot, the closest the existing HEN is to the ideal curve in an energy area plot the better the performance. In Figure 9a may be seen that there are at least three designs that could have a better performance than the simulation base case (e.g., design B, D and E).

a)   b)
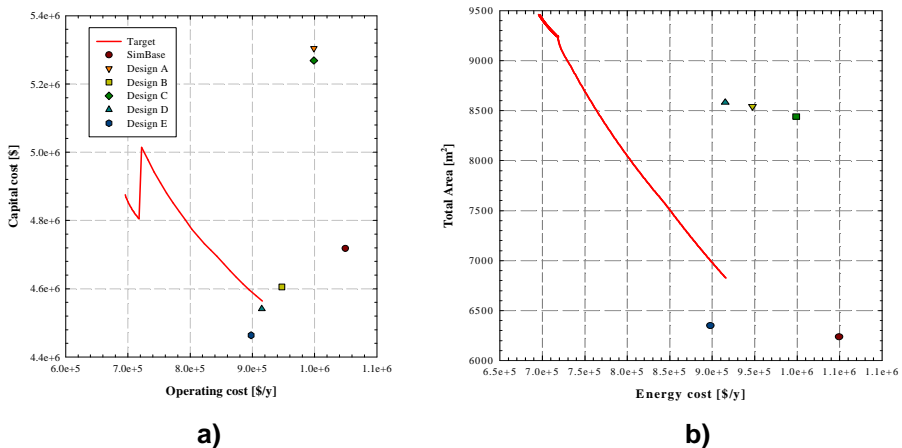
Figure 9. a) Performance of the designs. b) Efficiency
of the proposed designs respect to the ideal.

Figure 9b shows the efficiency of the designs considered. The closest to the ideal efficiency are the design E and the design considered in the simulation base case, indicating that those designs are using efficiently the heat transfer area. The designs A, B, C and D are far from the ideal performance.

It could be advantageous from the economical point of view to change the existing HEN with design E (Figure 10) that has lower energy consumption, capital and operational costs than the existing HEN. Considering the results from Table 4, total costs are decreased with approximately 9% and there is an energy saving of 15% of heating and 12% of cooling. However, the performance of this design needs to be evaluated through a simulation implemented in Aspen Plus or Aspen Dynamics to see if it is the best choice in all conditions (economics, dynamic behavior, controllability etc.).
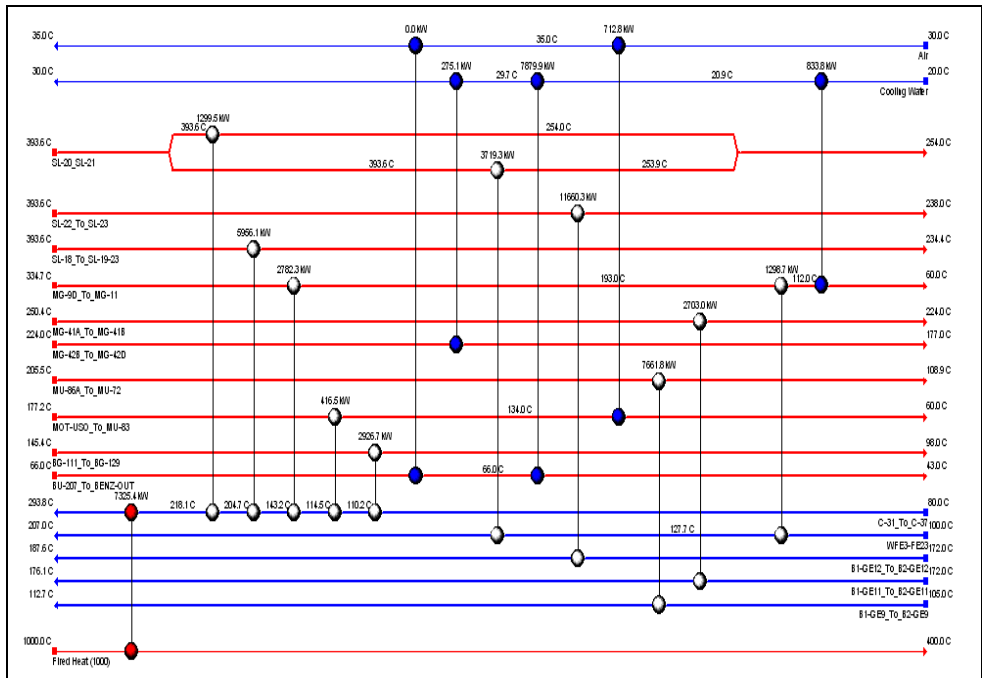

Figure 10. Heat exchanger network – Design E.

CONCLUSIONS

The fluid catalytic cracking is a dominant process in oil refineries and there has been a continuous effort to improve the efficiency and yield of the unit over the years.

The results of the present retrofit study confirmed that it is possible to save energy from the actual heat exchanger network. The improvement comprises adding heat exchangers, re-piping, and improving the performance of some heat exchangers. The closest to the ideal efficiency is the design E because it uses efficiently the heat transfer area and it is the best design comparative with the existing industrial HEN. In the real HEN there are process-to-process heat exchangers that cross the pinch temperature. Total costs are decreased with approximately 9% and there is an energy saving of 15% of heating and 12% of cooling.

No drastic changes have been suggested for the existing HEN, the new design was done trying not to modify the process-to-process heat exchangers, assuring that the process would not be affected.

Significant quantities of hot and cold utilities (water, gas, etc.) are saved by reducing the heating and cooling needs in the FCC plant. This is an important step in conserving and recycling the natural resources.

This optimization of the HEN in terms of the economical point of view gives a starting point to continue with the improvement of the industrial process. Future work will analyze the generated designs in terms of dynamic behavior and controllability.

ACKNOWLEDGMENTS

REFERENCES

1. A. B. Al Riyami, J. Klemes, S. Perry, *Applied Thermal Engineering*, **2001**, *21*, 1449.
2. F.S. Liporace, F.L.P. Pessoa, E.M. Queiroz, *Lat. Am. Appl. Res.,* **2002**, *32*, 2.
3. B. Linnhoff, "A user guide on process integration for efficient use of energy", Rugby Institution of chemical Engineers, **1997**.
4. R. Smith, "Chemical Process Design and Integration", John Wiley & Sons, **2000**.
5. W. D. Seider, J. D. Seader, D. R. Lewin, "Product & Process Design Principles", John Wiley & Sons, Inc, **2003**.
6. M. M. El-Halwagi, "Process System Engineering: Process Integration", vol. 7, Academic Press, **2006**.

Dedicated to Professor Liviu Literat, at his 80th anniversary

GASIFICATION PROCESS – A PRACTICAL WAY FOR SOLID FOSSIL FUELS DECARBONISATION

CĂLIN – CRISTIAN CORMOŞ[a], ŞERBAN PAUL AGACHI[a]

ABSTRACT. This paper investigates the technical aspects of solid fossil fuels decarbonisation by gasification process. More specifically, it focuses on the technical evaluation and the assessment of performance of an Integrated Gasification Combined Cycle (IGCC) scheme modified for Carbon Capture and Storage (CCS). One of the key units of such a plant is the gasification island, a number various commercial gasification reactors (mainly entrained-flow types of dry feed and slurry feed) are evaluated for decarbonisation of fossil fuels (coal).

The significant issues in the overall design of fossil fuels decarbonisation process using gasification process are: proper choice of gasification reactor and feedstock (e.g. fluxing or fuel blending), downstream syngas treatment options (shift conversion of carbon monoxide, syngas desulphurization and later carbon dioxide capture) and finally the usage of combustible decarbonised gas for various energy vectors poly-generation (e.g. power, H_2 etc.).

Finally, whole process for one case study (using Siemens gasification reactor) was mathematical modeled and simulated using ChemCAD software for the particular case of hydrogen and electricity co-production scheme based on coal with carbon capture and storage.

Keywords: *Fossil fuels decarbonisation, Gasification, Carbon Capture and Storage*

INTRODUCTION

Gasification of solid fuels (either only fossil fuels or in addition with various renewable energy sources such biomass or solid wastes) forms the core of Integrated Gasification Combined Cycle (IGCC) concepts which is one of the advanced clean coal power generation systems [1, 2]. Compared with conventional coal fired power plants, IGCC scheme has lower emissions of acid gases (NO_X, SO_X) and particulate matter. In addition, with respect to clean

---

[a] *Universitatea Babeş - Bolyai, Facultatea de Chimie şi Inginerie Chimică, Str. Kogălniceanu, Nr. 1, RO-400084 Cluj-Napoca, Romania, cormos@chem.ubbcluj.ro, sagachi@staff.ubbcluj.ro*

coal technology, IGCC has a better carbon dioxide capture potential, using pre-combustion capture whereas conventional coal fired power plants have to use post-combustion capture [2, 3].

The IGCC is an energy conversion process concept in which the solid fuel (e.g. coal) is gasified to produce a fuel gas (called syngas), which after purification (ash removal and desulphurization), is burnt in the gas turbine in a conventional Combined Cycle Gas Turbine (CCGT) to produce power. Because the gasification process produces a large amount of waste heat, which can be used for steam production, the steam systems in the CCGT heat recovery steam generator and gasification system are integrated together, hence the IGCC appellation (the combination of two thermodynamic cycles namely Brayton cycle and Rankine cycle) [4].

In gasification processes designed for fuel decarbonisation, oxygen plus steam or water is reacted with coal at high temperatures to produce syngas which mainly consists of carbon monoxide and hydrogen. After purification performed to remove ash and sulphur compounds, the mixture of CO and H_2 is normally used as a fuel gas for the gas turbine (no capture option). But for the capture option (pre-combustion capture of carbon dioxide), the hydrogen level is raised by catalytic conversion of carbon monoxide in the syngas with steam, the chemical reaction being:

$$CO \ + \ H_2O \ \leftrightarrow \ H_2 \ + \ CO_2$$
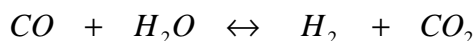
This step also enables the carbon present in the coal to be concentrate in form of carbon dioxide that can be later captured. After shift conversion, the gas, which now contains mainly carbon dioxide and hydrogen, is cooled to ambient temperature then sent to an Acid Gas Removal (AGR) system for CO_2 and H_2S removal. Here, CO_2 and H_2S are removed by chemical solvents similar with those used in post-combustion capture (alkanolamines such as methyl-diethanol-amine - MDEA) as well as by physical solvents (e.g. Rectisol[®], Selexol[®]) [5].

After AGR, the hydrogen-rich gas stream can be used for various purposes: to produce hydrogen for chemical and petro-chemical processes (e.g. ammonia and methanol synthesis, hydrogenation, hydrocracking and hydrodesulphurization processes etc.) or for co-production of hydrogen and electricity. In this last option, one of the main advantages of such a scheme is the possibility to run the plant full-load all the time. It is well known that power duty has daily, weekly and seasonal variations and the power generation has to follow the duty (demand). In such a case (e.g. during the night), the power plants have to run part-load or even to be switched off which implies severe reduction of the plant lifetime (thermal stress, corrosion etc.) and negative impact on plant economic indicators.

The co-production mode of hydrogen and electricity has the merits that during the low power duty periods, the plant can produce hydrogen which, apart from power, can be stored. In this case the plant is running full load all time with significant benefits in term of plant lifetime and economic indicators. In co-production mode, the hydrogen-rich gas is split in two: one stream is purified by Pressure Swing Adsorption (PSA) and then is sent to the hydrogen customers and rest is used in a CCGT for power generation.

This paper investigates the technical aspects of coal gasifier selection for co-production of electricity and hydrogen based on IGCC processes with carbon capture and storage [6-9]. More specifically, it focuses on the technical evaluation and the assessment of performance of a number of coal gasifiers based on existing moving-bed, fluidised-bed and entrained-flow gasification processes.

The key factors considered in the analysis are: gasifier throughputs, reliability and experience, gasifier pressure and temperature, cold gas efficiency (CGE), carbon conversion, water or steam requirement, downstream gas clean up issues, hydrogen production potential, implication of oxygen purity for hydrogen purification stage, implication of gasifier selection for AGR system etc. Based on these key factors, a list of the most promising coal gasifiers for electricity and hydrogen co-production based on IGCC processes with carbon capture is proposed.

After analyzing the most promising gasification reactors for coal, for one case the whole IGCC concept with carbon capture and storage will be modeled and simulated using ChemCAD software for generation of about 400 MW power and a flexible hydrogen output between 0 and 200 MW hydrogen (considering the hydrogen lower heating value – LHV) with about 90 % carbon capture rate (decarbonisation rate).

Plant concept and gasifier options for hydrogen and electricity co-production with carbon capture

An IGCC plant modified for co-production of hydrogen and electricity with carbon capture and storage is basically similar to that of existing IGCC plants for producing electricity only without carbon capture. The main differences are the need for shift conversion stage to increase hydrogen production and to concentrate the carbon species in form of carbon dioxide, an Acid Gas Removal (AGR) system which in addition to hydrogen sulphide (as in conventional technology) is capturing also carbon dioxide and a hydrogen purification stage by PSA.

A simplified flowsheet of the hydrogen and electricity co-production (HYPOGEN concept) plant based on coal with carbon dioxide capture is presented in the Figure 1 [10]. In this case, based on an entrained-flow design, a syngas boiler is used to recover waste heat before the syngas is sent to the shift converter. Other entrained-flow gasifiers dispense with this option and quench the gas with water to solidify and remove slag.

As shown, carbon dioxide stream is compressed to pressures more than 100 bar before being sent to storage site (geological storage or for Enhanced Oil Recovery - EOR). This also gives a difference between the type of plant and a conventional IGCC, the compression of carbon dioxide requiring a significant amount of energy which implies an energy penalty.
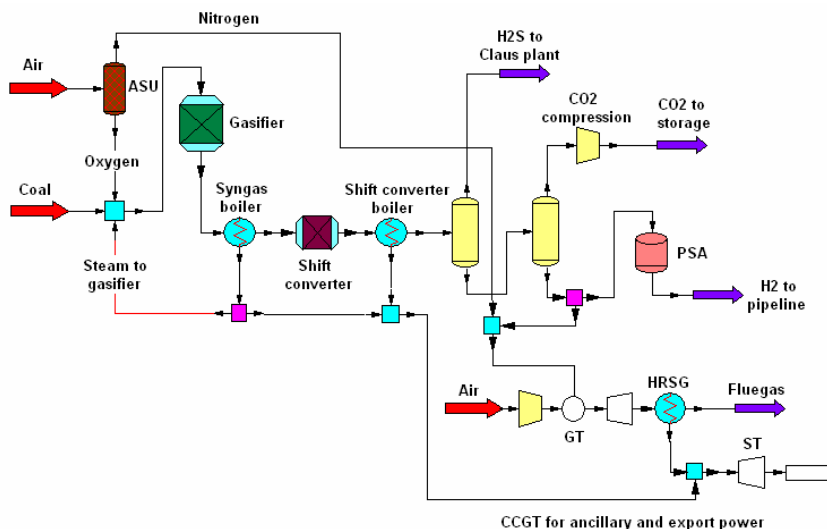
Figure 1. Hydrogen and electricity co-production scheme with carbon capture and storage based on coal gasification.

An other main difference is the addition of a Pressure Swing Absorption (PSA) system for purifying the hydrogen outlet stream of the plant. Because the need to find suitable solutions for replacing fuel oil-derived products (gasoline and diesel) for transport sector, the hydrogen stream purity is set to 99.95 % (vol.) to be used in Proton Exchange Membrane (PEM) fuel cells designed for mobile applications.

Gasification reactors can be grouped into the following three main categories: moving-bed gasifiers (sometimes also called fixed-bed gasifiers), fluidised-bed gasifiers and entrained-flow gasifiers [1, 10-11]. A short description of each of these categories is discussed below:

- *Moving-bed gasifiers* are characterized by a bed in which the fuel moves slowly downward under gravity as it is gasified. The phases circulation is a counter-current one. In such a counter-current arrangement, the hot gases from the gasification zone are used to preheat and pyrolyse the downward flowing coal. With this type of gasifier, the oxygen consumption is low but

pyrolysis products are present in the syngas and also the outlet temperatures are low (400 – 600°C). Within this category there are two different gasifier types: the dry ash type in which the temperature is kept below the ash melting point, and the slagging type in which the temperature in the gasifier heart is above the ash melting point.

The main shortcoming of this type of gasifier is that a considerable amount of methane will be produced, which reduces the amount of hydrogen that can be generated and decrease the carbon capture capabilities of the plant (methane cannot be captured by AGR) [10].

- *Fluidized-bed gasifiers* in which the bed is maintained in a fluidised condition by an upward flow of gaseous stream. This configuration offers extremely good mixing between feed and the oxidant, which promotes both heat and mass transfer. This ensures an even distribution of material in the bed, and hence a certain amount of partially un-reacted coal is removed with the ash (lower carbon conversion compared with other gasifier types). This gasifier type has moderate oxygen and steam consumptions [1].

Unfortunately operation of fluidised beds are restricted to temperatures below ash softening point (900 – 1050°C), as operation above this temperature would cause the ash to agglomerate. This implies the need for a highly reactive fuel. Coal is therefore not suitable as much fuel would remain in an un-reacted condition. Methane also is a problem for fluidised beds and this feature, plus the loss of carbon in the ash, results in this process being less ideal for hydrogen production or carbon capture.

- *Entrained-flow gasifiers* are reactors in which the particles of coal are relatively dispersed and are carried along by a blast of reactants and products in co-current flow. The residence time is just a few seconds and the temperatures are in the range of 1250 – 1600°C to ensure good carbon conversion. High temperature ensures that the syngas has very low methane content and because the temperature is high and the fuel is dry, there are no limitations on the type of coal.

The method of introducing the fuel into the gasifiers is specific to the design. There are, basically, two ways in which coal is transported into an entrained-flow gasifier: via water slurry (slurry feed gasifier), and via a gas, typically nitrogen (dry feed gasifier). For the slurry feed gasifier, the need to bring the water in the slurry up to gasifier temperatures, results in some of the coal having to be combusted, producing CO_2, as this reaction provides much more energy than the reaction of coal with oxygen to produce CO. The effect of this is to reduce the amount of hydrogen that can be produced, since the CO can subsequently react with steam to form hydrogen. As a conclusion regarding the gasification reactor feed system, the dry feed system ensures a higher energy efficiency of the gasifier [1].

The key factors that are considered for selection of gasifiers for hydrogen and electricity co-production with CO_2 capture are [1,10]: oxygen purity (usually 95 % O_2 vol., air blown gasifiers being unsuitable because of the nitrogen dilution), gasifier throughputs, reliability and experience on the industrial scale (400 MW power), cold gas efficiency (CGE) and carbon conversion (which are optimum in case of entrained-flow gasifiers), syngas cooling options (the quench type being desirable because the steam requirement of the shift conversion), hydrogen production potential (hydrogen and carbon monoxide content as high as possible in the syngas) and implication of gasifier reactor on Acid Gas Removal system (from this point of view a gasifier able to run at high pressure being desirable).

Considering the various commercial gasification reactors and their characteristics [1, 10-11] and analyzing these reactors against the above criteria, the most promising options for hydrogen and electricity co-generation schemes with carbon capture and storage are:

- Entrained-flow gasifier with dry feed and heat recovery (developed by Shell);

- Entrained-flow gasifier with dry feed and water quench (developed by Siemens formerly known Future Energy GmbH);

- Entrained-flow gasifier with slurry feed and water quench (developed by General Electric – Texaco).

The next section of this paper presents in detail a detailed modeling study for a plant concept based on Siemens gasification technology (entrained-flow gasifier with dry feed and syngas quench). The choice of Siemens gasification technology for an IGCC scheme with carbon capture for hydrogen and power generation is based on the following main factors: dry feed design which implies an increase energy efficiency compared with slurry feed design, water quench of the hot syngas which ensure the optimum condition for the shift conversion (no extra steam has to be added to the syngas), good cold gas efficiency and carbon conversion, good hydrogen production potential and clean syngas.

RESULTS AND DISCUSSIONS

This section presents a modeling study of a whole IGCC plant designed for hydrogen and electricity co-production with carbon capture based on Siemens gasification reactor. For the case study presented in detail below, the coal characteristics considered as feedstock are presented in Table 1.

The main sub-systems of the plant for co-generation of hydrogen and power co-generation with carbon capture and theirs design assumptions used in the mathematical modeling and simulation are presented in Table 2 [2, 8,12-15].

Table 1. Feedstock (coal) characteristics

Parameter	Coal
Proximate analysis (% wt)	
Moisture	8.10
Volatile matter	28.51
Ash	14.19
Ultimate analysis (% wt dry)	
Carbon	72.04
Hydrogen	4.08
Nitrogen	1.67
Oxygen	7.36
Sulphur	0.65
Chlorine	0.01
Ash	14.19
Lower heating value - LHV (MJ/kg a.r.)	25.353

Table 2. Main design assumptions for the plant concept

Unit	Parameters
Air separation unit (ASU)	Oxygen purity: 95 % (vol.) Delivery pressure: 2.37 bar Power consumption: 225 kWh/ton O_2 No integration with gas turbine
Gasifier (Siemens)	Pressure: 40 bar Pressure drop: 1.5 bar Temperature: >1400°C Water quench
Shift conversion (WGS)	Sulphur tolerant catalyst Two adiabatic beds Pressure drop: 1 bar / bed
Acid gas removal (AGR)	Solvent: Selexol® (mixture of di-methyl ethers of poly-ethylene glycols) Separate capture of CO_2 and H_2S Solvent regeneration: - thermal (heat) for H_2S step - pressure flash for CO_2 step
CO_2 compression and drying	Delivery pressure: 100 bar Compressor efficiency: 85 % Solvent used for drying: TEG (Tri-ethylene-glycol) Drying level: < 500 ppm H_2O
Claus plant & tail gas treatment	Oxygen-blown H_2S-rich gas composition: > 20 % (vol.) Tail gas recycled to H_2S absorption stage
Pressure Swing Adsorption (PSA)	Purified hydrogen: > 99.95 % (vol.) Purification yield: 85 % Tail gas pressure: 1.5 bar (recycled to the power island)
Gas turbine	Gas turbine type: M701G2 (Mitsubishi Heavy Industries Ltd.) Net power output: 334 MW Electrical efficiency: 39.5 % Pressure ratio: 21 Turbine outlet temperature (TOT): 588°C
Heat recovery steam generation (HRSG) and steam cycle	Three pressure levels: 118 bar / 34 bar / 3 bar Reheat of MP steam Steam turbine isoentropic efficiency: 85 % Steam wetness ex. steam turbine: max. 10 %
Heat exchangers	$\Delta T_{min.}$ = 10°C Pressure drop: 1 % of inlet pressure

The hydrogen and electricity co-generation plant based on Siemens gasification technology presented in Figure 1 was modeled and simulated using ChemCAD software. The case study was simulated in different situations (only electricity or various modes of hydrogen and electricity co-production). In case of power generation only mode, the gas turbine is running full load and for hydrogen and electricity co-production mode the gas turbine is gradually turned down to 80 % in order to displace an energy stream in form of hydrogen-rich gas which can be then purified in a Pressure Swing Adsorption (PSA) unit to produce a purified hydrogen stream (99.95 % vol.) to be used in transport sector (PEM fuel cells).

Table 3 presents the overall plant performance indicators (gross and net power output, electrical and hydrogen efficiencies, specific CO_2 emissions) in electricity only and hydrogen and electricity co-generation with carbon capture and storage.

Table 3. Overall plant performance indicators

Main Plant Data	Units	Power	Power + hydrogen		
Coal flowrate (a.r.)	t/h		165704		
Coal LHV (a.r.)	MJ/kg		25.353		
Feedstock thermal energy – LHV (A)	MW$_{th}$		1166.98		
Syngas thermal energy (B)	MW$_{th}$		934.75		
Cold gas efficiency (B/A * 100)	%		80.10		
Thermal energy of syngas ex. AGR (C)	MW$_{th}$		830.70		
Syngas treatment efficiency (C/B *100)	%		88.86		
Gas turbine output (1 x M701G2)	MW$_e$	334.00	314.97	296.27	277.58
Steam turbine output (1 ST)	MW$_e$	197.50	187.44	177.38	167.40
Expander power output	MW$_e$	0.78	0.72	0.66	0.61
Gross electric power output (D)	MW$_e$	532.28	503.13	474.31	445.59
Hydrogen output – LHV (E)	MW$_{th}$	0.00	50.00	100.00	150.00
ASU consumption + O$_2$ compression	MW$_e$	44.72	44.72	44.72	44.72
Gasification island power consumption	MW$_e$	8.08	8.08	8.08	8.08
AGR + CO$_2$ drying & compression	MW$_e$	40.07	40.07	40.07	40.07
H$_2$ compression	MW$_e$	0.00	0.66	1.33	2.01
Power island power consumption	MW$_e$	19.00	18.30	17.55	16.80
Total ancillary power consumption (F)	MW$_e$	111.87	111.83	111.75	111.68
Net electric power output (G = D - F)	MW$_e$	420.41	391.30	362.56	333.91
Gross electrical efficiency (D/A * 100)	%	45.61	43.11	40.64	38.18
Net electrical efficiency (G/A * 100)	%	36.02	33.53	31.06	28.61
Hydrogen efficiency (E/A * 100)	%	0.00	4.28	8.57	12.85
Cumulative efficiency (G+E/A * 100)	%	36.02	37.81	39.63	41.46
Carbon capture rate	%	92.35	92.35	92.35	92.35
CO$_2$ specific emissions	kg/MWh	76.12	80.16	86.27	93.41

Compared with classic IGCC technology for power generation without carbon capture which has an overall net energy efficiency of about 42 % [16], the modified IGCC technology for carbon capture is penalized by 7 – 8 % which is the energy penalty for the carbon capture process. This is the price in term of energy for decreasing the specific CO_2 emissions from about 800 kg/MWh (for no capture case) to about 76.12 kg/MWh for the capture case (92.35 % carbon capture rate).

Another fact that has to be mentioned for hydrogen and power co-production mode, is the overall energy efficiency of the plant that is increasing in the situation in which the ancillary power consumption is remaining virtually constant (see Table 3). This fact is very important and attractive for plant cycling (modification of the power generated by the plant according to the demand of the national grid) considering that for low electricity demand the plant can produce mostly hydrogen which compared with power can be stored to be used either for covering the peak loads or for other applications (transport sector, petro-chemical sector etc.).

Figure 2 presents the variations of net electrical efficiency, hydrogen efficiency and overall energy efficiency with hydrogen and power co-production rate (thermal energy of the hydrogen output stream).
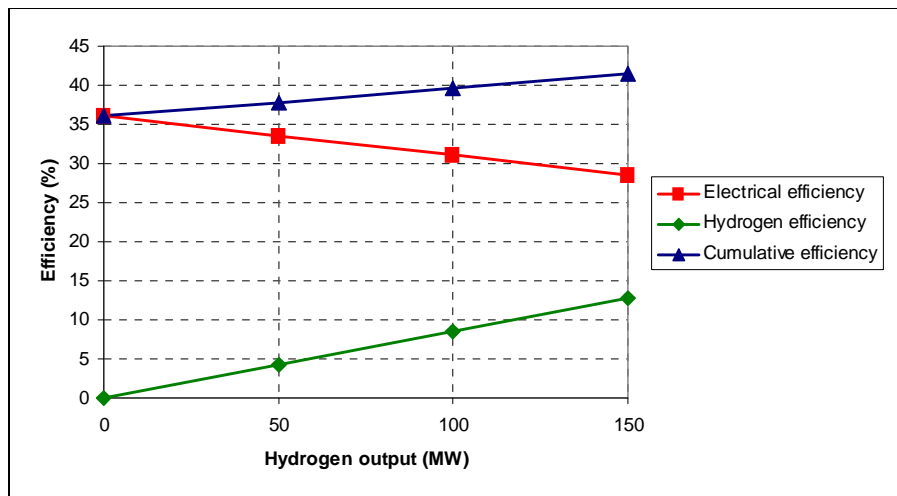
Figure 2. Variation of net electricity, hydrogen and overall efficiency vs. hydrogen and power co-production rate.

In the range of 0 to 200 MW hydrogen (based on 10.795 MJ/Nm^3 hydrogen lower heating value), the gas turbine can be gradually turned down to about 80 % of the nominal load [4]. For higher hydrogen plant flexibility

(for the case described above, i.e. more than 200 MW hydrogen), another approach must be used in plant design namely building a separate power block designed to provide the ancillary power for the plant [17, 18].

CONCLUSIONS

This paper assesses the main characteristics of coal gasifiers for hydrogen and electricity co-production scheme with carbon capture based on a modified IGCC plant design. The main aim has been to develop evaluation criteria and then to select the most appropriate coal gasification concepts for hydrogen and electricity co-production with carbon capture and storage (CCS) and to investigate how the gasifier selection affects the other sub-systems of the plant (e.g. Acid Gas Removal unit).

The most three promising concepts for hydrogen and electricity co-production with carbon capture based on coal gasification are all based on entrained-flow gasifiers (dry feed with heat recovery - Shell, dry feed with water quench – Siemens and slurry feed with water quench – GE Texaco).

The paper also presents in detail a case study for hydrogen and electricity co-production based on Siemens gasifier and with carbon capture step using a physical absorption (solvent Selexol®). This case study was modeled and simulated using ChemCAD software and the simulation results were used for quantification of main performance characteristics (overall plant efficiency, carbon capture rate, specific CO_2 emissions etc.).

ACKNOWLEDGMENTS

REFERENCES

1. C. Higman, M. Van der Burgt, "Gasification", Elsevier Science, second edition, **2008**, chapters 1-4.
2. International Energy Agency (IEA), Greenhouse Gas Program (GHG), *Potential for improvement in gasification combined cycle power generation with CO_2 capture*, **2003**, Report PH4/19.
3. International Energy Agency (IEA), Greenhouse Gas Program (GHG), *CO_2 capture in low rank coal power plants*, **2006**, Report 2006/1.
4. H. Cohen, G.F.C. Rogers, H.I.H. Saravanuamutto, "Gas Turbine Theory", 4th Edition, Addison Wesley Longman Ltd, **1996**, 131.

5. A. Kohl, R. Nielsen, "Gas purification", Gulf Publishing Comp., **1997**, chapter 2.
6. E. Tzimas, F. Starr, S. D. Peteves, "A large scale test facility for the production of hydrogen and electricity". The HYPOGEN project: A JRC – SETRIS perspective", European Commission, JRC, Institute for Energy, Petten, The Netherlands, **2005**, Report EUR 21651.
7. F. Starr, E. Tzimas, S.D. Peteves, "Near-term IGCC and steam reforming processes for the hydrogen economy. The development issues.", European Commission, JRC, Institute for Energy, Petten, The Netherlands, **2006**, Report EUR 22340.
8. P. Chiesa, S. Consonni, T. Kreutz, R. Williams, *International Journal of Hydrogen Energy*, **2005**, *30*, 747.
9. R. Domenichini, L. Mancuso, "IGCC plants – A practical pathway for combined production of hydrogen and power from fossil fuels", Foster Wheeler Italiana Spa, **2003**.
10. C. Cormoş, F. Starr, E. Tzimas, S. Peteves, A. Brown, "Gasifier concepts for hydrogen and electricity co-production with CO_2 capture", Third International Conference on Clean Coal Technologies, Cagliari, Sardinia, Italy, **2007**.
11. C. Cormoş, "Decarbonizarea combustibililor fosili solizi prin gazeificare", Presa Universitară Clujană, **2008**, chapters 3-4.
12. C. Cormos, F. Starr, E. Tzimas, S. Peteves, *International Journal of Hydrogen Energy*, **2008**, *33*, 1284.
13. K. Jordal, *International Journal of Greenhouse Gas Control*, **2008**, *2*, 468.
14. K. Damen, M. Van Troost, A. Faaij, W. Turkenburg, *Progress in Energy Combustion Science*, **2006**; *32*, 215.
15. J. Hetland, L. Zheng, X. Shisen, *Applied Energy*, **2009**, *86*, 219.
16. E. Tzimas, A. Mercier, C. Cormos, S. Peteves, *Energy Policy*, **2007**, *35*, 3991.
17. F. Starr, E. Tzimas, C. Cormos, S. Peteves, *Hydrocarbon Processing*, **2007**, *5*, 6.
18. F. Starr, E. Tzimas, S.D. Peteves, *International Journal of Hydrogen Energy*, **2007**, *32*, 1477.

Dedicated to Professor Liviu Literat, at his 80th anniversary

SEDIMENTATION SIMULATION OF COAGULATED YEAST SUSPENSIONS FROM WASTEWATER

VICTORIA GOIA[a], ADINA-LUCREȚIA GHIRIŞAN[a] AND VASILE-MIRCEA CRISTEA[a]

ABSTRACT. On the basis of mathematical modelling and numerical simulation the batch settling of coagulated yeast suspensions was analysed. Time and space behaviour of the solids height and critical height of sediment in gravitational settling, has shown similar results comparative to experimental data. The method offers the possibility to predict by simulation the settling rate for the consolidation region, a key settling variable difficult to be measured experimentally but important for the settler design.

Keywords: sedimentation, settling rate, coagulated yeast suspensions, simulation

INTRODUCTION

Solving the water pollution problem by colloidal and micro suspended particles resulting from breweries has been a challenge for a long time. As it is known for colloids and fine particles, main transport mechanisms include convection, Brownian diffusion, shear-induced diffusion, inertial lift, gravitational settling and lateral migration. Their relative importance strongly depends on the shear rate, particle size and bulk concentration. To improve the solid-liquid separation of micro-particles in aqueous suspensions before sedimentation and/or before filtration a common used method is aggregation (coagulation or flocculation). Some studies concerning settling of yeast micro-particles have shown that coagulation or flocculation, as a pre-treatment step before conventional sedimentation, could improve colloidal and micro-particles removal from aqueous suspension [1, 2].

Investigations of yeast particles sedimentation in water demonstrated that lack or low and limited separation may occur if no coagulant was added to induce a destabilization between yeast particles [3]. Pre-treatment by coagulation

---

[a] *Universitatea Babeş-Bolyai, Facultatea de Chimie şi Inginerie Chimică, Str. Kogălniceanu Nr. 1, RO-400084 Cluj-Napoca, Romania, vgoia@chem.ubbcluj.ro*

or flocculation using chemical additives destabilizes colloidal suspensions, allowing colloidal and fine particles to agglomerate into micro- and large flocks which settle more quickly than single particles because of their larger mass to surface area ratio.

The sedimentation behaviour of aggregated suspensions strongly depends on concentration. Experimental sedimentation in a batch system shows different regions of sedimentation, as presented in Figure 1.
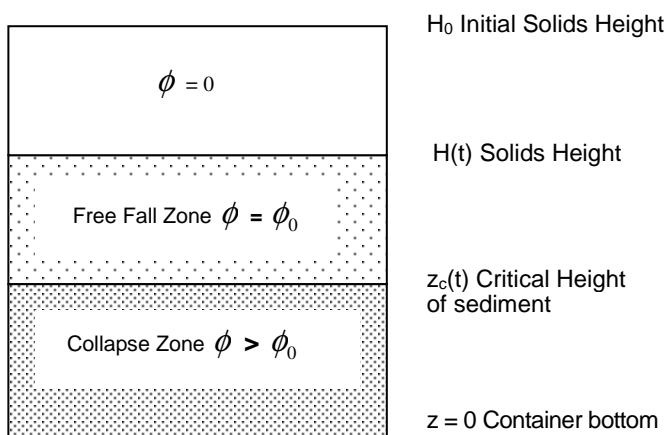
Figure 1. Schematic illustration of sedimentation zones.

In dilute suspensions ($\Phi = \Phi_0$) or at low degrees of aggregation, particles and aggregates settle independently and their motion is unaffected by the motion of other particles (free sedimentation). In more concentrated suspensions ($\Phi > \Phi_0$) or higher degrees of aggregation, sedimentation is influenced by hydrodynamic interaction with other moving particles and *hindered settling* or *zone settling* is observed [4-6]. The transition from free sedimentation to hindered settling occurs at a concentration which depends on the degree of aggregation. Zone settling may be found at quite low solids concentrations if the particles are aggregated to a large extent. For high concentrations of aggregated particles compression becomes significant and this is typically observed at the bottom of the sedimentation vessel.

Mathematical models of the sedimentation process are needed in industrial applications for the description, simulation, design and control of solid-liquid separation processes of suspensions, as it is also the case of coagulated yeast suspensions from wastewater.

According to Buscall and White [7], the system of equations (1) – (4) describing the sedimentation process consists in:

$$\frac{\partial \phi}{\partial t} = \frac{\partial (\phi u)}{\partial z} \tag{1}$$

$$u = \frac{u_{st}(1-\phi)}{r(\phi)}\left[1 + \frac{1}{\Delta \rho \cdot g \cdot \phi} \cdot \frac{\partial p}{\partial z}\right] \tag{2}$$

where:

$$\frac{\partial u}{\partial z} = 0 \quad \text{for} \quad p < P_y(\phi) \tag{3}$$

$$\frac{\partial u}{\partial z} = \frac{k(\phi)}{\phi}[p - P_y(\phi)] \quad \text{for} \quad p \geq P_y(\phi) \tag{4}$$

Considering that suspension is fully networked, the numerical modelling technique solves the system of equations and computes the time evolution of the two moving boundaries which describe the settling and the consolidation process [8].

For the simulation the mathematical model described below has been implemented in MatLab software. Dimensionless sedimentation equations are obtained by the use of the following scaling:

$$Z = \frac{z}{H_0} \qquad Z_c(T) = \frac{z_c(t)}{H_0} \qquad L(T) = \frac{H(t)}{H_0} \tag{5}$$

$$T = \frac{t \cdot u_{st} \cdot (1-\phi)}{r(\phi) \cdot H_0} \tag{6}$$

$$\Phi(Z,T) = \frac{\phi(z,t)}{\phi_0} \tag{7}$$

$$U(Z,T) = \frac{u(z,t) \cdot r(\phi_0)}{u_{st} \cdot (1-\phi_0)} \tag{8}$$

$$\Pi(Z,T) = \frac{P(z,t)}{P_y(\phi_0)} \qquad f(\Phi) = \frac{P_y(\phi)}{P_y(\phi_0)} \tag{9}$$

$$B(\Phi) = \frac{(1-\phi_0 \cdot \Phi) \cdot r(\phi_0)}{(1-\phi_0) \cdot r(\phi_0 \cdot \Phi)} \tag{10}$$

For the consolidation zone to exist:

$$\varepsilon = \frac{P_y(\phi_0)}{\Delta \rho \cdot g \cdot \phi_0 \cdot H_0} < 1 \tag{11}$$

95

The solution in the free-fall zone ($Z_c(T) \leq Z \leq L(T)$) may be obtained from the set of equations:

$$\Phi(Z,T) = 1 \tag{12}$$

$$U(Z,T) = -\frac{dL}{dT} \tag{13}$$

$$\Pi(Z,T) = \frac{1}{\varepsilon}\left[1 + \frac{dL}{dT}\right][L(T) - Z] \tag{14}$$

In the collapse zone ($0 < Z < Z_c(T)$) the dimensionless equations and boundary conditions are:

$$\frac{\partial \Phi}{\partial T} = \frac{\partial}{\partial Z}(\Phi \cdot U) \tag{15}$$

$$U(Z,T) = B(\Phi) \cdot \left[1 + \frac{\varepsilon}{\Phi} \cdot f'(\Phi)\frac{\partial \Phi}{\partial Z}\right] \tag{16}$$

$$\Phi(Z,0) = 1 \tag{17}$$

$$U(0,T) = 0 \tag{18}$$

$$\Phi(Z_c(T),T) = 1 \tag{19}$$

$$U(Z_c(T),T) = -\frac{dL}{dT} \tag{20}$$

The equation connecting the solids height to the critical height is:

$$\left[1 + \frac{dL}{dT}\right] \cdot [L(T) - Z_c(T)] = \varepsilon \tag{21}$$

The functions B(Φ) and f(Φ) may be detailed by:

$$B(\Phi) = \left[\frac{1 - \phi_0 \cdot \Phi}{1 - \phi_0}\right]^{5.5} \tag{22}$$

$$f(\Phi) = \frac{C^n \cdot \Phi^n - 1}{C^n - 1} \tag{23}$$

The parameter *C* is and defined by:

$$C = \frac{\phi_0}{\phi_g} \tag{24}$$

where the parameter ϕ_g represents the lowest volume fraction for which the flocculated particles are networked. The parameter n represents the index in yield stress function.

When equations are rewritten in terms of Φ and dimensionless solids flux $Q = \Phi U$, they describe the collapse zone by:

$$\frac{\partial Q}{\partial Z} = \frac{\partial \Phi}{\partial T} \qquad (25)$$

$$\frac{\partial \Phi}{\partial Z} = \frac{1}{\varepsilon \cdot f'(\Phi) \cdot B(\Phi)} \left[Q - \Phi \cdot B(\Phi) \right] \qquad (26)$$

$$\Phi(Z,0) = 1 \qquad (27)$$

$$Q(0,T) = 0 \qquad (28)$$

$$\Phi(Z_c(T),T) = 1 \qquad (29)$$

$$Q(Z_c(T),T) = -\frac{dL}{dT} \qquad (30)$$

$$\left[1 + \frac{dL}{dT} \right] \cdot \left[L(T) - Z_c(T) \right] = \varepsilon \qquad (31)$$

Equations (25) – (31) must be solved numerically to obtain the volume fraction $\Phi(Z,T)$, the solids height L(T), the solid flux Q(Z,T) and the critical height Z_c(T).

The significance of the symbols is: $B(\Phi)$ - scaled hydrodynamic drag function, C - constant in $f(\Phi)$, dp_{50} - mean particles diameter, $f(\Phi)$ - scaled yield stress function, g - gravitational constant, $k(\phi)$ - dynamic compressibility of the flocculated network, L(T) - scaled solids height, n - index in yield stress function, p – network pressure, $P_y(\phi)$ - yield stress of a flocculated suspension, Q - scaled solids flux, $r(\phi)$ - hydrodynamic interaction factor, t - time, T - scaled time, u - solids velocity vector, u_{st} - Stokes settling velocity of an isolated particle, U(Z,T) -scaled solids speed, w - fluid velocity vector, z - vertical spatial coordinate, z_c(t) - critical height, boundary of the consolidation zone, Z - scaled vertical spatial coordinate, Z_c(T) - scaled critical height, $\Delta\rho$ - difference between solid and fluid densities, ε - dimensionless number characterizing the flocculated suspension, η_l - fluid viscosity, ρ_s - density of the solids, ρ_l - liquid density, ϕ - volume fraction of suspension occupied by solids, ϕ_g - gel point of a flocculated suspension, ϕ_0 - initial volume fraction, $\Phi(Z,T)$ - scaled solids volume fraction, $\Pi(Z,T)$ - scaled network pressure.

Numerical values for the parameters taken into consideration in the model are:
- initial solids height H_0 = 102 mm
- fluid viscosity η = 10^{-3} Pa*s
- solid density ρ = 1100 kg/m^3
- sedimentation rate u_{St} = 2.725*10^{-4} m/s (determined for particles diameter d_p =50 µm)
- initial volume fraction $\phi_0 = 0.014$

The goal of the paper has been the implementation of the sedimentation model equations for the case of yeast suspensions from a brewery and comparison of the simulation results with experimental data in order to validate the model for further use of the simulator in equipment design and operation optimization of the sedimentation process.

RESULTS AND DISCUSSION

First, on the basis of the model described above, a simulator has been built in MatLab software environment. The simulator describes the sedimentation of suspensions in the free fall and consolidation zones. Second, the parameters of the simulator have been fitted to the particular case under study. Furthermore, the parameters n and C of the model have been chosen on the basis of the experimental results.

In order to find out the suitable value of the model parameter n for the investigated sedimentation process of coagulated yeast suspensions, different simulations have been performed, for different values of n. Analysing the simulation results it has been decided the most suitable value for n to be 5.

Consequently, the simulation of the sedimentation process was performed with the parameters C = 3 and n = 5. Figure 2 presents the computed scaled volume fraction Φ as a function of Z, in the consolidating zone and at various scaled time moments T.
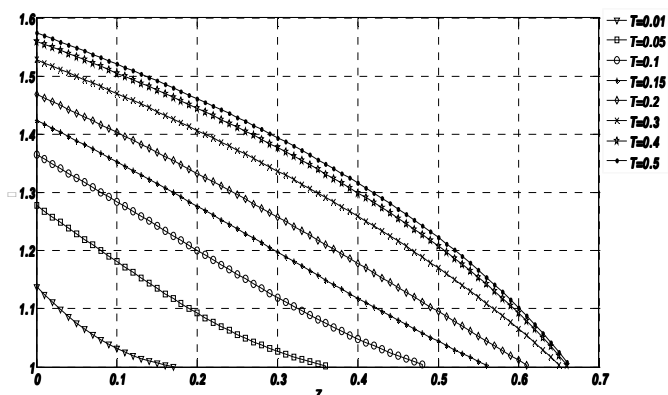
Figure 2. Volume fraction profiles for n = 5, C = 3, ε = 0.1, at different time moments.

Figure 3 shows the simulated solids height H(t) and the critical height of sediment $z_c(t)$ as a function of time.
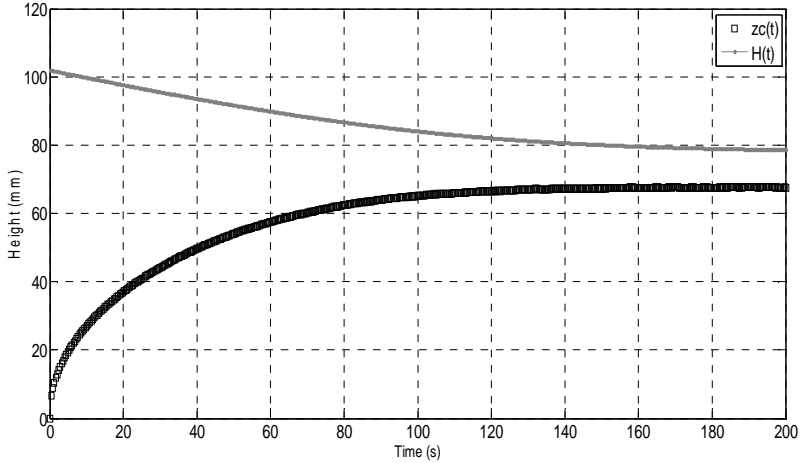
Figure 3. Critical height of sediment $z_c(T)$ and solids height H(t) for n =5, C =3, ε =0.1.

The experimental results show that at the initial time, t = 0, H(t) = H_0 = 102 mm and when all the large particles are settled H(t) = H_{final} = 78.588 mm.

Figure 4 shows the progress of the experimental solids height as a function of time, compared to the results obtained by the numerical simulation.
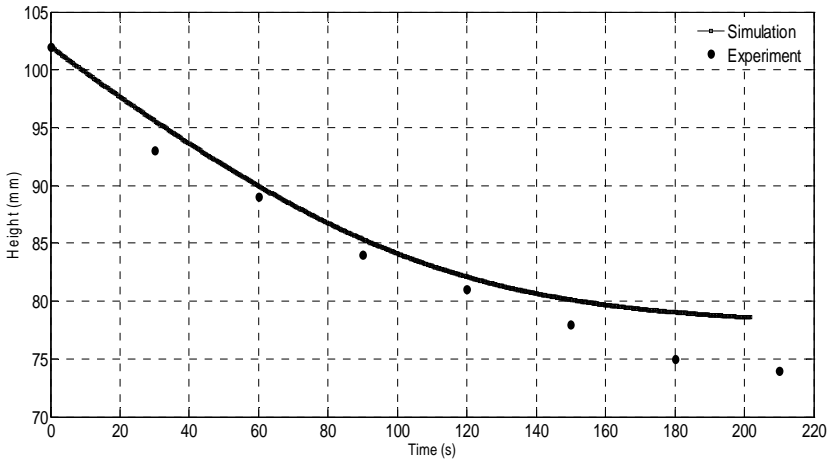
Figure 4. Comparison of solids height change in time for both experimental and simulated case.

Comparing the experimental and the modelling results it may be concluded that a good match between the simulation and the experiment was obtained. Comparison between the experimental sedimentation time and the simulated sedimentation time has been also performed and the results show values close one to each other: t_{exp} = 210 s and t_{sim} = 202 s.

CONCLUSIONS

The aim of this study was to build a sedimentation simulator in MatLab software, in order to investigate the sedimentation of coagulated yeast suspensions from wastewaters. The simulator reveals the complex time and space evolution of the sediment concentration in the settler.

An important outcome of the simulator is its ability to compute the change in time of the critical height, an important process variable which is very difficult to be experimentally observed due to the poorly delimited boundary of the critical sediment height.

The simulator also offers the means for investigating the influence of different settling parameters on the sedimentation process. Such parameters that influence the sedimentation and that can be observed with the simulator are: yeast particle diameter, initial suspension concentration, viscosity, differences between solid and liquid densities and gel point of flocculated suspensions. The simulator is also a useful tool for the computation of the theoretical sedimentation time (time when all the solid particles are settled).

As the simulator presents the complex time and space behaviour of important sedimentation variables, such as: sedimentation rate, solid concentration, time of sedimentation, it may be further used for the design and optimization operation of the settler.

EXPERIMENTAL SECTION

In order to determine the solids and critical heights the experimental measurements of sedimentation were carried out in a batch settling test with 5 graduated cylinders having D = 50 mm and H = 500 mm, by the same method described in the earlier work [1]. Wastewater from brewery "URSUS", Cluj-Napoca, Romania was used as suspended material for the experimental research. Untreated effluents typically contain suspended solids in the range of 10 – 60 mg/L, biochemical oxygen demand (BOD) in the range of 1,000 – 5,000 mg/L, chemical oxygen demand (COD) in the range of 1,800 – 3,000 mg/L, and nitrogen in the range of 30 – 100 mg/L. In the experimental sample Ferric chloride ($FeCl_3$) with the concentration 1150 ppm was used as coagulant. Sedimentation curve has been experimentally determined by the measurement of the moving solids height during time.

ACKNOWLEDGMENTS

REFERENCES

1. A. Ghirişan, M. Azad, *STUDIA Universitatis "Babeş-Bolyai", Chemia*, **2005**, *50(1)*, 113.
2. C. Posten, "Biological Aspects in Solid-Liquid Separation, A review for IFPRI", Institute of Mechanical Process Engineering, Karlsruhe, Germany, **2004**.
3. U. Stahl, U. Hues, K. Esser, *European Journal of Appl. Microbial Biotechnology*, **1983**, *17*, 199.
4. A. Rushton, A. S. Ward, R. G. Holdich, "Solid-Liquid Filtration and Separation Tehnology", Wiley-VCH, Weinheim, **1996**, chapters 3-5.
5. E. S. Tarleton, *Proceedings of the International Conference and Exhibition FILTECH Europa Dusseldorf, Germany,* **2001**, *1*, 20.
6. H. Nirschl, *Proceedings of the 10th Filtration Congress, Leipzig, Germany,* **2008**, *1*, 391.
7. R. Buscall, L.R. White, *J. Chem. Soc. Faraday Trans.* **1987,** *83*, 873.
8. I. Howells, K. Landman, A. Panjkov, C. Sirakoff, L. R. White, *Appl. Math. Modelling,* **1990**, *14*, 77.

Dedicated to Professor Liviu Literat, at his 80th anniversary

CASE STUDY OF STRUCTURAL SAFETY BASED ON ARTIFICIAL INTELLIGENCE

CĂLIN IOAN ANGHEL[a], IOAN LAZĂR

ABSTRACT. The paper provides a new insight into safety assessment using artificial intelligence methods. In safety index assessment, beside of the traditional *FORM/SORM* methods, a *minimax probability machine* approach was implemented. The core of the procedure based on a binary classification approach was developed according to a novel type of support vector machine in a *minimax* manner. The procedure, involving a link between artificial intelligence and structural reliability methods was developed as a user-friendly computer program in MATLAB language. For simplicity, only safety index approaches was presented. A numerical example replicating some previous related works reveals the opportunity of this approach in safety analysis.

Keywords: risk assessment, safety index, limit state function, support vector machine, minimax approach, pressure vessel.

INTRODUCTION

To avoid failure or major incidents technological systems must to be safe. Basically, safety can be thought as a state, a perceived state or a quality. Approaches of system safety presume planned, disciplined and systematic assessments to prevent or reduce accidents throughout the life cycle of a technological system. Structural safety related to process equipment is a part of the global safety of technological system. Because safety is a state, it cannot be quantified directly. Rather, assessing and controlling risk assure this state. The most usually definitions for risk in engineering applications are [1]:
- a combination of the likelihood and the consequences of a future event;
- the failure probabilities for a number of different scenarios;
- the product between the probability of occurrence and the quantified consequence of a future event.

---

[a] *Universitatea Babeş-Bolyai Cluj-Napoca, Facultatea de Chimie şi Inginerie Chimică, Str. M. Kogălniceanu Nr. 1, RO-400084 Cluj-Napoca, canghel@chem.ubbcluj.ro*

The equipment for process industries, are hardly affected by: fluctuations and variations in service loading and operating conditions, scatters in material properties and manufacturing process, uncertainties regarding the analytical models, continuous chemical corrosion and so on. Many engineering decisions concerning the safety of technological equipment for process industries are usually deterministic. These deterministic models provide a difficulty in handling variations and uncertainties in service conditions or variability concerning the main variables. To avoid these drawbacks, probabilistic methods became well-established tools in the risk assessment. The structural reliability procedures [2, 3] based on safety index and failure probability are still of greater importance in engineering applications. There are various methods to compute the safety index. Sampling-based methods (Monte Carlo Simulation, Latin Hypercube Sampling, etc.), analytical approximation methods like the Response Surface, the First-and Second-Order Reliability (*FORM/ SORM*) methods, advanced second moment method (ASM) or asymptotic techniques are among the most common methods used to estimate safety index or the failure probability. In general all these methods are time consuming, have limitations and an approximate nature. Despite of the recent important advances these traditional methods cannot fulfil in a satisfactory manner all the demands. The variability and uncertainty included in parameters of the model can determine major changes in the safety of the system. Within this context over the past decade intense effort has been devoted to bring ideas from the artificial intelligence field into engineering problems related to structural safety [4-7].

The aim of this paper is to present a procedure suitable for engineers in the stage of structural risk analysis. For simplicity it is based on the previous second mentioned definition of the risk. To compute the safety index the procedure focuses on the reliability concept developed in an artificial intelligence manner based on the support vector machine (SVM-a primarily two-class classifier) in a *minimax* approach. Some advantages of the support vector machine in *minimax* approach are: (a) provides an explicit direct upper bound on the probability of misclassification of new data, without making any specific distribution assumptions and (b) obtains explicit decision boundaries based on a global information of available data. The support vector machine and *minimax* approach, named *minimax probability machine classification*, has become an active research topic [8-11]. The problem of finding the safety index will be reported as a binary classification problem according to the traditional reliability methods better known by their acronyms *FORM/SORM*. The binary classification is applied to samples obtained by simulating a performance function or to values obtained by experimental analyses. Basically in structural safety methods the boundary between the two domains *S*-safe and *F*-unsafe is called the failure limit hyper surface and corresponds to a limit state function. This limit state

function is tantamount to a decision function that classifies the samples. In principle the problem becomes a binary classification one and the decision function becomes a function whose sign represents the class assigned to any sampled point. The proposed procedure named *minimax decision procedure*, involving a link between artificial intelligence and reliability methods was developed as a user-friendly computer program in MATLAB language. The main parts of the paper are: (1) introduction, (2) theoretical overview for safety index assessment in *minimax* approach, (3) numerical examples implemented in the *MATLAB* package and (4) conclusions. Numerical example is reported to the risk of failure for a thin-wall pressure vessel during its serviceable life. It is associated with structure's strength, corrosion effects and the presumption of miss regulated of heating/cooling closed loop system.

Safety Index Assessment in a Minimax Approach

Safety and safety index assessment of systems/structures are well established. Basic knowledge exists and many papers are available in the literature [2,3]. The paper focuses only on the methods better known by their acronyms *FORM/SORM*. Instead of these traditional methods, the safety index approach will be obtained based on a decisional procedure using a binary classification procedure. Because basic fundamentals and principles were presented elsewhere [6,7] only the main principle of implemented procedure will be presented. A starting point is the establishment of the performance or response function, which gives the relation between the inputs of the system and the chosen performance. This performance function depends on the set of governing input parameters representing vectors of all random variables, $\mathbf{x} = (x_1, x_2,...,x_d) \in \mathbf{R}^d$. If *PF* represents performance function and PF_{CR} represents a critical value of particular interest of this performance function, the limit state function (*LSF*) is the locus of points of the performance functions that can be defined as:

$$LSF = PF_{CR} - PF(\mathbf{x}) = 0 \text{ or } LSF = PF_{CR}/PF(\mathbf{x}) = 1. \tag{1}$$

The traditional *FORM/SORM* algorithms work into an equivalent standard normal $\mathbf{U}^d$ space to estimate the safety index and the failure probability. The transformation of the basic random variables $\mathbf{x} = (x_1, x_2,...,x_d) \in \mathbf{R}^d$ into equivalent independent and uncorrelated variates $\mathbf{u} = (u_1, u_2,...,u_d) \in \mathbf{U}^d$ should be made using the Rackwitz-Fiessler or Rosenblatt-Nataf or other similar isoprobabilistic transformations [2]. Therefore the limit state function is also transformed into equivalent standard normal $\mathbf{U}^d$ space by:

$$LSF(\mathbf{u}) = PF_{CR} - PF(\mathbf{u}) = 0 \text{ or } LSF(\mathbf{u}) = PF_{CR}/PF(\mathbf{u}) = 1 \tag{2}$$

$$F = \left\{ \mathbf{u} \in U^d \middle| LSF(\mathbf{u}) \leq 0 \text{ or } LSF(\mathbf{u}) \leq 1 \right\} \tag{3}$$

In practice the state of any system can be divided into two regions: (*F*)-the failure domain, a region where combinations of system parameters lead to an unacceptable or unsafe system response-defined by the existence of a performance function whose non-positive values establish the non-reliability domain (eqn.3) and (*S*)-the safety domain, a region where system response is acceptable, defined by the existence of a performance function whose positive values establish the safety domain:

$$S = \left\{ \mathbf{u} \in \mathbf{U}^d \middle| LSF(u) > 0 \;\; \text{or} \;\; LSF(u) > 1 \right\}. \tag{4}$$

Basically *LSF* is a boundary between the safe and failure regions. Geometrically *LSF* represents a failure limit hyper surface. The safety index $\boldsymbol{\beta}$ is reported to the point (often referred as the most probable point *MPP*) that lies closest to the origin of the system ($\boldsymbol{u^*} = (\boldsymbol{u_1^*}, \boldsymbol{u_2^*}, \ldots, \boldsymbol{u_d^*})$) in transformed reduced space $\boldsymbol{U^d}$ and belongs to the limit state surface. There is a direct relationship between the safety index and the probability of failure:

$$\boldsymbol{P_f} = \mathrm{Prob}\left\{ \boldsymbol{u} \in \boldsymbol{U^d} \middle| \boldsymbol{LSF}(\boldsymbol{u}) \leq 0 \;\; \text{or} \;\; \boldsymbol{LSF}/(\boldsymbol{u}) \leq 1 \right\} = \Phi(-\beta) \tag{5}$$

where $\Phi(\ldots)$ is the one-dimensional standard Gaussian (normal) cumulative density function. The eqn. (5) represents the first order approximation for the failure probability. Basically, this relationship is only approximate, but in the unique case of a linear limit state function of Gaussian distributed random variables the relationship is exact.

To improve this drawback our procedure *estimates the safety index* based on artificial intelligence methods. The safety index will report to an equivalent hyper plane (equivalent linear form of the limit state function) into a *binary minimax classification manner*. The proposed procedure estimates the location of the most probable point (*MPP*) and calculates the safety index $\boldsymbol{\beta}$. Once the location of the *MPP*, in the reduced standard normal space has been found and safety index $\boldsymbol{\beta}$ was calculated, the failure probability of the system may be achieved. Into a binary classification problem, a pattern may be given through the sets of labelled data-points in $\boldsymbol{R^n}$ (or in other space) as: {x1;x2,…xN} and {y1,y2…yM}. Usually the label of a training pattern represents the category or the class to which the pattern belongs, in our case C1-safety domain and C2-failure domain. The demanding problem is to find a function $f : \boldsymbol{R^n} \rightarrow \boldsymbol{R}$ which is positive on the first set and negative on the second, such as $f(x_i) > 0$, $i = 1, \ldots N$ and $f(y_i) < 0$, $i = 1, \ldots M$. If the inequalities hold we say that "*f*" or its 0-level set {x / f(x) = 0}, separates or classifies the two sets of points. This function "*f*" sometimes viewed as a decision function is often named as the classifier. The classifier is built in a random manner on a training (learning) set and is validated on a test set

(testing). Because training data is labelled, the classifier transforms these labels to new data (test data) as long as the feature space sufficiently distinguished each label as well. A heuristic approach to approximate linear discrimination (when the two sets of points cannot be perfectly linearly separated) is based on support vector classifiers. In the light of *SVM* a simplified reformulation for separating the set of *m* training vectors belonging to two separate classes, with a hyper plane, $\mathbf{w}^T \cdot z - b = 0$, is:

$$\left\{ \left(\bar{\mathbf{z}}_i, y_i \right) \middle| \bar{\mathbf{z}}_i \in R^n \;,\; y_i \in \{-1,+1\}, \; i = 1,..,m \right\}, \tag{6}$$

where y_i ($y_i \approx \text{sign}\left(\mathbf{w}^T \cdot z_i - b \right)$) is the associated "truth" given by a trusted source. The underlying problem of interest is to establish a decision function $f : \mathbf{R}^n \rightarrow \{\pm 1\}$ using input-output training labelled data from eqn. (6). In principle a decision function is a function *f(z)* whose sign represents the class assigned to data points **z**. If the points are linearly separable, in a two-class classification, then there exists an *n*-vector **w** and a scalar *b*. To optimally separate the sets of vectors (eqn. 6) is equivalent to maximising the separation margin or distance between two parallel hyper planes $\mathbf{w}^T \cdot z = b+1$ and $\mathbf{w}^T \cdot z = b-1$. Minimising the probabilities that data vectors fall on the wrong side of the boundary we can establish the classifier design. A possible way is the attempt to control the misclassification probabilities in a worse case by setting as minimising the worst case-maximum probability of misclassification of future data points. This is the *minimax* approach [12,13]. Basically, as was stated in a *minimax* approach reported as a binary classification problem, $\mathbf{z}_1$ and $\mathbf{z}_2$ denote random vectors data from each of two classes as $\mathbf{z}_1 \in$ Class C1 and $\mathbf{z}_2 \in$ Class C2. Thus to estimate the location of the most probable point a hyper plane that separates the two classes of points with maximal probability must be determined (eqn. 7).

$$H(\mathbf{w}, b) = \left\{ \mathbf{z} \middle| \mathbf{w}^T \cdot \mathbf{z} = b \right\}, \text{ where } \mathbf{w} \in \mathbf{R}^n \setminus \{0\} \text{ and offset } b \in \mathbf{R} \tag{7}$$

To overcome intricate non-linear classification problems, the kernel trick [8-13] is used to map the input data points into a high-dimensional '*d*' feature space $\mathbf{R}^d$, where a linear classifier corresponds to a non-linear hyper plane in the original space. In a *minimax* approach the classifier must minimise the misclassification probability by an optimal separating hyper plane that separates the two classes of points with maximal probability. In our safety index approach this optimal separating hyper plane is an equivalent failure

limit hyper surface and represents a boundary between the safe and failure regions. Because **w** is the normal to the hyper plane and $\|\mathbf{w}\|$ is the Euclidean norm of **w**, according to well-known statements [14], $|b|/\|\mathbf{w}\|$ is the perpendicular distance from the optimal separating hyper plane to the origin and then it can be identified as the reliability-safety index β.

$$\beta \cong |b|/\|\mathbf{w}\| \tag{8}$$

For non-linear classification problems in terms of a kernel function satisfying the Mercer's condition, the decision is transferred from the reduced original $\boldsymbol{U}^d$ space into reduced high dimensional feature space. For the output, it is not **w** that is returned, but instead of it the weights of the decomposition of **w** in the span of the data points are obtained [12,13]. The basis vectors can be interpreted as co-ordinate axes in the subspace and the "weights" of the basis vectors determine the corresponding "co-ordinate values" of the point. In our procedure there are some favourable circumstances where the linear discrimination works properly in the safety index assessment: (1) all projections of a standard normal distribution are also normal and generally linear functions of normally distributed data result also in normal distributions; (2) because the variates **u** are a set of standard uncorrelated variates the axes of the subspace $\boldsymbol{U}^d$ defined by these variates are orthogonal. Because the elements of kernel matrix were reduced to linear inner products and the classifier is provided in a linear configuration into a feature space, according to previous mentioned circumstances the general prerequisites for an exact assessment of eqn. (5) are fulfilled. The simulations are performed cyclic by multiple random trials. The performance of the procedure was evaluated based on test set accuracy (percentage of well-classified test data) and lower bound on the probability of correct classification of future data. Long random trials do not get improved accuracy or more reliable predictions, thus we considered appropriate to obey recent statements [11] and to work with a reduced learning set and to limit the random cyclic trials to $k = 50\ldots100$.

RESULTS AND DISCUSSIONS

Numerical application presents an example based on the already published paper [16]. The numerical analysis has been carried out for a thin-wall pressure vessel working into a technological process of natrium salicilate. The risk of failure is based on traditional permissible stress methods and serviceability limit state. It is reported to the structural condition beyond which the service criteria specified for the component are no longer met [17,18]. The limit state function (*LSF*) was established based on the presumption of miss regulated of multi-fluid heating/cooling closed loop system. This situation can

conduct to an uncontrolled value of pressure through the reactor jacket. Under these circumstances coupled with variations, uncertainties in service conditions, variability concerning the main variables and continuous chemical corrosion, it is possible that the pressure vessel cannot fulfil all the strength demands.

The main dimensional parameters of the pressure vessel, material characterization and operating technological conditions, are shown in Table1. Full statistic characterization of all the parameters on which the limit state function depends is not available. These parameters were set according to values known in practice or to values reported in literature [15,16].

Table 1. The main parameters and working conditions of the case study

Variable/Parameter	Symbol	Nominal value	Statistical distribution
Design thickness [mm]	So	6	LogNormal $\mu = 6$; $\sigma = 0.60$
Corrosion rate [mm/year]	Vc	0.1	Normal $\mu = 6$; $\sigma = 0.60$
Young Modulus [MPa]	E	2.12×10^5	Normal $\mu = 6$; $\sigma = 0.60$
Yield technical limit [MPa]	$\sigma_{0.2}$	255	Normal $\mu = 6$; $\sigma = 0.60$
Admissible stress [MPa]	σ_{ad}	170	Nominal value
Outer nominal diameter [mm]	D	445	LogNormal $\mu = 6$; $\sigma = 0.60$
Equivalent length for outer operating pressure [mm]	L	250	LogNormal $\mu = 6$; $\sigma = 0.60$
T_U - service life [year]	Tu	12	Normal $\mu = 6$; $\sigma = 0.60$
Operating pressure [MPa]	Poe	1.2	Normal $\mu = 6$; $\sigma = 0.60$
▪ Technological mixture -- NaOH and phenol; ▪ Steel K41.2b STAS 2883/2-80			

The state of stresses in various operating technological conditions obtained by simulations with the finite element method (FEM) using the professional package *COSMOS/M Designer II* is presented in Figure 1. The higher stresses were determined in the area of welded reactor jacket. Because stresses don't exceed permissible stress and stress concentrations are moderate, the structure is one that will not be expected to fail, thus a real structural safety may be suggested. Because uncertainties and variability concerning the main variables, in fact any structure has a risk, even though it can be extremely small. It follows that even though a structure is safe there is still the possibility of failure.

By the proposed procedure we can express a global risk of failure for the mentioned pressure vessel. According with main dimensional parameters

of the pressure vessel, material characterization and technological conditions (Table 1) the LSF system vectors are obtained by simulations of deterministic relationships (Table 2). These simulations might substitute real data as inputs to consequence models and illustrate the variability and uncertainty of the process.

a.

b.
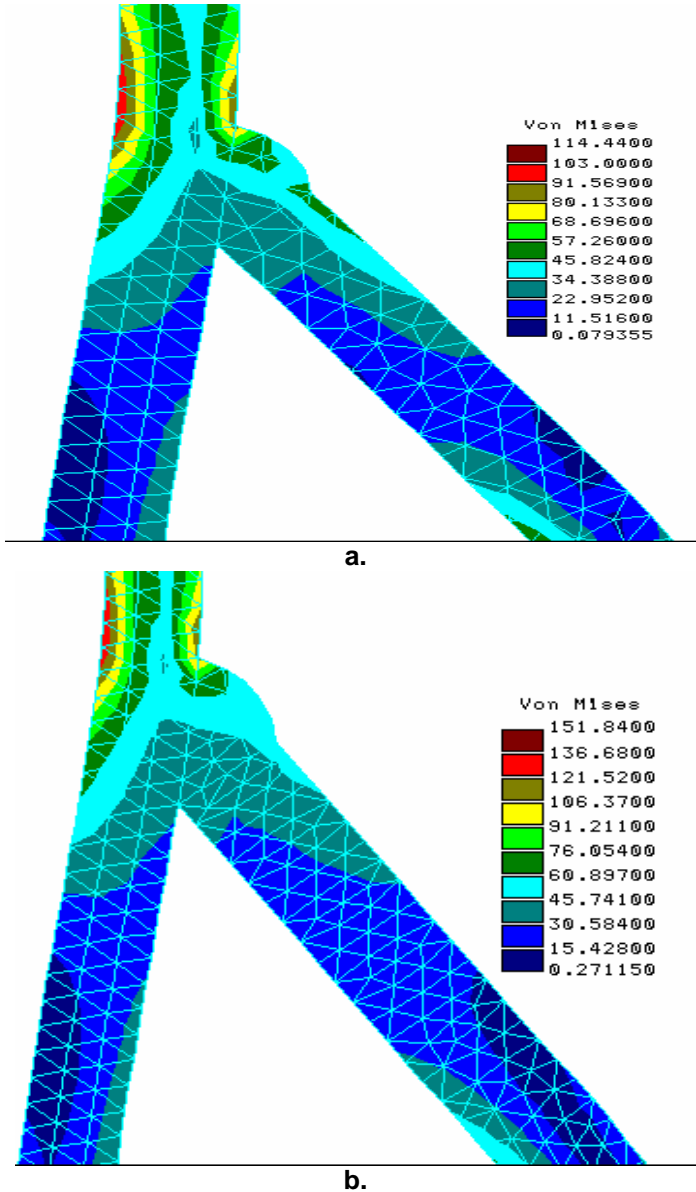
Figure 1. Equivalent Von Misses stresses in the area of welded reactor jacket
a. Von Misses stress at the beginning of the life cycle (So = 6 mm)
b. Von Misses stress along the life cycle (So = 4.8 mm)

The experiments are performed cyclic „k" times by multiple random trials. In each experiment the data was randomly split into (50%…90%) training and (50%…10%) test set. A number of different training and test sets are randomly chosen at each cycle. In each cycle the safety index β is evaluated and stored. The results of the proposed procedure are presented in Table 3. The performance of the procedure based on the test set accuracy (percentage of well-classified test data) and on the lower bound of correct classification of future data reveals a reasonable level. In every experiment the lower bound of correct classification of future data is smaller than the test set accuracy as was stated by [12,13]. Thus the lower bound is not violated and the linear approach is a robust one.

Table 2. Deterministic-explicit relations

Outer operating pressure in reactor jacket	Deterministic Numerical Values	
	Tu=0 [year]	Tu=12 [years]
Ellipsoidal closure $D^2/H*s \leq E/2*\sigma_{0.2} \rightarrow 0.0269 < 0.25$ – Plastic domain **Outer critical operating pressure** $P_{cr} = 8*s*\sigma_a*H/(D+(2H/D)*s)*D$	4.54 MPa	3.33 MPa
Cylindrical shell $1.5(2*s/D)^{0.5} \leq L/D \leq (D/2*s)^{1/3} \rightarrow$ $0.2463 < 0.55955 < 6.089$ - Short shell $s/D > 1.1*10^{-2}(L^2*\sigma^t_{0.2}/10^{-6}*D2*E^2) \rightarrow$ $1.3483*10^{-2} > 0.8524*10^{-2}$ **Outer critical operating pressure** $P_{cr} = 2*E^t*s/D*K1$ $K1=(1.5*E^t/\sigma_{0.2})+1.39*\sigma^t_{0.2}*D*L^2(C_{s2}-1)/ E^t*s^3$ $C_{s2}=1.5(1+0.93(C_{s1}-1.5)*(L*\sigma^t_{0.2}/ E^t*s)^2 *D/s)$ where $C_{s1} = 2.6$	4.36 MPa	3.067 MPa
Original explicit limit state functions _LSF_ $\Rightarrow$ **_LSF = P_{cr} – Poe_**		
Original explicit kernel function A polynomial kernel with a unit offset $K(z_i, z_j) = (z_i \cdot z_j +1)$		

Table 3. Results for safety index assessment based on averaged values

Safety index β	Probability of failure	LBCPFD [%]	TSA [%]
2.8131	0.00245	0.896	0.990
k = 100 cycles LBCPFD = lower bound on correct classification of future data TSA = test set accuracy (percentage of well-classified test data)			

The reported results are averaged over the entire random cyclic trials, as was stated [12,13]. Due to uncontrolled combinations of the variations in service loads, uncertainties and variability of any parameters, during service elapsed time, damage can occur. In fact, the mentioned pressure vessel has a risk, even though it is small. Extending Mc.Leods and Plewes's conversion scale to structural safety, this probability of failure $P_f = 0.00245$ is placed on the scale of risk in the range between $10^{-2} \ldots 10^{-4}$. This risk is characterized as a reduced one, when the failure is possible. It follows that the pressure vessel is still possibility of failure even though it is relative safe under a pure deterministic analysis.

CONCLUSIONS

The paper presents another insight into safety assessment and structural risk analysis using artificial intelligence methods. The proposed procedure offers a greater reliability in the safety prediction and reduction the risk of failure. High values for safety factor β lead to low values for the risk of failure. This approach improves some drawback of the traditional reliability methods, reduces the need for excessive safety margins in design or additional cumbersome experimental-analytical approaches. At the same time it focuses on uncontrolled combinations between the variations in service loads, uncertainties and variability of parameters, during service elapsed time. This is a key factor that could have a profound impact on the risk assessment. Based on numerical application we can highlight that using a corrosion decay model it is possible to establish a safer working life of the pressure vessel. These types of studies become recommended and necessary for engineers, especially for chemical engineers to work out optimal safety decisions, inspection and maintenance schedules.

REFERENCES

1. D.G. Elms, *Struct. Safety*, **1999**, *21*, 311.
2. R.E. Melchers, "Structural reliability analysis and prediction*"*, John Wiley & Sons, New York, **1999**.
3. O. Ditlevsen, O., H.O. Madsen, "Structural reliability", John Wiley&Sons. New York, **1996**.
4. J.E. Hurtado, D.A. Alvarez, *Journal of Structural Engineering*, **2003**, *129*(8), 1141.
5. J.E. Hurtado, *Struct.Safety*, **2004**, *26(3)*, 271.
6. C.I. Anghel, Al. Ozunu, *Chem. Pap.* **2005**, *59(6b)*, 469.
7. C.I. Anghel, *Int Jnl of Pressure Vessels and Piping*, **2009**, (in press).
8. V.N. Vapnik, "The nature of statistical learning theory", 2nd edition, Springer, New York, **2000**.

9. B. Scholkopf, C. Burges, A. Smola, (Eds.), "Advances in Kernel Methods. Support Vector Machines", MA MIT Press Cambridge, **1998**.
10. C.J.C. Burges, *Data Min. Knowl. Disc,* **1998**, *2*, 121.
11. A. Bordes, S. Ertekin, J. Weston, L. Bottou, *Journal of Machine Learning Research*, **2005**, *6*, 1579.
12. G.R.G. Lanckriet, EL. Ghaoui, C. Bhattacharyya, M.I. Jordan, in: T.G. Dietterich, S. Becker, Z. Ghahramani (Eds.), *Advances in Neural Information Processing Systems*, MA. MIT Press Cambridge, **2002**, *14*, 801 (http://robotics.eecs.berkeley.edu/~gert/)
13. G.R.G. Lanckriet, EL. Ghaoui, C. Bhattacharyya, M.I. Jordan, *Journal of Machine Learning Research*, **2002**, *3*, 555.
14. C. I. Anghel, I. Lazar, R.I. Iatan, "Proceedings – Conferinţa Natională de Echipamente, Instalaţii şi Inginerie de Proces"**, 2004**, 253.
15. Al. Pavel, D. Popescu, *Rev. Chim.*, **1998**, *49, 2*, 128.
16. *** ASME - Boiler And Pressure Vessel Code, Section VIII, The American Society of Mechanical Engineers; New York, 1**995**.
17. *** Eurocode pr.EN 13445-3, Unfired Pressure Vessels – Part 3: Design, **1999**.
18. *** Eurocode pr.ENV 1991-1, Eurocode 1: Basis of design and actions on structures, Part 1 Basis of Design, **1994**, (CEN/TC 250).

Dedicated to Professor Liviu Literat, at his 80th anniversary

SOIL AND SPRING WATER POLLUTION IN TWO PROTECTED NATURAL AREAS IN MARAMUREŞ DISTRICT

LAURA ARDELEAN[a], MARIA GOREA[b], ELENA CICAL[c], ANGELA MICHNEA[d]

ABSTRACT. This paper presents recent data on soil contamination with Pb, Cd, Cu and Zn at 5 and respectively 30 cm in depth and the pollution of surface waters in two protected areas in Maramureş County. The measured values are presented in comparison with the limits defined by the Romanian legislation. In the case of Creasta Cocoşului reservation, lead pollution reaches the intervention limit at 5 cm in depth and it exceeds the alert threshold at 30 cm. Lead contamination in Chiuzbaia reservation is also high at the 30 cm in depth, the Cd content exceeds the alert limit, while the values for Cu, Zn and Mn are over the normal admitted values. The high level of contamination with heavy metals of these areas is mainly related to local mining activities and non-ferrous metals concentrates processing.

Keywords: *soil pollution, heavy metals, natural protected areas*

INTRODUCTION

Maramureş County has a surface of 6304 km[2], including natural heritage areas of special value: 36 protected natural areas, of which one national park, Rodna Mountains Natural Park – Biosphere reservation, and one natural park, Maramureş Mountains Natural Park. These areas place Maramureş County on the 7th place in Romania as far as the number of protected areas is concerned (Fig.1).

The presence of several pollution sources in the area (former mining activity and metallurgic processing) involves a strict monitoring of the types

---

[a] *Garda Naţională de Mediu – Comisariatul Judeţului Maramureş, Str. G. Coşbuc, Nr. 52, RO-430222, Baia Mare, Romania, ardelaura@yahoo.com*

[b] *Universitatea Babeş-Bolyai, Facultatea de Chimie şi Inginerie Chimică, St. Kogălniceanu, Nr. 1, RO-400084, Cluj-Napoca, Romania, mgorea@chem.ubbcluj.ro*

[c] *SC Vital SA, Str. Ghe. Şincai, Nr. 19-21, RO-430311, Baia Mare, Romania*

[d] *Agenţia pentru Protecţia Mediului, Str. Iza, Nr. 1A, RO-430073, Baia Mare, Romania*

of soils and the physical-chemical features (heavy metals content, pH, humus amount) in relationship with vegetation (types, ecological preferences) but also of the quality of spring waters, especially in the protected areas.

The two reservations under study are presented on the map (Fig. 1); they are located north-east from Baia Mare municipality, where non-ferrous metal concentrates rich in Pb, Cd, Cu and Zn have been processed for the last fifty years in the local metallurgical plants. Some toxic gases and heavy metals powders (particulate emissions) have been, but in small amounts still are released in the air, transported by air currents and finally settled on the surface of the soil in various areas.

In spite of the fact that the activity of these plants have lately take place using more environmental-friendly technologies (according to European legislation) and less-polluting raw materials (including wastes) were used, soil and water pollution are still clearly visible, negatively affecting flora and fauna of the region and consequently, human health. By taking into account the long-term effects of pollution, but also by considering the need for preservation of some areas of high touristic potential, continuous investigation and monitoring activities take place. The two metallurgic plants include installations for pollution prevention and integrated control, IPPC, of which one (related to secondary copper processing) already works in agreement with the UE regulations, while the second one (related to primary lead processing) is currently submitted to specific transformations in the frame of a detailed programme to end in 2010, when the environmental requirements of the EU will have to be fulfilled.

The territory of Maramureş County and especially the areas in the vicinity of Baia Mare represent "environmental hot spots" proper due to the long period of mining activity and non-ferrous metallurgy; for this reason, such areas have been intensely investigated especially concerning heavy metals pollution [1].

The aim of the present work is the quantification of the pollution degree, concerning heavy metals (Pb, Cd, Cu, Zn and Mn), of soil and spring waters in two geological reservations: Creasta Cocoşului and fossiliferous reservation Chiuzbaia. Samples were collected from 5 and respectively 30 cm in depth and the measured and determined values were compared with the limits allowed by the Romanian legislation. Samples collected in the first step of the study were used to evaluate the pollution degree of the areas considered, as a preliminary stage of a more complex research concerning that region.

The obtained data are necessary for soil type mapping and correlation of their physical-chemical features with type and abundance of flora and fauna in the protected areas of Maramureş County, for the evaluation of soil quality and interpretations concerning the influence of pollutants on both vegetation and tourists in these areas.
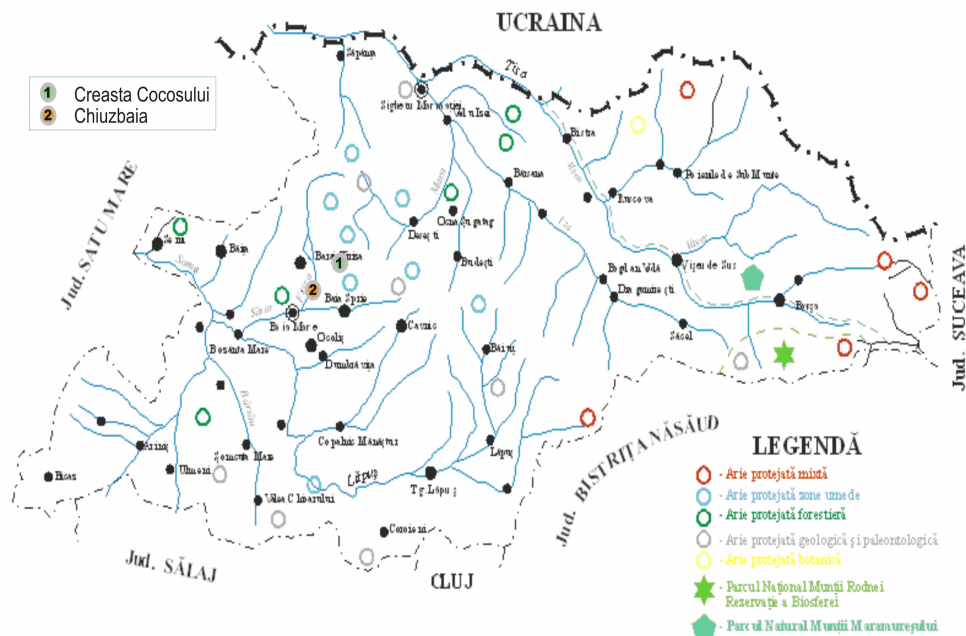
Figure 1. Schematic map of the protected areas in Maramureş County

RESULTS AND DISCUSSIONS

CREASTA COCOŞULUI protected area

The protected natural area Creasta Cocoşului was created in order to protect and conserve some natural elements of special ecological, scientific and landscape value and significance. The most prominent feature within the area is the Creasta Cocoşului itself, a steep and wavy ridge, about 200 m in length, located at an average altitude of 1200 m, with an almost vertical spatial display [2]. The results of the soil investigation in this area are presented in Table 1.

The data on soil samples collected at 5 cm in depth evidenced a high content of lead, about three times more than the intervention threshold in the samples collected from the uppermost part of the Creasta Cocoşului ridge and near the alert threshold for those collected near the spring below the ridge. The lower content in the second group of samples may be correlated to the local pattern of the air currents leading to a better protection of the area. The lead pollution degree is relatively higher (above the alert limit) also in the case of soil samples collected at 30 cm in depth, pointing to a long term "pollution history" in the area.

The experimental data for copper, zinc and manganese fall within the normal limits for this type of soils, however towards the upper limit in the case of copper and zinc. It is worth to mention that cadmium is missing from the investigated soil samples.

Concerning the organic matter content, the soil samples collected in the vicinity of the spring below the ridge are slightly polluted (organic C < 3 %), those collected near the top of the ridge at both 5 and 30 cm depth are medium polluted (< 4 % organic C) while those from the area near Masa Pintii are strongly polluted (> 4 % organic C).

Table 1. Results obtained on soil samples collected from Creasta Cocoşului reserve

Soil sample (Creasta Cocoşului reserve)	pH	Pb mg/kg	Cd mg/kg	Cu mg/kg	Zn mg/kg	Mn mg/kg	Humus %	Org. C %
The top of the ridge (5 cm depth)	4.1	311.65	0.0	21.40	90.06	323.18	6.63	3.84
(30 cm depth)	4.3	67.34	0.0	13.91	67.23	190.98	6.03	3.50
Near the spring below the ridge (5 cm depth)	4.5	57.26	0.0	13.15	79.63	366.02	2.72	1.58
Near "Masa Pintii" (5 cm depth)	4.5	294.18	0.0	18.90	92.22	176.61	7.95	4.61
Near *Masa Pintii* (30 cm depth)	4.4	86.026	0.0	15.463	103.99	205.15	7.21	4.18
Normal values [1,2]		20	1	20	100	900		
Alert threshold [1,2]		50	3	100	300	1500		
Intervention threshold [1,2]		100	5	200	600	2500		

[1]in the case of soils for sensitive usage, in mg/kg; [2]according to OMAPM 756/1997 approving Regulations on the evaluation of environmental pollution

Soil acidity showed relatively high (pH about 4) but relatively constant values with depth and horizontal distances in the sampled areas.

CHIUZBAIA protected area

The Chiuzbaia fossiliferous reservation is located at the base of Igniş Peak, between the Plopilor Valley and the "Biserica lui Spiridon" cliff; it is well-known and protected for its diatomite deposits interlayered with volcanic ash containing abundant rests of plant impressions. These geological deposits were formed in a lake surrounded by a dense forest. The leaf impressions point to the following plant species such as, oak (*Quercus*), alder (*Alnus*), beech (*Fagus*), maple (*Acer)*, chestnut (*Castanea)*, besides which birch tree

(*Betula*), hornbeam (*Carpinus*), *Giyptostrobus*, *Liriodendron*, *Magnolia*, *Finus*, elm etc, were present, pointing to a forest growing in a temperate, relatively warmer climate as compared to the present day one. The fossil flora from Chiuzbaia represents one of the richest and best preserved floras of Pliocene age from Romania: over 120 species of which 32 for the first time in Romania, 6 for the first time worldwide, and 3 new varieties have been identified [3].

Table 2. Results obtained on soil samples collected from the Chiuzbaia fossiliferous reserve

Soil sample (Chiuzbaia reserve)	pH	Pb mg/kg	Cd mg/kg	Cu mg/kg	Zn mg/kg	Mn mg/kg	Humus %	Org. C %
5 cm depth	4.7	376.04	3.88	26.61	145.18	1217.17	5.95	3.45
30 cm depth	4.7	236.98	3.25	17.62	136.21	1298.12	4.64	2.69
Normal values [1, 2]		20	1	20	100	900		
Alert threshold [1, 2]		50	3	100	300	1500		
Intervention threshold [1,2]		100	5	200	600	2500		

[1]in the case of soils for sensitive usage, in mg/kg; [2]according to OMAPM 756/1997 approving Regulations on the evaluation of environmental pollution

The experimental data on the soil samples from Chiuzbaia fossiliferous reservation collected at 5 and respectively 30 cm in depth are presented in Table 2.

These data point to a relatively higher pollution degree both at surface and in depth by comparison to the first protected area under study, which can be due to the closer proximity from the polluting source, *i.e.* Baia Mare town. A high Pb content, exceeding the intervention limit both at the surface and at depth can be mentioned; high amounts were registered also in the case of the other metals, Cu, Zn and Mn exceeding the normally admitted values. More than that, Cd – a very toxic metal, was also evidenced, in concentrations exceeding even the alert threshold.

Based on the carbon contents, the soils in this area may be classified as slightly (at 30 cm in depth) and medium (at 5 cm in depth) polluted with acidity values close to those recorded in Creasta Cocoşului reserve.

Spring waters

The evaluation of the pollution degree of spring waters in the monitored reserves was performed by investigating water samples from two springs along the tourist path starting from the Şuior mine perimeter, located in the

upper part of the climb towards Creasta Cocoşului ridge, while for Chiuzbaia fossiliferous reserve the water sample was collected from the spring located close to the forest road that crosses the reserve.

Table 3 presents the main physical-chemical characteristics of the tested water samples compared with reference values for surface and drinking waters.

The values in Table 3 obtained for this study show that lead and cadmium exceed the admitted limits in the waters in the case of Chiuzbaia Valley and the spring from the base of the Creasta Cocoşului ridge, supporting the data obtained for the soil samples in the same areas.

The acidity of these waters is higher than that of reference surface water and decreases from the top to the bottom of the ridge, probably as a consequence of the pH variation for the corresponding soils.

By comparing the data from Tables 2 and 3, it can be noticed that lead concentrations in soil represent special issues, all the investigated samples showing values higher than the alert threshold or in some cases even values exceeding the intervention limit.

CONCLUSIONS

In the two investigated protected areas, the soil is contaminated with heavy metals (Pb, Cd, Cu, Zn and Mn) in variable amounts depending on the location of the sampling site and depth. High pollution with Pb exceeding the alert threshold was evidenced in the top area of Creasta Cocoşului reserve and exceeding the intervention limit near the spring below the ridge at 5 and 30 cm in depth, as well as in all the investigated sites from Chiuzbaia reserve. The degree of pollution with organic matter varies from slightly polluted soils (at the spring below the Creasta Cocoşului ridge) to strongly polluted soils in the Masa Pintii area from Creasta Cocoşului reserve.

The allowable limits for heavy metals Pb and Cd are exceeded in the water samples collected from Chiuzbaia Valley and in the spring at the base of Creasta Cocoşului ridge as a result of soil pollution in these protected areas. The pH values for the spring waters are lower than those allowed for surface waters and they increase from the top to the base according to the variation of the pH values for the soils.

The high Pb values in some soil samples both at the surface and deeper into the soil suggest the possible influence of the Pb-containing particulate emissions from the dispersion furnace of the company that processes Pb ores in Baia Mare, taking into account that the two reservations are located NE from the metallurgical plant at a distance of only 4.5 km (Chiuzbaia reserve) and respectively 17.5 km (Creasta Cocoşului reserve). The lead content is higher in the samples collected from Chiuzbaia reserve, located closer to the metallurgical plant as compared to Creasta Cocoşului reserve.

Table 3. Physical-chemical features of spring waters

No.	Feature	Chiuzbaia Valley	Creasta Cocoşului – spring at the base of the ridge	Creasta Cocoşului- spring near the top of the ridge	Reference value (surface waters)[3]	CMA value (drinking water)[4]
1	pH	6.196	5.483	4.967	6.5-8.5	6.5-9.5
2	Conductivity, µS/cm	68.5	24.4	41.5		2500
3	CCOMn, mgO$_2$/l	1.84	2.4	2.72	5.0	
4	Chlorides, mg/l	7.09	7.09	6.38	25	250
5	Sulphates, mg/l	5.10	0.0	1.70	60	250
6	Calcium, mg/l	8.55	3.89	5.44	50	
7	Magnesium, mg/l	3.26	0.47	0.93	12	
8	Total hardness, Ge degrees	1.96	0.652	0.978		5
9	Nitrites, mg/l	0.0	0.0	0.0	0.01 mgN/l	0.5
10	Nitrates, mg/l	22.8	0.10	0.0	1.0 mgN/l	50
11	Ammonium, mg/l	0.025	0.0	0.0	0.4 mgN/l	0.5
12	Pb, mg/l	0.025	0.002	0.0	0.005	0.010
13	Cd, mg/l	0.001	0.002	0.0	0.0005	0.005
14	Cu, mg/l	0.0	0.0	0.0	0.02	0.1
15	Zn, mg/l	0.021	0.018	0.012	0.1	5.0
16	Fe, mg/l	0.087	0.023	0.045	0.3	0.2
17	Mn, mg/l	0.004	0.003	0.006	0.05	0.05

[3]according to the MMGA Order 161/2006 approving the Classification Norms for surface waters quality in the view of establishing the ecological status of the water bodies; [4]according to Law 458/2002 on the quality of drinking water

These preliminary data suggest that soil pollution has an anthropic source related to industrial air pollution by soil deposition of particulate emissions containing heavy metals, especially Pb. If the natural substrate in the area of the reservation would have been rich in heavy metals, these cations should have been present in higher concentrations also in the investigated spring waters.

EXPERIMENTAL SECTION

Soil sampling

Soil samples were collected according to the procedures defined for environmental pollution evaluation and the Romanian standard on soil sampling for pedological and agrochemical studies [4, 5].

Soil sampling at 5 cm in depth is significant for the evaluation of the bioasimilation processes of heavy metals by plants in the upper part of the soil, and thus the potential risks on the trophic chain. Metal distribution

patterns in deeper soil layers (30 cm in depth) may evidence the history of pollution or accidental infiltrations.

In the case of Creasta Cocoşului reservation, samples of both soil and water were collected, due to the local morphological-structural complexity of the landscape and of the co-existence of various altitudes.

The tested soils were collected in the upper part of Creasta Cocoşului area at 5 and respectively 30 cm in depth, from the vicinity of the spring at the bottom of the cliff at 5 cm in depth, and from Masa Pintii area at 5, and respectively 30 cm in depth. In the Chiuzbaia reservation, soil samples were collected at 5 cm and 30 cm in depth from a single sampling point.

Water sampling

Water samples were collected and investigated in agreement with the procedures defined by Romanian legislation (surface waters quality types and quality of drinking water, for spring waters) [6, 7].

Water samples were collected from the existing springs in the two reservations. In the case of Creasta Cocoşului area the springs are more abundant, thus two of the springs within the reservation were sampled. In the case of the Chiuzbaia fossiliferous reservation a single spring was tested.

Analytical procedures

The soil samples collected from the pre-established locations were packed in plastic bags and transported to the laboratory. There they have been air dried at room temperatures, then powdered and sieved on a 2 mm mesh. One gram from each dried soil sample was subsequently submitted to acid treatment for releasing the heavy metals into solution. After cooling, the solutions were filtered and diluted with bi-distilled water up to 25 ml volume. The heavy metal content (Pb, Cd, Cu and Zn) in these final solutiuons was determined using atomic absorption spectrometry.

The pH values and the humus content were measured in aqueous mixtures obtained from fresh samples (solid matter: liquid = 1:5), the latter by determining the content of organic carbon (warm oxidation with K dichromate in the presence of sulphuric acid and titration of the excess dichromate with Mohr salt solution).

The pollution degree of the studied soil samples was estimated based on the scale proposed by Parrakova [8], according to the organic carbon content C, as follows:
- unpolluted soil   0-1 %
- slightly polluted soil   1-3 %
- medium polluted soil   3-4 %
- heavily polluted soil   4-6 %

The water samples were collected in 500 ml plastic bottles that were prior to this carefully rinsed and dried in the laboratory; the samples were investigated right after they were brought to the laboratory from the field.

Conductivity and pH were measured by potentiometric methods using a laboratory conductometer and pH meter; the anions were determined by UV-VIS molecular absorption spectrometry while the metallic cations by atomic absorption spectrometry.

Equipment

The investigations on the soil and water samples were performed at the Laboratory for physical-chemical testing of the Agency for Environmental Protection Maramureş, Baia Mare, Romania, using a Varian SpectrAA-250 Plus atomic absorption spectrophotometer, an UV/VIS spectrophotometer with molecular absorption Cecil 8000 series, a WTW InoLab Level2 conductometer, and a WTW InoLab Level2 pH meter.

REFERENCES

1. E. Cordoş, C. Roman, M. Ponta, T. Frenţiu, R. Răuţiu, *Revista de Chimie*, **2007**, *58*, 470.
2. L. Ardelean, „Ecoterra", Ed. Fac. de Ştiinţa Mediului Cluj Napoca şi I.C.P.E. Bistriţa SA, **2006,** chapter 11.
3. R. Givulescu, "Flora fosilă a Miocenului superior de la Chiuzbaia (judeţul Maramureş*)"*, Editura Academiei Române, Bucureşti, **1990**, chapter 3.
4. Ordinul 756/1997 – pentru aprobarea Reglementării privind evaluarea poluării mediului, Monitorul Oficial, Partea I, nr.303bis/06.11.**1997**.
5. STAS nr. 7184/1-84, Soluri. Recoltarea probelor pentru studii pedologice şi agrochimice, **1984**.
6. Ordinul 161/2006 – pentru aprobarea Normativului privind clasificarea calităţii apelor de suprafaţă în vederea stabilirii stării ecologice a corpurilor de apă, Monitorul Oficial, Partea I, nr.511/13.06.**2006**.
7. Legea 458/2002 – privind calitatea apei potabile, Monitorul Oficial, Partea I, nr.552/29.07.**2002**.
8. S. Mănescu, M. Cucu, M. Diaconescu, "Chimia sanitară a mediului*"*, Editura medicală, Bucuresti, **1994**, chapter 4.

Dedicated to Professor Liviu Literat, at his 80th anniversary

SIMULATION OF THE REACTOR-REGENERATOR-MAIN FRACTIONATOR FLUID CATALYTIC CRACKING UNIT USING ARTIFICIAL NEURAL NETWORKS

VASILE MIRCEA CRISTEA[a], RALUCA ROMAN[a], PAUL ŞERBAN AGACHI[a]

ABSTRACT. The present work it is a successful approach for modelling the dynamic behaviour of the FCC unit, using Artificial Neural Networks (ANN). An analytical model, validated with construction and operation data, has been used to produce a comprehensive input-target set of training data. The novelty of the model consists in that besides the complex dynamics of the reactor-regenerator system, it also includes the dynamic model of the main fractionator. A new five-lump kinetic model for the riser is also included. Consequently, it is able to predict the final production rate of the main products, gasoline and diesel. The architecture and training algorithm used by the ANN are efficient and this is proved by the results obtained both on training set and set of input-target data not met during the training procedure. The same good ANN performance has been obtained by the comparison between dynamic simulations results emerged from the ANN model versus first principle modelling, both using the same randomly varying inputs. The computation time is considerably reduced when using the ANN model, compared to the use of the analytical model. The presented results show the incentives and benefits for further exploiting the ANN model as internal model for Model Predictive Control industrial implementation.

Keywords: *Fluid Catalytic Cracking Unit, Artificial Neural Networks, dynamic modelling*

INTRODUCTION

A modern petroleum refinery is composed of processing units that convert crude oil into valuable products such as gasoline, diesel, jet fuel, heating oil, fuel oil, propane, butane, and several secondary chemical feed stocks. Fluid Catalytic Cracking (FCC) is one of the most important conversion processes in a petroleum refinery, Figure 1. The main goal of this unit is to

---
[a] *Universitatea Babeş-Bolyai, Facultatea de Chimie şi Inginerie Chimică, Str. Kogălniceanu, Nr. 1, RO-400084 Cluj-Napoca, Romania, mcristea@chem.ubbcluj.ro*

convert high-boiling petroleum fractions called gasoil into high octane gasoline, high cetane diesel and heating oil. The process is complex, incorporating most processes of chemical engineering fundamentals, such as fluidization, heat/mass/momentum transfer and separation by distillation.

As presented in the schematic representation of FCCU, raw material is mixed with the regenerated catalyst in the reactor-riser. The cracking reactions and coke formation occur in the riser and the important products are then separated in the main fractionator. Due to coke deposition the deactivated catalyst needs to be regenerated in the regenerator [1].
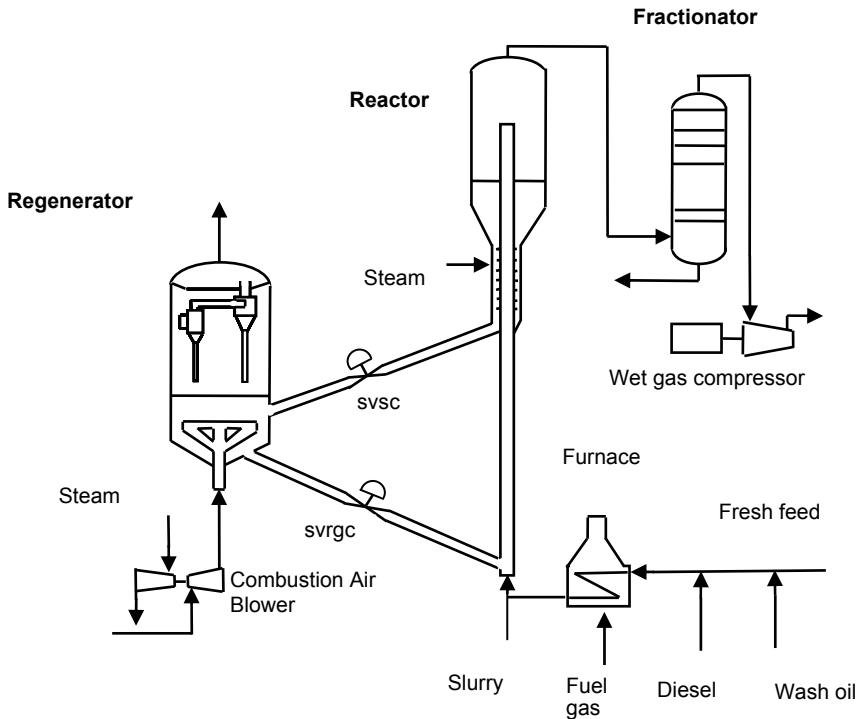
Figure 1. Schematic view of the FCCU plant.

Mathematical modelling in the chemical engineering field has a multidisciplinary character, dealing with different processes that have to be described. The mathematical models can be used in the system design, process control, identification of possible failures, training the operating personnel but also for the safety operation and assessment of environmental impact of the process.

From the point of view of the relationship between variables of a system, the models may be either analytical or statistical. Statistical mathematical models are based on observation data and measurements originating from the process (such as the Artificial Neural Networks models). Development of the analytical models is complex and time consuming as they imply a good knowledge of the phenomena and processes taking place inside the modelled system. They imply special instruction of a specialist in order to develop the specific equations. Statistical mathematical models are useful because they are simple from mathematical point of view and they do not need extended knowledge about the system, phenomena and processes underlying the system.

ANN models are able to capture the complexity of the intrinsic processes featuring the global process behaviour. Artificial Neural Networks are composed of simple elements, neurons, operating in parallel. The network function is determined by the connections between its neurons. The weighted connection paths link every two neurons to each other, the weighting structure providing the total network performance. Statistical models developed by means of ANNs and using process data are efficient alternatives to the traditional analytical models [2-4].

RESULTS AND DISCUSSION

The performance of a trained network can be measured by the errors on the training, validation and test sets, but it is often useful to investigate the network response in more detail. A regression analysis between the network response and the corresponding targets was first performed. The correlation coefficient (R-value) between the outputs and targets it is an efficient measure of how well the variation in the output is explained by the targets. For the training test the correlation coefficient, R-value, showed high values revealing a good correlation between targets and outputs.

The ANN was first designed and subsequently the quasi-Newton Levenberg-Marquardt algorithm was used to train the network. The 23 ANN-inputs are: spent and regenerated catalyst valve position; gasoline and diesel composition at the bottom and top of the main fractionator, gasoline and diesel composition on the 36th and the 37th stage of the main fractionator, reactor and regenerator temperature, main fractionator pressure, regenerator pressure, reactor and regenerator catalyst inventory; coke amount on the regenerated and spent catalyst; combustion air blower and wet gas compressor pressure; velocity of spent and regenerated catalyst, inventory of gas. All inputs are considered at the t sampling time. The last 21 variables are the process state variables and also represent the ANN outputs, but they are considered at the next sampling time, $t+\Delta t$.

A set of 201 input and output data (input/target pairs), provided by the FCCU analytical model, has been used for the ANN model development. The entire set has been divided into a set of data used for training the ANN and the rest for testing the quality of the training process.

Both for the training and testing sets of data, the R-correlation coefficient is very close to unity, indicating a very good fit between targets and the ANN model response and demonstrating a very good generalization property of the designed and trained ANN, Figure 2.

(a)

(b)

(c)

(d)

(e)

(f)
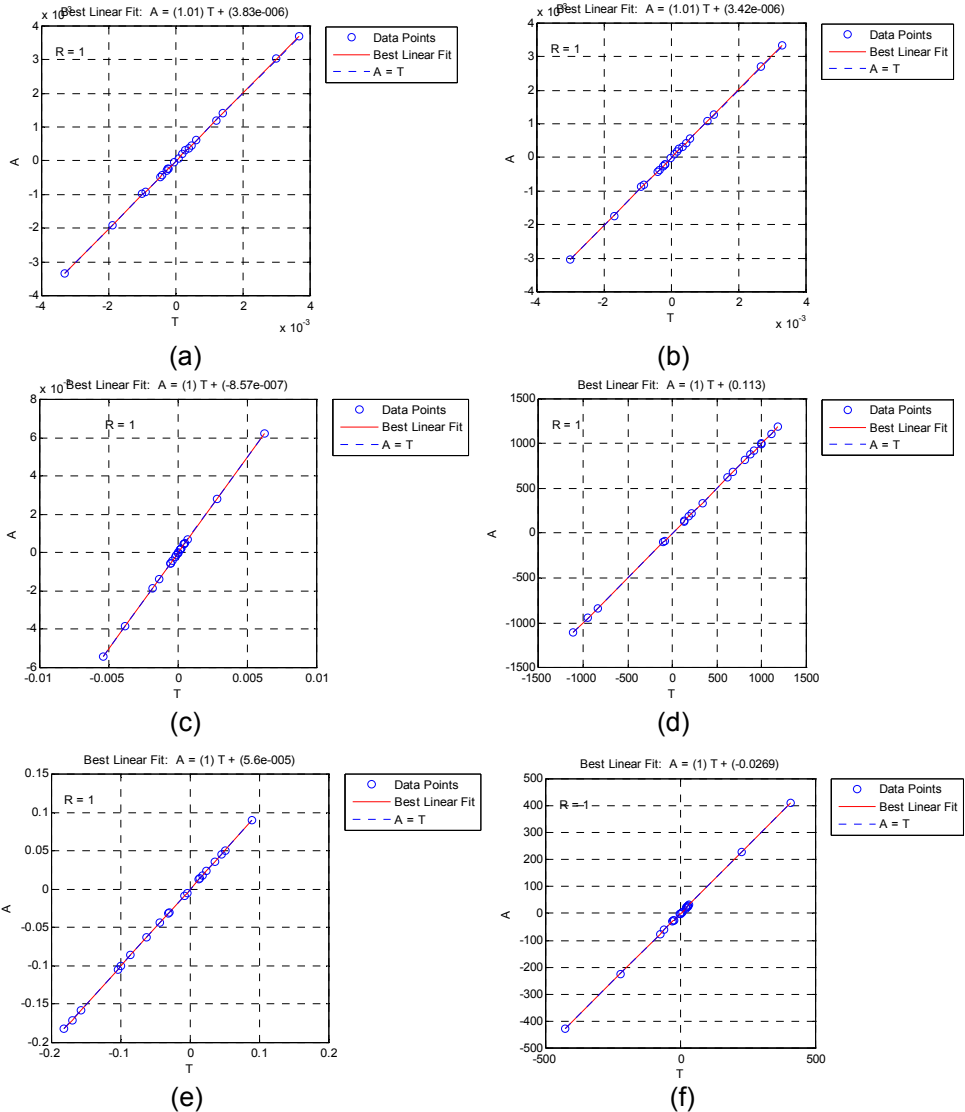
Figure 2. Results of the regression analysis between the ANN model response and the corresponding targets (testing set of data): (a)- gasoline composition on top of main fractionator, (b)- diesel composition on bottom of main fractionator, (c)- reactor temperature, (d)- column pressure, (e)-regenerator temperature, (f)- regenerator pressure.

The network outputs are plotted versus the targets as open circles. The best linear fit is indicated by a dashed line. The perfect fit line (output equal to targets) is indicated by the solid line. Figure 2 also shows that it is difficult to distinguish the best linear fit line from the perfect fit line, as they actually merge. The data set used for training has been chosen in correlation to the number of neurons in the hidden layer and covering the operating range of change of the input and output variables.

As a second, more comprehensive test, a random amplitude sequence has been generated for the input (manipulated) variables of the FCCU process: spent and regenerated catalyst slide valve opening position. They having random changes equally distributed in time. Within this final and complex test have been compared the induced evolutions of the process variables described by the ANN and the analytical models. The random amplitude sequence has been generated for both considered input (manipulated) variables with random changes equally distributed in time at multiples of 3000 seconds, as presented in Figure 3. The simulation has been performed for 15000 seconds and the evolution of the most important FCCU output variables was investigated and presented in Figure 4.
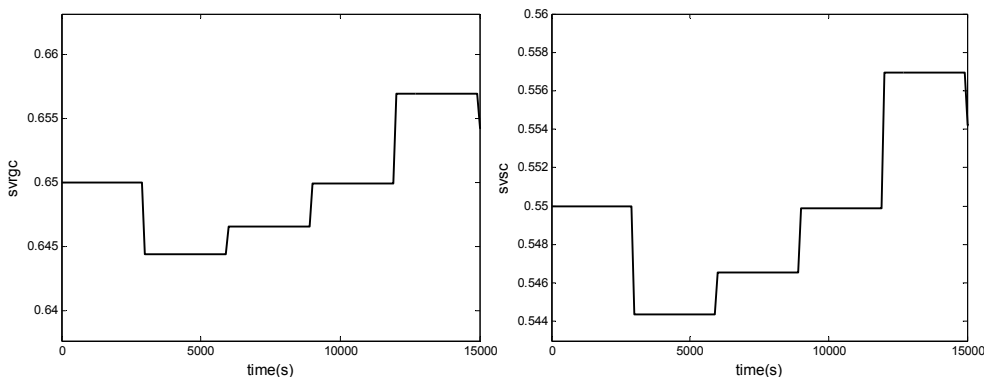
Figure 3. Amplitude sequence of the spent (svsc) and regenerated (svrgc) catalyst slide valve opening position.

The trained ANN is designed to predict one step ahead into the future the behaviour of the process variables. Applied repeatedly, the dynamic ANN predicts the time evolution of the state variables over a desired future time horizon. Again, this randomly generate testing set of data is completely different of the training one and not yet seen by the ANN.

The dynamic simulation results of the trained ANN model for the FCCU, compared to the analytical model, are shown in the Figure 4. As it may be noticed from these results, the developed ANN model has good dynamic performance. Results show the capability of the ANN model to capture the time evolution of the most important FCCU output variables.

129
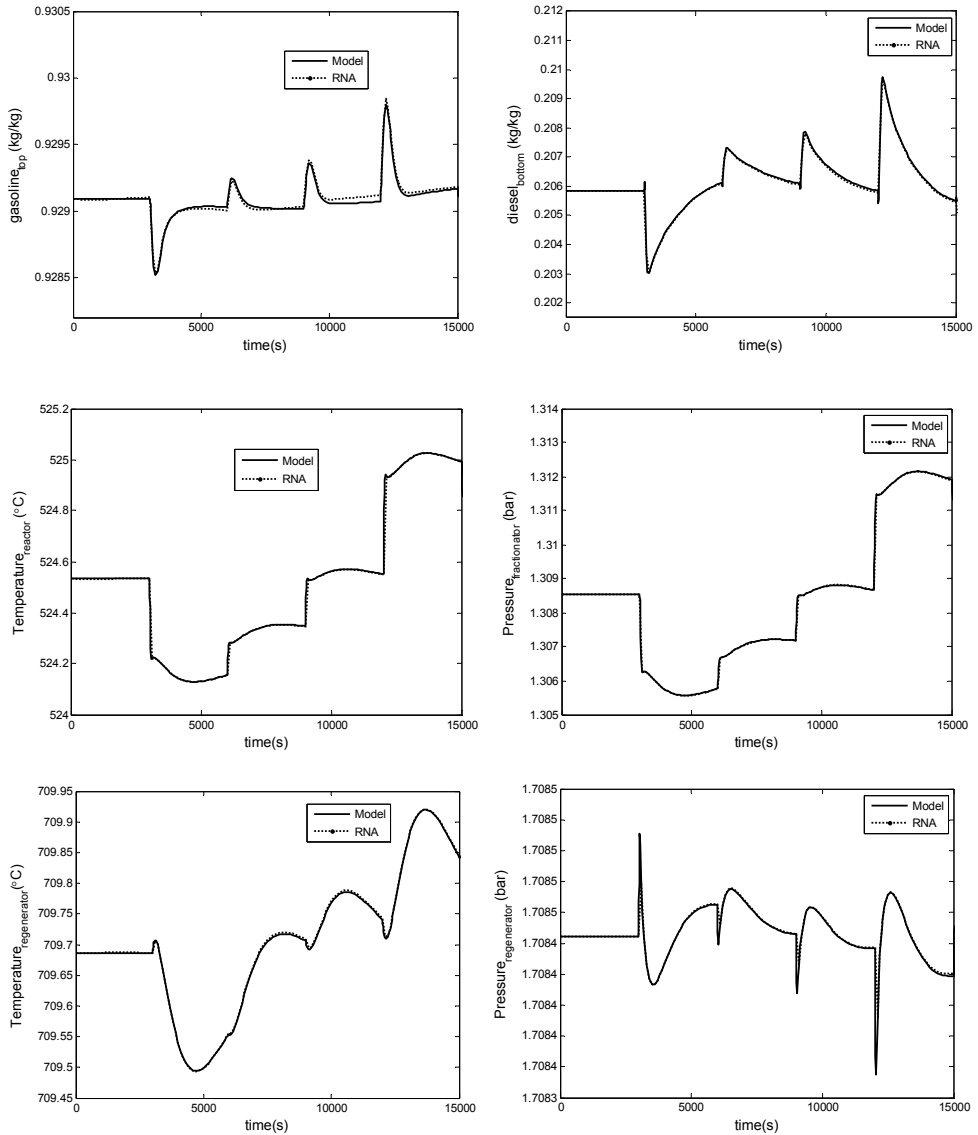
Figure 4. Comparative simulation results of the ANN and analytical model for the set of the most important FCCU variables.

It has been measured and compared the computation time needed for the dynamic simulation, using both the FCCU analytical and ANN based model. It was observed a substantial computation time saving in the case of the ANN. Using the ANN model the computational time is about 10 times

shorter compared to the first principle model requirement. This computation time reduction may have an important benefit on the real time implementation of the model based control algorithms.

CONCLUSIONS

The paper presents the simulation results of successfully using Artificial Neural Networks for modelling the dynamic behaviour of the complex FCC unit. First, a comprehensive input-target set of training data were produced using the FCCU analytical model. The first principle model was previously validated with experimental data taken from a real industrial FCC unit, Rompetrol Refinery, Romania. Correlation coefficients close to unity are shown on both training and testing steps, the last one being performed on sets of input-target data not met during the training procedure. The favourable fit between results emerged from the ANN versus analytical modelling, using randomly varying inputs, showed again that the ANN architecture and training algorithm are very efficient. They demonstrate a good generalization property of the ANN. The ANN developed model substantially reduces the computation effort and supplies the potential control algorithm with speed necessary for real time implementation. Due this favourable feature, the trained ANN model for the complex FCCU can be successfully used, as inherent model, for FCCU Nonlinear Model Predictive Control. This popular advanced control strategy may be efficiently used for improving the quality and the productivity of the gasoline and diesel products.

EXPERIMENTAL SECTION

An FCCU analytical model was available and it served as a rich database needed for the ANN training and testing procedure. The FCCU model has been developed based on reference construction and operation data taken from an industrial unit: Rompetrol Refinery, Romania. The new developed complex model of the FCCU reactor-regenerator-main fractionator and auxiliary systems (wet gas compressor, air blower, feed and preheat system, catalyst circulation lines) is a high order differential-algebraic equations system, consisting in 933 differential equations and more than 100 algebraic equations. The analytical model parameters have been validated with construction and operation data from the industrial unit. The developed analytical model is able to capture the major dynamic effects that may occur in the industrial FCCU system.

The ANN architecture for the FCCU statistical model is a double-layer feed-forward one with the backpropagation training algorithm used for computing the network biases and weights [5, 6]. In the ANN architecture two layers of neurons have been considered. The input layer has 23 neurons,

in the hidden layer 26 neurons have been used and the output layer consists in 21 neurons. The number of nodes in the hidden layer has been set on the basis of a trial and error process. Two ANN activation functions have been utilized: the tansing sigmoid transfer function for the hidden layer and the purelin linear transfer function for the output layer. The quasi-Newton Levenberg-Marquardt algorithm was employed for training the ANN. Overfitting has been avoided by the early stopping method which improved generalization. Random initial conditions have been used for the weights and biases, during the set of repeated sequence of training steps, in order to prevent convergence to undesired local minima. For improving the training procedure all input-output training data have been normalized using the maximum and minimum values of the input and output sets of data.

ACKNOWLEDGMENTS

REFERENCES

1. R. C. McFarlane, R. C. Reineman, *Computers and Chemical Engineering*, **1993**, *17*, (3), 275.
2. C. Jia, S. Rohani , A. Jutan, *Chemical Engineering and Processing*, **2003**, *42*, 311.
3. W.G. Vieira, V.M.L. Santos, F.R. Carvalho, J.A.F.R. Pereira, A.M.F. Fileti*, Chemical Engineering and Processing*, **2005**, *44*, 855.
4. M.V. Cristea, S. P. Agachi, M.V. Marinoiu, *Chemical Engineering and Processing*, **2003**, *42*, 67.
5. V. M. Cristea, P.S. Agachi, *Revista de Chimie*, **2007**, *58* (4), 406.
6. M.T Hagan, M.H. Menhaj, T, *IEEE Transaction on Neural Networks*, **1994**, *5*, 989.

Dedicated to Professor Liviu Literat, at his 80th anniversary

SOFTWARE APPLICATION FOR OBTAINING CERAMIC GLAZES WITH PRE-DEFINITE COMPOSITION AND PROPERTIES

ANA-MARIA CORMOŞ[a], FIRUȚA GOGA[a], JOSEPH GASPAR[a], DAN IRIDON[a]

ABSTRACT. The paper presents a software application developed for fast determination of glaze or glass properties with a known composition, optimization of glaze composition using the pre-definite properties and calculation of necessary of raw materials using the composition of glaze and available raw materials. The software application was developed using Matlab software package. A friendly and easy to use interface of the software application was built using GUIDE (Graphical User Interface Development Environment) components of Matlab.

Keywords: ceramic glazes, glaze properties, optimization of glaze composition

INTRODUCTION

The ceramic glazes are glass thin films that cover the ceramic products in order to improve some properties. The properties of ceramic glazes have to be in a concordance with the ceramic support. The oxide composition of glaze gives the properties of glaze.

A number of characteristics of glaze are important for the calculation of composition of mixture of raw materials, such as:
- complexity of composition (the large number of oxides);
- glaze properties are correlated with properties and composition of the ceramic body;
- raw materials available.

This work presents a fast method for calculation of raw material mixture composition for glaze production using pre-definite properties, and oxides composition of raw materials. Using the developed software application, the user could choose the most suitable raw materials, in order to reproduce accurate the chemical composition of glaze and subsequently the product properties.

[a] *Universitatea Babeş-Bolyai, Facultatea de Chimie şi Inginerie Chimică, Str. Kogălniceanu, Nr. 1, RO-400084 Cluj-Napoca, Romania, cani@chem.ubbcluj.ro*

The calculation steps are followed:
- determination of glaze oxides composition, using the firing temperature of ceramic product (by reading the Norton diagram);
- calculation of glaze properties using a pre-definite composition;
- calculation of composition of mixture of raw materials;
- optimization of the composition of glaze in function of the thermal expansion coefficient.

The main importance of this software application is to decrease the calculation time and the number of practical experiments which must be done for obtaining an optimal composition glaze.

RESULTS AND DISCUSSION

Determination of ceramic glaze composition

The chemical composition of glazes is complex and it corresponds to an alkali-silico-aluminate glass. The composition is adapted to the support product and is correlated with the product final usage.

The ceramic support implies on pre-definite properties for the optimal of glaze composition. Ceramist researchers [1] tried to correlate the glazes composition with its fusibility and built a two part diagram (Norton). That diagram allows pursuing the variation of molar composition for glaze vs. firing temperature (Figure1).
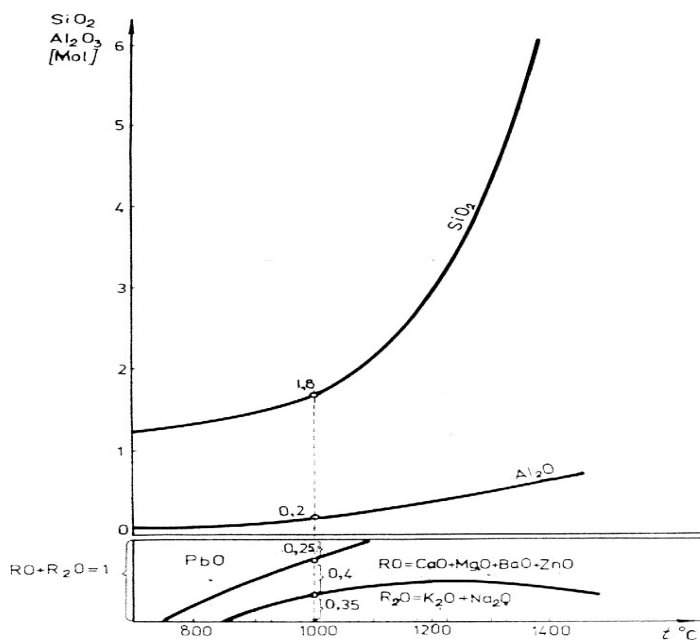
Figure 1. Norton Diagram.

134

Also, the glazes composition is characterized by certain indexes as follow:

- silica module - SiO_2/Al_2O_3 with value 4.2-6.2;
- acali module - Na_2O/K_2O with value 0.8 - 1.4;
- CaO/MgO with value with value 0.3 - 1.5;
- Acidity coefficient (acidity coefficient shows the activity of glaze vs. support product and allows estimation of stability of glaze in firing process).

The acidity coefficient depends of molar fraction of oxides from glaze:

$$A = \frac{y + 3 \cdot z}{1 + 3 \cdot x}$$

where:

y - molar concentration of SiO_2;

z - molar concentration of B_2O_3;

x - sum of molar concentration of oxides: Al_2O_3 and Fe_2O_3.

The variation of glaze characteristics vs. acidity coefficient is presented in Table 1 [2, 3].

Table 1. Variation of glazes characteristics vs. acidity coefficient

Acidity coefficient (A)	Glazes characterizations
0.7 - 1.25	Useable mat glazes if are rich in PbO
1.45	Mat glazes
1.90 – 2.0	Possible glazes
2.60	Normal glazes
2.90	Possible glazes
2.90	De-vitrification is produced

The developed software application allows determination of the oxide composition of glaze for a known temperature, using Norton diagram. Molar formula read from Norton diagram is converted in mass or molar percentage. Using the percentage composition of oxides, the desirable glaze properties are calculated: thermal expansion coefficient, density, and the refractive index and dispersion index. In order to validate the glaze composition, the developed software application could also be used to calculate the acidity coefficient.

Properties of the glazes in the solid state

The glaze properties are very important for reliability, prediction and design of the ceramic material.

The physical-mechanical properties are calculated using an additive relation described in next relation [4, 5]:

$$P = \sum_{i=1}^{n} p_i c_i \; , \qquad (1)$$

where:

P - property;

p_i - additive coefficient of the "i" oxide property;

c_i - concentration of "i" component in glaze, [mol %].

In practice, for some oxides (B_2O_3, SiO_2, PbO, TiO_2) the additive coefficients are strong influenced by the existence and concentration of the other oxides from the system.

In this article the following properties of glazes are calculated using the developed software: the thermal coefficient of expansion, the refractive index and dispersion index and density.

Glaze composition optimization

To obtain a glaze with a pre-define properties; an optimization of glazes composition is necessary. In this software application, the group multi-dynamic optimization method was used [6]. The application of this method is characterized by following elements: an initial solution (the initial glaze composition), the precision of determination of extreme point.

The developed software application optimizes the composition of glaze in function of the thermal expansion coefficient with preservation of acidity coefficient in a specific limit for glaze. The difference between thermal coefficient of expansion of glaze and support layer have to be smaller than 10^{-7}, in order that the glaze not cracks during the cooling.

Beside the two above mentioned coefficients, the oxide ratio is equally important to obtain a glaze ($4.2 < SiO_2/Al_2O_3 < 6.2$; $0.8 < Na_2O/K_2O < 1.4$; $0.3 < CaO/MgO < 1.5$). The developed application maintains the oxide ratio between the limits.

The calculation of composition of mixture of raw materials

The composition of mixture of raw materials is calculated using the equations of mass balance for any raw materials. The mass balance equations for "i" component is described by formula:

$$\sum_{j=1}^{n} c_{i,j} m_j = c_{i,am} m_{am} \qquad (2)$$

where: m_j -"j" raw material weight;

m_{am} – the total mass of blend;

$c_{i,j}$ – the concentration of "i" component in a "j" raw material;

$c_{i,am}$ – the concentration of "i" component in mixture.

Software application – Case Study

Solving of mathematical model and finding the optimum of raw materials composition was done using Matlab software [7]. For the end-users, the GUIDE component (Graphical User Interface Development Environment) of Matlab was used in order to create an interactive interface which allows an easy handling of application. The interface application is easy to use because is using the standard components of the graphic interface of Windows Operation System, and the users do not need to know Matlab syntax.

The main application window [8] (see Figure 2) contains the graphic elements for input data (temperature and composition) and commands for calculation of glaze properties, optimization of glaze composition and calculation of glaze formula. The glaze composition can be introduce in two ways using the Norton diagram (using the firing temperature) or read the glaze's composition from keyboard.

Using the "display" bottom the program can show the glaze composition (Figure 3).
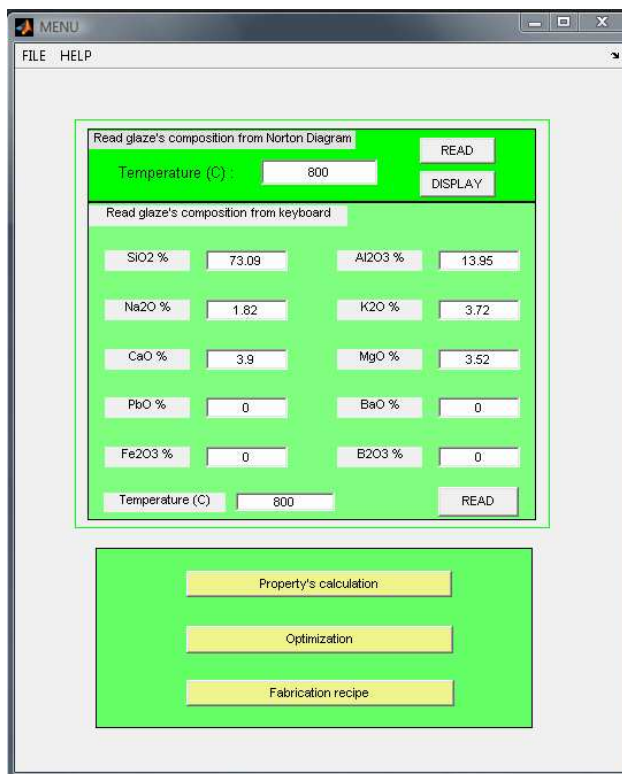
Figure 2. Main application window
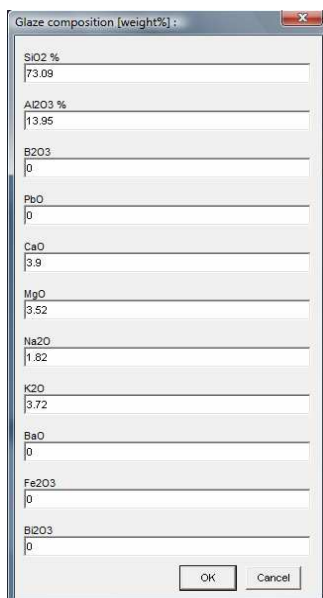
Figure 3. Glaze composition (weight %)

The optimization of the composition needs to know the glaze properties, because any numeric optimization method expects an initial solution. The glaze properties can be visualized using „Property's calculation" button from main window. The properties of glaze are showed in a new window (Figure 4).
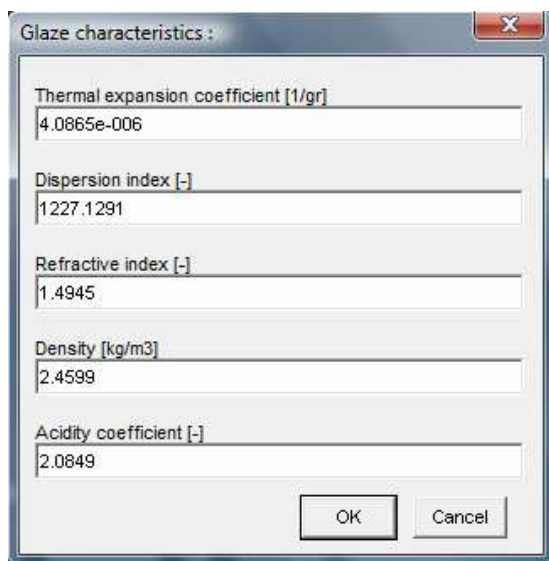
Figure 4. Glaze characteristics

Using the "Optimization" button from main application interface, a new window is open (Figure 5). The value of parameters for optimization: lower value and upper value of thermal coefficient of expansion and acidity coefficient are defined using this window. The calculation of optimal composition is done using the "Run" button and the composition result is display in a new window (Figure 6). The glaze properties after optimization are presented in Figure 7.

Figure 5. Optimization window.

Figure 6. Glaze [%weight] composition, after optimization.

Figure 7. Glaze characteristics, after optimisation.

Other option of application developed is the determination of fabrication formula using a raw material database. The raw materials database of the software application is presented in Table 2. The opening of the window for the calculation of composition of mixture of raw materials (Figure 8) is doing by using the „Fabrication recipe" button from main application window.

Table 2. Raw materials composition

Raw Materials	SiO₂ %weight	Al₂O₃ %weight	CaO %weight	MgO %weight	Na₂O %weight	K₂O %weight	LOI* %weight
Feldspatr	71.6	16.48	1.15	0.20	1.50	8.57	0.50
Kaolin	53.5	32.78	0.47	0.38	0.15	0.47	12.18
Sand	98.38	0.92	0.40	0.04	0.06	0.20	0.00
Talc	61.36	0.63	0.83	30.65	0.08	0.03	6.42
Wollastonite	51.82	1.01	44.30	1.13	0.20	0.32	1.22
Limestone	0.00	1.47	53.90	0.00	0.00	0.00	44.64
Soda ash	0.00	0.00	0.00	0.00	57.20	0.00	42.50
Dolomite	0.20	0.38	26.10	24.32	0.00	0.00	66.10
Alumina	0.00	1.70	32.00	0.00	0.00	0.00	66.10

* LOI = Loss on ignition

For determination of raw materials quantity, the user must specify: raw materials used for glazes production and the bases oxides that are used for calculations. The results, the quantity of raw materials are available in a text file, „compmp.txt"
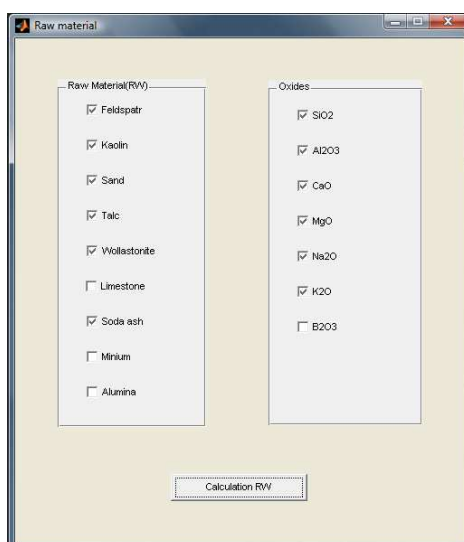
Figure 8. The calculation of composition of mixture of raw materials

In order to validate the software application, the raw materials used and calculated formula for a glaze was determinate, Table 3.

Table 3. Raw materials for glazes

Raw Material	Kg/Kg
Feldspatr	0.5389
Kaolin	0.0843
Sand	0.1808
Talc	0.1075
Wollastonite	0.0695
Soda ash	0.0693

The raw materials database of software application developed could be improved by adding new components and new oxides according to Seger formula.

CONCLUSIONS

The software application allows a fast determination of glazes or glass properties with a known composition, the optimization of glazes composition using the pre-definite properties and calculation of necessary of raw materials using the composition of glazes and available raw materials.

The main importance of this software application is to decrease the calculation time and the number of experiments which must be achieved for obtaining an optimal composition glaze.

The developed software application is helpful for students, chemical engineering, and scientific researchers who work in oxide materials science and not only. The using of application reduces significantly the necessary time for preparation of fabrication recipe.

REFERENCES

1. S. Stefanov, S.Batschwarov, "Ceramic Glazes", Bauverlag GmbH, Wiesbaden und Berlin, **1988**.
2. I. Teoreanu, N.Ciocea, A. Barbulescu, N.Ciontea, "Tehnologia produselor ceramice si refractare", Editura Tehnica, Bucuresti, **1985**
3. F. Goga, Teză de doctorat,"Sisteme oxidice vitroase cu rol de acoperiri ceramice" Cluj-Napoca, **2004**.
4. I. Ardelean, R. Ciceo-Lucacel, "Fizica si tehnologia materialelor oxidice", Cluj-Napoca, **2000**.
5. P. Baltă, "Tehnologia Sticlei", Ed. Didactică şi Pedagogică, Bucureşti, **1986**.

6. A. Imre, P. Agachi, "Optimizarea proceselor din industria chimică", Editura Tehnică, Bucureşti, **2002**.
7. L.A. Dobrozanski, R. Honysz, Z. Brytan, *Journal of Achievements in Materials and Manufacturing Engineering*, **2006,** 17 (1-2), 429.
8. ***, "MATLAB Users Guide", The MathWorks Inc, **2006**.

Dedicated to Professor Liviu Literat, at his 80th anniversary

MAGNETIC FLUIDS – MATERIALS WITH REMARKABLE APPLICATIONS

ANDRA TĂMAŞ[a], ZENO GROPŞIAN[a], ROMULUS MINEA[a]

ABSTRACT. The paper presents contributions to MF preparation through magnetite chemical co-precipitation followed by stabilization with oleic acid and dispersion into a carrier liquid, or through carrier liquid exchange technique (mineral or paraffin oil). Based on the estimation and correlation of fluid specific properties (concentration, density, dynamic viscosity, the saturation magnetization) has been presented the posibility to intensify the separation of aqueous two-phase systems with oily compounds content under magnetic filed action. The device contains a separator with immersed permanent magnets for oily phase separation from waste waters. It was established the separation efficiency as a function of separator feeding specific flow.

Keywords: extraction, magnetic fluids, magnetic separator, oily phase

INTRODUCTION

Magnetic fluids (MF) or ferrofluids (FF) are colloidal suspensions of ultrafine particles (~ 10 nm) of ferro- and ferri- magnetic materials stabilized and dispersed into a carrier liquid. MF represent macroscopic uniform two-phase systems. One phase–the liquid carrier- determines the chemical and mechanical properties of the system, the other–a ferromagnetic substance in ultradisperse state–specifies the magnetic properties of a system.

In order to maintain the aggregative stability of MF the adsorption of surfactant molecules on the particle surface may be employed. Adsorption layers (their effective width varying between 3 and 100 nm as a function of the structure and molecular weight of the solvent and stabilization agent) form the potential barrier preventing particles from approaching each other. The layer width should be sufficient to keep the particles from approaching each other to the distance when the Van der Waals and dipole interaction forces come into prominence. Besides, the adsorbed molecules should ensure the lyophilization of particles and their compatibility with the dispersion medium [1, 2].

---

[a] *Universitatea "Politehnica" din Timişoara, Facultatea de Chimie Industrială şi Ingineria Mediului, P-ţa Victoriei 2, RO-300006 Timişoara, andra.tamas@chim.upt.ro; r.minea@rdslink.ro*

MF were obtained for the first time at NASA (1960) as part of the spatial technology researches to realize a system with the function of control the fluid fuels flow in imponderability conditions.

The most used magnetic particles to MF preparation are: transition metals (Fe, Co, Ni, Zn), alloys (Fe-Co, Ni-Fe, Fe-Co-Ni), iron oxides, magnetite, ferrite ($Me_{x+y}Fe_2O_4$; Me=Co, Ni, Zn, Mn, Cu, Ba; $x + y = 1$), nitride (Fe_3N), boride (FeB), silica-coated iron particles [1-4].

The particles used are, preferably, of iron oxides because of their resistance to oxidation, rather than the transition metals, which have the benefit of higher saturation magnetization [5].

As stabilizers are used compounds with a COOH group able to fixed on the magnetic particle and a hydrocarbon chain which allows dispersion into a liquid carrier. Stabilizing effects were obtained using: fatty acids (oleic, elaidic, lauric, stearic, erucic, linoleic, linolenic) or their salts, nonylphenyl-polyethylene glycol, triethanolamine (TEA), glycol esters with dibasic fatty acids (adipic), perfluorocarboxylic acids salts ($C \geq 8$).

As carrier liquids are used: petroleum, hydrocarbons (B, T, X, hexane, heptane, decane etc), fluorinated and chlorinated hydrocarbons (dichloroethane, carbon tetrachloride, trichloroethane), C_{1-5} alcohols, water, ethylene glycol, oils (mineral, parafin or silicon), esters of adipic, sebacic, citric, ftalic acids [6].

Preparation of magnetic colloids: the size reduction by grinding of magnetic powder in the presence of a carrier solvent and a surfactant dispersing agent, for long periods of time (~ 1000 hours); by thermal decomposition of metal carbonyls ($Fe(CO)_5$, $Fe_2(CO)_9$, $Fe_3(CO)_{12}$, $Co_2(CO)_8$, $Co_4(CO)_{12}$, $Ni(CO)_4$) in various liquid organic media (B, T, pentane, alcohols etc), gases or in vacuum (as stabilizers are used different types of polymers which facilitates the formation of small particles, moreover, by adsorbing on the particles it furnishes the solution aggregative stability); stable ferromagnetic colloids of iron can be obtained using high-intensity ultrasound to sonochemically decompose volatile organometalic compounds [7]; the electrolytic deposition of fine Fe, Co, Ni particles or their alloys on a cathode made by a solid (Ni, Ag or steel) or liquid (Hg) metal from an electrolyte which contains the respective ions) in presence of a diluted solution of surfactant (oleic acid) in an hydrocarbon medium; by evaporation of a metal by making use of the electric discharge and subsequent condensation of a vapour in the form of hyperfine drops. MF preparation methods based on magnetite chemical co-precipitation or carrier liquid exchange are well-known [2, 8].

RESULTS AND DISCUSSION

MF preparation by chemical co-precipitation technique consists of magnetite precipitating from Fe^{2+} and Fe^{3+} solutions (usually $FeSO_4$, $FeCl_3$) in alkali (usually NH_4OH), followed by stabilization and precipitate washing and dispersion into desired carrier liquid.

Method of carrier liquid exchange consists in flocculation of magnetic stabilized particles with polar agents (e.g. acetone), magnetic sedimentation and redispersal in a second carrier liquid. Sometimes it is necessary to use another type of stabilizer. In this manner were prepared MF with mineral oil, paraffin oil or dioctyladipate as carrier liquids.

Physico-chemical properties of MF depend on magnetic material type, its concentration, the way of stability and the dispersion medium. Also, extremely important are, chemical composition of the magnetic material. In the case of magnetic particles based on ferrite is important Fe^{2+}:Fe^{3+} ratio, or other metals (Ni, Cr, Co) for mixed ferrites.

Magnetic component concentration has a direct effect on the liquid carrier density modification. For MF based on stabilized magnetite dispersed in petroleum, it was established the relation:

$$\rho_{MF} = \rho_P + 0.97 \cdot \theta \tag{1}$$

where: θ - magnetite concentration, $[kg \cdot m^{-3}]$, ρ_{MF}, ρ_P - MF and liquid carrier densities, $[kg \cdot m^{-3}]$.

Magnetization M has the applied field direction and its value is equal to the magnetic moments ($\overline{m}$) sum of the "n" particles contained in a volume unit:

$$\mu_0 \cdot M = n \cdot \overline{m} \tag{2}$$

In this manner, the magnetic attraction force (F_m) and pressure (P_m) have the next expressions:

$$F_m = \mu_0 \cdot M_S \cdot gradB \cdot V_d, \; P_m = -\mu_0 \cdot \int_0^H M \cdot dH \tag{3a, b}$$

where: $gradB$ - magnetic field gradient, M_s - the saturation magnetization, μ_0 - magnetic permeability and V_d the drops volume with magnetic component content.

Dynamic viscosity of MF, η, depends on the liquid carrier viscosity, η_0, and the stabilized particles volumic concentration, Φ, $[m^3 \cdot m^{-3}]$:

$$\eta / \eta_0 = 1/1 + a \cdot \Phi + b \cdot \Phi^2 \tag{4}$$

where a and b are specifically constants.

In nonmagnetic field, MF present a Newtonian behaviour. The temperature dependence of dynamic viscosity was expressed as Arrhenius type equations:

$$\eta = A \cdot e^{E_a/R \cdot T} \tag{5}$$

This fact allows to calculate the viscous flow activation energy, E_a, [$kJ \cdot mol^{-1}$], (Table 1):

Table 1. Some MF characteristics

Liquid carrier	Density, $kg \cdot m^{-3}$	Magnetization, Gs	Arrhenius type relation	E_a, $kJ \cdot mol^{-1}$
Petroleum	1085	300	$\eta = 2.38 \cdot 10^{-5} \cdot e^{1615/T}$	13.4
Petroleum	1430	600	$\eta = 2.57 \cdot 10^{-5} \cdot e^{1685/T}$	14.0
Toluene	1150	300	$\eta = 2.32 \cdot 10^{-5} \cdot e^{1385/T}$	11.5
Mineral oil	1235	350	$\eta = 1.56 \cdot 10^{-6} \cdot e^{3100/T}$	25.7
Paraffin oil	1220	400	$\eta = 2.33 \cdot 10^{-7} \cdot e^{4020/T}$	33.4

The interactions between MF and the external applied magnetic field (permanent magnets or electromagnets) are basic for the main applications in technical and biomedical field. The most MF applications are based on the possibility to place and control magnetic materials using a magnetic field with a suitable flux distribution: magnetodensimetric separation (based on the levitation effect of nonmagnetic or low magnetic bodies in ferrofluids under an external magnetic field action, applied to useful minerals with different densities separation); pressure transducers and magnetofluidic clinometers, magnetooptical sensors, electroacoustical transducers; pressure sealings (magnetic field placed the MF in the gap between the surfaces of mobile and stationary elements); ferrofluidic lubricating; ferrofluidic dampers (based on MF restraint in spaces subject to vibrations using magnetic field); liquid carriers for different heat-exchange devices, especially in devices for magnetocaloric energy conversion; biomedical applications (separation and purification processes, in immunoassays, as agents for the destruction of cells via magnetic fields, as contrast agents to enhance magnetic resonance imaging (MRI) and for targeted delivery of therapeutic agents, MF present good effects in the wound healing process of the skin lesions, anti-inflammatory effects and anti-radiation protection, as a magnet-controlled haemosorbent for extracorporeal detoxication of biological media); growth and organogenesis stimulation; vitroplants obtaining, intensification of two-phase systems separation (in mass transfer processes) [9-11].

MF based on oily compounds (hydrocarbons, mineral oils) can be used for oily components restraint through dissolution from waste or accidentally impurified waters. This process consists in oily component

distribution between the liquid carrier of the MF and the aqueous phase. The mass transfer process is amplified thanks to the intimate contact result from the strong phases mixing. This fact leads to some emulsions formation. It is possible to establish a correlation between the values of the separation time in gravitational (τ_g) and magnetic (τ_m) field, at different values of M_s for the oily phase and different magnetic field values [12]:

$$\tau_g / \tau_m = 1 + K \cdot gradB^a \cdot M_S^b \tag{6}$$

The coefficient K and the exponents a, b are specific to the used emulsion.

To intensify the separation of such two-phase system were tested separators based on electromagnets, rotating or immersed permanent magnets [12-15]. Through the direct setting between the magnet and the emulsion with MF content there is the possibility of a maximum attraction force development in the liquid layers in contact with the whole surface of the magnet (internal, external, frontal). Thus, the MF drops are submitted to an intense coalescence process obtained in a zone around the magnet body. The amount of MF retained on the magnet surface is much increased when the magnet is immersed in the aqueous medium due to the Archimedean force. The detailed scheme for the separator with immersed ring-shaped magnet (Dxdxh=130x60x54mm) is shown in Figure 1:
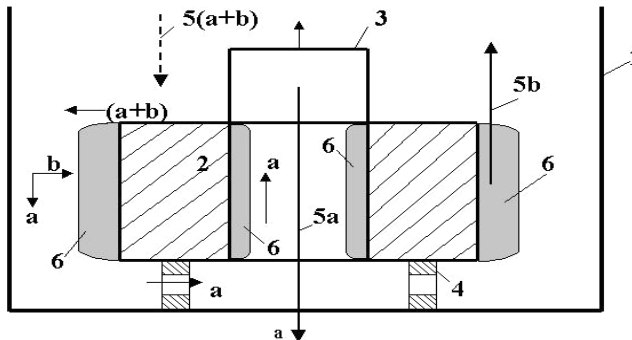

Figure 1. Separator for emulsions with magnetic fluid content.

The magnet **(2)** is placed into the cylindrical body of the separator **(1)** and the ring- shaped portion is continued, to the upper side, with a bell **(3)**. The role of this one is to direct the emulsion submitted to separation to the ring-shaped area between magnet and the separator body where it circulates descending, through the inferior frontal portion **(4)**, and after that the separated aqueous phase is collected in the inner part of the bell. The ferrofluid is collected as a continuous layer **(6)** on the magnet surface and is aspirated periodically. The separated water crosses the magnet inferior frontal portion and goes into the bell (route **5a**), in direct contact with the magnet inner surface, to remove all the unseparated MF drops.

Magnetic field distribution in the inner (a) and outer (b) position of a ring-shaped magnet is presented in Figure 2.

To establish the separation effect of the ring-shaped magnet, water with oil content (0.5÷2%) was used in which was added the proper amount of magnetic fluid so that the MF/water ratio was 1÷ 5 ml MF/1000ml water. After a strong combined mixing (mixer and recirculating pump) the emulsion was led through the separator, with various flow values. The magnetic fluid is retained around the magnet and the water with a high epuration degree is collected and analyzed.
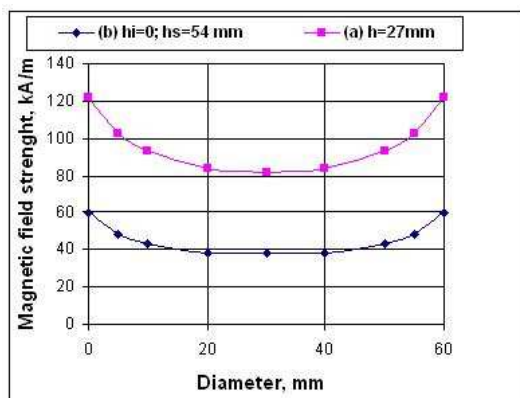
Figure 2. Magnetic field distribution.

The equipment that containe the magnetic separator is shown in Figure 3:

Figure 3. Pilot-equipment with magnetic separator (1-separator; 2- vessel with stirring; 3-stirrer; 4-recirculation pump; 5- tank for MF; 6- collecting vessel).

From the photoresistive experimental values the oily phase concentrations in the preepurated water samples were established. Based on these results we calculated the remove efficiencies (the ratio between the separated oil fraction and the one existent initially in water) of the organic magnetic phase after the wastewater passed through the separator (Table 2).

Table 2. The final concentrations of organic phase and the separation efficiencies

Specific flow, $m^3 \cdot m^{-2} \cdot h^{-1}$	$\Delta R/R$	Organic phase concentration $ml\ oil/1000ml\ water$		Separation efficiency, %
		initial	final	
3.47	0.316		0.67	96.6
6.53	0.485	20	1.30	93.5
9.92	0.583		1.75	91.2

It was found that the specific flow increasing leads to a less efficient separation of the organic component from the system. This conclusion is proved both by the photoresistance value increasing due to the less emulsion transparency (MF presence) and the remove efficiency decreasing.

CONCLUSIONS

Using chemical co-precipitation technique and carrier liquid exchange were prepared MF with estimated concentrations/magnetizations and good stability.

Petroleum, mineral or paraffin oil based MF present Newtonian behaviour, the temperature influence been represented by Arrhenius type equations.

For biphasic systems with MF, the external magnetic field action has an intensifying effect to phase separation.

It was built and tested a pilot-equipment for oily components recovery from waste waters using MF and a separator with immersed permanent magnet. The separation degree as a function of the waste waters specific flow was established.

EXPERIMENTAL SECTION

For stabilized magnetite preparation, aqueous solutions of $FeSO_4$ (0.35M) and $FeCl_3$ (0.7M), heated to 65°C were treated, under strong stirring, with a NH_4OH solution (25%), 20% excess. Afterwards, oleic acid diluted in petroleum is added (1:1). The heating is continued (t ~ 102°C) until the magnetic precipitate is separated in comparison with the aqueous solution which contained dissolved salts NH_4Cl and $(NH_4)_2SO_4$. Clarifying and recurrent washing of the stabilized magnetic precipitate are followed by its

dispersion into the carrier liquid (petroleum), under heating and stirring. Through filtration (that can be intensified using magnetic field), is obtained MF whose concentration depends on the added amount of the carrier liquid.

MF characterization required density, dynamic viscosity, saturation magnetization and Fe(II): Fe(III) ratio determination.

From petroleum based MF were obtained mineral or paraffin oil based MF (MF-MO, MF-PO) through the carrier liquid exchange technique.

REFERENCES

1. E. Blums, A. Cebers, M.M. Maiorov, "Magnetic Fluids", Walter de Gruyter Berlin, New York, **1997**.
2. R.E. Rosensweig, "Ferrohydrodynamics", Dover Publications, Inc. Mineola, New York, **1997**.
3. S. Taketomi, Y. Ozaki, K. Kawasaki, S. Yuasa, H. Miyajima, *J.Magn. Magn. Mater.*, **1993,** *122*, 6.
4. L.N. Donselaar, "Silica-magnetite colloids and magnetic fluids: Synthesis and particle interactions", PhD Thesis, Utrecht University, **1998**.
5. S.W. Charles, *Romanian Reports in Physics*, **1995**, *47* (3-5), 249.
6. D. Bica, R. Minea, Patent RO 93109, **1987**.
7. I. Bica, *Romanian Reports in Physics*, **1995**, *47* (3-5), 273.
8. E. Luca, Gh. Călugăru, R. Bădescu, C. Cotae, V. Bădescu, "Ferofluidele şi aplicaţiile lor în industrie", Ed. Tehnică, Bucureşti, **1978**.
9. I. Anton, I. De Sabata, L. Vekas, Conf. Maşini hidraulice şi hidrodinamică, IP Timisoara, **1985**, 141.
10. M. Şincai, D. Argherie, D. Gângă, D. Bica, L. Vekas, Proceedings of ISACB Congress, Gainesville, USA, **2002**.
11. R. Minea, A. Tămaş, M. Corneanu, G. Corneanu, *Annals of West Univ. of Timisoara, Series Chemistry*, **2003**, *12(3)*, 1561.
12. A. Tămaş, "Contribuţii la obţinerea şi caracterizarea fluidelor magnetice – Emulsii cu conţinut de fluide magnetice", Teză de doctorat, Univ. "Politehnica" Timisoara, **2004**.
13. Z. Gropşian, R. Minea, E. Brînzei, A. Tămaş, *Rev. Chim.(Bucuresti)*, **2004**, *55(8)*, 577.
14. A. Tămaş, R. Minea, *Romanian Reports in Physics*, **2006**, *58(3)*, 351.
15. R. Minea, A. Tămaş, E. Brînzei, M. Şuta, "The behaviour of emulsions with ferrofluid content in magnetic field", 4th European Congress of Chemical Engineering, Granada, Spain, **2003**.

Dedicated to Professor Liviu Literat, at his 80th anniversary

THE INFLUENCE OF SOLID SURFACE ON THE ADSORPTION OF ANTI-C1Q MONOCLONAL ANTIBODY AT ISOELECTRIC pH

IOAN BALEA[a], MARIA TOMOAIA-COTIŞEL[a*], OSSI HOROVITZ[a], GHEORGHE TOMOAIA[b], AURORA MOCANU[a]

ABSTRACT. The effect of solid surface and ionic strength, in a buffer solution at isoelectric pH (5.5), on the surface immobilization, and adsorption process of a mouse monoclonal antibody, type IgG1, anti-C1q, is investigated by atomic force microscopy (AFM). The adsorption is conducted on glass, amino silanized glass, and positively charged modified glass. The AFM images present a monolayer adsorption with a dominant lying flat orientation of the molecules. This suggests that van der Waals interactions and possibly hydrogen bonds between antibody molecules and the solid substrate are the dominant interactions upon electrostatic forces, in conditions of rather low surface charge densities, high ionic strength of buffer solutions, and antibody molecules without a net charge.

Keywords: anti-C1q monoclonal antibody, adsorption, AFM, ionic strength, surface charge

INTRODUCTION

Proteins and particularly antibodies are in the focus of interest for investigations by various modern physical methods. Their immobilization in stable adsorption layers on solid surfaces is important in diverse applications, therefore the antibody adsorption has been undertaken on a variety of surfaces, such as mica, silica, glass and gold [1-3], by using different techniques. Among them, atomic force microscopy (AFM) has proved as a versatile technique capable of providing information at nanometer and molecular level, e.g. the structural morphology and the spatial distribution of antibody molecules as well as the antibody layer thickness and roughness on the solid surface [4-11].

[a] *Universitatea Babeş-Bolyai, Facultatea de Chimie şi Inginerie Chimică, Str. Kogălniceanu, Nr. 1, 400048, Cluj-Napoca, Romania, mcotisel@chem.ubbcluj.ro*
[b] *Universitatea de Medicină şi Farmacie, Str. Mosoiu , Nr. 47, 400132, Cluj-Napoca, Romania*

The anti-C1q monoclonal antibody, the object of our present investigation, is a Y-shaped protein molecule, having a molecular weight of 150 KDa and an isoelectric pH of about 5.5. It is known that this antibody recognizes and reacts specifically with the globular heads of the C1q protein, which plays a central role in innate immunity, being involved in the early phase of the classical pathway of the complement system activation [12]. It is also known that the C1q protein is involved in the pathogenesis of a wide range of diseases [13-15], such as Alzheimer`s disease, prionic diseases and lupus erythematosus systemic. Immunohistochemistry uses this monoclonal antibody specific for C1q protein in ELISA [16], RIA (radio immunoassay), Western blotting and flow cytometry methods [17]. For example, ELISA is a solid-phase immunoassay [16] frequently used in immunology, biochemistry, biophysics, medical diagnostics, and other areas of medical science. This immunoassay involves the immobilization of one reactant, such as a specific antibody, on the solid surface usually by adsorption.

Usually in the antibody molecule we distinguish between the *Fab* fragment (antigen-binding fragment), which binds analyte (antigen) with high specificity, and the *Fc* fragment (constant fragment). For immunoassay applications, the control of adsorption and orientation of antibodies on surfaces is necessary to ensure that their active sites (the two "ends" of the Y-shaped molecule) are away from the surface and accessible to bulk solution, i.e. the Fc fragment (the "head" of the molecule) binds to the solid surface.

Here we investigate the effects of various adsorption surfaces and physical factors such as ionic strength over the adsorption process of the anti-C1q monoclonal antibody at the isoelectric point (IEP), where the net charge of the antibody is almost zero (pH = 5.5). We employed AFM to image the morphology of the adsorbed layer and to observe adsorption patterns on a variety of hydrophilic solid surfaces, such as glass, silanized glass and positively charged glass and for ionic strengths of 0.031 and 0.055. AFM is used to evidence the relative changes in the thickness of the antibody adsorbed layers and the possible surface aggregation (i.e. surface clusters).

RESULTS AND DISCUSSION

Ionic strength of buffer solutions. The ionic strength of a solution is defined as a function of the concentrations of all the ions present in a solution and of their charges:

$$J = \frac{1}{2} \sum_i c_i z_i^2$$

where c_i is the molar concentration of ion i (mol dm^{-3}), z_i is the charge number of that ion, and the sum is taken over all ions in the solution. In

order to calculate the ionic strength, a speciation of the buffer solutions had to be made. With use of the Hyperquad simulation and speciation (HySS) program [18], we obtain the distribution of species concentrations versus pH for the 10 mM solution of citric acid and citrates (Fig. 1). If we denote the citric acid $C_6H_8O_7$ as H_3A and its sodium salts by NaH_2A, Na_2HA and Na_3A, the species present in the buffer solutions at different pH = 5.5 are calculated to be about: H_2A^- 10%; HA^{2-} 80%; A^{3-} 10%.

Therefore, for the 10 mM buffer solution at pH = 5.5 the concentrations of the ionic species are: $[H_2A^-]$ = 1 mM; $[HA^{2-}]$ = 8 mM; $[A^{3-}]$ = 1 mM; $[Na^+]$ = 1 + 8·2 + 1·3 = 20 mM. The ionic strength is here:

$$J = \frac{1}{2}\left(1\cdot 1^2 + 8\cdot 2^2 + 1\cdot 3^2 + 20\cdot 1^2\right)\cdot 10^{-3} = 3.1\cdot 10^{-2}\,M$$
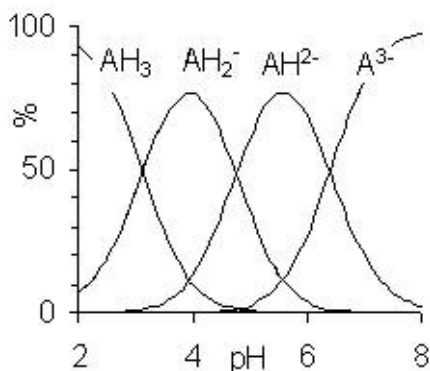
Figure 1. Species distribution versus pH calculated for a 10 mM solution of citric acid (AH_3) pK_{a1}=3.13, pK_{a2} = 4.76, pK_{a3}=6.40 and citrates.

By adding 0.15 M NaCl solution (0.5 mL), J = 0.15, to 2 mL buffer solution, the ionic strength becomes: $J = \dfrac{2}{2.5}3.1\cdot 10^{-2} + \dfrac{0.5}{2.5}\cdot 0.15 = 5.48\cdot 10^{-2}\,M$.

Solid surface characteristics. The following surfaces were used for antibody adsorption: freshly cleaned optically polished glass plates, and modified glass (positively charged glass - enriched in Al^{3+} ions, and amino silanized glass). It is known that glass plates in contact with water are negatively charged. The point of zero charge, i.e. the pH at which the surface density of positive charges is equal to the surface density of negative charges, for silica is around pH 2 to 3 [19, 20], that is at higher pH values the solid surface is negatively charged [21]. The same should apply to glass surfaces.
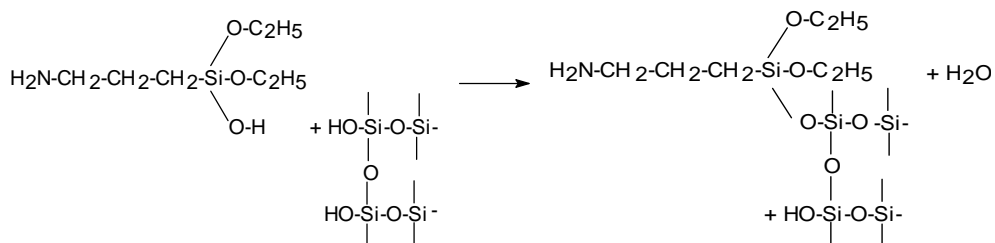
The chemical reactions describing amino silanization are [22]:
- the partial hydrolysis of the aminosilan with traces of water in the solvent (Scheme 1):

$$H_2N\text{-}CH_2\text{-}CH_2\text{-}CH_2\text{-}Si\substack{\diagup O\text{-}C_2H_5 \\ \text{-}O\text{-}C_2H_5 \\ \diagdown O\text{-}C_2H_5} + H_2O \longrightarrow H_2N\text{-}CH_2\text{-}CH_2\text{-}CH_2\text{-}Si\substack{\diagup O\text{-}C_2H_5 \\ \text{-}O\text{-}C_2H_5 \\ \diagdown O\text{-}H} + C_2H_5OH$$
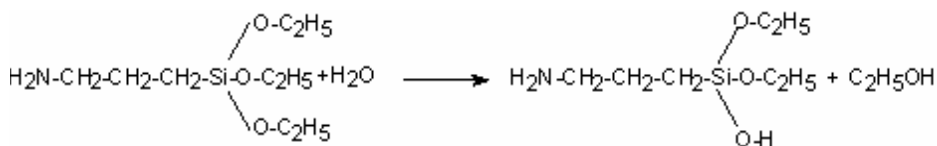
Scheme 1

- the binding on the glass surface (silicate ions) is given in Scheme 2:

Scheme 2

Surface charge measurements indicated that aminosilanization converts the glass surface from negative to positive potentials at neutral pH values [23]. The equilibrium between protonated amine groups (NH_3^+) and amine group (NH_2) is characterized by the K_a value of the conjugated acid of the amine; this constant can be estimated as being of the order of magnitude of the known value for propylamine [21]: $pK_a \approx 10.2$. That means that for a pH value of 10.2 there are around 50% uncharged $–NH_2$ and 50% protonated $–NH_3^+$ groups. At lower pH values, most of the amine group are protonated, giving a net positive charge to the surface.

As it was shown, only 30 to 50% of silanol groups are grafted during silanization reaction [24], and thus on an aminosilanized glass (or silica) surface, there are likely to be present both amine and silanol (Si-OH) groups.

All the used surfaces are very hydrophilic (contact angle $\theta = 0^o$), except for amino silanized glass surfaces which are poorly wettable. For amino NH_3^+ terminated silane monolayers on silicon, a contact angle between $\theta = 42^o$ for completely ionized NH_3^+ groups (at low pH values) and $\theta = 62^o$ for non ionized NH_2 groups (at high pH values) was reported [25]. The corresponding values for amino silanized glass surfaces should be similar.

Characterization of the adsorbed antibody layers. The differences both in morphology and in the thickness of adsorbed antibody layers might arise from the different orientation of the molecules on the surface, but also from structural modification/deformation of adsorbed protein molecules associated with different electrostatic interactions (attractions or repulsions) between antibody molecules within the antibody layers as well as among the antibody molecules and the solid surface. In order to evidence the influence of different factors on the surface morphology and molecular orientation of the

154

antibody molecules adsorbed on various solid supports, the height and roughness (RMS) of adsorbed layers obtained from antibody solutions, estimated from AFM images, are presented in Table 1.

Table 1. AFM characterization of anti-C1q antibody layers adsorbed on different solid surfaces at pH = 5.5 (scanned area 0.5 μm x 0.5 μm).

Fig.	J mol/L	Solid surface	Conc. mg/L	Height Å	RMS on area
2	0.031	Silanized glass	2	40-54	1.1
3	0.055	Silanized glass	1.6	40	0.7
4	0.031	Positively charged glass	2	40-53	1.6
5	0.055	Positively charged glass	1.6	40	0.9
6	0.055	Glass	1.6	42	0.7

The antibody adsorption was performed at three bulk antibody concentrations, at about 0.9, 1.6 and 2 mg/L in aqueous buffer solutions. An analysis of AFM images showed that the antibody adsorption reached a steady state saturation of the solid surface within 2 hours at 20 ^{o}C, in substantial agreement with its adsorption carried out for comparison at 17 hours at 4 ^{o}C. This is also in general agreement with data reported for the adsorption of other proteins (e.g. storage protein from aleurone cells of barley) on solid surfaces [26, 27]. Thus, even at low bulk concentration this antibody exhibits a quite high affinity to solid surfaces used.

Typical AFM images of antibody adsorption on *amino silanized glass surface* from a 2 mg/L solution (J = 0.031 M) are given in Fig. 2. For the same surface, but with a 1.6 mg/L antibody solution (J = 0.055 M), AFM images are given in Fig. 3. The main feature of the adsorbed layer is the almost uniform distribution of antibody particles on the silanized glass surface (Figs. 2 and 3; panels: a, b, c, d). The analysis of representative cross section profiles (Fig. 2e and 3e) show that the antibodies films are about 40 to 54 Å high (Table 1). The antibody particles have lateral dimensions typically in the range of 15 to 30 nm.

The anti C1q antibody belongs to the same type IgG1 as the mouse monoclonal antibody, anti-β-hCG [28]. For anti-β-hCG antibody on the basis of the X-ray crystallographic molecular dimensions of 3.8 x 8.5 x 14.2 nm [28-31] are given. For fibrinogen molecules the corresponding data are 4.5 x 4.5 x 47 nm [28, 32-34]. Considering that the size of anti-C1q antibody is close to the anti-β-hCG antibody, it is reasonable to suggest that the observed antibody particles are predominantly monomers. The scan height of about 4 nm for anti-C1q antibody molecules is closed to the short axial length of 3.8 nm of the antibody molecule. This finding reveals that antibody molecules adsorbed in the flat-on orientation with the antibody molecules lying flat on the solid surface. However some particles are larger and could have a certain declivity toward the surface. An almost compact
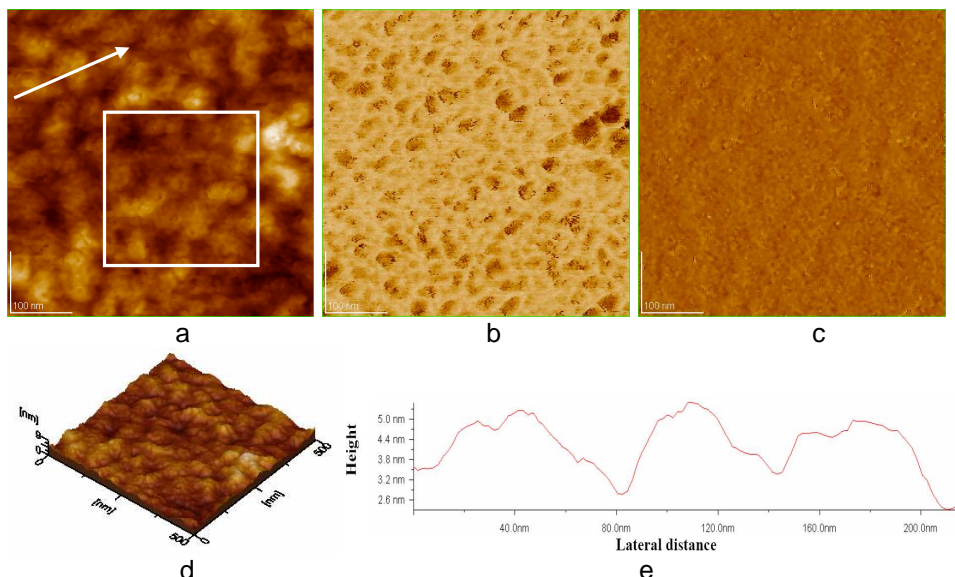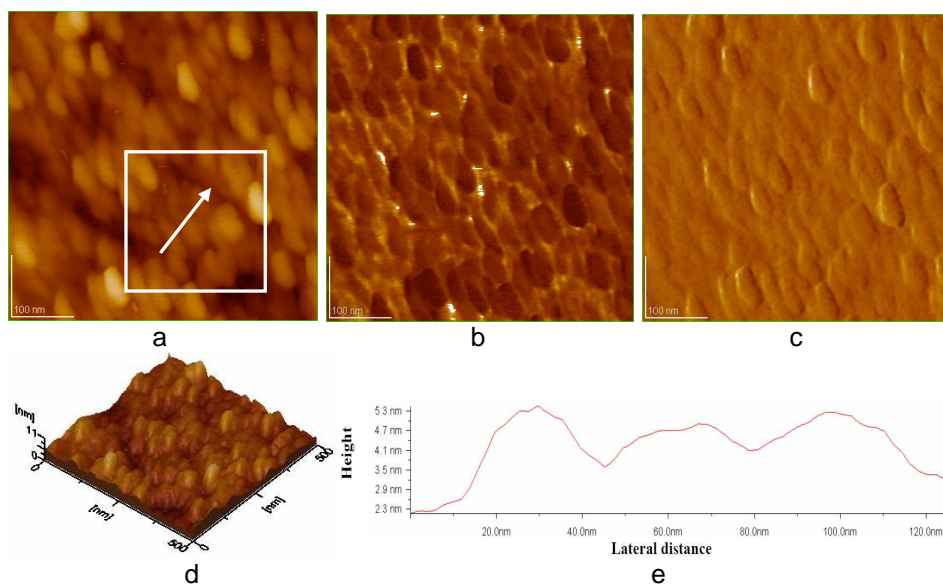
Figure 2. AFM images for antibody adsorbed on silanized glass from 2 mg/L antibody solution, J ≈ 0.031 M: a) 2D – topography; b) phase image; c) amplitude image; d) 3D-topography; e) profile of the cross section along the arrow in fig. (a).
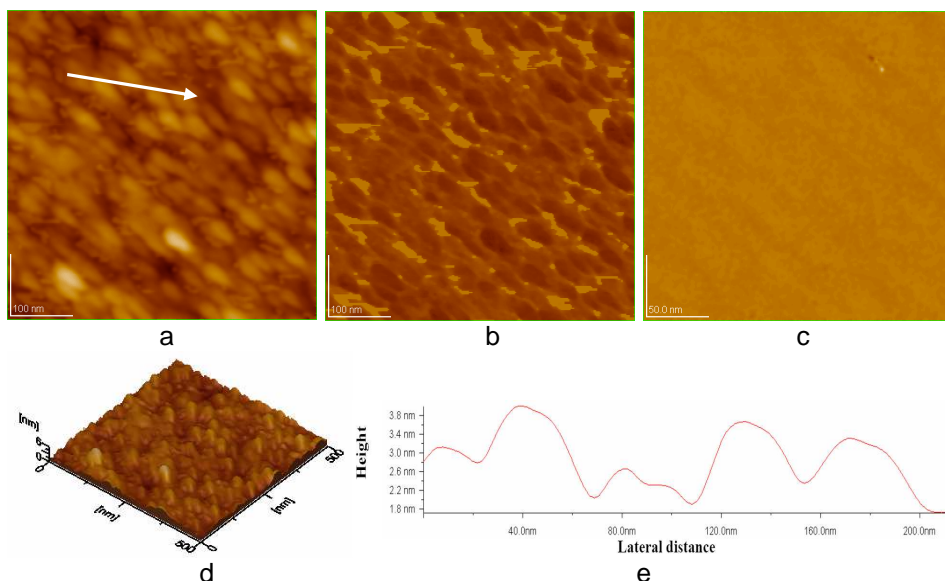
Figure 3. AFM images for antibody adsorbed on silanized glass from 1.6 mg/L antibody solution, J ≈ 0.055: a) 2D – topography; b) phase image; c) amplitude image; d) 3D-topography; e) profile of the cross section along the arrow in fig. (a).

layer of random orientations results, with representative granular structure in substantial agreement with the adsorption of IgG protein on silanized mica surface [35].

In the case of the *positively charged glass surface*, enriched in Al^{3+} ions (Figs. 4 and 5), the observed heights (Table 1) are similar to those for the amino silanized surface, both for 0.031 M and 0.055 M ionic strength, suggesting that antibody molecules form a monolayer of rather "lying flat" molecular orientation.

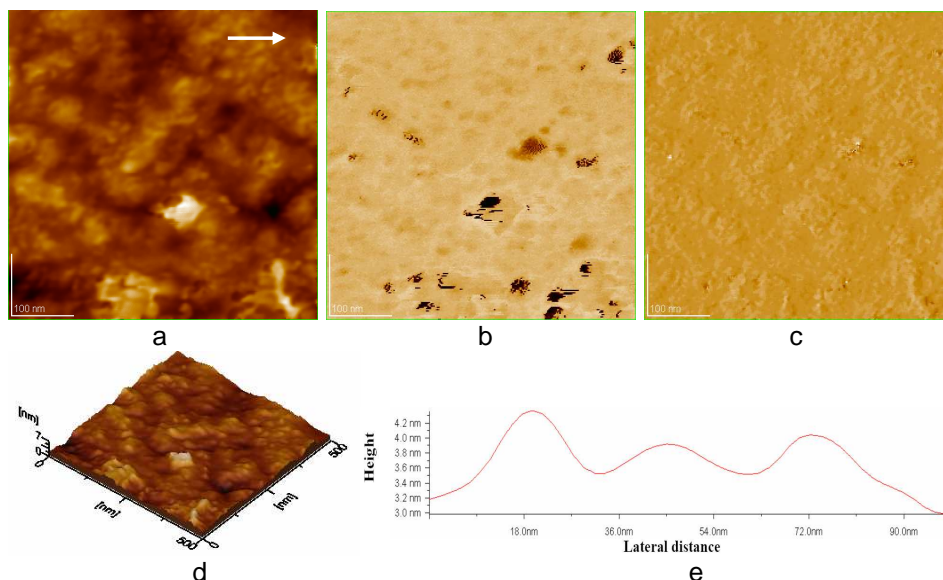**Figure 4**. AFM images for antibody adsorbed on glass (positively charged) from 2 mg/L antibody solution, J ≈ 0.031: a) 2D – topography; b) phase image; c) amplitude image; d) 3D-topography; e) profile of the cross section along the arrow in fig. (a).

Generally, it is found that at the isoelectric point, where the net charge of the antibody is zero, the *Fab* fragments will still carry positive charge while the *Fc* fragment will carry negative charge [36-38], and therefore the antibody molecule has a nonzero dipole moment. Physical adsorption is affected by several factors, such as van der Waals interaction, electrostatic interaction, hydrophobic effect, hydrogen bonding, pH values and ionic strength of the solution etc. A Monte Carlo simulation on models of antibody adsorption on charged surface [39] described the orientation of adsorbed antibody molecules as a result from the compromise between electrostatic and van der Waals interactions. The dipole moment of an antibody is an important factor for its orientation on charged surfaces when electrostatic interactions dominate. In this situation, on positively charged

solid surfaces the antibody molecules are oriented preferentially with the negative Fc "head" towards the surface, while on negatively charged surfaces the orientation with the positive Fab ends on the surface is preferred. These orientations are promoted by high surface charge density, high dipole moments of molecules and low solution ionic strength, where electrostatic interactions dominate. At low surface charge density and high solution ionic strength van der Waals interactions dominate, and the antibody molecules have a "lying-flat'' orientation on surfaces.
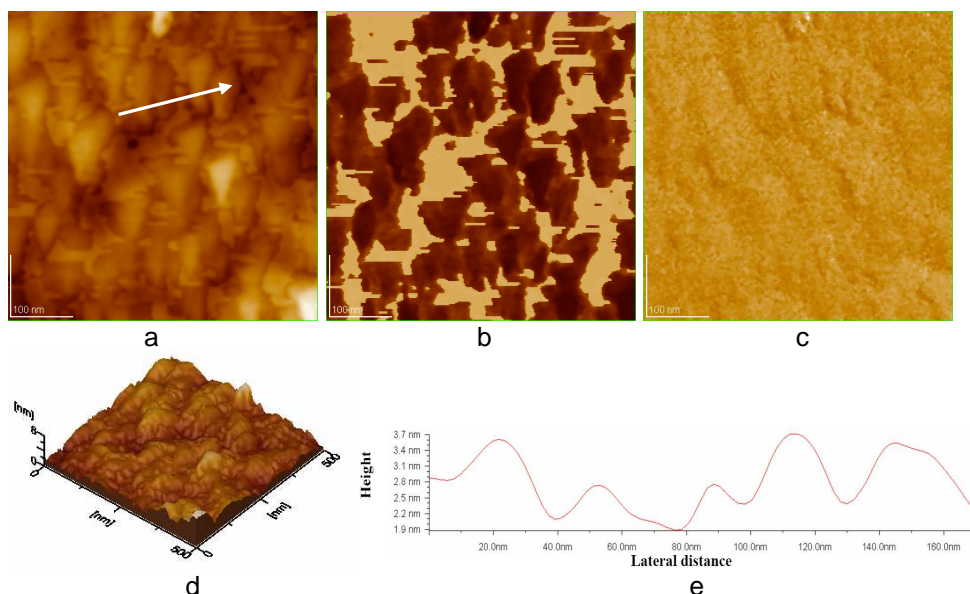
Figure 5. AFM images for antibody adsorbed on glass (positively charged) from 1.6 mg/L antibody solution, J ≈ 0.055: a) 2D – topography; b) phase image; c) amplitude image; d) 3D-topography; e) profile of the cross section along the arrow in fig (a).

Our results suggest that for the rather low positive charge densities on the modified glass surfaces and the quite high ionic strength of the solutions, the flat orientation is predominant. However, for the lower ionic strength (Figs. 2 and 4) both the height of the layers and their roughness (as measured by the RMS values of the adsorbed layers) are somewhat greater than for the higher ionic strength (Figs. 3 and 5) as expected from the above model.

The AFM images for the adsorbed anti-C1q antibody molecules on *glass surface* (Fig. 6), negatively charged, look very similar to the corresponding images for adsorption on positively charged glass and the height is also the same (Table 1). The orientation of the molecules should however be in this case with the Fab ends toward the surface ("head on"), but for the quite

high ionic strength of the buffer solution, the flat orientation given by van der Waals interactions dominates.

The model calculations [39] indicate that the intermolecular antibody-antibody interactions are much less important than antibody–solid surface interactions for the investigated systems, therefore protein–protein interactions do not significantly affect protein orientation even at high surface coverage and multilayer formation is not expected.

a   b   c

d   e

Figure 6. AFM images for antibody adsorbed on glass from 1.6 mg/L antibody solution, $J \approx 0.055$: a) 2D – topography; b) phase image; c) amplitude image; d) 3D-topography; e) profile of the cross section along the arrow in fig (a).

CONCLUSIONS

The interpretation of AFM images shows that anti-C1q monoclonal antibody adopts a flat on orientation with an average thickness of about 40 Å, when adsorbed on amino silanized glass, glass negatively charged or glass positively charged for isoelectric pH (about 5.5) of aqueous buffer solution of antibody, for used bulk concentrations of antibody 2 mg/L and 1.6 mg/L and at 0.031 M and 0.055 M ionic strengths. Only antibody monolayers seem to be formed on the used solid surfaces. At this isoelectric pH value, the anti-C1q antibody molecules are without net charge. Due to the uncharged antibody molecules, to the rather low surface charge density, and to the high ionic strength of the solutions screening the electrostatic interactions, these forces are not the dominant factor in controlling the adsorption and orientation of antibody molecules in this case. Van der Waals seems to play

159

here an important role in determining the orientation of adsorbed antibodies, as well as hydrogen bonding.

Thus, our data suggest that protein-solid surface attractive interactions, more than intermolecular protein-protein forces have a primary importance for molecular orientation within the adsorbed anti-C1q antibody layers. Further, the conformational changes induced in adsorbed anti-C1q antibody molecules due to the attractive interactions with the substrate might cause a distortion of the molecules.

Investigations at other pH values of the solution, where the antibody molecules bear a net positive (lower pH values than the isoelectric pH) or negative (higher pH values) charge will complete the study of the factors making possible the control of the orientation, and conformation of antibodies upon adsorption. This is of outstanding importance for the numerous applications of antibodies in biotechnology and clinical medicine, where the antibody is employed as a molecular recognition element that binds specifically to its antigen with high affinity and is often required to be immobilized on a solid support.

EXPERIMENTAL SECTION

The antibody used in this study was a mouse monoclonal anti-C1q. The antibody was purchased (Cat. No. A201) from Quidel Corporation (San Diego, CA, USA). It was used in 10 mM citric acid / sodium citrate buffer of pH value of 5.5. The ionic strength of the solution was adjusted by adding 150 mM NaCl solution. Three antibody concentrations were prepared, about 0.9, 1.6, 2 mg/L All chemicals used in the present work (citric acid, trisodium citrate, Na_2HPO_4, NaH_2PO_4, NaOH, NaCl) were of analytical reagent grade and used without further purification.

Prior to each adsorption experiment, the glass surface (plates with an area of 2x2 cm^2) was cleaned under known protocol, followed by strong rinsing with deionized water with resistivity bigger than 18 Mohm cm. Then, some clean glass surfaces were further modified as described bellow.

In order to obtain positively charged glass, the glass plates were washed with detergent, rinsed with water and dried. After this, they were washed again with chromic mixture, rinsed with a lot of water, and dried. In the next step, the glasses were immersed in a 2 mM solution of $Al(NO_3)_3$ at 90° C for 30 min. Afterwards, the glass plates were washed with deionized water and dried.

The silanization was made using aminopropyltriethoxysilane [22, 40, 41] as follows. The glass plates we cleaned as shown above. Later, the glasses we boiled with chromic acid for one hour and cooled slowly to the room temperature. The glass plates were washed extensively with bidistilated water

and dried at 100° C for 1 hour. Then, the glass plates were immersed in a 1 % solution of aminopropilethoxysilan in methanol (freshly prepared) at room temperature for one hour. Further, the glass plates were washed with methanol, treated with ultrasounds in methanol medium and dried for one hour at 100° C.

The antibody coating layers on the solid substrates were prepared by immersing the solid substrate vertically in the antibody aqueous solutions at room temperature for 2 hours or for 17 hours at 4 ^{o}C. After the adsorption (incubation) time, each sample was withdrawn and gently rinsed with deionized water and dried at room temperature, under a beaker and prepared for AFM investigation. As an alternative some samples were dried under a weak but stable nitrogen stream and then immediately subjected to AFM imaging. In the last situation, the drying took less than 0.5 min. As recently mentioned [28], such a short drying process does not provoke the antibody structural modifications or its surface aggregation.

Then, all samples were investigated by AFM in tapping mode, to minimize the force exerted from the scanning tip on the adsorbed antibody layers. The AFM imaging was performed on JEOL 4210 equipment. All measurements were performed in air at room temperature for high lateral image resolution. Standard cantilevers, non-contact conical shaped of silicon nitride coated with aluminum, were used. The sharpened tips were on cantilevers with a resonant frequency in the range of 200 - 300 kHz and with a spring constant of 17.5 N/m. AFM images were collected at a scan angle 0° and at a scan rate of about 1 Hz.

To unravel structural features, the antibody adsorbed layers were visualized from large scan area of 20 x 20 μm^2 to relatively small areas of 1x1 and 0.2 x 0.2 μm^2. AFM observations were repeated on different areas of the same film. The images were obtained from at least five macroscopically separated areas on each sample. All images were processed using the standard procedures for AFM. AFM images consist of multiple scans displaced laterally from each other in y direction with 512 x 512 pixels. All AFM experiments were carried out under ambient laboratory conditions (about 20 ^{o}C) as previously reported [26, 27, 42]. The AFM images on samples prepared in both drying procedures show no observable drying patterns under the experimental working conditions. This study is done under comparable surface packing density, at the same adsorption time (2 hours at room temperature), at quasi saturation of surface with antibody.

ACKNOWLEDGMENTS

REFERENCES

1. J. P. Gering, L. Quaroni, G. Chumanov, *Journal of Colloid and Interface Science*, **2002**, *252*, 50.
2. Q. Weiping, X. Bin, W. Lei, W. Chunxiao, Y. Danfeng, Y. Fang, Y. Chunwei, W. Yu, *Journal of Colloid and Interface Science*, **1999**, *214*, 16.
3. F. Caruso, E. Rodda, D. N. Furlong, *Journal of Colloid and Interface Science*, **1996**, *178*, 104.
4. N. H. Thomson, *Journal of Microscopy*, **2005**, *217*, 193.
5. A. S. Lea, A. Pungor, V. Hlady, J. D. Andrade, J. N. Herron, E. W. Voss, Jr., *Langmuir*, **1992**, *8*, 68.
6. J. N. Lin, B. Drake, A. S. Lea, P. K. Hansma, J. D. Andrade, *Langmuir*, **1990**, *6*, 509.
7. W. D. Marcus, H. Wang, S. M. Lindsay, M. R. Sierks, *Nanomedicine: Nanotechnology, Biology, and Medicine*, **2008**, *4*, 1.
8. L. S. Shlyakhtenko, B. Yuan, S. Emadi, Y. L. Lyubchenko, M. R. Sierks, *Nanomedicine: Nanotechnology, Biology, and Medicine*, **2007**, *3*, 192.
9. M. Targosz, A. Labuda, P. Czuba, R. Biedron, M. Strus, A. Gamian, J. Marcinkiewicz, M. Szymonski, *Nanomedicine: Nanotechnology, Biology and Medicine*, **2006**, *2*, 82.
10. B. Walivaara, A. Askendal, I. Lundstrom, P. Tengvall, *Journal of Colloid and Interface Science*, **1997**, *187*, 121.
11. R. M. MacCallum, A. C. R. Martin, J. M. Thornton, Journal of Molecular Biology, **1996**, *262*, 732.
12. R. Ghai, P. Waters, L. T. Roumenina, M. Gadjeva, M. S. Kojouharova, K. B. Reid, R. B. Sim, U. Kishore, *Immunobiology*, **2007**, *212*, 253.
13. A. J. Tenner, M. I. Fonseca, *Advances in Experimental Medicine and Biology*, **2006**, *586*, 153.
14. L. Truedsson, A. A. Bengtsson, G. Sturfelt, *Autoimmunity*, **2007**, *40*, 560.
15. H. Zanjani, C. E. Finch, C. Kemper, J. Atkinson, D. McKeel, J. C. Morris, J. L. Price, *Alzheimer Disease & Associated Disorders*, **2005**, *19*, 55.
16. J. E. Butler, L. Ni, R. Nessler, K. S. Joshi, M. Suter, B. Rosenberg, J. Chang, W.R.Brown, L.A. Cantarero, *Journal of Immunological Methods*, **1992**, *150*, 77.
17. E. Potlukova, P. Kralikova, *Scandinavian Journal of Immunology*, **2008**, *67*, 423.
18. L. Alderighi, P. Gans, A. Ienco, D. Peters, A. Sabatini. A. Vacca, *Coordination Chemistry Reviews*, **1999**, *184*, 311.
19. G.A. Parks, *Chemical Reviews*, **1965**, *65*, 177.
20. A. Carré, F. Roger, C. Varinot, *Journal of Colloid and Interface Science,* **1992**, *154*, 174.
21. A. Carré, V. Lacarrière, W. Birch, *Journal of Colloid and Interface Science,* **2003**, *260*, 49
22. J.A. Kiernan, Microscopy Today, **1999**, *99*, 22.
23. E. Metwalli, D. Haines, O. Becker, S. Conzone, C. G. Pantano, *Journal of Colloid and Interface Science,* **2006**, *298*, 825.

24. E.F. Vansant, P. Van der Voort, K.C. Vranken, „Characterization and Chemical Modification of the Silica", in: *Studies in Surface Science and Catalysis*, Vol. *93*, Elsevier, Amsterdam, **1995**.
25. A. Liebmann-Vinson, L. M. Lander, M. D. Foster, W. J. Brittain, E. A. Vogler, C. F. Majkrzak, S. Satija, *Langmuir*, **1996**, *12*, 2256.
26. M. Tomoaia-Cotisel, A. Tomoaia-Cotisel, T. Yupsanis, Gh. Tomoaia, I. Balea, A. Mocanu, Cs. Racz, *Revue Roumaine de Chimie*, **2006**, *51*, 1181.
27. M. Tomoaia-Cotisel, in: M. Zaharescu, E. Burzo, L. Dumitru, I. Kleps, D. Dascalu (Eds.), „Convergence of Micro-Nano-Biotechnologies", Romanian Academy Press, Bucharest, **2006**, pp. 147-161.
28. X. Wang, Y. Wang, H. Xu, H. Shan, J. R. Lu, *Journal of Colloid and Interface Science*, **2008**, *323*, 18.
29. E. W. Silverton, M. A. Navia, D. R. Davies, *Proceedings of the National Academy of Sciences of the USA*, **1977**, *74*, 5140.
30. J. Deisenhofer, *Biochemistry*, **1981**, *20*, 2361.
31. M. Marquart, J. Deisenhofer, R. Huber, W. Palm, *Journal of Molecular Biology*, **1980**, *141*, 369.
32. A. Toscano, M. M. Santore, *Langmuir*, **2006**, *22*, 2588.
33. P. Cacciafesta, A.D.L. Humphris, K. D. Jandt, M. J. Miles, *Langmuir*, **2000**, *16*, 8167.
34. K. L. Marchin, C. L. Berrie, *Langmuir*, **2003**, *19*, 9883.
35. H. X. You and C. R. Lowe, *Journal of Colloid and Interface Science*, **1996**, *182*, 586.
36. J. Buijs, W. Norde, J. W. T. Lichtenbelt, *Langmuir* **1996**, *12*, 1605.
37. J. Buijs, P. A. W. van den Berg, J. W. T. Lichtenbelt, W. Norde, J. Lyklema, *Journal of Colloid and Interface Science*, **1996**, *178*, 594.
38. F. Fogolari, R. Ugolini, H. Molinari, P. Viglino, G. Esposito, *European Journal of Biochemistry*, **2000**, *267*, 4861.
39. J. Zhou, H.-K. Tsao, Y.-J. Sheng, S. Jiang, *Journal of Chemical Physics*, **2004**, *121*, 1050.
40. O. Seitz, M. M. Chehimi, E. Cabet-Deliry, S. Truong, N. Felidj, C. Perruchot, S. J. Greaves, J. F. Watts, *Colloids and Surfaces A: Physicochemical and Engineering Aspects*, **2003**, *218*, 225.
41. J.A. Kiernan, "Histological and Histochemical Methods", 3rd ed. Butterworth-Heinemann, Oxford, **1999**.
42. O. Horovitz, Gh. Tomoaia, A. Mocanu, T. Yupsanis, M. Tomoaia-Cotisel, *Gold Bulletin*, **2007**, *40(4)*, 295.

Dedicated to Professor Liviu Literat, at his 80th anniversary

NO₂ DISPERSION PROCESS SIMULATION IN URBAN AREAS BY ANALITICAL-EXPERIMENTAL METHODS

DANA SILAGHI-PERJU[a], HARIETA PÎRLEA[b], GHEORGHIŢA JINESCU[c], GABRIELA-ALINA DUMITREL[b], DELIA PERJU[b]

ABSTRACT. In the current global context when the accent on environmental pollution problems are more and more pressing, the study of nitrogen dioxide emissions reduction possibilities as well as the modelling ways of the phenomenon that accompany the dispersion of this pollutant in its cycle in nature is current and of a particular importance. According to this approach, in the paper is presented a simulation method of nitrogen dioxide pollution level in a certain reference point. The contribution of each pollution source at the global pollution in that point is also specified.

Keywords: atmospheric pollution, NO₂ dispersion process, modelling, simulation

INTRODUCTION

It was determined that large cities are subjected to a higher degree of air pollution due to industrial activities, traffic and heating systems. Timişoara is a city that belongs to this category. Therefore, knowing the level of pollution, and, more precisely, the origin of pollution, is highly important for finding ways to reduce or counteract the negative effects that it induces.

In the following paper, simulation at a certain reference point of the pollution level by nitrogen dioxide is carried out, stating the percentage share held by each pollution source taken into consideration. In order to do this, concentrations of nitrogen dioxide were estimated at a certain reference point coming from: micro power plants, the two thermal power plants in

---

[a] *Universitatea POLITEHNICA din Timişoara, Facultatea de Inginerie Mecanică, Blv. Mihai Viteazu, Nr. 1RO-300222 Timişoara, Romania, dsilaghi@mec.upt.ro*

[b] *Universitatea POLITEHNICA din Timişoara, Facultatea de Chimie Industrială şi Ingineria Mediului, Piaţa Victoriei, Nr. 2, RO-300006 Timişoara, Romania, harieta.pirlea@chim.upt.ro*

[c] *Universitatea Politehnica Bucureşti, Facultatea de Chimie Aplicată şi Ştiinţa Materialelor, Str. Polizu, Nr. 1, RO-011061 Bucureşti, Romania, jinescu_gheorghita@yahoo.com*

Timişoara and road traffic. The reference point chosen in the study was set in the center of the town, on Mihai Viteazul Boulevard, at the headquarters of the Environmental Protection Agency Monitoring Laboratory Timişoara. This point was chosen due to the fact that here there have been made measurements of the concentrations of nitrogen dioxide by the Environmental Protection Agency Timişoara, and the values obtained, based on sets of mathematical models, were compared with the latter.

RESULTS AND DISCUSSION

In order to simulate the NO_2 dispersion processes in the urban area, the emissions coming from stationary and mobile sources were considered.

The stationary sources which were taken into account for this study are: micro power plants, and the city's two thermal power plants, CET Center and CET South. In the present paper, the generic "micro power plant" refers to the following sources of heat:

$\Rightarrow$ residential micro power plants - providing heat for homes,

$\Rightarrow$ small capacity industrial plants – providing heat in the industrial sector,

$\Rightarrow$ stoves that operate with gas.

The simplified assumptions used for the NO_2 emission estimation coming from micro power plants are:

- micro power plants were treated as 5 stationary point sources of pollution;
- all micro power plants were considered to be of medium class, without filters, having a 90% efficiency (Hermann type);

The algorithm used in the calculus of NO_2 emissions coming from micro power plants is presented in the Figure 1 [1]:
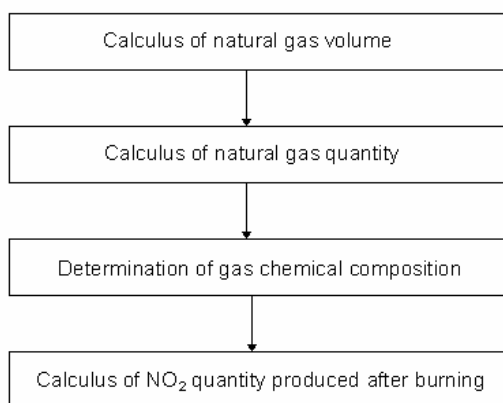
Figure 1. Algorithm used in the calculus of NO_2 emissions coming from micro power plants.

As concern the estimation of NO$_2$ emission coming from the two thermal power plants of the city, the simplified assumptions were:

- CET Center and CET South were studied as two stationary point sources of pollution;
- The NO$_2$ emission for each thermal power plant was calculated as the sum of NO$_2$ emissions coming from all power plant boilers.

The data coming from Colterm Timisoara, were generated according to the Romanian standards by EMPOL software [2-7].

The values of NO$_2$ emissions coming from the micro power plants and the two thermal power plants of the city were used in the Gaussian model [8,9] in order to compute, in the reference point, the concentrations of nitrogen dioxide emissions from the stationary sources for each day of the months: January, April, July and October 2004.

As a result of these data, there have been performed monthly averages, as presented in Table 1.

Table 1. Concentrations of NO$_2$ at the reference point, from the 7 stationary sources [µg/m^3]

Month	Conc. derived from micro power plants					Conc. derived from Cet's		NO$_2$ total conc
	North	South	East	West	Center	CET Center	CET South	
01	1.02E+00	1.17E-02	1.83E-02	1.03E+00	1.45E+00	3.49E+00	4.55E-02	7.06E+00
04	7.22E-10	6.96E-02	2.88E-02	9.33E-02	4.99E-05	4.92E-01	1.06E-02	0.69E+00
07	1.75E-09	1.27E-02	1.79E-03	1.08E-01	5.39E-06	1.65E-03	5.34E-04	0.13E+00
10	5.51E-09	4.61E-01	2.65E-01	2.44E-01	7.64E-04	1.12E+00	0.00E+00	2.09E+00

It has been determined that, at the reference point, the highest value of the concentration of nitrogen dioxide derived from stationary sources has been recorded in January. Of the stationary sources, CET Center is the source with the largest share of pollution in the city center. CET South has an almost undistinguishable influence, and, out of the micro power plants, the biggest influences have those situated in Centre and Western part of the town.

In Figure 2 a), b), c) and d), the percentage share that each of the 7 sources of pollution by nitrogen dioxide at the reference point is shown, derived from stationary sources.

January

a)

April

b)

July

c)

October

d)
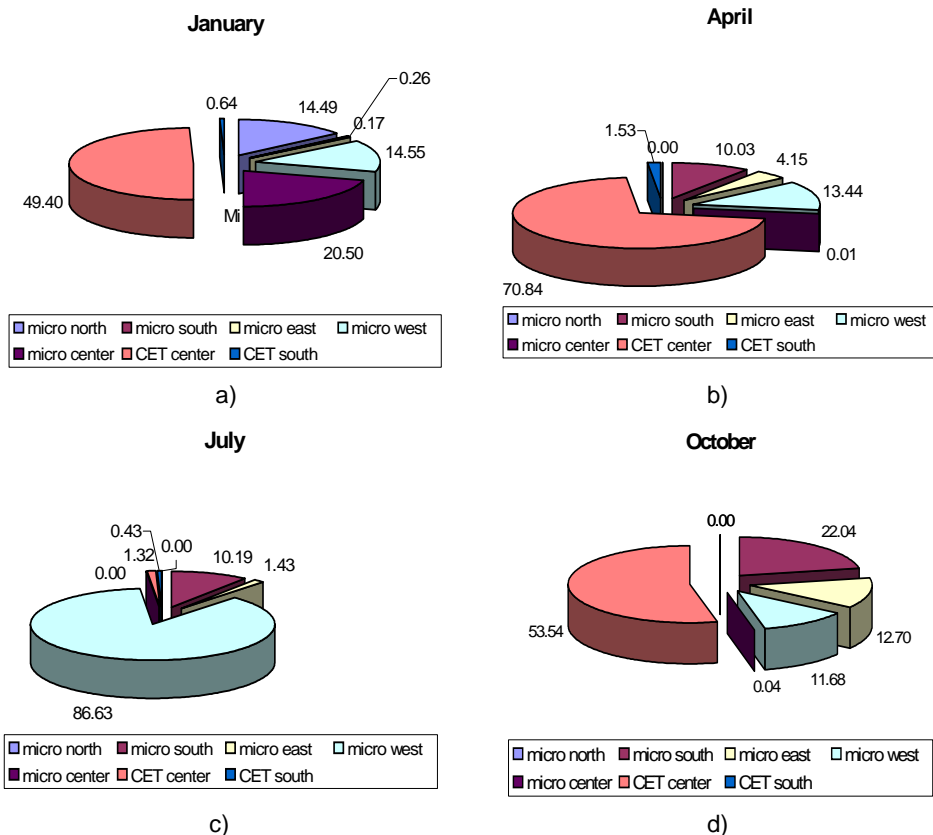
Figure 2. The percentage share held by each of the 7 stationary
pollution sources with nitrogen dioxide.

From Figure 2, it can be noted that in the months in which temperatures require the operation of the two thermal power plants, the largest share of pollution from the stationary sources comes from CET Center. The influence of the second thermal power plant is not significant because it is located outside the city and the preponderant direction of the wind in Timişoara is not towards the reference point taken into account.

By *mobile sources* one can understand all motorized means of transport, noted generically by "road traffic". The parameters needed to calculate the concentration of nitrogen dioxide at the reference point taken into account from mobile sources are:

• the quantitative emission of nitrogen dioxide coming from road traffic. In order to establish the value of this emission, it was considered that all of Timişoara's fleet and the transiting vehicles are equipped with EURO 3.

The current legislation provides that for cars equipped with EURO 3 the NO$_2$ emission standard is 0.5 [g/Km] [10].

• dispersion area volume. Since the emission standard estimated by specialized laws is expressed in [g/Km], it was necessary to establish an area of dispersion having a 1 Km length. It is known that the sensor for the analysis and detection of nitrogen dioxide is located at a height of 3 m. The device with which the measurements were made belongs to the Environmental Protection Agency Timişoara and it is located inside its Monitoring Laboratory. The width of the road in this area of the city is 15 m. Therefore, the area of dispersion is located on Mihai Viteazul Boulevard, also the site of the reference point taken into account, and has the following characteristics: length - 1 Km, width – 15 m, height – 3 m, thus the volume of dispersion is 45 000 m^3.

• the number of cars transiting the dispersion area taken into account in the time required the sensor to sample for an analysis. The sensor's time sequence is 60 s.

In order to estimate the concentrations of nitrogen dioxide emissions coming from mobile sources (road traffic) at the point of reference the relation (1) [8] was used:

$$C_r = \frac{N \cdot 10^6}{V} \cdot n \qquad (1)$$

where:

C$_r$ – the concentration of NO$_2$ in the reference point coming from traffic, [μg/m^3]

N – the European emission standard, [g / km], N = 0.5 g / km

V – volume of the dispersion area, [m^3], considered 45 000 m^3,

n – number of mobile sources [pcs].

The algorithm presented above was applied for the same months of 2004, as in the case of stationary sources. Out of the values obtained, monthly averages were made of the concentrations of nitrogen dioxide emissions from mobile sources (road traffic), and these are presented in Table 2. In calculating these values, the number of mobile sources was chosen according to the traffic specific of each month.

Table 2. Concentrations of NO$_2$ at the reference point, coming from road traffic

Month	Number of mobile sources/time sequence [pcs]	Concentrations of NO$_2$ at the reference point, coming from road traffic [μg/m^3]
January	6.5	72.22
April	4	44.44
July	2.25	25.00
October	3	33.33

One can notice that the concentrations values of nitrogen dioxide coming from road traffic at the reference point are considerably higher than from those coming from stationary sources.

The simulation of the pollution process by nitrogen dioxide in the city of Timişoara, at a given point of reference, is done by estimating the concentrations of nitrogen dioxide at that point of reference - described at the beginning of this paper, coming from stationary and mobile sources. For this, the balance equation was derived for this pollutant:

$$C_{ref} = C_1 + C_2 + C_3 + C_4 + C_5 + C_6 + C_7 + C_r \qquad (2)$$

where:

C_{ref} – total concentration of nitrogen dioxide in the reference point, $[\mu g/m^3]$.

C_1, C_2, C_3, C_4, C_5 – NO_2 concentration in the reference point resulted from the north, south, east, west and center microplants $[\mu g/m^3]$.

C_6, C_7 – NO_2 concentration in the reference point resulting from the Center CET and South CET, $[\mu g/m^3]$.

C_r – NO_2 concentration in the reference point resulting from the road traffic, $[\mu g/m^3]$

The total concentration of nitrogen dioxide at the point of reference for the months taken into consideration, calculated using a mathematical model [8] is presented in Table 3.

Table 3. The nitrogen dioxide concentrations values at the given global reference point

Month	NO_2 concentration in the reference point resulting from the stationary sources $[\mu g/m^3]$	NO_2 concentration in the reference point resulting from the road traffic $[\mu g/m^3]$	NO_2 concentration in the reference point $[\mu g/m^3]$
January	7.06	72.22	79.28
April	0.70	44.44	45.14
July	0.13	25.00	25.13
October	2.09	33.33	35.42

Comparing the influence of stationary and mobile sources on nitrogen dioxide pollution at the given reference point, it has been determined that mobile sources have an overwhelming weight in relation to the stationary ones (> 90%). In Figure 3 the share of stationary and mobile sources at NO_2 pollution globally at the given reference point is presented.

Influence of stationary and mobile sources on nitrogen dioxide pollution at the given reference point - January

9%

91%

☐ Stationary sources ■ Mobile sources

Influence of stationary and mobile sources on nitrogen dioxide pollution at the given reference point - April

2%

98%

☐ Stationary sources ■ Mobile sources

Influence of stationary and mobile sources on nitrogen dioxide pollution at the given reference point -July

0%

100%

☐ Stationary soures ■ Mobile sources

Influence of stationary and mobile sources on nitrogen dioxide pollution at the given reference point -October

6%

94%

☐ Stationary sources ■ Mobile sources

Figure 3. The share of stationary and mobile sources at NO$_2$ pollution at the reference point.

From the graph, one can notice that, in April and July, the stationary sources have a negligible influence on nitrogen dioxide pollution in the town center.

Testing the mathematical model accuracy has been achieved by comparing the results obtained by applying the model with the experimental ones, provided by the Environmental Protection Agency Timişoara (Table 4).

Table 4. Mathematical model testing

Month	Measured NO$_2$ concentration in the reference point [µg/m^3]	Calculated NO$_2$ concentration in the reference point [µg/m^3]	Relative error, %
January	81.48	79.28	2.70
April	50.00	45.14	9.72
July	28.11	25.13	10.60
October	31.23	35.42	-13.42

The small differences between the results as well as the values of relative errors confirm that the case study presented in this paper was properly addressed and the developed mathematical models characterize well enough the processes that accompany the NO_2 pollution phenomenon from Timisoara city.

CONCLUSIONS

At studied reference point, the major influence on nitrogen dioxide pollution is held by mobile sources. The share of this pollution is >90%.

Regarding the stationary sources, the largest share of nitrogen dioxide pollution is held by the micro power plants from the city center and CET Center.

By comparing the results of the mathematical model characterizing the global pollution with nitrogen dioxide with the experimental data, one can notice a good conformity between them, thus proving that the case study has been properly addressed.

REFERENCES

1. H. Pîrlea, D. Silaghi-Perju, D. Perju, C. Rusnac, *Revista de chimie*, **2006**, *57(7)*, 743.
2. Ordonanţă de urgenţă nr. 152 din 10 noiembrie 2005 privind prevenirea şi controlul integrat al poluării, **2005**.
3. Hotărâre Nr. 541 din 17 mai **2003** privind stabilirea unor măsuri pentru limitarea emisiilor în aer ale anumitor poluanţi proveniţi din instalaţii mari de ardere - cu modificările aduse de: Hotărârea Guvernului nr. 322/2005 şi Hotărârea Guvernului nr. 1502/**2006**.
4. Anexa la ordinul 462/**1993** - metodologia de determinare a poluantilor atmosferici produsi de surse stationare, Institutul de Cercetari si Ingineria Mediului - Splaiul Independentei nr. 294, sector 6, Bucuresti.
5. Ordinul Nr. 462 din 1 iulie **1993** pentru aprobarea Conditiilor tehnice privind protectia atmosferei si Normelor metodologice privind determinarea emisiilor de poluanti atmosferici produsi de surse stationare.
6. Colterm Timişoara, "Manual pentru centrale mari", metodologie internă, **1992**.
7. Directiva europeană privitoare la emisiile de gaze poluante (NO_x şi SO_x) din termocentrale – Large Combustion Plant (LPC) Directive (2001/80/EC), Official Journal of the European Union, **2001**, L. 309, 27/11/2001, 1.
8. D. Perju, H. Pîrlea, G.A. Brusturean, D. Silaghi-Perju, S. Marinescu, *Revista de chimie,* **2008**, *59 (10)*, 1112.
9. H. Pirlea, G.A. Brusturean, D. Silaghi Perju, D. Perju, *Chem. Bull. "Politehnica" Univ. Timişoara*, **2008**, *53(67)*, 244.
10. Directiva 98/69/EC a Parlamentului şi Consiliului European din 13 Octombrie **1998** privind măsurile măsurile ce trebuie luate împotriva poluării aerului cu emisii provenite de la autovehicule. Modifică Directiva Consiliului 70/220/EEC.

Dedicated to Professor Liviu Literat, at his 80th anniversary

CLUJ POLYNOMIAL DESCRIPTION OF TIO$_2$ NANOSTRUCTURES

ANIELA ELENA VIZITIU[a] AND MIRCEA V. DIUDEA[a]

ABSTRACT. Operations on maps are well known theoretical tools for transforming a given polyhedral tessellation. In this article, we propose a new method to design a titanium nanostructure. To describe the topology of such structures, we applied Cluj counting polynomial.

Keywords: TiO$_2$ nanostructures, molecular design, polynomial description

INTRODUCTION

After the discovery of carbon nanotubes many researchers addressed the question about the possible existence of nanotubular forms of other elements and they tried to obtain inorganic nanostructures [1-3]. Among numerous oxide nanostructures, the titanium nanotubular materials are of high interest due to their chemical inertness, endurance, strong oxidizing power, large surface area, high photocatalytic activity, non-toxicity and low production cost. The application of TiO$_2$ nanotubes to photocatalysis, in solar cells, as nanoscale materials for lithium-ion batteries and as gas-sensing material was discussed in the literature [4–10]. The nanotubes (TiO$_2$) were synthesized using various precursors [11–17], carbon nanotubes, porous alumina or polymer membranes as templates [8–24], fabrication by anodic oxidation of Ti [25–27], sol–gel technique [28–32] and sonochemical synthesis [33]. Models of possible growth mechanisms of titanium nanotubes are discussed [16, 17, 32] but the details of the atomic structure of the nanotube walls and their stacking mode are unknown. TiO$_2$ NTs are semiconductors with a wide band gap and their stability increases with increasing of their diameters. The numerous studies for the use of nanotubular titania in technological applications require a lot of theoretical studies of stability and other properties of such structures. Theoretical studies on the

---

[a] *Universitatea Babeş-Bolyai, Facultatea de Chimie şi Inginerie Chimică, Str. Kogălniceanu, Nr. 1, RO-400084 Cluj-Napoca, Romania, diudea@chem.ubbcluj.ro*

stability and electronic characteristics of TiO_2 nanostructures were presented in ref. [34, -36]. In the present paper we report a new method to design TiO_2 nanostructures using map operations, and then we describe their topology by the Cluj polynomial.

RESULTS AND DISCUSSION

Models and computational method

The titanium nanostructures can be achieved by map operations: the sequence consists of Du[Med(M)], applied on the polyhex tori or tubes (Figure 1).
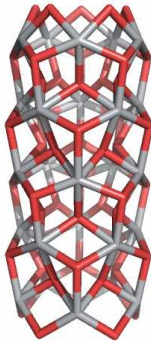
(a) Du[Med(TUH(8,8))]   (b) Du[Med(H832)]
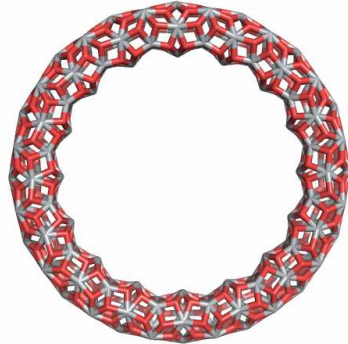
Figure 1. TiO_2 nanotube (a) and nanotorus (b).

A map M is a combinatorial representation of a (closed) surface [37,38]. Several transformations (*i.e.*, operations) on maps are known and used for various purposes.

Let us denote in a map: v – the number of vertices, e - the number of edges, f – the number of faces and d – the vertex degree. A subscript "0" will mark the corresponding parameters in the parent map.

Recall some basic relations in a map:

$$\sum d\, v_d = 2e \tag{1}$$
$$\sum s\, f_s = 2e \tag{2}$$

where v_d and f_s are the number of vertices of degree d and number of s-gonal faces, respectively.

174

Medial Me

Medial is achieved by putting new vertices in the middle of the original edges [38]. Join two vertices if the edges span an angle (and are consecutive within a rotation path around their common vertex in *M*). Medial is a 4-valent graph and *Me*(*M*) = *Me*(*Du*(*M*)), as illustrated in Figure 2. The transformed map parameters are:

$$Me(M): \quad v = e_0 \,; \ e = 2e_0 \,; \ f = f_0 + v_0 \tag{3}$$

The medial operation rotates parent *s*-gonal faces by π/s. Points in the medial represent original edges, thus this property can be used for topological analysis of edges in the parent polyhedron. Similarly, the points in dual give information on the topology of parent faces.
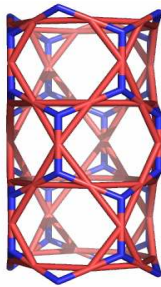
(a) (b)Me[TUH(8,4)]   (b)Me[H(8,8)]
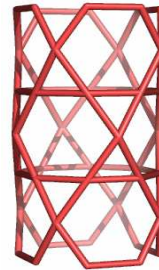
Figure 2. Medials of a polyhex nanotube.

Dual Du

The dualization of a map starts by locating a point in the center of each face. Next, two such points are joined if their corresponding faces share a common edge. It is the (Poincaré) *dual Du*(*M*). The vertices of *Du*(*M*) represent the faces of *M* and *vice‑versa* [38].

Figure 3. The duals of the Platonic polyhedra.

175
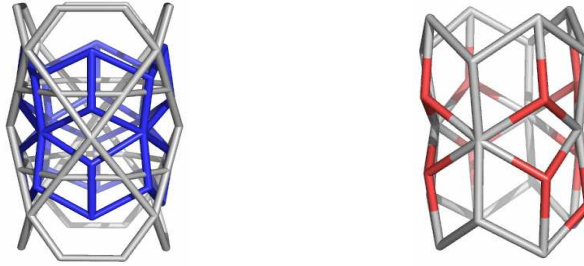
Figure 4. The dual of medial of a polyhex nanotube.

In the transformed map, the following relations exist:

$$Du(M): \ v = f_0; \ e = e_0; \ f = v_0 \tag{4}$$

Dual of the dual returns the original map: $Du(Du(M)) = M$. Tetrahedron is self dual while the other Platonic polyhedra form pairs: Du(Cube) = Octahedron; Du(Dodecahedron) = Icosahedron (Figure 3). The dual of medial of a polyhex nanotube will give a (4(3,6)) net which essentially correspond to the TiO2 lattice (Figure 4).

Cluj polynomial

Cluj polynomials are defined on the basis of Cluj matrices as:

$$CJ(G, x) = \sum_k m(G, k) \cdot x^k \tag{5}$$

They count the vertex proximity of the vertex i with respect to any vertex j in G, joined by an edge $\{p_{e,i}\}$ (the Cluj-edge polynomials) or by a path $\{p_{p,i}\}$ (the Cluj-path polynomials), taken as the shortest (distance DI) or the longest (detour DE) paths. In Equation (5), the coefficients $m(G, k)$ are calculated from the entries of Cluj matrices.
The summation runs up to the maximum $k = |\{p\}|$ in G.

A Cluj fragment, [39-43] $CJ_{i,j,p}$, collects vertices v lying closer to i than to j, the endpoints of a path $p(i,j)$. Such a fragment collects the vertex proximity of i against any vertex j, joined by the path p, with the distances measured in the subgraph $D_{(G-p)}$, as shown in the following equation:

$$CJ_{i,j,p} = \left\{ v \middle| v \in V(G); D_{(G-p)}(i,v) < D_{(G-p)}(j,v) \right\} \tag{6}$$

176

In graphs containing rings, more than one path could join the pair (*i, j*), resulting in more than one fragment related to *i* (with respect to *j* and a given path *p*). The entries in the Cluj matrix are taken, by definition, as the maximum cardinality among all such fragments:

$$[\mathbf{UCJ}]_{i,j} = \max_{p} \left| CJ_{i,j,p} \right| \tag{7}$$

In trees, due to the unique nature of paths joining any two vertices $CJ_{i,j,p}$ represents the set of paths going to *j* through *i*. In this way, the path *p(i,j)* is characterized by a single endpoint, which is sufficient for the unsymmetrical matrix UCJ. When the path *p* belongs to the set of distances *DI*(*G*), the suffix DI is added to the name of matrix, as in **UCJDI**. When path *p* belongs to the set of detours *DE*(G), the suffix is DE. The Cluj matrices are defined in any graph and, except for some symmetric graphs, are unsymmetrical and can be symmetries by the Hadamard multiplication with their transposes:

$$\mathbf{SM_p = UM \bullet (UM)^T} \tag{8}$$

If the matrices calculated on edges (*i.e.*, on adjacent vertex pairs) are required, the matrices calculated from paths must be multiplied by the adjacency matrix **A** (which has the non-diagonal entries of 1 if the vertices are joined by an edge and, otherwise, zero)

$$\mathbf{SM_e = SM_p \bullet A} \tag{9}$$

The Cluj polynomials published previously [44] referred to some partitions of the Cluj matrices given by the layer/shell matrices, and provide no direct interpretation of the counting content.

The polynomial coefficients are counted from the Cluj matrices by the TOPOCLUJ software program [45] and also by a simple routine for collecting the entries in the unsymmetrical matrices **UCJ**. In the case of the *CJDI$_e$* polynomial, an orthogonal edge-cutting procedure can be used [46]. The same procedure has been used by Gutman and Klavžar to calculate the Szeged index of polyhex graphs [47].

Cluj polynomial in Tio$_2$ nanotori

Cluj polynomial in non-twisted toroidal TiO$_2$ structures is composed by two terms, according to the proximities at the two ends of the edges (in a bipartite graph), which are topologically equivalent. Examples and formula for calculating CJ polynomial are given in Table 1. Observe there is no difference in CJ polynomial for the two different embeddings: H and V, in Diudea's nomenclature [48].

Table 1. Data for the non-twisted toroidal TiO_2 structures and analytical formula of Cluj CJ_e

Tori H	CJ_e Polynomial	ToriV	CJ_e Polynomial
H[10,10]	$300x^{70}+300x^{80}$	V[10,10]	$300x^{70}+300x^{80}$
H[10,20]	$600x^{145}+600x^{155}$	V[10,20]	$600x^{145}+600x^{155}$
H[8,8]	$900x^{220}+900x^{230}$	V[10,30]	$900x^{220}+900x^{230}$
H[12,12]	$192x^{44}+192x^{52}$	V[10,50]	$1500x^{370}+1500x^{380}$
H[10,60]	$432x^{102}+432x^{114}$	V[10,70]	$2100x^{520}+2100x^{530}$

$$CJ_e(G,x) = b_a \cdot x^{e_{ka}} + b_b \cdot x^{e_{kb}}$$

$$e_{ka} = e_1 \cdot k + (k-1)\cdot(c/2)$$

$$e_{kb} = e_{ka} + c$$

$$e_1 = c^2 - (c/2)\cdot(c/2+1)$$

$$b = 3\cdot c\cdot n = b_a = b_b$$

$$k = n/c$$

CONCLUSIONS

A new method for designing TiO_2 nanotubular structures, based on map operations, was proposed. Cluj polynomial description proved to be a good tool for searching the topology of a nanostructure, particularly nanostructures of titania. Omega polynomial description of such nanostructures will be presented in a future paper.

ACKNOWLEDGEMENTS

REFERENCES

1. R. Tenne, *Chem. Eur. J.*, **2002**, *8*, 5296
2. C. N. R. Rao, M. Nath, *Dalton Trans.* **2003**, *1*, 1.
3. G. R. Patzke, F. Krumeich, R. Nesper, *Angew. Chem., Int. Ed.* **2002**, *41*, 2447.
4. H. Imai, M. Matsuta, K. Shimizu, H. Hirashima, N. Negishi, *Solid State Ionics*, **2002**, *151*, 183.
5. M. Adachi, Y. Murata, I. Okada, S. Yoshikawa, *J. Electrochem. Soc.* **2003**, *150*, G488.
6. Y. Zhou, L. Cao, F. Zhang, B. He, H. Li, *J. Electrochem. Soc.* **2003**, *150*, A1246.

7. O. K. Varghese, D. Gong, M. Paulose, K. G. Ong, C. A. Grimes, *Sens. Actuators B*, **2003**, *93*, 338.
8. O. K. Varghese, D. Gong, M. Paulose, K. G. Ong, E. C. Dickey, and C. A. Grimes, *Adv. Mater.* **2003**, *15*, 624.
9. C. A. Grimes, K. G. Ong, O. K. Varghese, X. Yang, G. Mor, M. Paulose, E. C. Dickey, C. Ruan, M. V. Pishko, J. W. Kendig, A. J. Mason, *Sensors*, **2003**, *3*, 69.
10. G. K. Mor, M. A. Carvalho, O. K. Varghese, M. V. Pishko, C. A. Grimes, *J. Mater. Res.* **2004**, *19*, 628.
11. T. Kasuga, M. Hiramatsu, A. Hoson, T. Sekino, K. Niihara, *Adv. Mater.* **1999**, *11*, 1307.
12. S. Zhang, J. Zhou, Z. Zhang, Z. Du, A.V. Vorontsov, Z. Jin, *Chin. Sci. Bull.* **2000**, *45*, 1533.
13. G. H. Du, Q. Chen, R. C. Che, Z. Y. Yuan, L.-M. Peng, *Appl. Phys. Lett.* **2001**, *79*, 3702.
14. D.-S. Seo, J.-K. Lee, H. Kim, *J. Cryst. Growth* , **2001**, *229*, 428.
15. C.-H. Lin, S.-H. Chien, J.-H. Chao, C.-Y. Sheu, Y.-C. Cheng, Y.-J. Huang, C.-H. Tsai, *Catal. Lett.* **2002**, *80*, 153 .
16. B. D. Yao, Y. F. Chan, X. Y. Zhang, W. F. Zhang, Z. Y. Yang, N. Wang, *Appl. Phys. Lett.* **2003**, *82*, 281.
17. W. Wang, O. K. Varghese, M. Paulose, C. A. Grimes, *J. Mater. Res.* **2004**, 19, 417.
18. J. Sun, L. Gao, Q. Zhang, *J. Mater. Sci. Lett.* **2003**, *22*, 339.
19. P. Hoyer, *Langmuir,* **1996**, *12*, 1411
20. H. Imai, Y. Takei, K. Shimizu, M. Matsuda, H. Hirashima, *J. Mater. Chem.* **1999**, *9*, 2971.
21. S. M. Liu, L. M. Gan, L. H. Liu, W. D. Zhang, H. C. Zeng, *Chem. Mater.* **2002**, *14*, 1391.
22. Y.-L. Shi, X.-G. Zhang, H.-L. Li, *Mater. Sci. Engin.* A, **2002**, *333*, 239.
23. X. H. Li, W. M. Liu, H. L. Li, *Appl. Phys. A*, **2003,** *80*, 317.
24. T. Peng, H. Yang, G. Chang, K. Dai, K. Hirao, *Chem. Lett.* **2004**, *33*, 336.
25. D. Gong, C. A. Grimes, O. K. Varghese, W. Hu, R. S. Singh, Z. Chen, E. C. Dickey, *J. Mater. Res.* **2001**, *16*, 3331.
26. O. K. Varghese, D. Gong, M. Paulose, C. A. Grimes, E. C. Dickey, *J. Mater. Res.* **2003**, *18*, 156.
27. G. K. Mor, O. K. Varghese, M. Paulose, N. Mukherjee, C. A. Grimes, *J. Mater. Res.* **2003**, *18*, 2588.
28. B. B. Lakshmi, P. K. Dorhout, and C. R. Martin, *Chem. Mater.* **1997**, *9*, 857.
29. T. Kasuga, M. Hiramatsu, A. Hoson, T. Sekino, K. Niihara, *Langmuir,* **1998**, *14*, 3160.
30. S. Kobayashi, K. Hanabusa, N. Hamasaki, M. Kimura, H. Shirai, *Chem. Mater.* **2000**, *12*, 1523.
31. M. Zhang, Y. Bando, K. Wada, *J. Mater. Sci. Lett.* **2001**, *20*, 167.
32. Y. Q. Wang, G. Q. Hu, X. F. Duan, H. L. Sun, Q. K. Xue, *Chem. Phys. Lett.* **2002**, *365*, 427.
33. Y. Zhu, H. Li, Y. Koltypin, Y. R. Hacohen, A. Gedanken, *Chem. Commun.* **2003**, 2616.

34. V. V. Ivanovskaya, A. N. Enyashin, A. L. Ivanovskii, *Mendeleev Comm.* **2003**, *13*, 5.
35. V. V. Ivanovskaya, A. N. Enyashin, A. L. Ivanovskii, *Russ. J. Inorg. Chem.* **2004**, *49*, 1.
36. A. N. Enyashin, G. Seifert, *Phys. Stat. Sol.* **2005** , 242, 7**,** 1361.
37. P. W. Fowler and T. Pisanski, *J. Chem. Soc. Faraday Trans.*, **1994**, *90*, 2865.
38. T. Pisanski and M. Randić, in *Geometry at Work*, (Ed. C. A. Gorini) M. A. A. Notes, **2000**, 53, 174.
39. M.V. Diudea, I. Gutman, L. Jäntschi, *Molecular Topology*. Nova Science, Huntington, New York, 2001.
40. M. V. Diudea, Cluj Matrix Invariants. *J. Chem. Inf. Comput. Sci.* **1997**, *37*, 300.
41. M. V. Diudea, B. Parv, I. Gutman, Detour-Cluj Matrix and Derived Invariants. *J. Chem. Inf. Comput. Sci.* **1997**, *37*, 1101.
42. M. V. Diudea, G. Katona, I. Lukovits, N. Trinajstić, Detour and Cluj-Detour Indices. *Croat. Chem. Acta*, **1998**, *71*, 459.
43. D. Opris, M. V. Diudea, Peptide Property Modeling by Cluj Indices. *SAR/QSAR Environ. Res.* 2001, *12*, 159.
44. M. V. Diudea, Cluj Polynomials. *Studia Univ. "Babes-Bolyai"*, **2002,** *47*, 131.
45. O. Ursu, M. V. Diudea, TOPOCLUJ software program, Babes-Bolyai University, Cluj, **2005**; Available, on line at http://chem.ubbcluj.ro/~diudea.
46. M. V. Diudea, A. E. Vizitiu, D. Janežič, Cluj and related polynomials applied in correlating studies, *J. Chem. Inf. Model.*, **2007**, *47(3),* 864.
47. I. Gutman, S. Klavzar, An Algorithm for the Calculation of the Szeged Index of Benzenoid Hydrocarbons. *J. Chem. Inf. Comput. Sci.* **1995**, *35*, 1011.
48. M. V. Diudea, in: M. V. Diudea, Ed., Nanostructures-Novel Architecture, NOVA, New York, **2005**, 111.

Dedicated to Professor Liviu Literat, at his 80th anniversary

WATER ACTIVITY – INDICATOR OF FOOD SAFETY AND THE FACTORS THAT INFLUENCE THE BIOCHEMICAL STABILITY OF SOFT DRINKS

MIREL GLEVITZKY[a], DELIA PERJU[b], GABRIELA-ALINA DUMITREL[b], MARIA POPA[c], MIHAELA LAURA VICĂ[a]

ABSTRACT. The aim of this paper is to evaluate the water activity value of different food products, as well as to test the different functional ingredients and the best preserving conditions that inhibit the development of microorganisms in soft drinks – the analysed products that have the highest a_w value. Using the experimental data, a sensitivity analysis with respect to water activity was performed. According to this analysis, the paper suggests the using of water activity value as indicator that ensure the sanitation of soft drinks.

Keywords: water activity, soft drinks, microbiology, HACCP

INTRODUCTION

The moisture of foods is an important factor for the products stability or shelf-life. The limitations of water content measurement as an indicator of safety and quality are attributed to differences in the intensity which water associates with other components in the product [1].

The osmotic pressure of food products can be measured by their water activity (a_w) and is expressed as it follows:

$$a_w = \frac{p}{p_0} = \frac{ERH[\%]}{100} \qquad (1)$$

p – water-vapour pressure above the product surface at the given T temperature, [N/m^2];

[a] *Direcţia Sanitar-Veterinară şi Siguranţă Alimentară Alba, Str. Lalelelor, Nr. 7A, RO-510217 Alba Iulia, Romania, glevitzky-alba@ansv.ro*
[b] *Universitatea POLITEHNICA din Timişoara, Facultatea de Chimie Industrială şi Ingineria Mediului, Piaţa Victoriei Nr. 2, RO-300006 Timişoara, Romania, alina.brusturean@chim.upt.ro*
[c] *Universitatea "1 Decembrie 1918" din Alba Iulia, Facultatea de Ştiinţe, Str. Nicolae Iorga, Nr. 11-13, RO-510009 Alba Iulia, Romania, mpopa@uab.ro*

p_0 – water-vapour pressure above the surface of pure water at the product temperature, [N/m^2].

a_w reflects the amount of free water in food products, which is available to microorganisms for chemical reactions, biochemical reactions, transfer of metabolites through the cell's layers [1]. It corresponds to the equilibrium relative humidity, ERH [%] at the T temperature.

By measuring and controlling the water activity, it is possible to predict and identify the type of microorganism which could be a potential source of degradation and infection [2, 3].

The biological stability of soft drinks is influenced by: the level of initial contamination, the chemical composition of the drink, the thermal treatment, the preservatives adding and the storage temperature [4].

The decrease of the water activity value delays the growth of the microorganisms, it slows down the enzyme catalyzed reactions and eventually delays the non-enzymatic browning. Another possibility for decreasing a_w and thus for increasing the food shelf life is the use of additives with a higher capacity of keeping the water (sodium, sugar) [1].

Microorganisms develop within large pH limits. When the pH is acid (values of pH<4.5), a small number of microorganisms develops, which can be stopped by thermal treatment [5, 6].

The pH value of soft drinks influences the growing of the microorganisms. The acidifying process - by adding acids - is used in preserving many different types of foodstuffs. The citric acid is one of the acids used to reduce the pH level of soft drinks [7].

It has been identified that the three primary factors controlling the microbial growth are water activity, temperature and pH [8]. Starting from these findings mathematical models were developed in order to predict the combined effect of temperature, pH and water activity on the growth rate of bacteria [9, 10].

The FDA's Good Manufacturing Practice Regulations incorporates water activity guidelines in defining food safety regulation. In food industry, a science based system - Hazard Analysis and Critical Control Points (HACCP) identifies where hazards might occur in the process and puts into place actions to prevent the hazards from occurring.

The purpose of this study is to measure the water activity values and to correlate them with the growth of microorganisms in fruit juices and the presence of different additive substances with preservative proprieties.

EXPERIMENTAL SECTION

Foodstuffs present on the Romanian market were used (Fruttia orange nectar, Crimbo bacon, Miacarn salami, Unirea margarine, FCOJ MTrade Juice, white flour of 000 PF Brudar type, Mib Prodcom strawbery jam, Florisa

honey, Price nuts, spices–Mix Vegetal, Cazan pasta, powder eggs, Mio Delicia cookies, toast and powder milk). For each product the a_w was determined.

In order to test the factors that can lead to the decrease of the water activity value, the product with the highest water activity was chosen from the list of the tested products (the soft drink with fruit content – Fruttia orange nectar).

In order to test the influence of the ingredients on the water activity, 7 soft drinks with 50% fruit content were prepared. In the composition of the 7 samples, along with 93.12 g/l orange concentrate, respectively deionized water, the ingredients presented in Table 1 were also added:

Table 1. Ingredients used in preparing the soft drinks with 50% fruit content

Sample	Ingredients	Quantity, g/l
1	(control sample)	-
2	Sugar syrup 65^{0}Brix	120.22 (crystal sugar 78 g)
3	Fructose	50
4	Lemon concentrate	1.2
5	Citric acid sol. 50%	1.6
6	Sodium benzoate	0.15
7	Potassium sorbate	0.15

The ingredients were added under stirring and pasteurized for 30 seconds at 85^{0}C. The each of 7 samples was divided in 4 fractions that were bottled in cold conditions in PET bottles. One fraction (which contains the 7 samples) was immediately analyzed after the bottling, t_{0h}, and the others were kept for 48 hours in closed bottles as it follows: refrigerating (+5^{0}C), at room temperature (+25^{0}C) and in a drying oven at +40^{0}C. All the samples were brought before the analyses at the room temperature.

The water activity (a_w) was determined with the Aquaspector apparatus AQS-2-TC [11] and the *pH* with the ph-metre WTW pH 340i and an electrochemical cell: Electrode SenTix 81. All the analyses were done three times, the final result being the average of the three analyses.

The yeast and the mould (Y&M) were determined through the following procedure: 1 mL of analyzed sample was transferred using a pipette into a Petri plate of 9 cm diameter. 15 ml of cultivation medium *Yeast-Glucose-Chloramphenicol-Agar* (Organics) melted and cooled to 45^{0}C were poured, mixing homogenously. Incubation took place at 25^0±1^{0}C for a period of 3-5 days. The yeasts and mould colonies grown on the cultivation medium could be easily detected on the entire surface of the Petri plate. Evaluation: absent/mL [12].

The total bacteria count (TCB) in the soft drinks with fruit content was calculated by introducing 1 ml of analysed sample into the Petri plate (9 cm in diameter), on which 12-15 ml of *Orange Serum Agar* (Merck) culture, melted and cold at 45^{0}C is added. The content is mixed up by stirring. The incubation is done at 30^{0}C for 72±2 hours. After incubation period all the colonies growth on the Petri plate are counted. Evaluation: maximum 30 CFU/ml [13].

The coliform bacteria (Colif.) were determined with the following procedure: 1 mL sample was transferred to a 9 cm-diameter Petri plate using a pipette. 12 ml of the cultivation medium *Violet red bile lactose agar (VRBL agar)* melted and cooled to 45^0C were poured, mixing homogenously. After the complete solidification of cultivation medium, 4 ml *VRBL agar* was added on the surface of existing medium. Incubation took place at $30^0 \pm 1^0$C for 24 ± 2 hours. The dark-red colonies with at least 0.5 mm diameter are counted. Evaluation: absent/mL [14].

RESULTS AND DISCUSSION

The values of the water activity for the studied food products are presented in Table 2, in a decreasing order of the water activity. This order was established on the basis of a qualitative sensitivity analysis [15].

Table 2. Values of the water activity index for different types of food

No.	Food	Water activity, a_w
1.	Fruttia orange nectar	0.951
2.	Crimbo bacon	0.942
3.	Miacarn salami	0.908
4.	Unirea margarine	0.887
5.	FCOJ MTrade Juice	0.813
6.	000 PF Brudar white flour	0.854
7.	Mib Prodcom strawberry jam	0.796
8.	Florisa honey	0.688
9.	Price nuts	0.639
10.	Mix Vegetal spices	0.504
11.	Cazan pasta	0.481
12.	Powder eggs	0.427
13.	Mio Delicia cookies	0.350
14.	Toast	0.336
15.	Powder milk	0.292

The effect of the ingredients used for preparing the soft drinks was studied both by analysing the physico-chemical parameters: a_w and pH (Table 3) and by microbiological control of the samples (Table 4).

Table 3. The water activity value and the pH of the samples kept in different conditions

Sample	a_w				pH			
	t_{0h}	t_{48h}			t_{0h}	t_{48h}		
		$+5^0$C	$+25^0$C	$+40^0$C		$+5^0$C	$+25^0$C	$+40^0$C
1	0.945	0.947	0.997	0.950	3.802	3.761	3.714	3.608
2	0.934	0.953	0.986	0.980	3.737	3.587	3.612	3.400
3	0.925	0.932	0.983	0.963	3.734	3.694	3.445	3.413
4	0.910	0.916	0.947	0.924	3.387	3.390	3.328	3.232
5	0.907	0.909	0.922	0.913	3.314	3.245	3.293	3.155
6	0.911	0.914	0.918	0.917	3.701	3.640	3.681	3.464
7	0.906	0.910	0.914	0.910	3.694	3.461	3.440	3.406

The physico-chemical analyses performed immediately after preparation are presented comparatively to the ones carried out after 48 hours of keeping at different temperatures. According to the storage temperature, we can notice an increase of the a_w on the whole, but more emphasized at the samples kept at the room temperature. The pH values have a slight tendency to decrease in time.

Table 4. The result of the microbiological control of the samples kept in different conditions

Sample	$t_{0 h}$			$t_{48 h}$ (+5^{0}C)			$t_{48 h}$ (+25^{0}C)			$t_{48 h}$ (+40^{0}C)		
	Y&M	TCB	Colif.	Y&M	TCB	Colif.	Y&M	TCB	Colif.	Y&M	TCB	Colif.
1	>1000	>300	Abs	>300	4	Abs	>500	18	Abs	>1000	>1000	Abs
2	100	>300	Abs	25	Abs	Abs	64	>300	Abs	>300	>300	Abs
3	>300	40	Abs	48	Abs	Abs	100	50	Abs	>300	39	Abs
4	2	23	Abs	Abs	Abs	Abs	2	32	Abs	5	26	Abs
5	9	9	Abs	1	Abs	Abs	5	Abs	Abs	>300	1	Abs
6	4	18	Abs	Abs	2	Abs	4	3	Abs	>300	8	Abs
7	3	4	Abs	Abs	Abs	Abs	2	1	Abs	35	6	Abs

At room temperature and at higher temperatures (+40^{0}C) the enzymatic and microbiological reactions take place faster, which leads to the fast degradation of the samples, as compared to the refrigerated samples.

Sodium benzoate, potassium sorbate, citric acid or lemon concentrate delay the growth of the microorganisms. The experimental data show that pH and water activity values decrease when citric acid or lemon concentrate are added as acidifiants to the fruit juice (sample 4 and 5). The microbiological values, shown in Table 4, in correlation with water activity and pH values confirm that it's useful to add acidifiants and preservatives to the fruit juice.

The lemon concentrate (sample 4) - as a natural source of citric acid - can be used in juices with high content of fruit as a natural acidifier which also inhibit the microorganisms growth.

The soft drinks with fruit content have a reduced pH level and contain considerable amounts of carbohydrates (sample 2 and 3), so that they become favourable selective environments for yeast growth. The alterations can be due to the yeast and bacteria that can come from sugar or microbiota of soft drinks.

The quality management applications (TQM-total quality management) and the aspects related to food safety are at the moment a global concern that continues to increase due to their impact on international trade [16]. Thus, the HACCP system is based on preventing and reducing the risks and dependence on inspection and end-product testing [17]. A practical approach of the studies, involves a voluntary control of the stage corresponding to the storage of the end-product before bottling **by preparing the sheet that tests the water activity value a_w**. According to the obtained product and based on

the literature and history data (antecedents) the limiting value of a_w can be established in the company (regarding the studied soft drinks and taking into consideration the thermal treatment carried out, the maximum value of a_w was set at 0.910).

The plan for this new stage is presented in Table 5:

Table 5. The analysis and the evaluation of the hazards of the cooling/storage stage of the soft drinks

Hazard						Means of administration	Preventive/control measures	Document registration	Responsible
Type	Description	Acceptable level	G^4	F^5	R^6				
B^1	Y&M	30	Med	Low	2	PRP^7 Hygiene plan	-Respecting and monitoring the temperature conditions when it is cold and the water activity index ≤ 0.910 when it is stored -Sensor – specific calibration -Personal instruction	-Chart to monitor the water activity -PLC^8 memory	Production responsible
	Colif. bacteria	Abs	Med	Low	2				
	TCB	$2/cm^2$	Med	Low	2				
	Staphylococcus aureus	Abs	Med	Low	2				
C^2	Traces of washing powders / disinfectants	Abs	Low	Low	1				
F^3	Fitting remains	Abs	Low	Low	1	Maintenance plan			
	Hairs (from the operator)	Abs	Low	Low	1	Hygiene plan			
	Traces of vaseline / lubricant	Abs	Low	Low	1	Maintenance plan			
	Glass pieces	Abs	Med	Low	2				

B^1-biological, C^2-chemical, F^3-physical, G^4-gravity, F^5- frequency of appearance, R^6-risk, PRP^7-preliminary programme, PLC^8-Programme Logical Controller, Med-medium

The analysis of this plan leads to idea that the cooling/storage of soft drink constitutes PCC – critical control point with biological, chemical and physical risk for the safety of the food product, imposing monitoring at each charge. Based on this study, as well as on the analysis and evaluation of the hazards that may occur during the production of 50% fruit soft drinks, it has concluded that the cooling/storage stage of end-product must be integrated in the HACCP plan. Thus, a new phase of a_w monitoring is proposed in the flow sheet. It is presented in Figure 1.
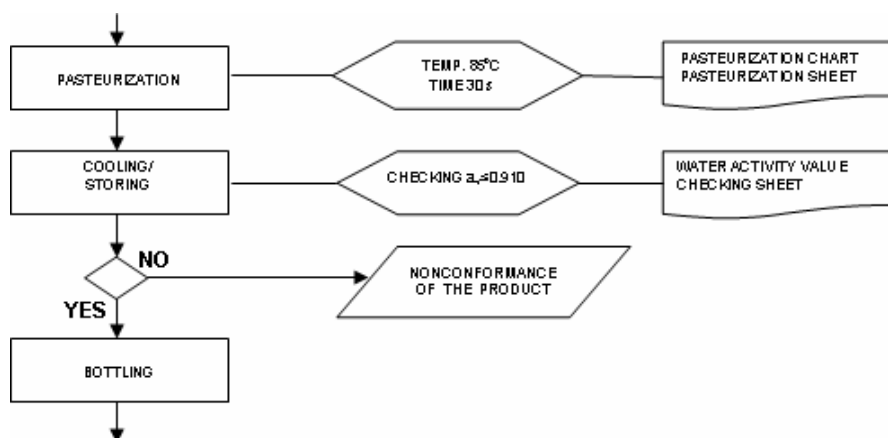
Figure 1. Flow sheet chart that include a_w monitoring.

The inconvenience of this flow sheet chart is that the final product that doesn't have the appropriate value of a_w is not recycled. The cyclicity of the process is not possible because the soft drink quality would be considerably reduced by another thermal treatment.

CONCLUSIONS

The acidifiers, such as citric acid and lemon concentrate, as well another known additives with preservative proprieties are inhibitors of the microorganisms growth. Their functionality is under the influence of product pH and the conservation temperature, factors which contribute to the stability of the drink. The water activity can be reduced by replacing sugar with fructose or artificial sweeteners.

The monitoring of the water activity value is favorable and adequate for using it as a general method for ensuring the sanitation of soft drinks. The control of free water amount constitutes the only practical mechanism for ensuring food safety.

REFERENCES

1. A. X. Lupea, "Transformări ale biocompuşilor procesaţi în scop alimentar", Publishing House CEP USM, Chişinău, **2004**, 299.
2. A. J. Fontana, "Water activity's role in food safety and quality", Deagon Devices, Washinton, accessed on: 01.02.**2007**.
3. M. Glevitzky, I. Bogdan, G.-A. Brusturean, D. Perju, D. Silaghi-Perju, *Revista de chimie,* **2008**, *59 (5),* 595.

4. V. Dan, "Microbiologia alimentelor" Publishing House Alma, Galați, **2001**, 175.
5. S.J. Forsythe, P.R. Hayes, "Food Hygiene, microbiology and HACCP", Aspen Publishers, Gaithersburg, Maryland, **1998**.
6. M.D. Ranken, R.C. Kill, C.G. Baker, "Food Industries Manual" 24th edition, Springer-Verlag, electronic release **2005**.
7. B.M. Lund, Tony C. Baird-Parker and all, "Microbiological Safety and Quality of food", vol I, II, Springer-Verlag, electronic release **2005**.
8. S. Sureshkumar, V. Venkataramanujam, K. Dushyanthan, A. Kalaikannan, *American Journal of Food Technology*, **2006**, *1(2)*, 166.
9. Alonzo A. Gabriel, *Food Chemistry,* **2008,** *108*, 1106.
10. K. R. Dave, *Journal of Applied Bacteriology,* **1989**, *67*, 483.
11. ***AOAC Official Methods 978.18. Water activity, **1995**.
12. SR ISO 7954:2001, "General guidance for the enumeration of yeasts and moulds", **2001**.
13. SR EN ISO 4833:2003, "Horizontal method for the enumeration of microorganisms", **2003**.
14. ISO 4832:2006, "Horizontal method for the enumeration of coliforms – colony count technique", **2006**.
15. S. Ungureanu, "Sensibilitatea sistemelor dinamice", Ed. Tehnica, Bucureşti, **1988**, 222.
16. A.W. Barendsz, *Food Control*, **1998**, *9(2-3)*, 163.
17. ***Best practices in food safety. National guidelines – The HACCP food safety system, Publishing House Uranus, Bucharest, **2007**, 14.

Dedicated to Professor Liviu Literat, at his 80th anniversary

SYNTHESIS AND CHARACTERIZATION OF SOME THERMORESISTANT PIGMENTS BASED ON THE $Al^{3+} \rightarrow Cr^{3+}$ SUBSTITUTION

SILVANA IANOŞEV[a], RADU LAZĂU[a], MARIANA SUBA[a], CORNELIA PĂCURARIU[a], IOAN LAZĂU[a]

ABSTRACT. The paper presents the obtained results in the synthesis of some thermoresistant pink pigments with different structures, such as: corundum ($Al_{2-x}Cr_xO_3$), spinel ($ZnAl_{2-x}Cr_xO_4$, $MgAl_{2-x}Cr_xO_4$) and perovskite ($LaAl_{1-x}Cr_xO_3$). An unconventional synthesis method has been used in order to increase the substitution of Al^{3+} with Cr^{3+}. The method used is based on the thermal decomposition of organic complex combinations containing as ligand the glyoxylate dianion, ($C_2H_2O_4^{2-}$). The evolution of the crystalline phases with temperature has been investigated by XRD. The colorimetric characterization of the obtained pigments has been studied by diffuse reflectance spectrophotometry.

Keywords: thermoresistant pink pigments, chromophore chromium (Cr^{3+}, Cr^{4+}), mineralizers.

INTRODUCTION

$Al^{3+} \rightarrow Cr^{3+}$ substitution in the crystalline networks of some oxide compounds leads to a wide range of pigments with colors varying from pink → red → purple → chestnut red. These pigments develop a special interest due to their color and difficulty to achieve constant nuances in a number as large as possible of vitreous compositions to be colored.

The α-Al_2O_3 - α-Cr_2O_3 continuous isomorphy represents the basis of the $Al^{3+} \rightarrow Cr^{3+}$ substitution [1].

In the crystalline structure of the two oxides, as well as in the solid solutions, they form, Al^{3+} and Cr^{3+} cations octahedrally coordinated. α-Cr_2O_3 is green, whilst α-$Al_{2-x}Cr_xO_3$ solid solutions are pink for $x \leq 0.10$. This major color difference is assigned to the compression of the Cr^{3+} cations in the

---

[a] *Universitatea "Politehnica" din Timişoara, Facultatea de Chimie Industrială şi Ingineria Mediului, Piaţa Victoriei Nr. 2, RO-300006 Timişoara, Romania, radulazau@gmail.com*

electrostatic field of the anions, when Cr^{3+} cations take the place of Al^{3+} cations (with smaller ionic radius). The corresponding absorption bands in the VIS electronic spectrum move towards lower wavelengths and the color consequently changes from green (α-Cr_2O_3) to pink (α-$Al_{2-x}Cr_xO_3$) [2].

The development of the pink color requires the uniform (statistical) inclusion of Cr^{3+} cations in the $Al_{2-x}Cr_xO_3$ network and thus, the initial raw materials mixture has to be as homogenous as possible. Nevertheless, the synthesis temperature has to ensure the structuring of the solid solution crystalline network.

In the case of the classical (ceramic) method based on the thermal treatment of some Al_2O_3 and Cr_2O_3 mechanical mixtures, the temperatures required for the formation of the pink solid solutions are very high, often above 1300ºC. When the mixture is melting (which is the case of the ruby single crystals fabrication), the homogeneity is achieved in the melt and the specific color is ruby-red. Still, this requires temperatures above 2100ºC, which are not to be take into account in the case of thermoresistant pigments synthesis. A much more interesting and promising direction is represented by the unconventional methods. They start from highly homogenous precursors mixtures, usually at ionic scale.

It is possible to obtain pink pigments not only by using $Al^{3+} \rightarrow Cr^{3+}$ substitution in the Al_2O_3-Cr_2O_3 system, but also in more complex systems, which provide appropriate host - crystalline networks for Cr^{3+}. Among these, the most interesting crystalline network is that of spinel, in the ZnO-Al_2O_3-Cr_2O_3 system [3]. Recently, the perovskite structure [4, 5] in the Ln_2O_3-Al_2O_3-Cr_2O_3 system (Ln= Y, La, Nd, Dy, Gd) and also the cordierite structure $2MgO·(2-x)Al_2O_3· xCr_2O_3·SiO_2$ [6-8] have developed practical interest.

The aim of the paper is to highlight the particularity and the advantages offered by one of the unconventional methods currently used in the synthesis of the thermoresistant pigments based on the $Al^{3+} \rightarrow Cr^{3+}$ substitution in various structures: corundum, spinel and perovskite. The effect of the mineralizer's addition has also been studied.

RESULTS AND DISCUSSION

The unconventional method chosen to obtain the studied pigments is based on the annealing of the organic complex combinations formed during ethylene glycol oxidation by the desired metal nitrates.

The results mentioned in literature [9-11], as well as some of our own previous results [12-18], have proven the possibility to obtain oxide compounds by annealing these complex combinations at temperatures at least 200 - 300ºC lower than in the case of the classical method based on the annealing of mechanical mixtures of oxides and/or salts.

The method is based on the 1,2-ethanediol to glyoxylate dianion oxidation reaction by the nitrate anion, according to the reaction:

$$C_2H_4(OH)_2 + 2NO_3^- \rightarrow C_2H_2O_4^{2-} + 2NO + 2H_2O \tag{1}$$

One or more metallic nitrates can be used in the oxidation reaction, depending on the designed product. For example, in order to obtain $ZnO \cdot Al_2O_3$ spinel, 1,2 - ethanediol is being oxidized by a mixture of $Al(NO_3)_3$ and $Zn(NO_3)_2$ in the molar ratio 2:1. It has been established [19] that in this particular case the following reactions take place:

$$Al(NO_3)_3 + H_2O \rightarrow Al(OH)(NO_3)_2 + HNO_3 \tag{2}$$

$$6C_2H_4(OH)_2 + 4\ Al(OH)(NO_3)_2 + 2Zn(NO_3)_2 \xrightarrow{xH_2O}$$
$$\rightarrow Al_4Zn_2(OH)_4(C_2H_2O_4)_6 \cdot xH_2O + 12NO + 12H_2O \tag{3}$$

$$NO(g) + 1/2O_2(g) \rightarrow NO_2(g) \tag{4}$$
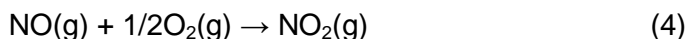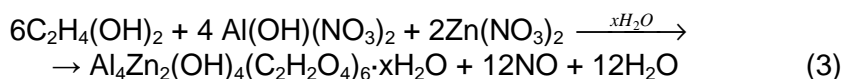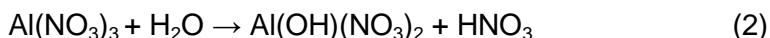
During the reaction HNO_3 and NO_2 evolve and the complex combination separates as a solid product. This decomposes during the annealing and an oxide powder forms, together with CO_2 and H_2O. At the beginning the resulting powder is amorphous, but an increase in the temperature leads to the formation of the designed oxide compound (reaction 5):

$$Al_4Zn_2(OH)_4(C_2H_2O_4)_6 + 6O_2 \xrightarrow{t>250°C} 2(ZnO \cdot Al_2O_3) + 12CO_2 + 8H_2O \tag{5}$$
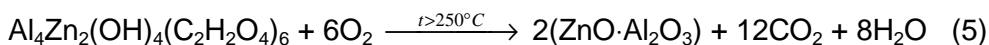
In the case of other metal nitrates, it may be possible that the oxidation reaction of 1,2 - ethanediol takes place differently, with the formation of carboxylates. Still, the intimate mixtures of the precursors preserve the advantage of the high initial homogeneity of the reaction mixtures and thus, enhance the reactions of the designed products, which take place at temperatures 200 or 300ºC lower than in the case of the traditional method.

In order to enhance the chromophore binding in the host-crystalline network, two of the common mineralizers have been used (CaF_2 and LiF), as well as the recently mentioned in the literature Li_2O. The latter is proven to develop a very good effect on the obtaining of mauve pigments with cassiterite structure [20] and pink pigments with tin sphene structure [21].

In Table 1 there are presented the studied compositions.

The observations made on annealed samples at different temperatures, as well as on the color of the rinsing water, phase analysis and diffuse reflectance spectra are shown as follows.

Trichromatic coordinates (L*a*b*) of some of the obtained samples are presented in Table 2. The three coordinates of CIELAB represent the lightness of the color (L^* = 0 yields black and L^* = 100 indicates diffuse white; specular white may be higher), its position between red/magenta and

green (**a***, negative values indicate green, while positive values indicate magenta) and its position between yellow and blue (**b***, negative values indicate blue and positive values indicate yellow).

Table 1. Studied compositions

Sample number	Molar ratio						Mineralizer (1%)	Crystalline network
	$Al(NO_3)_3$	$Cr(NO_3)_3$	$Zn(NO_3)_2$	$Mg(NO_3)_2$	$La(NO_3)$	Ethylene glycol		
0.	-	2	-	-	-	3	-	Corundum - eskolaite
1.1.	1.90	0.10	-	-	-	2	-	Corundum
1.2.	1.90	0.10	-	-	-	2	CaF_2	Corundum
1.3.	1.90	0.10	-	-	-	2	Li_2O	Corundum
1.4.	1.90	0.10	-	-	-	2	LiF	Corundum
1.5.	1.80	0.20	-	-	-	2	-	Corundum
1.6.	1.80	0.20	-	-	-	2	CaF_2	Corundum
1.7.	1.80	0.20	-	-	-	2	Li_2O	Corundum
1.8.	1.80	0.20	-	-	-	2	LiF	Corundum
2.1.	1.90	0.10	1	-	-	3	-	Spinel
2.2.	1.90	0.10	1	-	-	3	CaF_2	Spinel
2.3.	1.90	0.10	1	-	-	3	Li_2O	Spinel
2.4.	1.90	0.10	1	-	-	3	LiF	Spinel
3.1.	1.90	0.10	-	1	-	3	-	Spinel
3.2.	1.90	0.10	-	1	-	3	CaF_2	Spinel
3.3.	1.90	0.10	-	1	-	3	Li_2O	Spinel
3.4.	1.90	0.10	-	1	-	3	LiF	Spinel
4.1.	0.95	0.05	-	-	1	2.5	-	Perovskite
4.2.	0.95	0.05	-	-	1	2.5	CaF_2	Perovskite
4.3.	0.95	0.05	-	-	1	2.5	Li_2O	Perovskite
4.4.	0.95	0.05	-	-	1	2.5	LiF	Perovskite

a) Pigments with corundum structure $Al_{2-x}Cr_xO_3$

All the samples within the series 1 (1.1 ÷ 1.8) are amorphous after annealing at 500ºC. At 900ºC δ-Al_2O_3 is present in the XRD pattern and after annealing at 1000ºC α-Al_2O_3 is present as single phase.

The color of the samples within the series 1 varies much, depending on the composition and annealing temperature.

The free chromium as soluble Cr^{6+} (aluminium chromate), assessed by the color of the rinsing water varies with the annealing temperature and the mineralizer used. Since the objective was to reach an advanced chromium binding degree in the crystalline network of corundum, we considered the quantitative assessment of free chromium was not necessary. The purpose was to find the working conditions to allow the development of an

intense color by the homogenous inclusion of the chromophore Cr^{3+} in the host crystalline network. From this point of view, the color of the samples is more intense at 1100ºC than at 1000ºC, and there is no significant difference between the colors at 1200ºC compared to 1100ºC.

Table 2. CIELAB trichromatic coordinates of the samples annealed at different temperatures

Sample number	Sample	Mineralizer [wt.%]	Temperature [ºC]	L*	a*	b*
0.	Cr_2O_3	-	1100	44.4697	-14.8240	16.7534
1.5.	$Al_{1.80}Cr_{0.20}O_3$	-	1100	67.3149	2.8066	2.0216
1.6.	$Al_{1.80}Cr_{0.20}O_3$	CaF_2	1100	66.4278	4.2003	1.2662
1.7.	$Al_{1.80}Cr_{0.20}O_3$	Li_2O	1100	65.7919	3.1277	1.2063
1.8.	$Al_{1.80}Cr_{0.20}O_3$	LiF	1100	66.4393	1.9980	1.7037
2.1.	$ZnAl_{1.90}Cr_{0.10}O_4$	-	1100	79.4996	15.2079	2.3690
2.2.	$ZnAl_{1.90}Cr_{0.10}O_4$	CaF_2	1100	87.7384	9.8321	2.9288
2.3.	$ZnAl_{1.90}Cr_{0.10}O_4$	Li_2O	1100	82.4761	15.6099	2.5786
2.4.	$ZnAl_{1.90}Cr_{0.10}O_4$	LiF	1100	85.6378	11.8808	1.8574
3.1.	$MgAl_{1.90}Cr_{0.10}O_4$	-	1200	85.1272	5.8948	0.6873
3.4.	$MgAl_{1.90}Cr_{0.10}O_4$	LiF	1200	80.0045	6.8176	1.8102
4.1.	$LaAl_{0.95}Cr_{0.05}O_3$	-	1000	81.9325	7.5195	7.7448
4.2.	$LaAl_{0.95}Cr_{0.05}O_3$	CaF_2	1000	67.7153	8.9423	4.0135
4.1.	$LaAl_{0.95}Cr_{0.05}O_3$	-	1200	52.6236	13.9397	5.9973
4.2.	$LaAl_{0.95}Cr_{0.05}O_3$	CaF_2	1200	42.4616	14.8593	6.0388

Interesting differences have been noted between samples obtained with mineralizer addition:

- The samples with 1% CaF_2, which is considered in the literature as a highly efficient mineralizer, show a less intense color than in the case of the similar sample without CaF_2 content (within series 1). Accordingly, the samples with CaF_2 show higher free soluble chromium content.

- Samples with 1% Li_2O present a more intense color and lower free soluble chromium content than in the case of samples with CaF_2 or without mineralizer.

- Samples with LiF are very similar to those with Li_2O.

The negative effect of CaF_2 is assigned to the Ca^{2+} cation, with marked alkaline nature, which determines the calcium chromate ($CaCrO_4$) formation, enhancing the displacement of the $Cr^{6+} \leftrightarrow Cr^{3+}$ equilibrium towards Cr^{6+}.

The increase of the Cr^{3+} content in the series 1.5 ÷ 1.8 leads to impurifying of the pink color with green.

The explanation of the pink color in the case of the solid solutions resulted by the substitution of Al^{3+} with Cr^{3+} cations lays in the higher Cr^{3+} radius ($r_{Cr^{3+}} = 0.62\,Å$, $r_{Al^{3+}} = 0.53\,Å$ after Shannon and Kingery cited in [22]). Thus, Cr^{3+} cations are subjected to compression, which leads to a more intense electrostatic repulsion between the load of the oxygen anions in the corners of the coordination polyhedron (octahedron) and the *3d* electrons of the chromophore, implicitly increasing the splitting parameter $Δ_o$. The effect of $Δ_o$ increase is a displacement of the absorption bands corresponding to the *$3d^3$* electrons transitions towards higher frequencies ($ΔE=h\nu$), lower wavelengths respectively, with a change in color from green ($α$-Cr_2O_3) to pink-red (ruby, $α$-$Al_{2-x}Cr_xO_3$). This displacement of the absorption bands may be easily observed on the diffuse reflectance spectra presented in Figure 1.
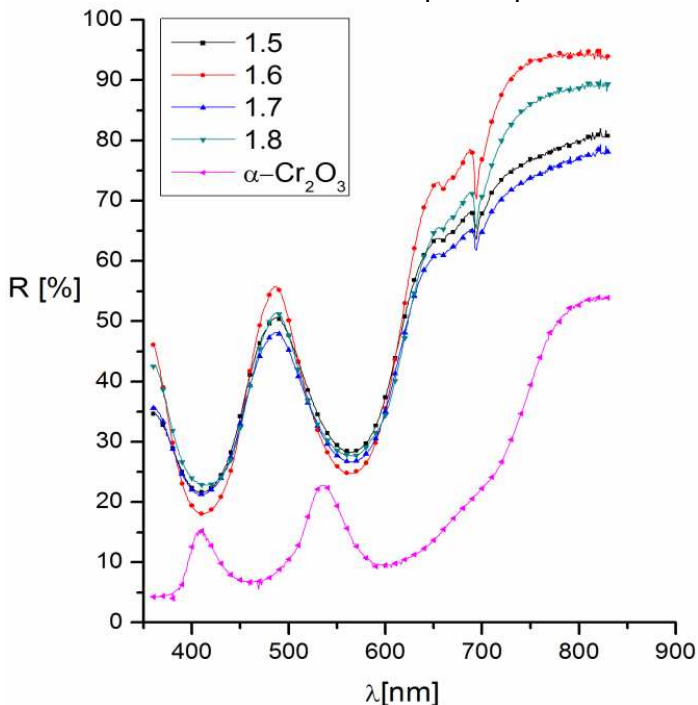
Figure 1. Diffuse reflectance spectra of samples 1.5-1.8 annealed at 1200ºC and $α$-Cr_2O_3.

b) *Spinel structure pigments*

The compositions presented in Table 1 show two groups of spinel structure pigments:

194

- derived from zinc spinel $ZnAl_{2-x}Cr_xO_4$, samples 2.1. ÷ 2.4;
- derived from magnesium spinel $MgAl_{2-x}Cr_xO_4$, samples 3.1 ÷ 3.4.

In both series, the effect of mineralizer addition (CaF_2, Li_2O, LiF) upon the color development has been studied.

There is very few information in literature concerning the use of magnesium spinel for thermoresistant pigments. Usually, the zinc spinel is the one used for obtaining a wide range of colors by Al^{3+}, Zn^{2+} or both cations substitution with different chromophore cations (Cr^{3+}, Fe^{3+}, Co^{2+}, Ni^{2+}, Mn^{2+}, etc.). This situation is due to both experimental results and to thermodynamic calculus. Starting from the thermodynamic standard functions of each chemical compound [23] and considering the relations for the temperature dependence of the thermal effects ($\Delta_rH_T^0$) and Gibbs energy ($\Delta_rG_T^0$) [24], the thermodynamic calculations have been done. The $\Delta_rH_T^0 = f(T)$ dependence (Figure 2) calculated for zinc and magnesium spinels show that the reaction of the spinel starting from oxides as raw materials (the classical method) is more exothermal for $ZnAl_2O_4$ than for $MgAl_2O_4$. Moreover, the $\Delta_rG_T^0 = f(T)$ calculated dependence show that zinc spinel forms easier than magnesium spinel (Figure 3).
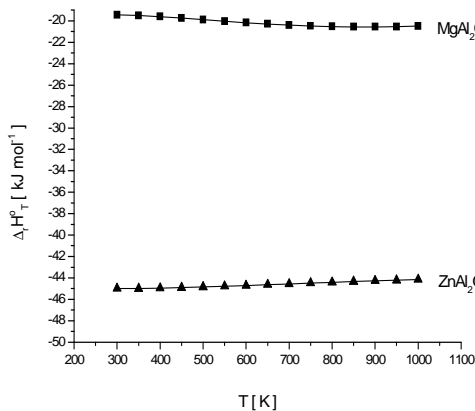
Figure 2. $\Delta_rH_T^0 = f(T)$ dependence for the reactions of zinc and magnesium spinels.
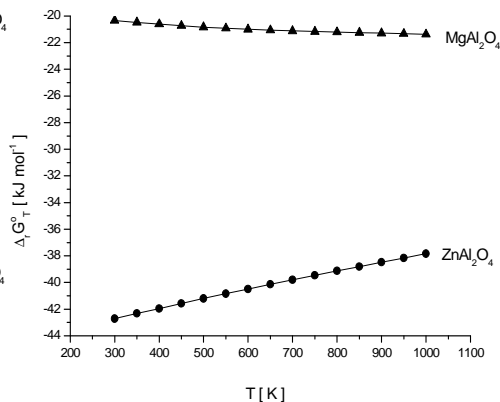
Figure 3. $\Delta_rG_T^0 = f(T)$ dependence for the reactions of zinc and magnesium spinels.

$ZnAl_2O_4$ formation by solid state reaction takes place quite easily and thus, the zinc spinel represents an accessible base for thermoresistant pigments, whilst $MgAl_2O_4$ is more difficult to obtain.

Pink pigments derived from $MgAl_2O_4$ have been obtained by the method based on annealing the complex combinations, which enhances the formation of the designed products.

The results of the XRD phase analysis in the case of the samples annealed at temperatures comprised between 500ºC and 1000ºC confirmed the easier formation of the zinc spinel (samples 2.1 ÷ 2.4). At 600ºC this is present as single phase in the XRD pattern. In the case of $MgAl_2O_4$ (samples 3.1÷ 3.4) the powder is amorphous. The spinel presents a good crystallization degree at 800ºC.

One notes that in the case of the traditional synthesis method, when starting from a mixture of $MgCO_3$ and aluminum hydroxide, the spinel is still not the single phase present at 1200ºC [25].

The diffuse reflectance spectra of the synthesized zinc and magnesium spinels are presented in Figures 4 and 5.
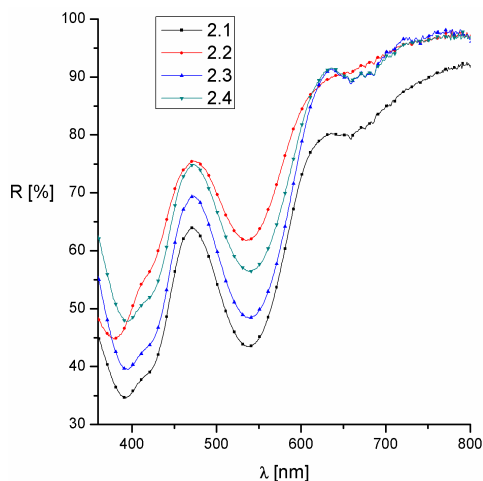
Figure 4. Diffuse reflectance spectra of samples 2.1 ÷ 2.4 annealed at 1100ºC.
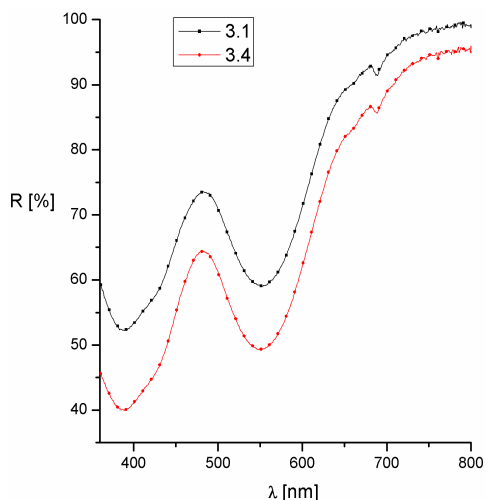
Figure 5. Diffuse reflectance spectra of samples 3.1 and 3.4 annealed at 1200ºC.

From the point of view of the pink color development via the $Al^{3+} \rightarrow Cr^{3+}$ partial substitution, the observations are similar to those made in the case of the corundum solid solutions:

- the temperature required to obtain an intense pink is 1100ºC. It is only in the case of the magnesium spinel, when raising the temperature up to 1200ºC leads to a color enhancement. This may be assigned to the specific $MgAl_2O_4$ formation conditions, which are more sensitive to temperature.

- the effect of mineralizers additions is similar to the 1. series – negative for CaF_2 and positive for Li_2O and LiF, with the same explanation for the negative role of Ca^{2+} ions.

c) Perovskite structure pigments

The crystalline structure of perovskite is one of the most recent used in thermoresistant pigments synthesis [26-28]. Starting from the ABO_3 stoichiometry, where $A^{3+}= Y^{3+}$, La^{3+}, Nd^{3+}, etc. (large radius cations) – dodecahedrally coordinated, and $B^{3+}= Al^{3+}$ (relatively small radius cations) octahedrally coordinated, there may be obtained pink pigments by $Al^{3+} \rightarrow Cr^{3+}$ partial substitution.

The formation of the above-mentioned pigments (samples 4.1 – 4.4) via thermal decomposition of the complex combinations, as well as the influence of the mineralizers upon the color, were studied.

The diffuse reflectance spectra of the samples with no mineralizer, respectively with CaF_2 as mineralizer, at 1000 and 1200℃ there are presented in Figures 6 and 7.
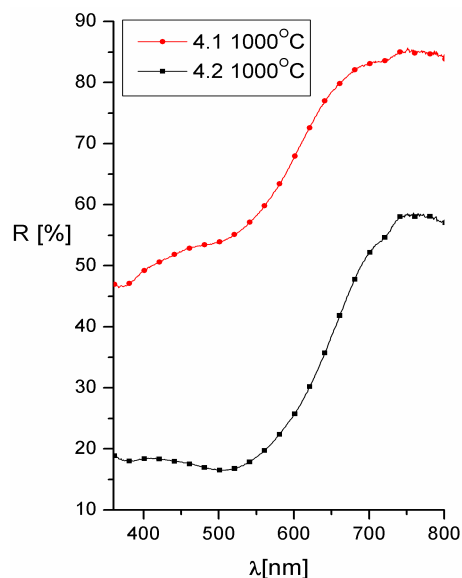
Figure 6. Diffuse reflectance spectra of samples 4.1 and 4.2 annealed at 1000℃.
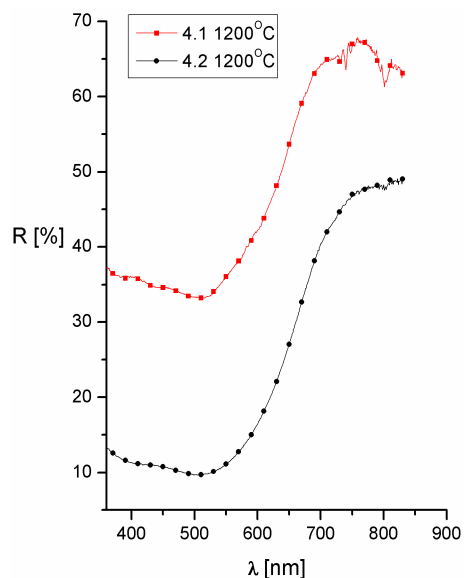
Figure 7. Diffuse reflectance spectra of samples 4.1 and 4.2 annealed at 1200℃.

These spectra are practically identical with those of the same pigments obtained by the traditional method at 1400℃ [4].

One can note the presence of the specific wide absorption band between 450 and 600nm. At both 1000 and 1200°C samples with CaF_2 show lower reflectance values, which indicate more intense colors than in the case of the samples with no mineralizer addition.

The XRD patterns presented in figure 8 show that the sample annealed at 600°C is amorphous and starting with 750°C perovskite is the single phase in the sample. The yellow color of the sample annealed at 600°C is assigned to Cr^{6+} as lanthanum chromate and the pink color at 750°C is associated with the presence of perovskite.

Regarding the oxidation number of chromium, which is substituting the octahedrally coordinated Al^{3+} cations in the perovskite network, the literature data are still controversial. Some authors [29-31] consider that chromium is trivalent. But if one takes into account the diffuse reflectance spectra of these pigments (Figures 6 and 7), which are essentially different from those of the pink pigments with corundum and spinel pigments, this hypothesis is questionable.
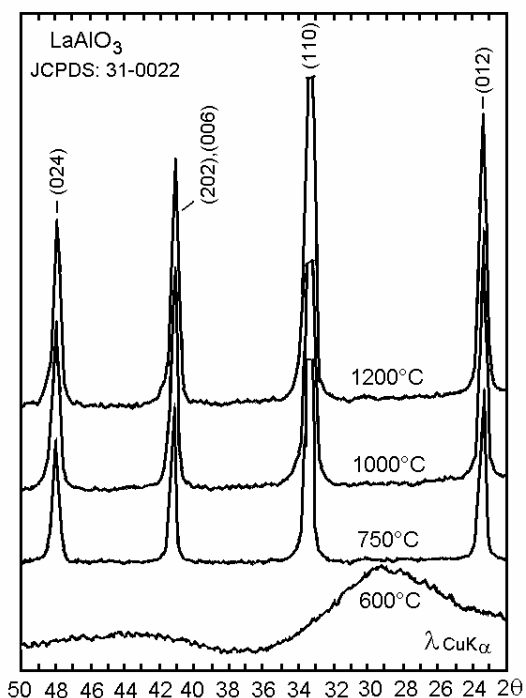
Figure 8. XRD patterns of La^{3+}, Al^{3+} and Cr^{3+} glyoxilate annealed at different temperatures.

The diffuse reflectance spectrum of pink perovskite pigments show a large absorption band between 380 and 600nm, very similar to that of the tin sphene ($CaO \cdot SnO_2 \cdot SiO_2$) pigments – in which the presence of octahedrally coordinated Cr^{4+} is already accepted, as a result of the $Sn^{4+} \rightarrow Cr^{4+}$ substitution [32-35]. Based on this analogy, one can assume the presence of Cr^{4+} as well in the pink perovskite pigments. As a matter of fact, Pavlov [34] indicates the presence of Cr^{4+} in $YAlO_3$, in which Al^{3+} is partly substituted by chromium. The overall structure is electrically neutral due to cationic vacancies generated by the substitution $4Al^{3+} \rightarrow 3Cr^{4+}$. Another possibility is the coupled substitution $(La^{3+} + Al^{3+}) \rightarrow (Ca^{2+} + Cr^{4+})$, where Ca^{2+} cations come from the used mineralizer (CaF_2) – a plausible hypothesis taking into account the marked positive influence of CaF_2 upon the color of these pigments. Unlike the case of corundum and spinel pigments, where CaF_2 has a negative effect, in the case of perovskite the $La^{3+} \rightarrow Ca^{2+}$ substitution (as A – type cations) enhances the $Al^{3+} \rightarrow Cr^{4+}$ substitution and hence, the color. $La^{3+} \rightarrow Ca^{2+}$ substitution is possible due to the close values of the ionic radius of the two cations and also to the Ca^{2+} possibility to form a perovskite network (see the case of $CaTiO_3$ – where the tetravalent B cations are octahedrally coordinated).

CONCLUSIONS

The method based on the annealing glyoxylate-like complex combinations enables the chromium (Cr^{3+}, Cr^{4+}) containing pigments formation at temperatures at least 200-300ºC lower than in the case of the classical method.

Zinc spinel ($ZnAl_2O_4$) and the pink pigments derivated from this are easier to obtain than magnesium spinel ($MgAl_2O_4$), which is in accordance with the thermodynamic data.

The method used ilustrates the possibility to obtain magnesium spinel and substitute Al^{3+} with Cr^{3+} even at 800℃, whilst in the traditional method temperatures above 1200℃ are needed.

Choosing the right mineralizers to enhance the color and reduce the soluble chromium ratio must be done according to the crystalline network type, basicity of the host-network cations, desired substitutions and final chromophore oxidation number.

CaF_2 is not recommended in the case of corundum and spinel structure pigments. The use of LiF or Li_2O leads to the desired pink pigments at temperatures between 1000 and 1100℃.

In the case of perovskite, the use of CaF_2 clearly enhances the specific color of these pigments.

EXPERIMENTAL SECTION

Organic combinations obtained by the oxidation reaction of 1,2-ethanediol with the desired metal nitrates according to the reactions (1), (2), (3), (4) and (5) were dried in a drying oven at 110°C and annealed in porcelain crucibles at temperatures between 500°C a nd 1200°C in static air using an electrical (Nabertherm) furnace.

The free chromium content (soluble Cr^{6+}) after annealing the samples has been assessed by the colour of the rinsing water. After drying, the samples were subjected to colorimetric characterization by diffuse reflectance spectrophotometry – using a Varian CARY 300 spectrophotometer with integration sphere, D65 illuminant at 10 degrees observer's angle. The CIELAB trichromatic coordinates L*a*b* were established using Varian CARY WinUV Color 3.1. software. The phase composition analysis of the samples was investigated by XRD, using a DRON 3 diffractometer with CuK_α radiation.

REFERENCES

1. E. M. Levin, C. R. Robbins, H. F. McMurdie, "Phase Diagrams for Ceramists" The *American Ceramic Society*, Ohio, **1964**, 309.
2. L. E. Orgel, *Nature*, **1957**, *179*, 1348.
3. R. A. Eppler, "Ullman's Encyclopedia of Industrial Chemistry", VCH Verlagsge-sellschaft mbH, D-6940, Weinheim, **1986,** *A5*, 545.
4. G. Baldi, N. Dolen, **,** *Mater. Eng.*, **1999**, *2*, 151.
5. G. Monros, CIMTEC 2002 -10th International Ceramics Congress International Symposium, "Science for new Technology of Silicate Ceramics" , Advances in Science and Technology, Florence, Italy, **2002**, *34*, 255.
6. V. P. Pîrkov, L. I. Cerepanina, A. N. Denisov, L. A. Bizir, *Steklo i Keramika*, **1981**, *5*, 22.
7. I. Lazău, C. Păcurariu , R. M. Jurca, G. Kovacs, *J. Building Mater.*, **1999**, *29,* 85.
8. S. Ianoşev, I. Lazău, C. Păcurariu, A. Avramescu, *Process. Applic. Ceram.*, **2008**, *2*, 39.
9. M. Bîrzescu, M. Cristea, M. Ştefănescu, Gh. Constantin, Brevet Rom. **1990**, *102501*.
10. M. Ştefănescu, V. Sasca, M. Bîrzescu, D. Crişan, M. Mracec, "*Rev. Roum. Chim.*, **1998**, *40*, 788.
11. M. Bîrzescu, C. Păcurariu, M. Ştefănescu, *Chem. Bull.* POLITEHNICA Univ.(Timisoara),**1996**, *41*, 80.

12. C. Păcurariu, Teză de doctorat, Universitatea "Politehnica" Timişoara, **1997**.
13. C. Păcurariu, I. Lazău, D. Becherescu, I. Boboş, *Rev. Roum. Chim.*, **1997**, *42*, 447.
14. C. Păcurariu, M. Bîrzescu, I. Lazău, M. Brezeanu, D. Becherescu, *Mater. Eng.*, **2000**, *11,* 129.
15. C. Păcurariu, M. Ştefănescu , I. Lazău, M. Bîrzescu, *Key Eng. Mater. Trans. Tech. Publications*, Switzerland, **1997**, *113*,132.
16. I. Lazău, C. Păcurariu, R. Lazău, *Interceram*, **2002**, *51*, 266.
17. C. Păcurariu, I. Lazău, D. Becherescu, R. Lazău, *Mater. Eng.*, **2003**, *14*, 97.
18. S. Ianoşev, I. Lazău, C. Păcurariu, A. Goleanu, *Proceedings of 2nd International Congress on Ceramics*, Verona, Italy, **2008.**
19. M. Bîrzescu, M. Ştefănescu, M. Brezeanu, M. Andruh, The 3rd Ntional Congress of Chemistry, Bucharest, **1988**, 46.
20. T. Bartiş, R. I. Lazău, D. Becherescu, I. Lazău, C. Păcurariu, O. Matea, *Rev. Chim.*, **2007**, *58*, 1035.
21. T. Bartiş, R.I. Lazău, D. Becherescu, I. Lazău, C. Păcurariu, O. Matea, *Rom. J. Mater*, **2007**, *37*, 113.
22. W. Richerson, D.David, "Modern Ceramic Engineering", Marcel Dekker Inc., New York, **1992**.
23. O. Knache, K. Kubaschewski, K. Hesselmann, "Thermochemical Properties of Inorganic Substances", Second Edition, Springer-Verlag, Berlin, **1991**.
24. R. Ianoş, I. Lazău, C. Păcurariu, "Sinteza compuşilor oxidici prin metoda combustiei", Editura Politehnica, **2008**.
25. M. F. M. Zawrah, A. A. El Kheshen, *Br. Ceram. Trans.*, **2002**, *101*, 71.
26. G. Baldi, N. Dolen, *Mater. Eng.*, **1999**, *2*, 151.
27. G. Monros, CIMTEC 2002 -10th International Ceramics Congress International Symposium, "Science for new Technology of Silicate Ceramics", Advances in Science and Technology, Florence, Italy, **2002**, *34*, 255.
28. R. Olazcuaga, A. El Kira, P. Maestro, R. Tastu, G. Le Flem, *Rev. Chim. Minerale,* **1984**, *21*, 221.
29. I. Rotsche, R. Schroder, I. Reichel, *Silikattechnik*, **1985**, *10*, 316.
30. E. A. Filipova, A. I. Glebîceva, L. A. Bizir, N. N. Kazakova, *Steklo i Keramika*, **1983**, *7*, 23.
31. L. Tcheichvili, W. A. Weyl, *The Glass Industry*, **1963**, 208.
32. M. A. Heyns, P. M. Harden, *J. Phys. Chem. Solids*, **1999**, *60*, 277.
33. I. Shingo, K. Shigeto, K. Ikuo, H. Masahiko, *J. Ceram. Soc. Japan*, **1986**, *94*, 457.
34. R. S. Pavlov, V. B. Marzá, JB. Carda, *J.Mater. Chem.*, **2002**, *12*, 2825.
35. R. Lazău, Teză de doctorat*,* Ed. Politehnica, Timişoara, **2007**.

Dedicated to Professor Liviu Literat, at his 80th anniversary

MASS TRANSFER IN SUBLIMATION PROCESS

MIRELA SMARANDOIU[a], IOAN MAMALIGA[a], STELIAN PETRESCU

ABSTRACT. This paper is a study of mass transfer in entrainer sublimation, when the solid-gas interface is plane. A mathematical model is established, that allows the calculation of the sublimation process time, or the sublimation front position as a time function. The mathematical model is experimentally checked, using naphthalene cylindrical particles, fixed on special supports, with are offering a plane surface in contact with the entrainer, here is hot air. It is also studied the influence of temperature and entrainer flowrate on sublimation rate.
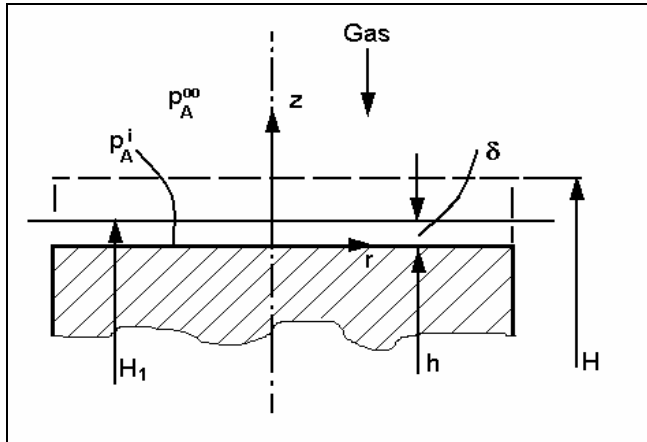
Keywords: entrainer sublimation, mass transfer

INTRODUCTION

The sublimation is a physical process used for separation or purification of solid chemical substances. Although it is a technical process, the literature contains a small number at papers regarding mass and heat transfer [1-17].

Regarding the mass transfer, the existing papers focus both a theoretical and experimental studies [1-6], at a single particle level, or group of particles in fixed or fluidized bed. Some authors [10-17] approach the simultaneous mass and heat transfer in sublimation processes.

The present paper is a study of mass transfer in entrainer sublimation, when the solid-gas interface is plane. A mathematical model is established, that allows the calculation of the sublimation process time, or the sublimation front position as a time function. The mathematical model is experimentally checked, using naphthalene cylindrical particles, fixed on special supports, with are offering a plane surface in contact with the entrainer and here is hot air. It is also studied the influence of temperature and entrainer flow rate on sublimation rate.

---

[a] *Universitatea Tehnica "Gh. Asachi" din Iaşi, Facultatea de Inginerie Chimică şi Protecţia Mediului, Bd. D. Mangeron, Nr. 71, RO-700050, Iaşi, Romania, imamalig@ch.tuiasi.ro*

Mathematical model

Figure 1 presents the physical model of entrainer sublimation with plane solid-gas interface. According to this model, the entrainer moves towards the solid surface. At interface it is formed a limit diffusion layer, with δ thickness. The partial pressure of sublimation substance (A) at interface is p_A^i, and the gas phase volume is p_A^∞. The mass transfer direction from the interface to the gas phase volume is Oz.

Figure1. The physical model for mass transfer
at entrainer sublimation.

Since the mathematical modeling used in this paper looks to find one equation to determine the process time, at the sublimation front position, the starting point is the convective diffusion equation:

$$\frac{\partial p_A}{\partial t} = D_A \frac{\partial^2 p_A}{\partial z^2} \tag{1}$$

The initial and at limit terms, are:

$$t = 0, \qquad h = H \tag{2}$$

$$t > 0, \qquad z = h, \qquad \left|\begin{array}{l} p_A = p_A^i \\[2mm] \dfrac{D_A}{RT}\dfrac{\partial p_A}{\partial z} = \rho_S \dfrac{dh}{dt} \end{array}\right. \tag{3}$$

$$t > 0, \qquad z = H_1, \qquad p_A = p_A^\infty \tag{4}$$

In order to simplify solving the differential equation, we adopt pseudo-stationary condition, considering the partial pressure constant on an infinitesimal

204

time interval. Solving the equation (1) under these conditions leads to the following solution:

$$p_A = \frac{p_A^i - p_A^\infty}{h - H_1}(z - H_1) + p_A^\infty \tag{5}$$

Deriving the equation (5) in relation to z it gives:

$$\frac{dp_A}{dz} = \frac{p_A^i - p_A^\infty}{h - H_1} \tag{6}$$

The limiting condition (3) it can be written:

$$\frac{D_A}{RT} \frac{p_A^i - p_A^\infty}{h - H_1} = -\rho_S \frac{dh}{dt} \tag{7}$$

The integration of equation (7) comes to:

$$t = \frac{\rho_S RT}{k(p_A^i - p_A^\infty)}(H - h) \tag{8}$$

The distance from the interface, h, can be represented as a function of the sublimation degree, defined by the relation:

$$\eta_A = \frac{m_A^0 - m_A}{m_A^0} = \frac{V_S^0 - V_S}{V_S^0} = 1 - \frac{h}{H} \tag{9}$$

$$h = H(1 - \eta_A) \tag{10}$$

Replacing relation (10) in (8) gets to:

$$t = \frac{\rho_S RTH}{k(p_A^i - p_A^\infty)} \eta_A \tag{11}$$

Using equation (9) and (11), one can calculate the duration of sublimation process function of h and η_A, or the sublimation front position (expressed by h) as a function of time.

RESULTS AND DISCUSSIONS

It was experimentally determined the mass variation of each naphthalene support in time, at variable temperature and air flow rate values. The results are presented in Table 1.

Using those data and equation (9), was determined the variation of sublimation degree for the naphthalene from supports, in time. The results are presented in Table 2.

Table1. Mass variation at three temperatures (50°C, 60°C and 70°C) and entrainer flow rate in the range 1.5 -3.5 m³/h

Mv (m³/h)	T (°C)	t (min)				
		5	10	15	20	25
1.5	50	0.0057	0.0130	0.0153	0.0367	0.0394
	60	0.0059	0.0348	0.0384	0.0716	0.1119
	70	0.0200	0.0844	0.1234	0.1701	0.2336
2.0	50	0.0154	0.0198	0.0337	0.0389	0.0537
	60	0.0220	0.0404	0.0537	0.786	0.1151
	70	0.0358	0.0740	0.1117	0.1518	0.2360
2.5	50	0.0163	0.0176	0.0264	0.0280	0.0657
	60	0.0136	0.0264	0.0592	0.0782	0.1254
	70	0.0410	0.0790	0.1208	0.1620	0.2395
3.0	50	0.0094	0.0196	0.0306	0.0416	0.0592
	60	0.0209	0.0480	0.0655	0.0916	0.1311
	70	0.0386	0.0829	0.1420	0.1763	0.2511
3.5	50	0.0106	0.0217	0.0343	0.0437	0.0666
	60	0.0215	0.0488	0.0795	0.0945	0.1547
	70	0.0481	0.0920	0.1313	0.1934	0.2886

Table 2. Degree of sublimation at three temperatures (50°C, 60°C and 70°C) and entrainer flow rate in the range 1.5 -3.5 m³/h

Mv (m3/h)	T (°C)	t (s)				
		300	600	900	1200	1500
1.5	50	0.0063	0.0144	0.0170	0.0408	0.0438
	60	0.0065	0.0386	0.0420	0.0796	0.1244
	70	0.0224	0.0938	0.1372	0.1890	0.2597
2.0	50	0.0171	0.0220	0.0370	0.0432	0.0597
	60	0.0244	0.0449	0.0597	0.0874	0.1279
	70	0.0398	0.0822	0.1241	0.1688	0.2624
2.5	50	0.0181	0.0195	0.0293	0.015	0.0730
	60	0.0151	0.0293	0.0658	0.0869	0.1394
	70	0.0455	0.0878	0.1343	0.1801	0.2663
3.0	50	0.0104	0.0217	0.0340	0.0462	0.0658
	60	0.0232	0.0533	0.0728	0.1018	0.1457
	70	0.0429	0.0921	0.1579	0.1960	0.2792
3.5	50	0.0117	0.0241	0.0381	0.0485	0.0740
	60	0.0239	0.0542	0.0884	0.1050	0.1720
	70	0.0534	0.1023	0.1460	0.2150	0.3209

The variation of sublimation degree for naphthalene is a measure for the time evolution of the sublimation process.

The Figures 2 and 3 are graphical representation for h=f(t) functions, with the specified values for temperature and different air flow rate. As one can see, the height of sublimation front drops in time, regard less the temperature and entrainer flow rate values. As temperature rise, the height of sublimation front gets small, the reduction being pronounced at greater temperatures. The entrainer flow rate determines a positive influence on sublimation front height.
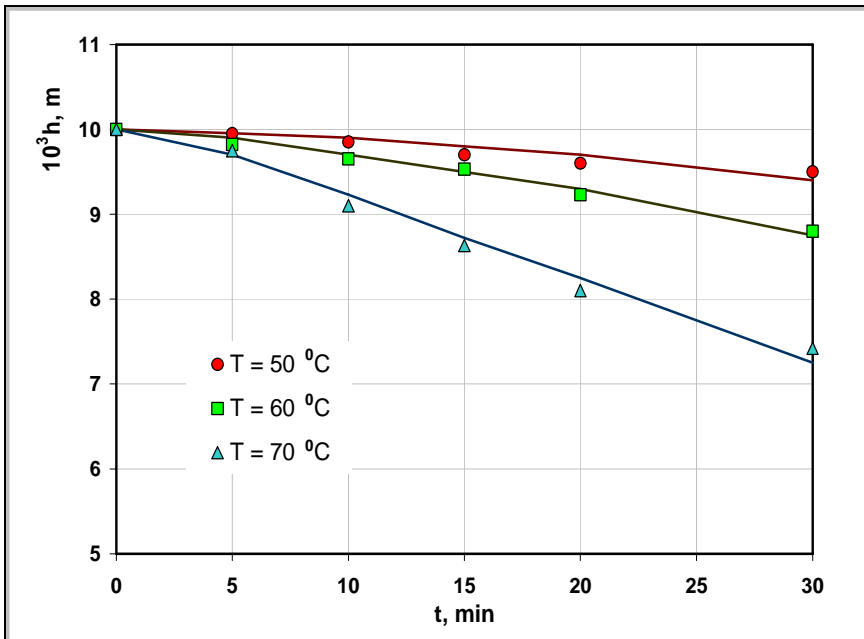
Figure 2. Sublimation front vs time at three temperatures (50°C, 60°C and 70°C) and entrainer flow rate $M_V = 1.5$ m^3/h.

In continuation, was determined the average sublimation rate, using the relation:

$$v_s = \frac{1}{t}\int_0^t v_s(t)dt \tag{12}$$

The sublimation rate $v_s(t)$ were computed with the relation:

$$v_s(t) = -\frac{dm}{S \cdot dt} \tag{13}$$

Figures 4 and 5 contain the dependencies $v_s=f(M_v)$ for many different temperatures, and $v_s=f(T)$ at different entrainer flow rate values. One can note that both entrainer debit and temperature have a positive influence on average sublimation rate. In the entrainer flow rate variation range between 1.5-3.5 m^3 /h, which is equivalent to entrainer velocity values through sublimation room between (0.409-0.955) m/s, the entrainer flow rate has a low influence on the sublimation rate. Temperature ranging from 50-70^0 C has a greater influence.
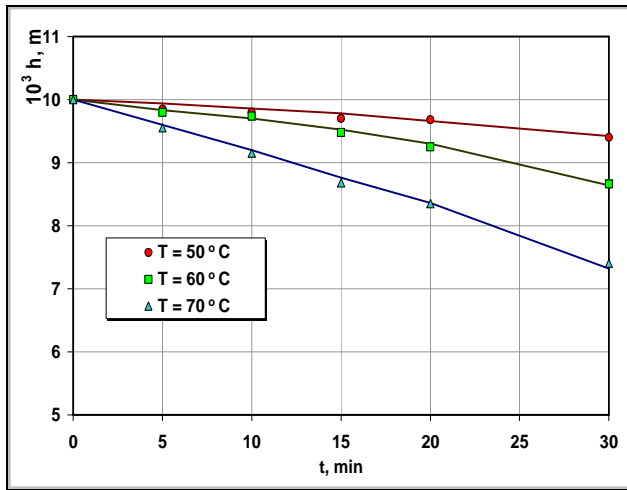
Figure 3. Sublimation front vs time at three temperatures(50°C, 60°C and 70°C) and entrainer flow rate M_V =3.5 m^3/h.
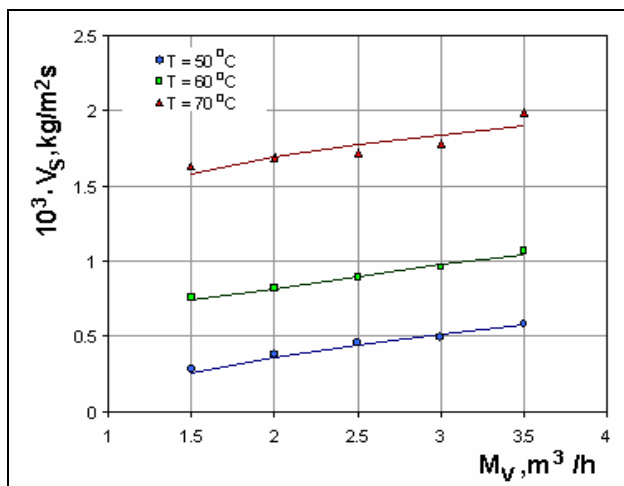
Figure 4. Sublimation rate as function of air flow rate at three temperatures (50°C, 60°C and 70°C).
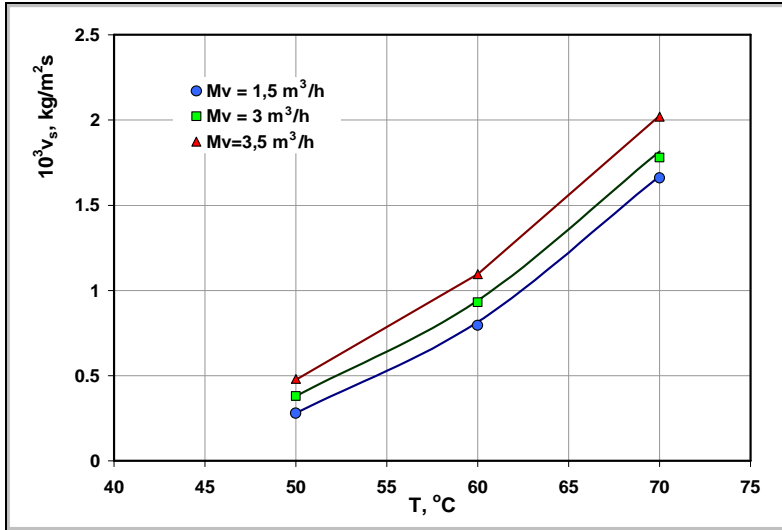
Figure 5. Sublimation rate as function of temperature
at three air flow rates (1.5, 3.0 and 3.5 m³/h).

Based on average sublimation rate values, was determined the individual mass transfer coefficient, using mass transfer equation:

$$v_s = \frac{k}{RT}(p_A^i - p_A^\infty) \tag{14}$$

The calculation of mass transfer coefficient involves knowledge of partial pressure values at gas-solid interface, which depends on the temperature at interface T_i. In order to determine the temperature at interface, the following equations were used:

$$\alpha(T_\infty - T_i) = \frac{k}{RT}(p_A^i - p_A^\infty)\Delta H_s \tag{15}$$

$$\ln p_A^i = 31.2352 - 8587/T_i \tag{16}$$

$$Nu = \left(\frac{Pr}{Sc}\right)^{0.4} Sh \tag{17}$$

$$D_A = 8.177 \cdot 10^{-7} \cdot T^{1.983} \tag{18}$$

The equations (16), (17) and (18) were taken from literature [12].

The values for individual mass transfer coefficient obtained, are presented in Table 3. The results from this table show similar dependencies of coefficient K, similar to sublimation rate.

Table 3. Individual mass transfer coefficient $10^2 \cdot k, \ (m/s)$ calculated at three values of temperature and air flow rate in the range 1.5 – 3.5 m³/h

$T \ (^oC)$	$M_V \ (m^3/h)$				
	1.5	2.0	2.5	3.0	3.5
50	5.611	7.647	9.356	8.430	9.485
60	7.393	7.604	8.285	8.662	10.222
70	7.712	7.793	7.904	8.291	9.529
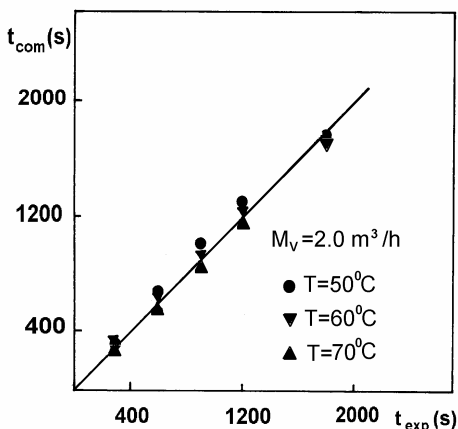
Figure 6. Comparison between experimental and calculated data at three temperatures (50°C, 60°C and 70°C) and air flow rate M_V =2.0 m³/h.
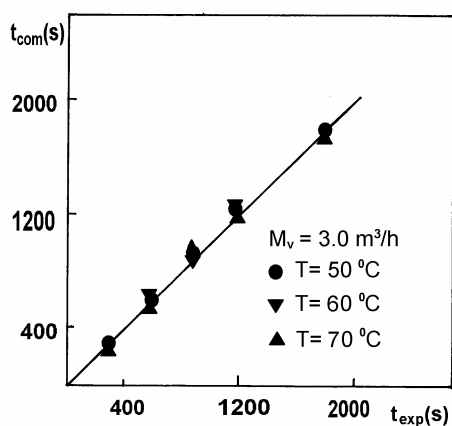
Figure 7. Comparison between experimental and calculated data at three temperatures (50°C, 60°C and 70°C) and air flow rate M_V =3.0 m³/h.

In this paper was studied the mass transfer at entrainer sublimation on plane solid-gas interface. A mathematical model for the sublimation process was established, which allow determination of process duration, or sublimation front height, or sublimation degree as a function.

Using naphthalene filled supports, which provide plane surface in contact with the entrainer, it was experimentally determined the variation of sublimation degree and sublimation front height in time, at numerous values for entrainer (air) temperature and velocity. It was also determined the average sublimation rate, and individual mass transfer coefficient, both on the same values for entrainer temperature and flow rate.

The results show that flow rate and temperature have a positive influence on sublimation rate and individual mass transfer coefficient.

By comparing the experimental data with these calculated using the mathematical model, a good concordance is obtained.

List of symbols

p_A - component A partial pressure, N/m^2
D_A - component A diffusion coefficient, m^2/s
t   - time, s
H   -support slot height, m
h   -sublimation front height, m
R   - universal gas constant, J/kgK
ρ_s -component a density in solid state, kg/m^3
δ   -limit diffusion layer thickness, m
k - individual mass transfer coefficient, m/s
m^0_A – component A mass at the initial moment, kg
m_A- component A mass at the given time t=t, kg
η_A- component A sublimation grade
i   -symbol for interface
∞   -symbol for gas phase volume
V_S^0- initial solid phase volume, m^3
V_S –solid phase volume at t=t, m^3
S   -mass transfer surface area, m^2
Δm –naphthalene support mass variation, kg
Δt   -time interval, s
α   - heat transfer individual coefficient, W/m^2 K
ΔH_S- latent sublimation heat, J/kg
T   -temperature

$$Nu = \frac{\alpha l}{\lambda}$$ - Nusselt number

$$Sh = \frac{kl}{D_A}$$ - Sherwood number

$$Pr = \frac{C_p \eta}{\lambda}$$ - Prandtl number

$$Sc = \frac{\eta}{\rho D_A}$$ - Schmidt number

η   -gas phase dynamic viscosity, Pa*s
ρ   -gas phase density, kg/m^3
C_p -gas phase specific heat, J/kg K

l   -characteristic length, m

λ -gas phase thermal conductivity coefficient, W/m K

EXPERIMENTAL SECTION

In order to make the experiments, we used the laboratory installation presented in the Figure 8. According to Figure 8, the installation is composed from a cylindrical column (1), made from heat resistant glass, and which represents the sublimation chamber, the air heating room (the entrainer) (2), the fan for air transportation (3), the rotameter for air flow rate measurements (4), the thermometers (5) and (6), the valve which regulates the air flow rate (7), and the autotransformer used to adjust the temperature in sublimation chamber. The sublimation chamber is equipped inside with a device (1a) to hold the support on which the sublimation particle will be fixed. The entrainer (air) gets in the sublimation chamber through a coupling positioned in upper side, and gets out through the existing at lower side. The heating room makes the entrainer warm using an electrical resistance powered by the current supply through autotransformer (8).
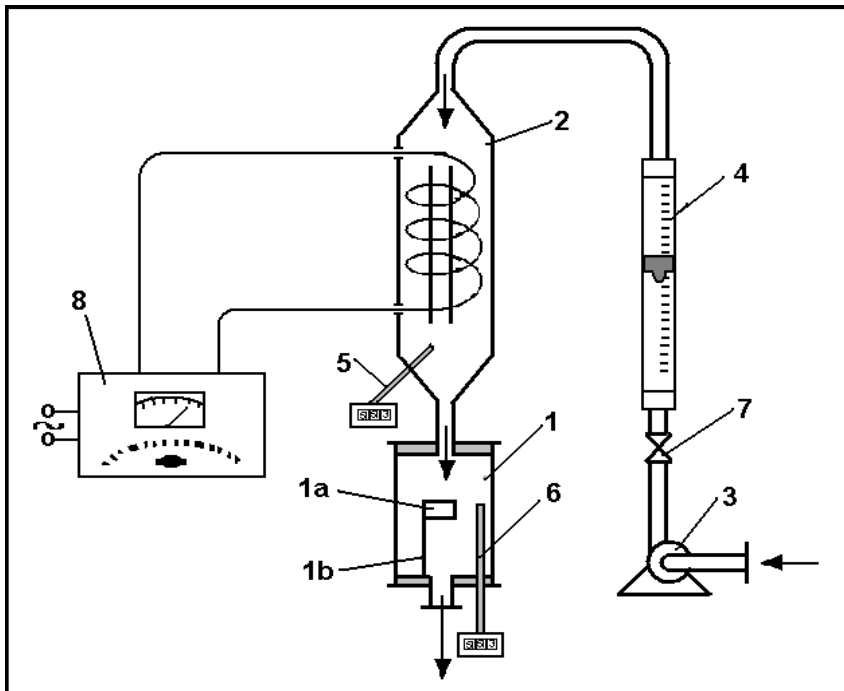
Figure 8. Experimental setup. 1 - cylindrical column, 2 –, air heating room
3 – fan, 4 –rotameter, 5, 6 – thermometers, 7 – valve, 8 – autotransformer.

For the experiments it was used naphthalene, with air as entrainer. The naphthalene was inserted melted in the cylindrical slot of each support. The support allows the contact with the gaseous entrainer only on the frontal side of the naphthalene cylinder solidified in the slot. This has a diameter d=10 mm and height H=100 mm.

In each of the experiments a single naphthalene support was used. The temperature in sublimation room during each experiment was kept constant. Three temperatures were used: 50^0 C, 60^0 C, 70^0 C and several values of entrainer flow rate (air):1.5, 2.0, 2.5, 3.0 and 3.5 m^3/h.

REFERENCES

1. E. Bratu, "Operatii unitare in ingineria chimica", E.T. Bucuresti, **1985**, chapter 28.
2. J. H. Perry, "Perry' Chemical Engineers' Handbook" 4th Ed., Mc Graw Hill, New York, **1963**, section 17.
3. P. K. Halder, D. Amitara, *Proc. Int. Conf. Fluid. Bed. Combust.* 12 th, **1993**, *2*, 1223.
4. J. J. Lombrano, M. C. Villaran, *J. Chem. Eng. Jpn.*, **1993**, *26(4)*, 389.
5. F. W. Larry, W. Bruce, D. J. William, *Appl. Energy*, **1993**, *46(2)*, 161.
6. N. J. Nassif, W. S. Janna, G. S. Jakubowski, *Int. Heat Mass Transfer*, **1995**, *38(4)*, 691.
7. C. Keumnam T. F. Irvine Jr., J. Karni, *International Journal of Heat and Mass Transfer*, **1992**, *35(4)*, 957.
8. H. H. Songin, *J. Heat Transfer*, **1991**, *113(3)*, 772.
9. S. W. Peng, G. Q. Chen, *International Journal of Energy Research*, **1993**, *17(3)*, 193.
10. S. W. Peng, G. Q. Chen, *J. Heat Transfer*, **1994**, *116(1)*, 215.
11. R. Joulie, G. M. Rios, *Drying Technology,* **1993**, *11(1)*, 157.
12. S. P. R. Mendes, *Exp. Therm. Fluid. Sci.*, **1991**, *4(5)*, 510.
13. S. Zhai, H. Su, R R. Taylor, N.K.H. Slater, *Chem. Eng. Sci.*, **2005**, *60*, 1167.
14. J. Y. Kim, T. H. Song, *Int. J. Heat Mass Transfer*, **2003**, 46, 3051.
15. S. D. Hwang, I. H. Jang, H. H. Cho, *Int. J. Heat Fluid Flow*, **2006**, 27, 21.
16. M. A. Siddiqi, B. Atakan, *Thermochimica Acta*, **2006**, *452*, 44.
17. H. Wu, Z. Tao, G. Chen, H. Deng, G. Xu, S. Ding, *Chem. Eng. Sci.*, **2004**, *59*, 2921.

Dedicated to Professor Liviu Literat, at his 80th anniversary

MOLECULAR DYNAMICS SIMULATION OF THE HEAT TRANSFER BY NATURAL CONVECTION

SOARE GHEORGHE[a]

ABSTRACT. The heat transfer by natural convection between a surface of Cu (001) and water was studied with molecular dynamics simulation. A temperature gradient in a metal wall generates an electric charges gradient. On the cold face of the wall there are more electrons, as a result of the Thomson effect. On metal surface there are defects (dislocations, steps, terraces, kinks) and the electrons are not uniformly distributed. On the high defects there are more electrons than on the deep defects. From energetically point of view the metal surface is inhomogeneous. The molecules of the liquid are adsorbed on the metal surface and a small fraction of the molecular orbital overlaps on the orbital of the metal. The overlap allows the phonon exchange process between the adsorbed liquid molecules and the metal atoms. The proposed model takes into account both the process of metal surface reconstruction and the process of molecular cluster formation in liquid. The high defects are active centres which generate the movement of the liquid clusters over the metal surface. The results of the simulations show that the combination of these processes can gives a consistent prediction of the heat transfer coefficient by natural convection.

Keywords: convection, heat transfer, modelling, molecular scale

INTRODUCTION

It is an indubitable fact that flow and thermal phenomena can be only understood fundamentally by a molecular approach. Unfortunately, very few works were dedicated to study heat transfer mechanism through natural convection to molecular scale. A molecular model of the convection heat transfer mechanism is proposed in an anterior work [1], and a modality of calculation of the heat transfer efficiency in the molecular mechanism was analyzed in the work [2]. In an other work [3], the equilibrium of heat conduction in a very thin solid film, using molecular dynamics simulation with different boundary conditions, material, parameters and lattice configurations

---

[a] *Universitatea Politehnica din Bucureşti, Facultatea de Chimie Aplicată şi Ştiinţa Materialelor, Str. Polizu, Nr. 1, RO-011061 Bucureşti, Romania, g_soare@chim.upb.ro*

was studied. Many issues involved in the convection heat transfer are common and other scientific fields such as nano-tribology. Some of them are: adsorption of the molecules of lubricant on the solid surface and molecularly arrangement and flow of the lubricant in the boundary layer. More works were published in the area of the nanotribology [4-11]. In these works different aspects of the friction have been approached at molecular scale: static lubrication, dynamic lubrication, lubrication in boundary regime, the influence of molecule configuration, molecular rearrangements in a molecularly thin film between two solid surfaces during shear, etc.

In the present work a physical model and a mathematical model of convection heat transfer at molecular scale are proposed. The models take in consideration the elementary phenomena which take place on the solid fluid interface: adsorption, diffusion over surface, solid surface reconstruction and the transfer of the phonons to the adsorbed molecules of fluid. Molecular dynamics simulation helps to clarify some aspects of the convection mechanism.

RESULTS AND DISCUSSION

Physical model

To formulate physical model consider metal flat plate of Figure 1, in contact with two fluids (a hot fluid with temperature t_1 and a cold fluid with temperature t_2). The surfaces of the wall are heterogeneous in terms of energy. The heat transfers from hot fluid to cold fluid, in conformity with the molecular mechanism which was formulated by author in [1] and [2], and shown in Figure 1. An improved version of the physical model will be presented briefly below. The existence of a temperature gradient in direction of the solid wall thickness, $(t_{w1} > t_{w2})$, generates a gradient of density of the free electrons of metal (Thomson effect), so on the colder surface the density of the free electron N_2 is greater than the density of the electrons which are on the warmer surface, N_1.
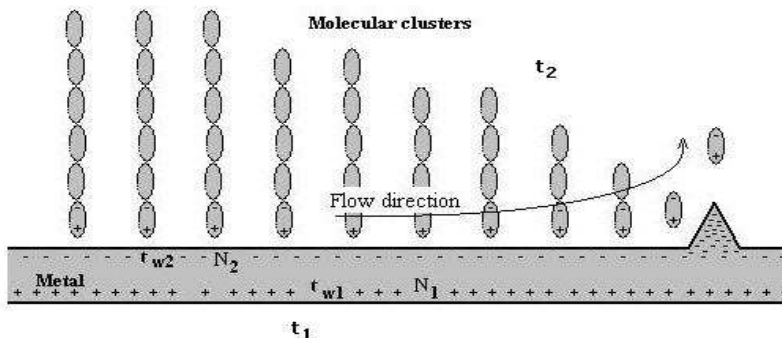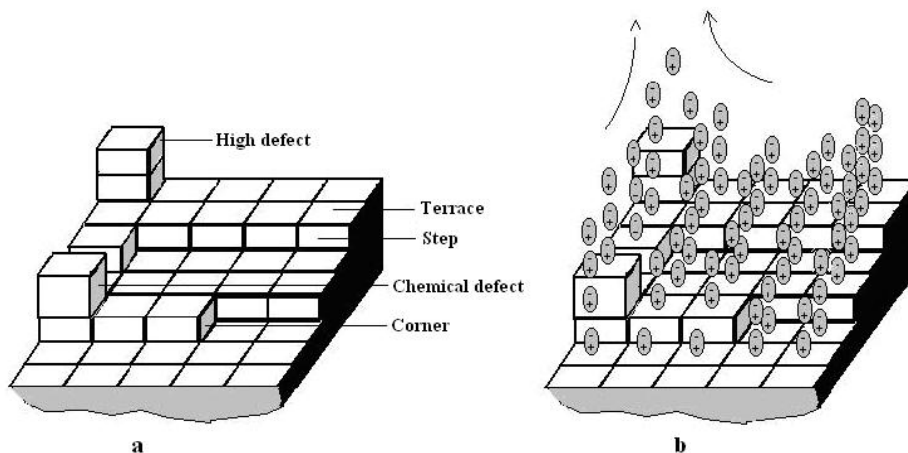

Figure 1. Physical model.

Figure 2. a) Possible defects of the solid surface. For simplicity, the atoms of the solids were represented as a parallelepiped,
b) Molecular multilayer adsorbed on the surface. The two arrows indicate the flow of the molecules and clusters of molecules.

The cold face is loaded with negative electrical charges and the hot face remains positively charged. Free electrons can not be spread evenly on the surface of the metal because the surface is not a perfect plane. Because of surface defects (dislocations, terraces, stairs, corners), see Figures 1 and 2, these electrons are preferentially distributed on the surface. On the high defects the electron density is greater than the electron density on both deep defects and the terraces which exist on the metal surface. For this reason, on the high defects is a greater intensity of the electric field which is generated by these electric charges. The molecules of liquid are adsorbed on the metal surface. Adsorbed molecules move over the surface and capture phonons from the crystalline metal. The movement is a result of the following forces action:

- the forces of attraction and repulsion between molecules in fluid;
- the forces of attraction and repulsion between the molecule of the fluid and solid;
- the forces of attraction and repulsion between the adsorbed molecule and nearest high defects, where the electric field is more intense.

Movement of the adsorbed molecules is directed towards nearest high defect, which becomes an active centre that generates natural convection.

Migration of the molecules over the surface, under the action of the above-mentioned forces, intensifies the emission of the phonons. Permanent dipoles molecules can migrate more quickly than originally non polar molecules. But a non polar molecule becomes a polar one as a result of an

217

inductive polarization process. In accordance with the mechanism proposed in this theory, the process of heat transfer by natural convection implies: adsorption, polarization and an induced movement towards the active centres of the solid surface, the phonons capture and expulsion of molecules outside the solid-fluid interface.

Effectiveness of the phonons absorption process

The absorption of the phonons is conditioned by adsorption of liquid molecules on the solid surface, and it involves formation of bounds between the fluid molecules and metal atoms. These bounds imply overlapping of atomic and molecular orbital. If the overlapping degree is higher, the capture of the phonon is more efficient, meaning that will increase the quantity of transferred energy. Also, the overlapping of the orbital allows an exchange of electrons between the molecules and atoms of metal, which means an energy exchange process.
In this work we consider that the degree of overlapping orbital is, in conformity with [2]:

$$\eta = \frac{EB_{ms}}{E_{ms}} \tag{1}$$

 where:

$$EB_{ms} = \frac{E_{m-m}}{2} + E_s^0 \, (1 - C_F) + \gamma_P \, (\chi_m - WF_s)^2 \tag{2}$$

In which:

$$C_F = 2 \, (1 - \frac{V_s}{N_A})$$

$$E_{ms} = 4 \, \varepsilon \left[\left(\frac{\sigma}{r} \right)^{12} - \left(\frac{\sigma}{r} \right)^6 \right] \tag{3}$$

In equations (1 – 3) EB_{ms} is the energy of a hypothetical chemical bond of molecule with solid surface [12], E_{ms} is the Lennard-Jones (LJ) 12-6 potential energy between molecule and solid surface, E_{m-m} is molecule-molecule bond energy, E^o_S – electron energy on surface, N_A - a constant, WF_S - work function of the metal surface (energy), r - current distance surface-molecule, Vs - valence of the solid, γ_P – a constant, χ - electronegativity, ε – LJ energy parameter, σ - LJ length parameter.

Solid surface reconstruction

The reconstruction of the surface of the metal should be understood as a change in topography of the surface, imposed by the forces which act

on the solid-fluid interface during the convection heat transfer [13]. Under the action of such forces, deep defects and high defects are continuing to appear on the solid surface. The probability with which an atom of a crystal forms a high defect is given by Boltzmann factor:

$$P = e^{-\frac{E_d}{K_{\mathbf{B}} T}}$$ (4)

In which: E_d is the energy of displacement of a particle, K_B - Boltzmann constant, T - absolute temperature.

If there are N_S atoms per unit area of solid, the number n_S of defects is:

$$\frac{n_S}{N_S - n_S} = e^{-\frac{E_S}{K_{\mathbf{B}} T}}$$ (5)

But n_S is much smaller than N_S and then we can write:

$$n_S = N_S \, e^{-\frac{E_S}{K_B T}}$$ (6)

The high defects appear together with the Schottky defects too, by bringing of an atom from the crystal at surface. The number of these defects, in a similar way, is expressed as follows:

$$n_V = N_V \, e^{-\frac{E_V}{K_B T}}$$ (7)

In which: E_V is the energy necessary to transport an atom from inside of the crystal to the surface, and N_V - the number of atoms inside unit volume per unit surface. The total number of high defects on the solid surface, in thermal equilibrium, is:

$$n_T = n_S + n_V$$ (8)

Mathematical model

On the base of the physical model, presented above, was formulated the mathematical model, taking into account all this elementary processes and the assumptions which follow:
- the temperature of the surface of the wall is constant;
- in solid, the transversal acoustic phonons are only considered;
- the attractive and repulsive forces, presented above, are electrostatic in nature.
Mathematical model is formed, mainly, from equations (1-11).
The convection heat transfer coefficient is expressed in the classical way:

$$\alpha = \frac{Q}{A\left(t_w - t_f\right)} \tag{9}$$

In equation (9), A is the heat transfer area, Q – heat flow rate, t_w – temperature of the surface of the wall, and t_f - fluid temperature.

The heat flow rate is the energy of the absorbed phonons in the interval of time in which the molecules are adsorbed on the solid surface. The energy of a phonon is:

$$\varepsilon = h\upsilon \tag{10}$$

In which: h is Plank constant and υ - phonon frequency.

The time in which the molecules of fluid are adsorbed on the surface is calculated with velocity of the molecules. The velocity is a result of the forces which act on the molecules [3].

The coverage degree x_a of metal surfaces by adsorption molecules of liquid has been calculated with a specific equation [17]:

$$x_a = \frac{k_0}{\sqrt{T}} \exp\left(\frac{E_a}{K_B T}\right) \tag{11}$$

In which: k_0 is a constant, T - absolute temperature and E_a – adsorption energy.

The equation includes the influence of temperature, so that coverage of the surface with adsorbed molecules of liquid is a function of both the temperature and the topology of the surface of the wall.

The basis of the calculations

In order to calculate the convection heat transfer coefficient it was considered the surface of copper Cu (001), a face-centered-cubic metal. On this surface high defects are placed in the four tips of a square. In our simulations, we considered that all high defects are in the same form and contain the same number of atoms, namely 50 atoms in a conical arrangement with four layers. The surface of the copper is in a process of restructuring and the number of defects is a function of temperature, as equations (6) and (7) show, and the topological data of the surface are in a continuous change when temperature changes. The defects can diffuse over copper surface [14]. Rising of the temperature leads to rising of the number of defects, but the form and dimensions of the defects are conserved. It was not taken into account reduction in the number of defects (active centres) by the phenomenon of self-coalescence. In order to calculate the force which acts on the clusters we considered the closest 25 active centres around a cluster. The molecules of liquid form cluster with variables size. The energy of the clusters was calculated with a Lennard-Jones

potential, and the energy of adsorption metal-cluster was calculated with a Lennard-Jones potential too, [6] and [15]. The number of molecules in an adsorbed cluster on the surface decreases because of the shear stress that appears during of the flowing. In the dynamic simulation of their diffusion, the liquid clusters have a rectilinear trajectory and the velocity is a function of time.

Results of simulations

The convection heat transfer coefficient was calculated with an own computer program of calculation, based on the mathematical model described above, and using MATLAB programming language. The heat transfer process by natural convection from the surface of Cu (001) to water was simulated. Calculus of the convection heat transfer coefficient was made in the assumption that water forms linear clusters with 6 molecules (hexamers), which are oriented perpendicularly to the surface of heat transfer. Figure 3 shows the convection heat transfer coefficient as a function of difference between the solid temperature and the liquid temperature. Values obtained with the classical equations (12, 13) [16], and those obtained with the proposed model are in good harmony.

$$Nu = 0.54 \left(Gr \, Pr \right)^{1/4} \quad for \ 10^4 < Gr \, Pr < 10^7 \tag{12}$$

$$Nu = 0.15 \left(Gr \, Pr \right)^{1/3} \quad for \ Gr \, Pr > 10^7 \tag{13}$$
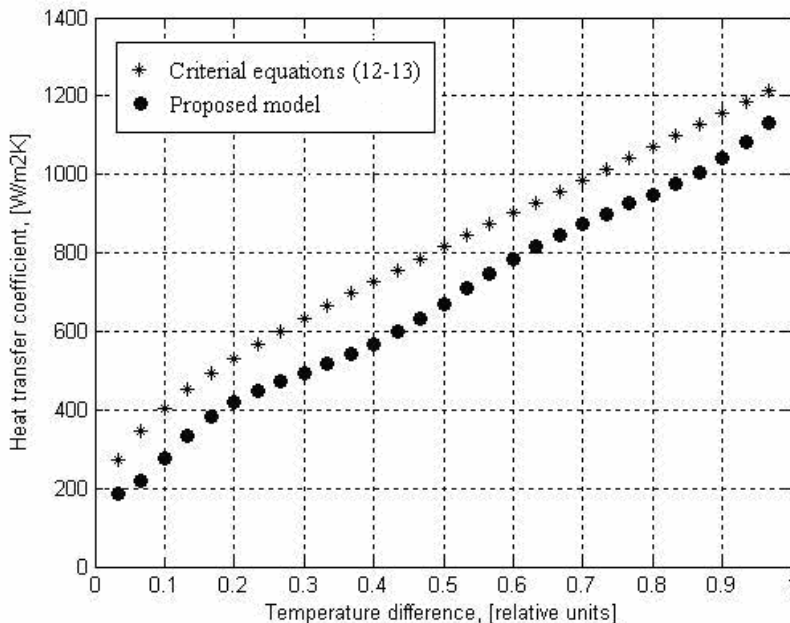
Figure 3. Heat transfer coefficient by natural convection in the system water / Cu (001).

The sinuosity of the curve obtained with the proposed model in this work is due to the phenomenon of surface reconstruction and is frequently observed in experimental measurements.
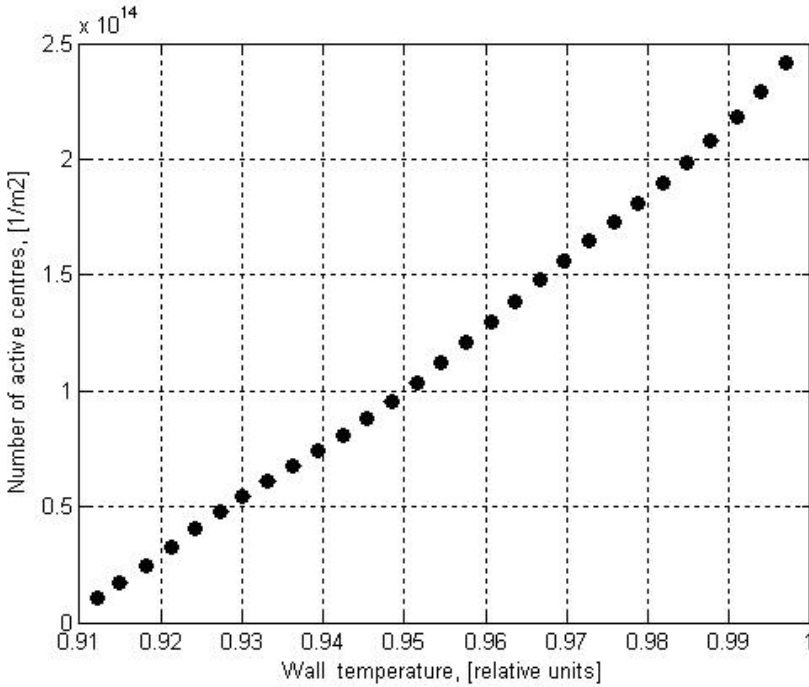

Figure 4. The restructuring of the copper surface quantitatively expressed by the number of active centres involved in the convection heat transfer.

As noted above, surface reconstruction is the modification of copper surface topology as a result of the copper atoms diffusion to the surface. Increasing of the metal temperature leads to increasing of the number of high defects, which are in fact cluster of atoms of copper. The result of the copper surface restructuring simulation is quantitatively expressed by the number of active centres involved in the convection heat transfer. Figure 4 shows this phenomenon.

But, increasing the number of active centres increase intensity of heat transfer process by natural convection, Figure 5.

Through the phenomenon of surface reconstruction, the natural convection mechanism is similar to the mechanism of heat transfer in boiling. The intensity of the heat transfer in boiling increases with the difference temperature because the number of nucleation centres increases.

222

Another issue considered is that of changing the thickness of adsorbed molecular layer, flowing on the surface solid. In the process of heat transfer, the thickness of the adsorbed fluid multilayer does not remain constant.
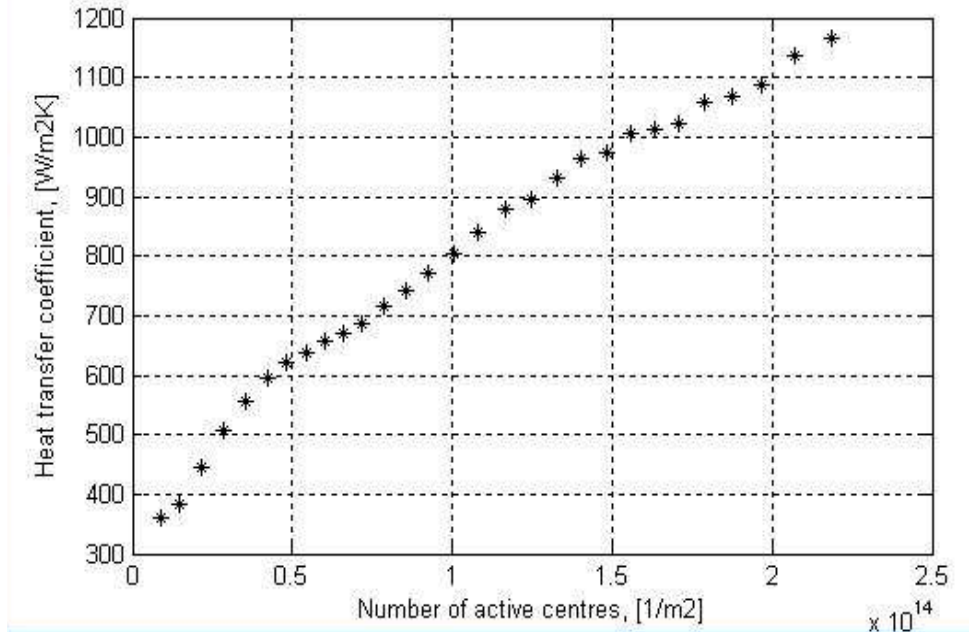
Figure 5. Reconstruction of the surface affects intensity
of the natural convection.

We considered that water molecular clusters initially consist in six molecules linearly arranged. The thickness of this layer of molecules varies due the impulse transfer process, which implies a shear stress. Figure 6 shows this change in thickness of the layer, for a difference between the temperature of the wall and the temperature of the water of 5K.

The heat transfer coefficient data, presented above in Figure 3, were obtained, taking account changing in the thickness of the layer of water molecules adsorbed in the form of cluster. Results of simulations show that cluster mass strongly influences the convection heat transfer coefficient, i.e. increases with decreasing of the cluster's mass.
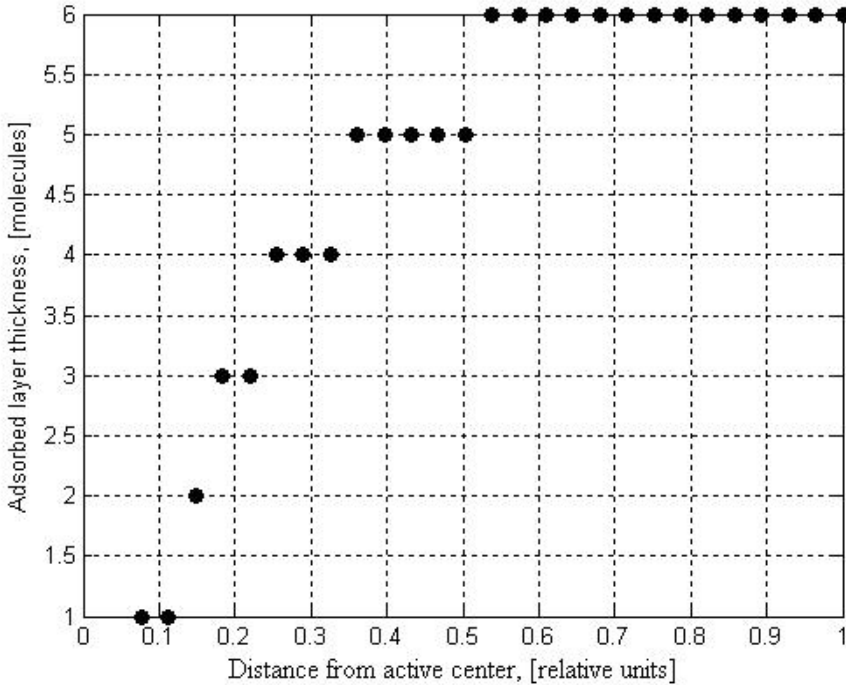
Figure 6. Changing the thickness of the water multilayer during of the convection heat transfer.

This change in thickness of the multimolecular layer is similar to that of reducing the hydrodynamic boundary layer, known from boundary layer theory, when the flow changes from laminar regime to turbulent regime.

CONCLUSIONS

A physical and a mathematical model of convection heat transfer, at molecular scale, were formulated.

Using molecular dynamics method and with an own computer program, the convection heat transfer and the surface reconstruction of the Cu (001) were simulated. The convection system which was investigated is water on Cu (001). The mass and dimensions of the molecular clusters largely affect the rate of heat transfer. If the mass decreases, the convection heat transfer coefficient increases.

The phenomenon of surface reconstruction, its influence on the intensity of convection heat transfer process, and continuously changing of the boundary layer thickness were outlined quantitatively.

Simulation of the process at molecular scale emphasizes the conclusion that between the mechanism of natural convection and the mechanism of heat transfer in boiling there is an obvious similarity.

The results of the simulations show that combining all these processes we can give a consistent prediction of the heat transfer coefficient by natural convection.

Proposed model is a more realistic image of the process of natural convection than the boundary layer theory.

REFERENCES

1. G. Soare, Proceedings of the 15-th International Congress of Chemical and Process Engineering 25-29 August **2002**, Praha, Czech Republic.
2. G. Soare, Proceedings of the 4-th European Congress of Chemical Engineering, 21-25 Sept **2003**, Granada, Spain.
3. H. Xue, C. Shu, *Int. J. Num. Meth. Heat Fluid Flow*, **1999,** *9*, 60.
4. J. Gao, W. D. Luedtke, D. Gourdon, M. Ruths, U. Landman, *J. Phys. Chem. C*, **2004,** *108*, 3410.
5. T. S. Cui, C. McCabe, P. T. Cummings, H. D. Cochran, *J. Chem. Phys.* **2003,** *118*, 8941.
6. G. He, M. H. Muser, M. O. Robbins, *Science*, **1999**, *284*, 1650.
7. E. A., Jagla, *Phys. Rev. Lett.*, **2002,** *88*, 5504.
8. Z. R. Lei, J. A. Gellman, F. C. McFaden, *Langmuir*, **2001,** *17*, 6240.
9. E. Manias, I. Bitsanis, G. Hadziioannou, G. Ten Brinke, *Langmuir*, **1996**, *12*, 4587.
10. E. Manias, I. Bitsanis, G. Hadziioannou, G. Ten Brinke, *Europhys. Lett.*, **1996**, *33*, 371.
11. R. I. Masel, "Principles of Adsorption and Reaction on Solid Surfaces", John Wiley & Sons, Inc., NY, **1996**, chapter 3.
12. M. Muser, O. M. Robbins, *Phys. Rev. B*, **2000,** *61*, 2335.
13. C. Kittel, "Introduction to Solid State Physics", 5-th Ed., John Wiley & Sons, Inc., NY, **1976**, chapter 17.
14. J. Yang, W. Hu, M. Xu, *Applied Surface Science*, **2008,** *255*, 1736.
15. J. Shuz, O. J. Davies, *Phys. Stat. Sol. A*, **1983**, *78*, 595.
16. P. F. Incropera, P. D. DeWitt, "Introduction to Heat Transfer", John Wiley & Sons, Inc., NY, **2002**, chapter 9.
17. M. S. Pierce, K-C. Chang, D. C. Hennessy, V. Komanicky, A. Menzel, H. You, *J. Phys. Chem. C. Lett.*, **2008,** *112*, 2231.

Dedicated to Professor Liviu Literat, at his 80th anniversary

SIMULATION OF A POLYMERIZATION LAMINAR FLOW REACTOR

IONUȚ BANU[ab], SORIN BÎLDEA[a], GRIGORE BOZGA[a], JEAN-PIERRE PUAUX[b]

ABSTRACT. The paper presents a simulation study of the methyl methacrylate solution polymerization process occurring in a laminar flow tubular reactor. The simulation results are evidencing the main particularities of the polymerization process induced by the laminar flow of the reaction mixture, as well as the practical suitability of this operating regime. The influence of the main process parameters on the reactor behavior is investigated. Also a comparison of the process simulation results obtained in laminar flow and plug flow assumptions is presented.

Keywords: MMA polymerization, laminar flow reactor

INTRODUCTION

The poly-methyl methacrylate (PMMA) is a polymer with good optical and mechanical properties. Currently it is obtained by free-radical polymerization of the methyl methacrylate (MMA), which can be performed in batch or tubular reactors. Solution polymerization is a convenient technique to avoid the usual heat transfer difficulties specific for bulk polymerization. The usual solvents for polymerization of MMA are toluene [1, 2] and ethyl acetate [3, 4], while azobis-isobutyronitrile (AIBN) or benzoyl peroxide (BPO) are used as initiators. One of the difficulties in modeling MMA polymerization system is the description of diffusion phenomenon in viscous reaction mixture (the so-called gel effect or Trommsdorf effect) [5]. For bulk polymerization, the gel effect is important at high monomer conversions. For solution polymerization, it is significant at high monomer to solvent ratios. A complete study of the behavior of a MMA semi-batch polymerization reactor with solvent and monomer addition in different operating conditions was published by Louie and Soong [6].

---

[a] *Universitatea Politehnica din Bucureşti, Facultatea de Chimie Aplicată şi Ştiinţa Materialelor, Str. Polizu, Nr. 1, RO-011061 Bucureşti, Romania, g_bozga@chim.upb.ro*
[b] *Université de Lyon, Université Claude Bernard, Lyon, France*

The description of the mixture flow is one of the most important issues in the building of a mathematical model for the polymerization processes taking place in tubular reactors. Ideal flow models were used by Baillgou et Soong [7], Ponnuswamy et al [1] and Crowley et Choi [8]. They considered constant axial flow velocities with small corrections due to the density change [7, 9]. The complexity of the kinetic mechanism and the heat transfer which is hindered by the varying viscosity also make difficult the development of the mass and heat balance equations.

It is well known that, on axial direction of a tubular reactor, the convective transport is dominant, while in the radial direction the transport by diffusion mechanism is more important. The validity of these hypotheses was verified in the published literature [10, 11]. Cintron-Cordero et al [12] developed a two-dimensional flow model and compared the flow equations with or without the convective terms in radial direction. They observed that the errors are smaller than 3 % when the radial convection was neglected. Lynn et al [13] showed that the hypothesis of constant axial velocity will generate some errors due to the large variations in viscosity of the reaction mixture. They also proposed a method to calculate the profile of the axial velocity in a two-dimensional model, which was implemented in other published studies (Wyman et Carter [14], Baillagou et Soong [2]). If the axial dispersion is taken into account, the solution is obtained by discretization of both axial and radial directions [9, 11]. If axial dispersion is not considered, the method of lines is commonly used for the discretization in radial direction [15].

The objective of this study is to theoretically investigate the main features of the MMA solution polymerization process in a laminar flow tubular reactor. The kinetic model for the MMA solution polymerization process was chosen in one of our previous papers [16] by reviewing the published kinetic models. Further it is used to solve the mathematical model of MMA laminar flow polymerization reactor. The mathematical model and the solution method are discussed. Afterwards, the results of the simulation study as well as the influence of various operating parameters on the reactor behavior are presented and analyzed.

RESULTS AND DISCUSSIONS

Mathematical model of the MMA polymerization process in a laminar flow tubular reactor

The polymerization technique investigated in this work is the steady state MMA polymerization in solution. The kinetic model published by Baillagou and Soong [7, 17] is used. The gel effect is described by the model proposed by Chiu et al [5], the constitutive equations being presented in Table 1. The characteristics of the reactor are displayed in

Table 2. Because of the strong exothermicity of the polymerization reaction, a high value of length to diameter ratio is chosen, which provides a sufficiently high heat transfer area.

Table 1. Gel effect constitutive equations [17]

$$k_t = \frac{k_{t,0}}{1 + \dfrac{k_{t,0}\theta_t\lambda_0}{D_{ef}}} \; ; k_p = \frac{k_{p,0}}{1 + \dfrac{k_{p,0}\theta_p\lambda_0}{D_{ef}}} \; ; D_{ef} = \exp\left(\frac{2.3\phi_m}{A + B\phi_m}\right)$$

$$\theta_t = \frac{1}{4.4533\times10^{18} c_{I,0} \exp\left(-\dfrac{17413}{T}\right)}$$

$$\theta_p = \frac{1}{2.5292\times10^{15} \exp\left(-\dfrac{14092}{T}\right)}$$

$$A = 0.168 - 8.21\times10^{-6}\left(T - T_{gp}\right)^2 \; ; B = 0.03$$

Table 2. Reactor characteristics

Process parameter	Numerical value
Total mass flow rate / [kg/s]	10^{-3}
Feed initiator concentration (c_{I0}) / [mole/L]	0.05
Toluene mass fraction in the feed	0.5
Reactor length / [m]	8
Reactor diameter (d_t) / [m]	2×10^{-2}
Feed temperature / [^{O}C]	80
Thermal agent temperature / [^{O}C]	80

The radial convection terms are ignored because the tube length is much larger than the radius. In the axial direction, mass diffusion and heat conduction are assumed to be negligible compared to the convective terms. Variations of monomer conversion and consequently of mixture viscosity and density produce strong variations in the axial velocities. The flow is considered fully developed at the reactor entrance and the velocity profiles along the reactor axis are calculated using the method proposed by Lynn and Huff [13]. The physical properties (density, viscosity, thermal conductivity) of the reaction mixture are estimated using relations published in literature [2, 7, 17, 18].

The mathematical model of the polymerization process includes the mass balance equations for initiator (1) and monomer (2), the equations describing the evolutions of the *m*-moments (*m*=0, 1, 2) of live and dead polymer molecular weight distribution (3) and (4), as well as heat balance equation (5).

$$\frac{\partial c_I}{\partial z} = -\frac{c_I}{u_z}\frac{\partial u_z}{\partial z} + \frac{1}{u_z}\left(\frac{D}{r}\frac{\partial c_I}{\partial r} + D\frac{\partial^2 c_I}{\partial r^2}\right) + \frac{r_I}{u_z} \tag{1}$$

$$\frac{\partial c_M}{\partial z} = -\frac{c_M}{u_z}\frac{\partial u_z}{\partial z} + \frac{1}{u_z}\left(\frac{D}{r}\frac{\partial c_M}{\partial r} + D\frac{\partial^2 c_M}{\partial r^2}\right) + \frac{r_M}{u_z} \tag{2}$$

$$\frac{\partial \lambda_m}{\partial z} = -\frac{\lambda_m}{u_z}\frac{\partial u_z}{\partial z} + \frac{1}{u_z}\left(\frac{D}{r}\frac{\partial \lambda_m}{\partial r} + D\frac{\partial^2 \lambda_m}{\partial r^2}\right) + \frac{r_{\lambda_m}}{u_z} \tag{3}$$

$$\frac{\partial \mu_m}{\partial z} = -\frac{\mu_m}{u_z}\frac{\partial u_z}{\partial z} + \frac{1}{u_z}\left(\frac{D}{r}\frac{\partial \mu_m}{\partial r} + D\frac{\partial^2 \mu_m}{\partial r^2}\right) + \frac{r_{\mu_m}}{u_z} \tag{4}$$

$$\frac{\partial T}{\partial z} = \frac{1}{\rho c_p u_z}\left(\frac{k}{r}\frac{\partial T}{\partial r} + k\frac{\partial^2 T}{\partial r^2}\right) + \frac{r_T}{\rho c_p u_z} \tag{5}$$

Axial symmetry, the absence of the mass transfer through the reactor wall and the continuity of heat flux at the reactor wall impose the following boundary conditions:

$$r = 0: \frac{\partial c_M}{\partial r} = \frac{\partial c_I}{\partial r} = \frac{\partial \lambda_m}{\partial r} = \frac{\partial \mu_m}{\partial r} = \frac{\partial T}{\partial r} = 0$$

$$r = R: \frac{\partial c_M}{\partial r} = \frac{\partial c_I}{\partial r} = \frac{\partial \lambda_m}{\partial r} = \frac{\partial \mu_m}{\partial r} = 0, \frac{\partial T}{\partial r} = \frac{U}{k}\left(T_b - T\right) \tag{6}$$

The inlet boundary conditions are:

$$z = 0: c_M = c_{M0} , c_I = c_{I0} , \lambda_m = 0 , \mu_m = 0 , T = T_f \tag{7}$$

It is considered that the main resistance to the heat transfer occurs inside the reactor. Therefore, the overall heat transfer coefficient, U, is approximated by the internal partial heat transfer coefficient calculated by the equation (8), where the variation of the viscosity at the wall is neglected and the ratio η / η_p approaches unity [18]:

$$Nu\left(\frac{\alpha d_t}{k}\right) = 3.66 + \frac{0.19 Gz^{0.8}}{1 + 0.177 Gz^{0.467}}\left(\frac{\eta}{\eta_p}\right)^{0.14} \tag{8}$$

The generating terms r_p (with p = I, M, λ_m, μ_m, T) in equations (1) - (5) are [1]:

$$r_I = -k_d c_I \tag{9}$$

$$r_M = -\left(k_p + k_{tm}\right) c_M \lambda_0 \tag{10}$$

$$r_{\lambda_0} = 2 f k_d c_I - k_t \lambda_0^2 \tag{11}$$

$$r_{\lambda_1} = 2 f k_d c_I + k_p c_M \lambda_0 + \left(k_{tm} c_M + k_{ts} c_S\right)\left(\lambda_0 - \lambda_1\right) - k_t \lambda_0 \lambda_1 \tag{12}$$

$$r_{\lambda_2} = 2 f k_d c_I + \left(2\lambda_1 + \lambda_0\right) k_p c_M + \left(k_{tm} c_M + k_{ts} c_S\right)\left(\lambda_0 - \lambda_2\right) - k_t \lambda_0 \lambda_2 \tag{13}$$

$$r_{\mu_0} = \left(k_{tm} c_M + k_{ts} c_S\right)\lambda_0 + \left(k_{td} + 0.5 k_{tc}\right)\lambda_0^2 \tag{14}$$

$$r_{\mu_1} = \left(k_{tm} c_M + k_{ts} c_S\right)\lambda_1 + k_t \lambda_0 \lambda_1 \tag{15}$$

$$r_{\mu_2} = \left(k_{tm} c_M + k_{ts} c_S\right)\lambda_2 + k_t \lambda_0 \lambda_2 \tag{16}$$

In the energy balance, as generally accepted, only the heat generated in propagation reactions and chain transfer to monomer is considered [7, 17]:

$$r_T = -\Delta H_p \left(k_p + k_{tm}\right) c_M \lambda_0 \tag{17}$$

The polymerization enthalpy, $\Delta H_p = -5.48 \times 10^4 \, \text{J/mol}$, is taken from the reference [19]. The same diffusivity coefficient having a value of $D = 10^{-10} \, \text{m}^2/\text{s}$ is used in equations (1) - (4) for all the species [2].

In this work the derivatives with respect to the radial direction are approximated by a second order finite difference scheme. After discretization, the equation (1) becomes:

$$\frac{dc_{M,i}}{dz} = c_{M,i+1} \frac{1}{u_{z,i}} A_i + c_{M,i} \frac{1}{u_{z,i}} \left(-\frac{\partial u_{z,i}}{\partial z} - B_i \right) + c_{M,i-1} \frac{1}{u_{z,i}} C_i + \frac{r_{M,i}}{u_{z,i}} \quad (18)$$

Where the coefficients A_i, B_i, C_i are given by:

$$A_i = \frac{D}{2r_i \Delta r} + \frac{D}{(\Delta r)^2}; \ B_i = -\frac{2D}{(\Delta r)^2}; \ C_i = -\frac{D}{2r_i \Delta r} + \frac{D}{(\Delta r)^2}, \ i = 2,3,..,N \quad (19)$$

At $i = 1$ the equation (1) becomes indeterminate since both r and $\frac{\partial c_M}{\partial r}$ be-come zero. Applying the l'Hospital rule and assuming symmetry about the centerline [20]:

$$A_1 = \frac{4D}{(\Delta r)^2} \ ; \ B_1 = -\frac{4D}{(\Delta r)^2} \ ; \ C_1 = 0 \quad (20)$$

To minimize the calculation effort, the derivative $\frac{\partial u_z}{\partial z}$ was approximated by finite difference ratios:

$$\frac{\partial u_{z,k}}{\partial z} = \frac{u_{z,k} - u_{z,k-1}}{z_k - z_{k-1}} \quad (21)$$

where k refers to integration steps in the axial direction.

As a result, the original PDE's were transformed into a system of ODE's along the axial coordinate. The ODE's were solved by a Runge-Kutta procedure method implemented in MATLAB® [21].

Reactor simulation

In order to select the number of intervals on the radial coordinate, a comparison of different discretization grids was performed. Practically identical results were obtained when the number of grid points was increased over 50. Therefore, a number of 50 radial points was chosen, as a compromise between accuracy and calculation effort.
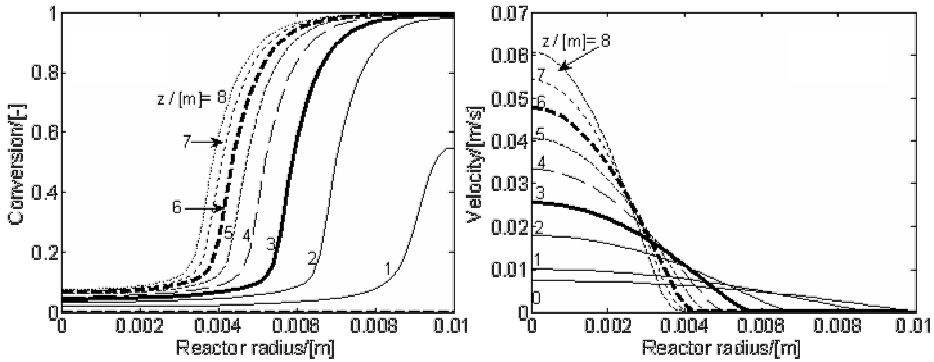
Figure 1. Profiles for monomer conversion (left) and axial velocity (right), at different positions (z) along the reactor.
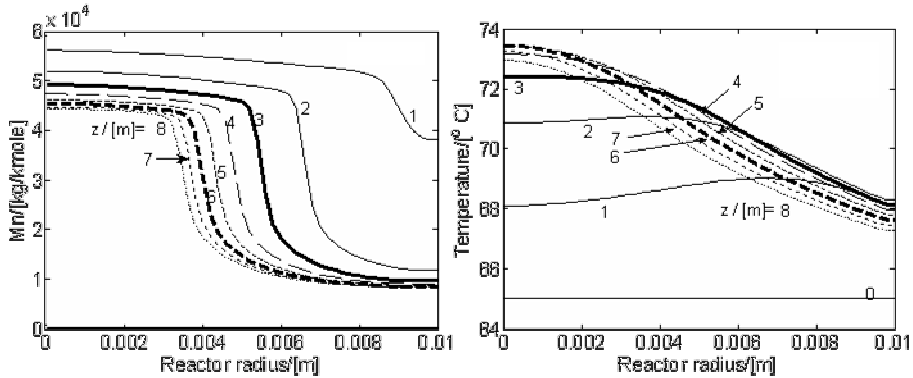
Figure 2. Number-average molecular weights (left) and temperature (right) profiles, at different positions (z) along the reactor.

Figures 1 and 2 present simulation results for the reactor with characteristics given in Table 2. The radial conversion profiles are relatively abrupt, with a fast transition from small values to almost complete conversion (Figure 1). As seen from Figure 1, two flowing zones are developed inside the tubular reactor: a central zone where the fluid velocity is relatively high and a peripheral (plugged) zone where the fluid velocity is relatively low, approaching zero in the proximity of the wall. Consequently, the maximum residence time occurs in the neighborhood of the wall, and minimum one in the center of tube. The differences in residence times give monomer conversions that drastically vary in radial direction, with values smaller than 10 % in the central zone and nearly 100% in the peripheral zone.

Figure 2 presents radial profiles of the number average molecular weights and temperature. In the plugged region close to the wall the polymer number-average molecular weight drastically decreases. This could be explained

by the small ratio of propagation to the termination rate, unfavorable to the formation of long chains, in the last two thirds of reactor length. Due to low amounts of monomer, the polymer radicals initiated in this region present a slow growth. Moreover, the high concentration of solvent promotes termination by chain transfer to solvent, finishing prematurely the newly produced chains.

Due to the high ratio of heat transfer area to reaction volume, only a moderate rise of the reaction temperature along the reactor is observed (Figure 2). The radial temperature profile presents a maximum, which moves from the neighborhood of the wall towards the center, as the axial position increases. This is explained by the heat generation rate, higher in the peripheral zone corresponding to the first meters of reactor length.

Influence of heat transfer area

To investigate the influence of the ratio between heat transfer area and reaction volume, the reactor diameter and length were varied keeping constant the mean residence time (defined as the ratio between the reactor volume and feed volumetric flow) of the reaction mixture through the polymerization reactor. The dimensions of the reactors used in these simulations are presented in Table 3, the other process parameters being specified in Table 2. In this section, only the results for extremes configurations are presented (Reactor 2 and Reactor 3), the others being already presented above.

Table 3. Reactor configurations

Reactor configuration	Length, [m]	Diameter, [m]
Reactor 1	8	2×10^{-2}
Reactor 2	2	4×10^{-2}
Reactor 3	32	1×10^{-2}

The results illustrated in Figures 3 to 5 prove that the reactor with high ratio of heat transfer area to reactor volume produces more homogenous final products and assures a more even thermal regime. The homogeneity is proved by the values of polydispersion index, a maximum value of 5 being obtained for Reactor 2 comparatively with a maximum value of 3 for Reactor 3.

As seen from Figure 5, the temperature profiles in Reactor 3 are more uniform due to a higher heat transfer area that is allowing a more efficient evacuation of the reaction heat. Moreover, the maximum value is located at the reactor centerline.

Comparatively, the temperature profiles in the Reactor 2 case present an evident maximum, shifted to the centerline only with advancement of the polymerization mixture along the axial coordinate of the reactor. A rise in temperature of almost 3 °C for Reactor 3 pr oduces higher molecular weight polymer close to the reactor wall, due to the small influence of chain transfer to solvent reaction in this region.
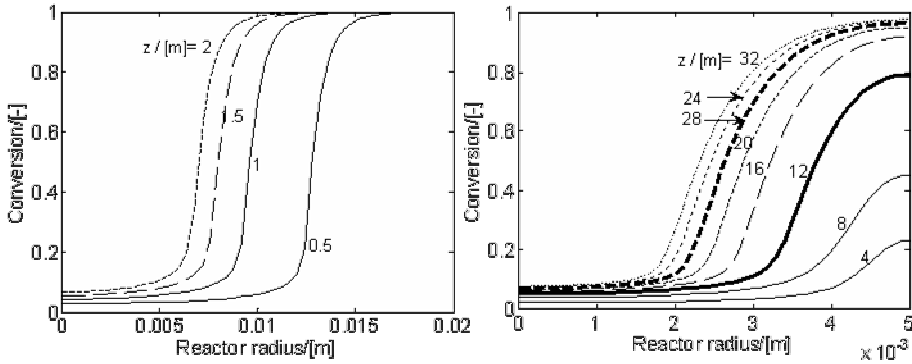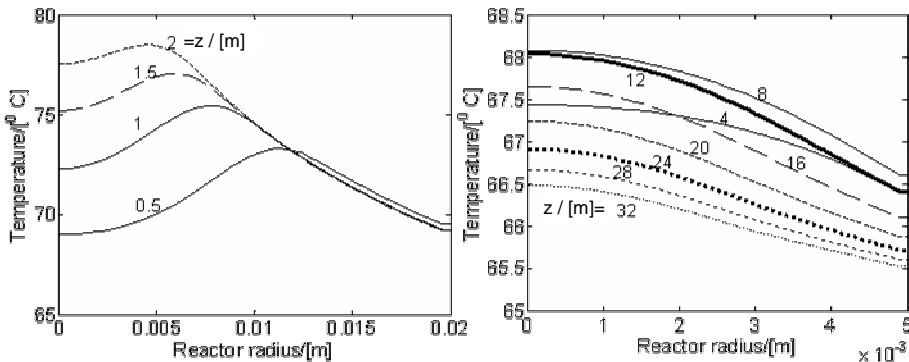
Figure 3. Radial profiles of monomer conversion, at different positions along the reactor. Left: Reactor 2; Right: Reactor 3.
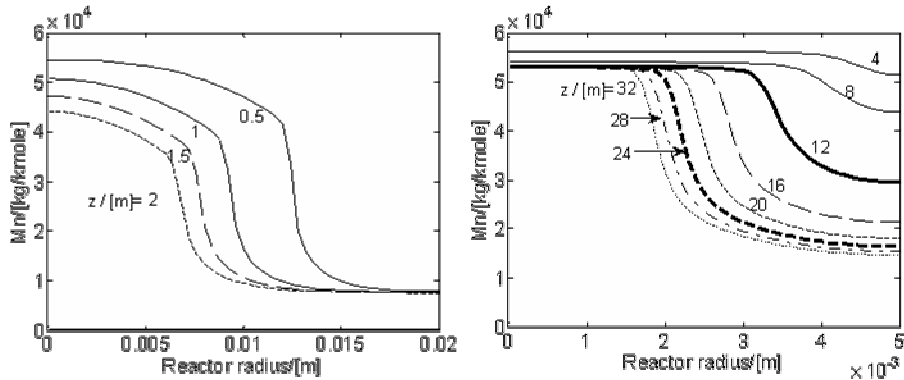
Figure 4. Radial profiles for number-average molecular weights, at different positions (z) along the reactor. Left: Reactor 2; Right: Reactor 3.


Figure 5. Radial profiles for temperature, at different positions (z) along the reactor. Left: Reactor 2; Right: Reactor 3.

235

Influence of initiator concentration

The initiator concentration has an important role in MMA polymerization, higher initiator concentrations producing polymers with lower molecular weights. Three values for the initiator concentrations (0.025, 0.05 and 0.1 mole/L) were tested for the Reactor 1 configuration (Table 3).
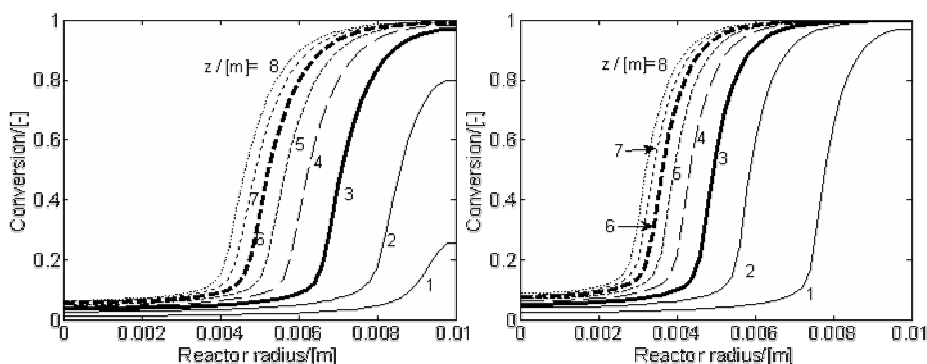
Figure 6. Monomer conversion profiles for initial initiator concentration of 0.025 mole/L (left) and 0.1 mole/L (right).
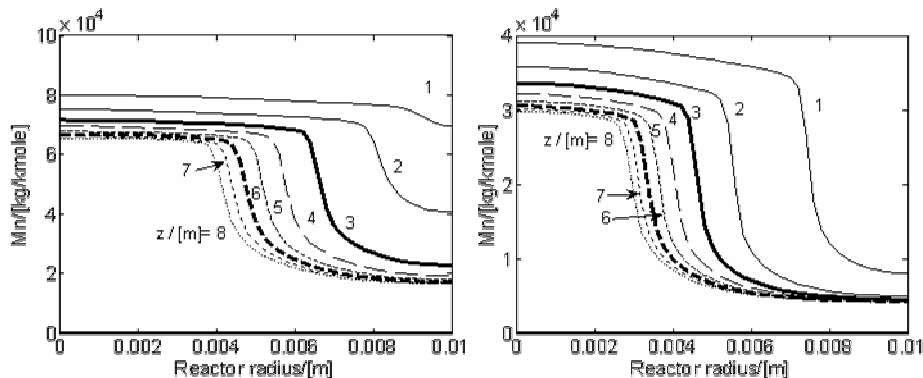
Figure 7. Number average molecular weight profiles for initial initiator concentration of 0.025 mole/L (left) and 0.1 mole/L (right).

Small initiator concentrations lead to a low initiation rate, and consequently to a small number of live polymer chains. This has two effects: first, a decrease of propagation rate having as result a low monomer conversion on the first 2 m of the reactor (Figure 6); second, an important increase of final polymer molecular weight (Figure 7). Also a small propagation rate decreases the amount of heat generated (low temperature levels) with an

increasing effect on the polymer molecular weight. Consequently, the initial initiator concentration proves to be an important parameter to control the final molecular weights of the polymer.

Influence of solvent concentration

It is well known that higher solvent fraction improves the heat transfer but also induces higher solvent separation costs. Three solvent mass fractions were tested for Reactor 1 configuration (Table 3).
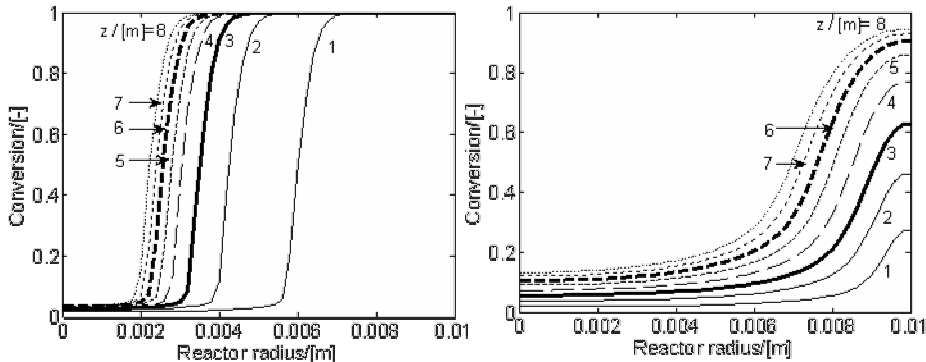
Figure 8. Monomer conversion profiles for smallest (ws = 0.3, left) and highest (ws = 0.7, right) feed weight solvent fraction.
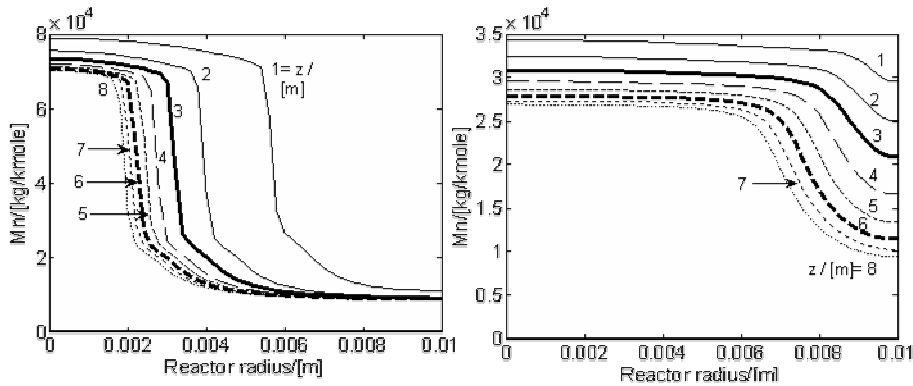
Figure 9. Number-average molecular weight for smallest (ws = 0.3, left) and highest (ws = 0.7, right) feed solvent fraction.

Increasing the fraction of solvent leads to lower reaction temperature through two mechanisms: a) less heat is generated due to lower amount of monomer; b) heat transfer through the wall is improved due to a lower resistance. Because the propagation step has a higher activation energy

compared to the termination reactions, the conversion is lower (Figure 8) and shorter chains are obtained (Figure 9). Smaller monomer concentration additionally contributes to lower propagation rates, with the same effect.

It should be remarked that increasing the solvent concentration leads to a polymer product with a more homogeneous molecular weight distribution. Thus, the polydispersion index is 7.65 and 2.27, for solvent fraction of 0.3 and 0.7, respectively.

The simulation results presented above are evidencing that the velocity profile of the laminar flow leads to a polymer of lower quality and the reactor volume is less efficiently used. This drawback becomes more important when the reaction mixture contains less solvent. The use of static mixers could change the velocity profile in order to approach the ideal case of plug-flow. This will be analyzed in the following section.

Comparison between laminar flow and plug flow reactor

A comparison between the simulation results obtained in the plug flow and laminar flow assumptions was finally performed (Figure 10). For the laminar flow polymerization tubular reactor, the values of monomer conversion and number-average molecular weight presented here are averages over the reactor cross-section.
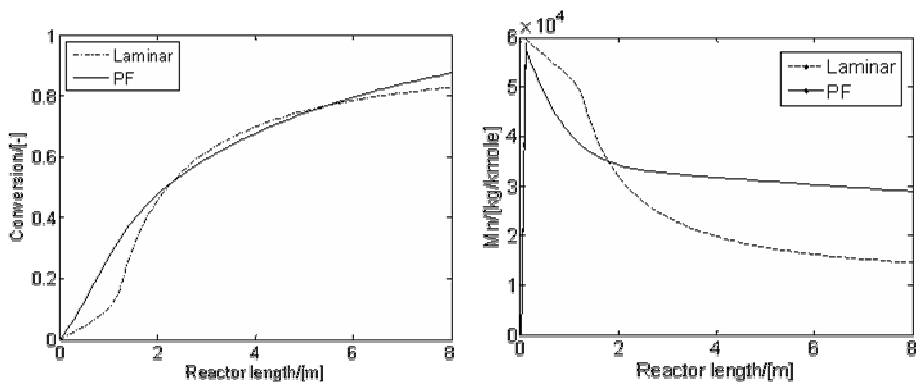
Figure 10. Plug flow and laminar flow reactor simulated monomer conversion and number-average molecular weights axial profiles (Reactor 1).

The two models predict similar values for the monomer conversion. However, the plug-flow reactor produces a polymer with a higher molecular weight and a narrow distribution (the polydispersion index of the final product is 2.13, compared to 3.21 for the laminar flow reactor). This is an argument for the practical effectiveness of static mixers in tubular reactors, in order to promote velocity profiles that approach the plug-flow.

CONCLUSIONS

In this paper the modeling of a tubular reactor for MMA polymerization was performed, considering laminar flow conditions. The influence of the main operating parameters (initiator and solvent concentration, heat transfer area) on the reactor behavior was studied.

Small diameter reactors (large specific heat-transfer areas) are more efficient from the point of view of heat transfer, the radial temperature variations are smaller and a product with more homogenous molecular weight is obtained. However, the main drawback of a small diameter is the large pressure drop induced by high flow velocity.

The results illustrate that laminar flow gives an inefficient utilization of the reaction volume, particularly at small solvent to monomer ratios. Due to low velocities near the wall, the polymer accumulates in this region and the heat transfer becomes less efficient.

These inconveniences could be removed by a reactor with a relatively large diameter but equipped with static mixers which homogenize the reaction mixture and improve the radial heat transfer through the polymer layer.

The trends of the main changes induced by the use of static mixers were evidenced by a comparative simulation of the same process in a plug flow tubular reactor. A polymer with higher molecular weight and smaller polydispersion index was predicted in the plug-flow reactor simulation, practically at the same final monomer conversion.

Symbols used

c_M	[mole/L]	monomer concentration
c_I	[mole/L]	initiator concentration
c_S	[mole/L]	solvent concentration
d_t	[m]	reactor diameter
D, D_{ef}	[m^2/s]	mass diffusion coefficients
f	[-]	initiator efficiency
Gz	[-]	Graetz number
k	[W·m^{-1}·K^{-1}]	thermal conductivity
k_d	[s^{-1}]	initiation rate constant
k_p, $k_{p,0}$	[L·mole^{-1}·s^{-1}]	chain propagation rate constant
k_t, $k_{t,0}$, k_{tc}, k_{td}	[L·mole^{-1}·s^{-1}]	termination rate constant (global, by combination and by disproportionation, respectively)
k_{tm}	[L·mole^{-1}·s^{-1}]	chain transfer to monomer rate constant
k_{ts}	[L·mole^{-1}·s^{-1}]	chain transfer to solvent rate constant
M_n	[kg/kmole]	number-average molecular weight

Nu	[-]	Nusselt number
r	[m]	radial coordinate
T, T_f, T_b	[K]	reaction, feed and jacket temperature
u_z	[m·s^{-1}]	axial velocity
z	[m]	axial coordinate

Greek symbols

α	[W·m^{-2}·K^{-1}]	partial heat transfer coefficient
ΔH_p	[J·mol^{-1}]	polymerization enthalpy
η	[Pa·s^{-1}]	reaction mixture viscosity
λ_m	[-]	mth order moments for free-radicals concentrations distribution (m = 0, 1, 2)
μ_m	[-]	mth order moments for polymer concentrations distribution (m = 0, 1, 2)
φ_m, φ_p	[-]	monomer and polymer volumetric fractions

REFERENCES

1. S. R. Ponnuswamy, "On-line measurements and control of a batch polymerization reactor", University of Alberta, Edmonton, **1984**, 252.
2. P. E. Baillagou, D. S. Soong, *Polymer Engineering & Science*, **1985**, *25(4)*, 212.
3. A. D. Schmidt, A.H. Ray, *Chemical Engineering Science*, **1981**, *36*, 1401.
4. S.-M. Ahn, S.-P. Chang, H.-K. Rhee, *Journal of Applied Polymer Science* **1998**, *69*, 59.
5. W. Y. Chiu, G. M. Carrat, D.S. Soong, *Macromolecules*, **1983**, *16*, 348.
6. B. M. Louie, D. S. Soong, *Journal of Applied Polymer Science*, **1985**, *30*, 3707.
7. P. E. Baillagou, D. S. Soong, *Chemical Engineering Science*, **1985**, *40(1)*, 75.
8. T. J. Crowley, K. Y. Choi, *Ind. Eng. Chem. Res.*, **1997**, *36*, 3676.
9. A. Husain, A. E. Hamielec, *AiChE Symposium Series*, **1976**.
10. J. S. Vrentas, C. H. Chu, *Chemical Engineering Science*, **1987**, *42(5)*, 1256.
11. J. S. Vrentas, W. J. Huang, *Chemical Engineering Science*, **1986**, *41(8)*, 2041.
12. R. Cintron-Cordero, R. A. Mostello, J. A. Biesenberger, *Can. J. Chem. Eng*, **1968**, 46.
13. S. Lynn, J. E. Huff, *AIChE Journal*, 1971, *17(2)*, 475.
14. C. E. Wyman, L. F. Carter, *AiChE Symposium Series*, **1976**.
15. J. W. Hamer, W. H. Ray, *Chemical Engineering Science*, **1986**, *41(12)*, 3083.
16. I.Banu, G. Bozga, I. Nagy, J. P. Puaux, *Chemical Engineering and Technology*, **2008**, *31(10)*, 1516.

17. P. E. Baillagou, D. S. Soong, *Chemical Engineering Science* **1985**, *40(1)*, 87.
18. R. H. Perry, D. W. Green, J. O. Maloney, "Perry's Chemical Engineer's Handbook", McGraw Hill, New York.**1997**, chapter 5.
19. J. Brandrup, E. H. Immergut, E.A. Grulke, "Polymer Handbook" John Wiley and Sons, Inc., New York, **1999**, section II.
20. B. E. Nauman, "Chemical Reactor Design, Optimization, and Scale up", McGraw-Hill, **2002**, chapter 8.
21. The MathWorks, I., *MATLAB Documentation*, **1984-2008**.

Dedicated to Professor Liviu Literat, at his 80th anniversary

ELECTROCHEMICAL BEHAVIOR AND APPLICATIONS OF PHENOTHIAZINE DERIVATIVES BASED ON *BIS*-(10*H*-PHENOTHIAZIN-3-YL)-METHANE

ALEXIA BONNIFET[a], DELIA GLIGOR[b], CASTELIA CRISTEA[b] LIANA MARIA MUREŞAN[b]

ABSTRACT. The electrochemical behavior of two phenothiazine derivatives, *bis*-(10*H*-phenothiazin-3-yl)-methane (I) and 1,1-*bis*-(10*H*-phenothiazin-3-yl)-ethane (II), was studied comparatively by cyclic voltammetry in dimethylsulfoxide solution and adsorbed on graphite electrodes. Compound I presents a more favorable electrochemical behavior than compound II, both in solution or adsorbed. The obtained modified electrodes present electrocatalytic activity towards NADH oxidation. Their electrocatalytic efficiency, evaluated from cyclic voltammetry, revealed the following decreasing sequence: I > II.

Keywords: Phenothiazine derivatives, Modified electrodes, NADH electrocatalytic oxidation.

INTRODUCTION

The employment of various organic compounds as mediators in facilitating electron transfer from enzyme molecules to electrode surface including phenothiazine derivatives has been reported in the literature [1]. It is known that phenothiazine derivatives, a pharmaceutically important class of heterocycles, with electron-rich sulfur and nitrogen heteroatoms, have been used as electron donor components. [2].

The cyclic voltammetric responses for phenothiazine derivatives adsorbed onto graphite electrodes recommend them for the low potential, sensitive and stable determination of dihydronicotinamide adenine dinucleotide (NADH) [3-7].

The determination of NADH is very important because NADH and its oxidized form, NAD$^+$, are the coenzymes for a large number of dehydrogenase

---

[a] *Université de Rouen, I.U.T. de Rouen, Mont-Saint-Aignan, France*
[b] *Universitatea Babeş-Bolyai, Facultatea de Chimie şi Inginerie Chimică, Str. Kogălniceanu, Nr. 1, RO-400084 Cluj-Napoca, Romania, limur@chem.ubbcluj.ro*

enzymes (more than 300) and components of biomarker systems. However, the direct electrochemical oxidation of NADH at a bare electrode takes place at high overpotential. So, much effort has been devoted to reduce the overpotential of the oxidation of NADH by using redox mediators, including phenothiazine derivatives [8].

In this context, the aim of this work is the study of the electrochemical properties of two new phenothiazine derivatives, *bis*-(10*H*-phenothiazin-3-yl)-methane (**I**) and 1,1-*bis*-(10*H*-phenothiazin-3-yl)-ethane (**II**), in solution and adsorbed on graphite electrodes as possible mediators for NADH oxidation. Cyclic voltammetry measurements (CV) were used to investigate the electrochemical behavior of compounds **I** and **II** under various experimental conditions (different potential scan rates). The modified electrodes obtained by adsorption of these new phenothiazine derivatives on graphite electrodes were tested for electrocatalytic oxidation of NADH.

RESULTS AND DISCUSSION

Electrochemical behavior of compounds in solution

Variable experimental conditions (pH, and scan rates) were employed for the investigation of the electrochemical behavior of compounds **I** and **II** by CV in DMSO solution. Figure 1 presents the cyclic voltammograms obtained for compounds **I** and **II** in DMSO solution, on graphite electrodes. The cyclic voltammograms are characterized by two peak pairs, with formal standard potential *vs.* Ag/AgCl/KCl$_{sat}$ in the positive domain (Table 1).
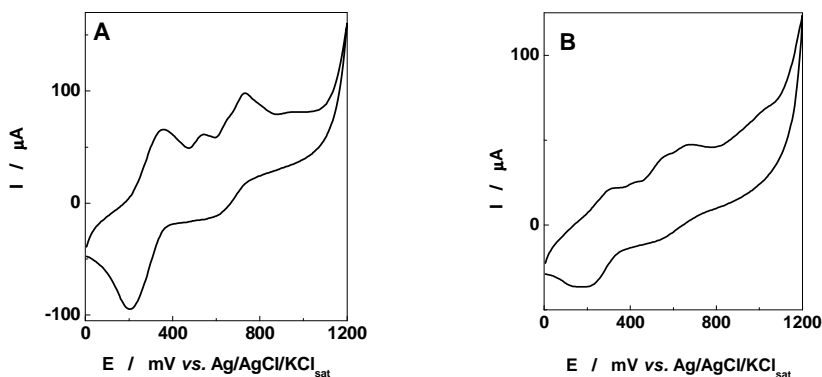

Figure 1. Cyclic voltammograms recorded on graphite electrode for compounds **I** (A) and **II** (B), dissolved in DMSO. Experimental conditions: starting potential, 0 mV *vs.* SCE; potential scan rate, 10 mV s^{-1}; supporting electrolyte, dimethylsulfoxide + 10^{-1} M KCl, pH 7.

Table 1. Electrochemical parameters of the voltammetric response of compounds **I-II** in solution. Experimental conditions: as in Figure 1

Compound	Peak	E_{pa} (mV)*	E_{pc} (mV)*	ΔE_{peak} (mV)
I	1	349	208	141
	2	722	602	120
II	1	290	212	78
	2	667	543	124

* mV *vs.* Ag|AgCl/KCl$_{sat}$

The first oxidation peak, may be assigned to one-electron oxidation leading to the formation of a stable radical cation (labeled **a** in Scheme 1) generated by one phenothiazine structural unit present in the molecular structure ($E_I^{0/+1}$= 349 mV and $E_{II}^{0/+1}$= 290 mV). The second oxidation peak appears shifted anodically ($E_I^{0/+2}$= 722 mV and $E_{II}^{0/+2}$= 667 mV) and may be assigned to two-electron oxidation leading the formation of phenazathionium cation (labeled **b** in Scheme 1). These oxidation potentials values are in agreement with the reported electrochemical data for unsubstituted phenothiazine ($E^{0/+1}$= 270 mV and $E^{0/+2}$= 750 mV *vs.* Ag/AgCl/KCl$_{sat}$ [9]. In the CV of compound I, presented in figure 1, a peak characterized by lower current intensities appears at intermediate values (aprox. 500 mV) and could be assigned to the formation of a *bis*-radical-cation (labeled **c** in Scheme 1).
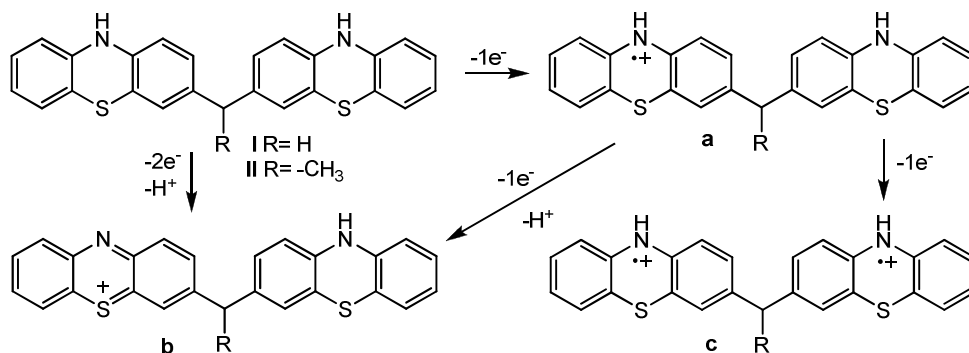
Scheme 1

The values of ΔE_{peak} showed that compounds **I** and **II** presents irreversible electrochemical behavior (ΔE_p > 59 mV) on graphite.

A small positive shift of the E_{pa} values for compound **I** was observed (see Table 1) as compared with compound **II**, suggesting that the latter is

oxidized easier taking benefit of a weak inductive electron donor effect of the alkyl substituent.

Electrochemical behavior of adsorbed compounds

Figure 2 shows the voltammetric response corresponding to compounds **I** and **II**, adsorbed on the surface of graphite electrode, in a phosphate buffer solution (pH 7). The voltammogram of compound **I** (Figure 2A) shows one well-defined peak pair and one oxidation shoulder. The oxidation waves can be assigned to the formation of stable radical cations generated by the two phenothiazine structural units present in the molecular structure. The first oxidation wave ($E_{pa}^{0/+1}$= 89 mV *vs.* SCE) can be assigned to the radical cation formation of one phenothiazine unit in the molecular structure. The shoulder ($E_{pa}^{+1/+2}$= 400 mV *vs.* SCE), involving the oxidation of the phenothiazinium radical cation to the *bis*-phenothiazinium dication appears shifted anodically and it is characterized by a much lower current intensity, may be due to the electron withdrawing effect induced by the positive charge in the radical cation.

Figure 2B shows the cyclic voltammograms of compound **II** containing a principal oxidation peak $E_{pa}^{0/+1}$ situated close to 5 mV *vs.* SCE. Thus, compound **II** appear to undergo oxidation processes slightly easier as compared to the compound **I**, presenting the same behavior as in solution.
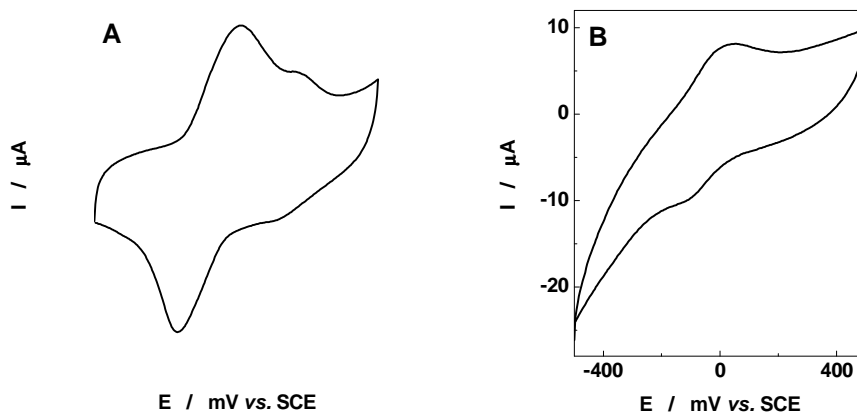
Figure 2. Cyclic voltammograms of compounds **I** (A) and **II** (B) adsorbed on graphite. Experimental conditions: starting potential, -500 mV *vs.* SCE; potential scan rate, 50 mV s^{-1} (A) and 10 mV s^{-1} (B); supporting electrolyte, 0.1 M phosphate buffer, pH 7.

The voltammetric behavior of compounds **I** and **II**, characterized by the electrochemical parameters summarized in Table 2, points out to an irreversible process ($\Delta E_p > 59$ mV), for each investigated compound. The values of the standard formal potentials $E^{0'}$ show greater values for compounds **I** and **II** in comparison with pure phenothiazine, which is characterized by standard formal potential value $E^{0'} = -107$ mV *vs.* SCE, in the same experimental conditions. This fact suggests the more difficult oxidation of both studied compounds as compared to the parent unsubstituted phenothiazine. This behavior can be explained by the bigger size of compound **I** and its different steric orientation towards the electrode surface and reflects the increased stability of compound **I.** It can be observed also from Table 2 that the supplementary substitution with methyl groups of compound **II** leads to a decrease of ΔE_{peak} although compound **I** exhibits the relative current ratio I_{pa}/I_{pc} close to one, specific to adsorbed conditions [10].

Table 2. Electrochemical parameters of the voltammetric response for graphite electrodes modified with compounds **I-II**. Experimental conditions: scan rate, 10 mV s^{-1}; supporting electrolyte 0.1 M phosphate buffer, pH 7

Compound	E_{pa} (mV)*	E_{pc} (mV)*	ΔE_{peak} (mV)	$E^{0'}$ (mV)	E_{FWHM} (mV)		I_{pa}/I_{pc}
					anodic	**cathodic**	
I	89	-59	148	15	206	169	1.00
II	5	-95	100	-45	200	107	3.82

* mV *vs.* SCE

As expected for surface confined redox species [11], the cyclic voltammograms recorded in a wide range of potential scan rates (10-400 mV s^{-1}) showed a linear dependence of the peak currents (I_p) on the electrode potential scan rate (v) (results not shown), for compounds **I** and **II** adsorbed on graphite electrodes. The slopes of the log I_p *vs.* log v plots for the compounds **I** and **II** were close to the theoretical value (1), in phosphate buffer pH 7.

For both studied compounds, the width at half peak height (E_{FWHM}) was different to that corresponding to the ideal case ($E_{FWHM} = 90.6/n$ mV, where n is the number of electrons). The observed discrepancies prove the existence of repulsive interactions between the adsorbed redox species (radical cations generated in the anodic process) [11,12]. Additionally, as expected for lateral interaction [10], it was noticed that the peak parameters were affected by the surface coverage.

In conclusion, compound **I** presents a more favorable electrochemical behavior than compound **II**, both in solution and adsorbed on graphite electrodes.

Electrocatalytic activity for NADH oxidation

Starting from the favorable electrochemical behavior of the compounds **I** and **II** adsorbed on graphite, their electrocatalytic activity towards NADH oxidation was tested by CV. As can be seen from Figure 3, an enhancement of the anodic peak current, observed in the NADH presence, associated with the progressive diminishing of the cathodic one, proved the electrocatalytic effect for compounds **I** and **II**. The electrocatalytic efficiency, estimated as the ratio $(I_{cat})_{NADH}/(I_{cat})$ was found decreasing in the following sequence: **I** (1.70, measured at -38 mV *vs.* SCE) > **II** (1.12, measured at +28 mV *vs.* SCE).
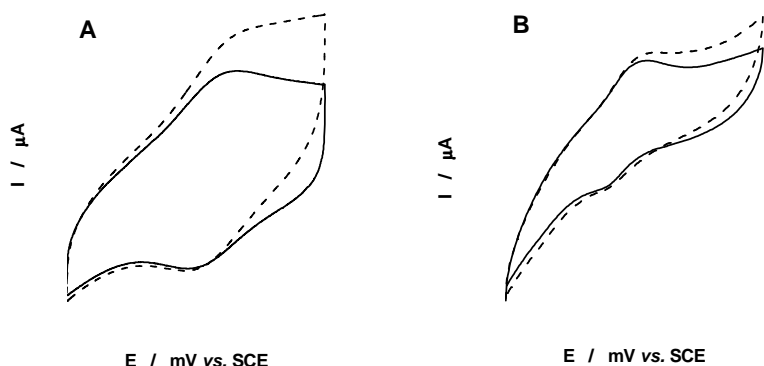
Figure 3. Cyclic voltammograms of compounds **I** (A) and **II** (B) adsorbed on graphite electrodes, in absence and in presence of NADH 5 M. Experimental conditions: starting potential, –200 mV *vs.* SCE (A) and –500 mV *vs.* SCE (B); scan rate, 10 mV s^{-1}; supporting electrolyte, 0.1 M phosphate buffer, pH 7.0.

CONCLUSIONS

By comparing the electrochemical behavior of two new phenothiazine derivatives, *bis*-(10H-phenothiazin-3-yl)-methane (**I**) and 1,1-*bis*-(10*H*-phenothiazin-3-yl)-ethane (**II**), it was put on evidence that compound **I** is more difficult to oxidize than compound **II**, on graphite electrodes. in the same experimental conditions (in solution and in adsorbed state). However, the catalytic efficiency of compound I adsorbed on graphite toward NADH oxidation was better than that of compound II. Both graphite electrodes

modified with compounds I and II present electrocatalytic effect towards NADH oxidation.

EXPERIMENTAL SECTION

Materials

Bis-(10*H*-phenothiazin-3-yl)-methane (**I**) and 1,1-*bis*-(10*H*-phenothiazin-3-yl)-ethane (**II**) (Scheme 2) are the two phenothiazine derivatives used for electrochemical studies.
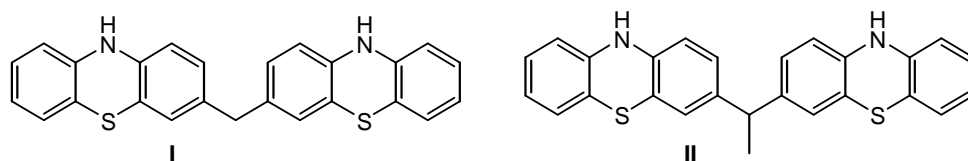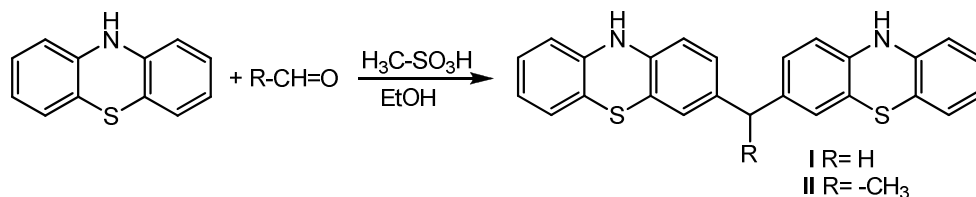

Scheme 2

The supporting electrolyte for voltammetric measurements in solution was dimethylsulfoxide (DMSO, Merck, Darmstadt, Germany) containing 0.1 M KCl and for adsorbed system, phosphate buffer solutions. Phosphate buffer solutions were prepared using $Na_2HPO_4 \cdot 2H_2O$ and $NaH_2PO_4 \cdot H_2O$ from Merck (Darmstadt, Germany).

β-Nicotinamide adenine dinucleotide, reduced form (NADH) was purchased from Sigma (St. Louis, MO, USA) as disodium salt. All other reagents were of analytical grade and used as received.

Synthesis and characterization

Bis-(10*H*-phenothiazin-3-yl)-methane (**I**) was synthesized by the condensation of phenothiazine with formaldehyde according to previously reported procedures [13]. 1,1-*bis*-(10*H*-phenothiazin-3-yl)-ethane (**II**) was synthesized according to similar procedures by the condensation of phenothiazine with acetaldehyde in the presence of catalytic amounts of methanesulfonic acid (Scheme 3).

Scheme 3

The structure assignment of **I** and **II** is supported by spectroscopic data. FT-IR spectroscopy indicates the stretching vibration of N-H bonds by the absorption band situated at about 3330 cm^{-1}. In particular, **II** can be clearly identified by the appearance of the aliphatic protons in NMR spectra. 300 MHz ^{1}H-NMR spectrum shows a quartet signal situated at 4.5 ppm and a doublet signal situated 1.22 ppm for the four protons of the ethylidene group. For the NH groups in the two equivalent phenothiazine units the signal of the protons appears situated at 8.5 ppm. The substitution in position 3 of the phenothiazine units was assigned according to the aromatic protons coupling pattern observed for the signals situated in the 6.5-7 ppm range in the homocorrelation COSY–45 spectrum.

NMR spectra were recorded using a 300 MHz Brucker NMR spectrometer.

FT-IR spectra were recorded using a Brucker Vector 22 FT-IR spectrometer.

1,1-*Bis*-(10*H*-phenothiazin-3yl)-ethane (**II**)

10*H*-phenothiazine (2.5 mmol) solved in ethanol (20 mL), acetaldehyde (1 mmol) and methanesulfonic acid (1 mL) were heated to reflux for 12 hours and generated a green precipitate which was filtered. The precipitate was thoroughly washed with cold ethanol and then it was solubilized in tetrahidrofurane. The insoluble part was removed by filtration. After removing the solvent, 0.25 g green precipitate was obtained (yield 60%).

^{1}H-NMR (300MHz, DMSO-d$_6$): δ=1.22 ppm (d, 3H), 4.50 ppm (q, 1H), 6.66 ppm (d, J=6.20 Hz, 2H), 6.76 ppm (d, J=6 Hz, 2H), 6.79 (m, 4H), 6.82 (d, J=6.2 Hz, 2H), 6.96 ppm (d, J=5.8 Hz, 2H), 7.05 (t, 2H), 8.52ppm (s, 2H).

Electrodes preparation

A spectrographic graphite rod (Ringsdorff-Werke, GmbH, Bonn-Bad Godesberg, Germany), of ~ 3 mm diameter, was wet polished on fine (grit 400 and 600) emery paper (Buehler, Lake Bluff, Ill., USA). Then, a graphite piece of suitable length was carefully washed with deionized water, dried, and finally press-fitted into a PTFE holder in order to obtain a graphite electrode having, in contact with the solution, a flat circular surface of ~ 0.071 cm^2.

The modified graphite electrodes were obtained by spreading onto the electrode surface 2 µl of 1 mM phenothiazine derivative solution in dimethylsulfoxide and leaving them for 20 minutes at room temperature to evaporate the solvent. Before immersion in the test solution the modified electrodes were carefully washed with deionized water.

Electrochemical measurements

CV measurements were carried out in a conventional three-electrode electrochemical cell. A saturated calomel electrode (SCE) served as reference electrode and a coiled Pt wire served as counter electrode. The cell was connected to computer-controlled voltammetric analyzers (Autolab-PGSTAT10, Eco Chemie, Utrecht, Netherlands or Voltalab, Radiometer).

ACKNOWLEDGMENTS

REFERENCES

1. Y. E. Sorunmu, M. Nguyen, J. P. Sapp, W. Gorski, T. D. Phan, X. Wei, *Electroanalysis*, **2006**, *18*, 2375.
2. L. Yang, J.-K. Feng, A.-M. Ren, *J. Org. Chem.*, **2005**, *70*, 5987.
3. J. Kulys, G. Gleixner, W. Schuhmann, H. L. Schmidt, *Electroanalysis*, **1993**, *5*, 201.
4. A. A. Karyakin, E. E. Karyakina, W. Schuhmann, H. L. Schmidt, S. D. Varfolomeyev, *Electroanalysis*, **1994**, *6*, 821.
5. D. Dicu, L. Muresan, I. C. Popescu, C. Cristea, I. A. Silberg, P. Brouant, *Electrochim. Acta*, **2000**, *45*, 3951.
6. D. Gligor, L. Muresan, I. C. Popescu, I. A. Silberg, *Rev. Roum. Chim.*, **2002**, *47*, 953.
7. D. Gligor, L. Muresan, I. C. Popescu, I. A. Silberg, *Rev. Roum. Chim.*, **2003**, *48*, 463.
8. S. A. Kumar, S.-M. Chen, *Sensors*, **2008**, *8*, 739.
9. J. P. Billon, *Bull. Soc. Chim. Fr.*, **1960**, 1784.
10. M. J. Honeychurch, G. A. Rechnitz, *Electroanalysis*, **1998**, *5*, 285.
11. R. W. Murray, "Techniques of Chemistry", Wiley, **1992**, chapter XXII.
12. E. Laviron, L. Roulier, *J. Electroanal. Chem.*, **1979**, *101*, 19.
13. C. Cristea, G. Cormos, D. Gligor, I. Filip, L. Muresan, I. C. Popescu, *J. New Mat. Electrochem. Sys.*, accepted, **2008**.

Dedicated to Professor Liviu Literat, at his 80th anniversary

MINERALOGY OF DEGRADATION PROCESSES AFFECTING THE MORTAR FROM BURU DAM (ARIEŞULUI VALLEY, CLUJ COUNTY)

NICOLAE HAR[a], MARIA GOREA[b], MARCEL BENEA[a]

ABSTRACT. The objective under study is represented by the dam construction work across Arieş River on the area of Buru locality (Cluj County). The mortar used in dam construction is affected by carbonation, sulphates attack and alkali-silica reactions. Carbonation is materialized by calcite precipitation in matrix mortar, visible as efflorescences on surface and along the fissures within the mortar. Sulphate attack results in ettringite II genesis, located in the pores of the mortar. The alkali-silica reactions lead to the formation of silica gels deposited on the internal walls of the pores where they progressively crystallize and turn into cryptocrystalline silica. There are various causes for alteration processes, from atmospheric factors to the microenvironment resulted from the high polluants concentration into the Arieş River water.

Keywords: mortar, carbonation, sulphate attack, alkali – silica reactions

INTRODUCTION

The degradation processes affecting mortars represent the major factor determining their durability. These are controlled by both the exploitation condition for the works consisting of building materials and hydraulic binders, and the structural-textural and compositional properties of the mortar.

Concrete is a complex composite material used in various construction works, thus exposed to a wide range of destructive factors. The complexity of concrete types increased in time, due to increasing social requirements. The concrete applications and the exposure conditions represent great challenges for concrete durability. Thus it is important to be forseen the defects that may occur during the exploitation and that possibly can damage the concrete structure.

[a] *Universitatea Babeş – Bolyai, Facultatea de Biologie şi Geologie, Str. Kogălniceanu, Nr. 1, RO – 400084, Cluj-Napoca, Romania, har@bioge.ubbcluj.ro*

[b] *Universitatea Babeş – Bolyai, Facultatea de Chimie şi Inginerie Chimică, Str. Kogălniceanu, Nr. 1, RO – 400084, Cluj-Napoca, Romania, mgorea@chem.ubbcluj.ro*

Atmospheric factors such as rain – some of them acid, wind, drying-wetting or frost-thaw cycles affect the external surface of concrete in a large extent. Dissolution and gradual leaching of concrete under the action of slightly acid rains, or physical degradation due to drying-wetting cycles are easily predictable. The surface of concrete saturated in water is vulnerable to frost-thaw cycles which can trigger other destructive mechanisms [1].

The most frequent process brought about the atmospheric factors is concrete carbonation, this leading to a decrease of the concrete pH value from 13 to 8; and so initiates the steel reinforcement corrosion [2]. In concrete, the formation of carbonates is caused by the reaction between the product of cement hydration, $Ca(OH)_2$, and aggressive atmospheric or water dissolved CO_2. of The first phase of the process is calcite; it precipitates in the pores of the concrete, leading to its compaction and thus to an increase of its mechanical resistance. However, aggressive waters with variable contents of CO_2 can also infiltrate inside the concrete and dissolve the $Ca(OH)_2$. The higher rate of dissolution process considerably increases the pores water pressure, and consequently the concrete wall can be crossed by water. CO_2 reacts with $Ca(OH)_2$ forming a new calcite generation.

The following chemical reactions are responsible for these processes:

$$Ca(OH)_2 + CO_2 = CaCO_3 + H_2O$$
$$CaCO_3 + CO_2 + H_2O = Ca(HCO_3)_2$$
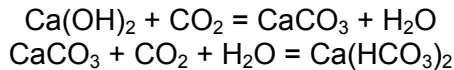
Another cause for concrete degradation is the SO_4^{2-} bearing water. This ion reacts with $Ca(OH)_2$ from concrete, resulting a wide range of sulphate minerals. Gypsum ($CaSO_4 \cdot 2H_2O$) is the most widespread mineral identified in the strengthened concrete pores; its crystallization accompanied by a volume increase further intensify the internal tensions that possibly result in the concrete destruction. Another potential phase the ettringite ($Ca_6Al_2O_6(SO_4)_3 \cdot 31H_2O$) that forms according to the reaction:

$$Ca_3Al_2O_6 \ 6 \ H_2O + 3 \ Ca^{2+} + 3 \ SO_4^{2-} + 25 \ H_2O = Ca_6Al_2O_6(SO_4)_3 \ 31H_2O$$
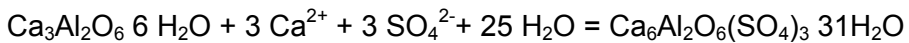
The solid state reaction is accompanied by large volume variations that finally can damage the concrete or mortar. The intensity of the sulphate attack depends on SO_4^{2-} concentration in the water, as well as the presence of other cations and anions in the solution. The presence of primary ettringite resulted from the reaction of the calcium hydroaluminates from the cement matrix with the gypsum added for controlling the concrete strengthening and that of the secondary ettringite formed by water-related sulphate attack has been already evidenced [3].

Concrete composition

Concrete is a composite material consisting of cement matrix and natural or synthetic aggregates, the latter contributing up to 70 % to its mass, and having various grain sizes according to the concrete type and usage. Cement stone is obtained by hydration of mineralogical components of cement via an exothermal reaction leading to the formation of calcium hydrosilicates, hydroaluminates or hydroferrites that confer the final strength to the products [4]. The reactions are not a linear combination of hydration processes affecting individual components; for example, during the hydration of Ca_3SiO_5 and $Ca_2 SiO_4$ an amount of $Ca(OH)_2$ is released, which is not formed in the hydration of $Ca_3Al_2O_3$ and respectively $Ca_4 Al_2Fe_2O_{10}$. The aggregates are particles of various sizes of sand, fragments of natural rocks, synthetic materials, or waste materials, the most usual types being represented by natural rocks. The type of aggregate and its grain size depend on the composition and type of concrete.

The composition of a regular Portland cement stone is assumed to consist of 70 % C-S-H (calcium hydrosilicates) gels, 20 % portlandite, $Ca(OH)_2$, 3 % calcium hydroaluminates and sulpho-hydroaluminates and 3 % non-hydrated material [5]. Calcium hydrosilicates with high CaO content release a higher amount of $Ca(OH)_2$ as compared to those with low content of CaO, or to other hydrocomponents in the system [6]. Portlandite, $Ca(OH)_2$, from the cement matrix is concentrated at the interface with the aggregate particles giving birth to an aureole, or at the border of the pores resulted after the release of porosity water [7]. In contact with infiltration waters, $Ca(OH)_2$ gradually passes into solution until reaching its solubility limit, moment when the dissolution process ends. The solutions saturated in calcium hydroxide react with atmospheric, or the dissolved CO_2 with the bicarbonate ion from the infiltration waters leading to the formation of $CaCO_3$ and the decrease of the solution's pH; these processes finally result in the concrete degradation.

The aim of this study was to try to identify of degradation processes that altering the mortar used in the Buru dam (Cluj County), and the alteration minerals. The dam was made of concrete and finished by mortar (Figure 1). The dam mortar degradation si visible mainly due to the white efflorescences developed along irregular fissures cutting the mortar. The fissures affect the whole thickness of the mortar; they form a network imprinting a mosaic-like aspect enhanced by the presence, along their trajectory, of striking whitish carbonate deposits contrasting with the dark-grey colour of the mortar. Destruction processes show various intensities, from poorly-fissured areas to the detachment of irregular mortar fragments from the surface of the mortar layer. Samples were collected from intensely-fissured areas bearing white carbonate crusts. Sampling concerned the whole thickness of the mortar layer.

Figure 1. Fissures with carbonate deposits at the base of Buru dam (Cluj County).

RESULTS AND DISCUSSION

Petrographical features of the mortar. The Buru dam consists of concrete finished with mortar. The mortar layer up to 1 cm thickness consists of aggregate (65 %) and matrix (35 %). Structurally (Figure 2), the mortar is porphyroclastic (clasts -Terminology used in the petrography of natural rocks where *clast* means a fragment with variable composition and/or shape. *Porphiritic* refers to size-related features, suggesting inechigranular patterns, *i.e.* large sizes of the clasts as compared to the grains of the matrix of aggregate - of various compositions bound in a fine, crystallized matrix) and shows a porous texture. The primary pores are filled by secondary minerals resulted from degradation processes.

The aggregate consists of fragments of minerals and rocks. The mineral fragments are up to 1.0 mm in size and they are represented by quartz, microcline, plagioclase feldspar, muscovite, biotite, chlorite, green hornblende, garnet, vesuvianite etc. The lithic fragments consist of quartzites, micaschists, sericitic schists, gneisses, sandstones with carbonate cement, limestones. As a rule, the rock fragments are rounded but also angular in some cases; they show variable sizes, up to 1.5 – 3 mm. The mineralogic and petrographic characteristics of the aggregate suggest its source in the alluvia of the Arieş Valley. Granular fragments of non-hydrated clinker have been identified in the mortar, consisting of alite, belite and brownmillerite (Figure 3).

The matrix is finely-crystallized and microscopically it shows variable colouring. The carbonated areas are dominantly colourless, while the non-carbonated ones show brownish hues due to the co-existing iron hydroxides.
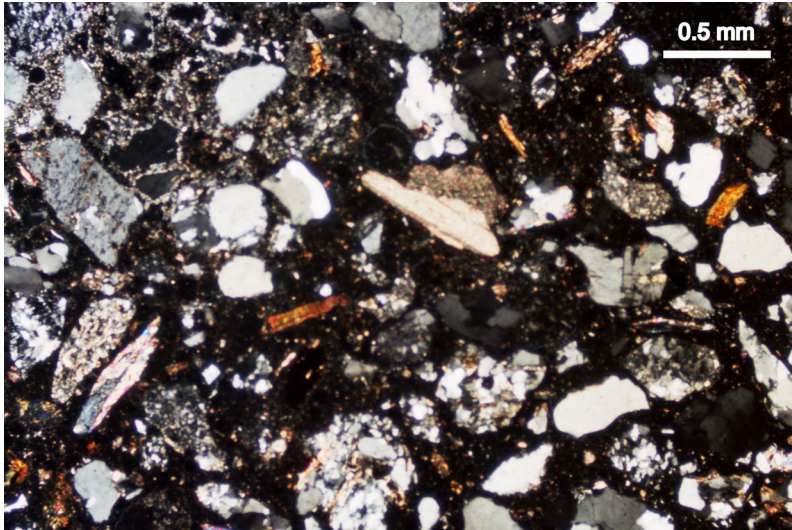
Figure 2. Porphyroclastic features of the mortar in the Buru dam. The matrix is finely-crystallized and impregnated with iron hydroxides (N+).
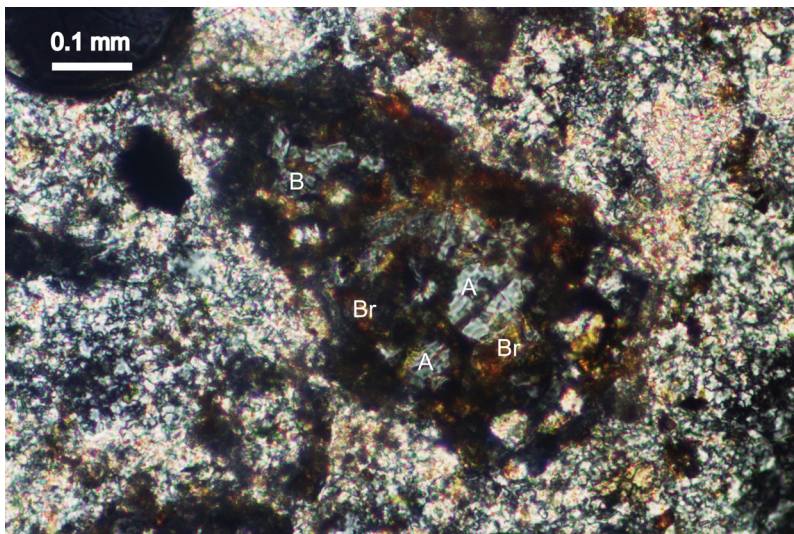
Figure 3. Non-hydrated clinker fragment in the matrix of the mortar (N+):
A – alite, B – belite, Br – brownmillerite

Mineralogical features of the degradation processes. Mineralogic and petrographic studies on the mortar of Buru dam have evidenced several degradation processes. Genetically, two types could be separated:

- Mechanical processes caused by frost-thaw phenomena. They are illustrated by the occurrence of fissures in the mortar mass, as well as at the concrete/mortar interface;
- Chemical–mineralogical processes: carbonation, sulphate attack and formation of silica gels following the alkalies – silica reactions (ASR). These processes are favoured by the mechanical ones and they consist in specific reactions between the hydration components of the mortar matrix and the various ions dissolved by the infiltration waters percolating through the pores and fissures within the mortar. They result in neoformation minerals specific to each degradation process. The spatial relationships among the new formed minerals and the primary components of the mortar, as well as those among new formed minerals typical to each degradation process allowed the chronological reconstruction of the alteration processes pathway.

Carbonation represents spatially, the most widespread degradation process. It was identified both macroscopically and microscopically and it consists in the impregnation of the mortar matrix and primary pores with granular calcite aggregates, as well as in the occurrence of crustiform white efflorescences along the fissures and in their proximity. It has to be noticed that carbonation occurs at the mortar/air, as well as to the mortar/concrete interfaces. The investigated samples pointed to a clear zonation of the carbonation process. Two distinctive areas could be identified in thin sections, under the microscope (Figure 4):

- Zone I – developed at the surface of the mortar, consisting of crustiform efflorescences built-up of successive layers of calcite with porous-spongy features. This particular texture of the crustiform calcite does not allow a good conservation of the material when thin sections are prepared transversal to the mortar layer. The stratified deposition of the secondary calcite is also obvious along the internal walls of the fissures within the mortar (Figure 5). X-ray diffractograms on samples from the white crusts have evidenced the presence of calcite and quartz, identified based on their specific d/n (Å) values (Figure 6). The source for quartz was, most probably, the sand used when the mortar was prepared.
- Zone II – occurs at the external margin of the mortar layer. It is up to 3 mm thick and it is characterized by the presence of finely granular calcite massively impregnating the mortar matrix. Calcite from zone II has been also identified in the pores of the mortar, where it fills the central area (Figure 8).
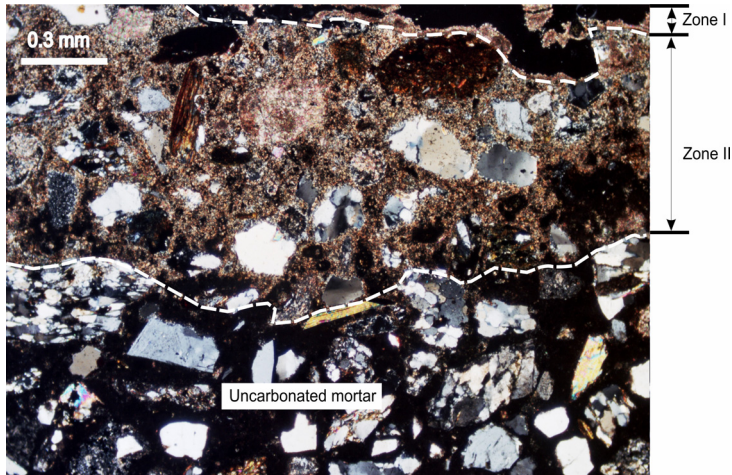
**Figure 4.** Zonation of the carbonation process (N+).
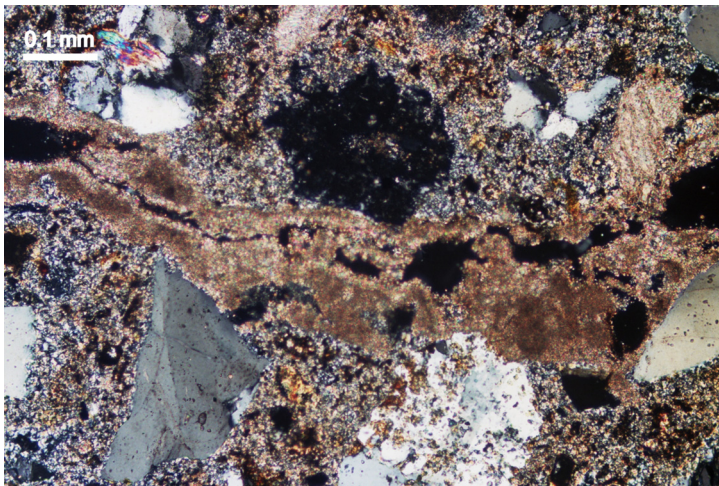
Figure 5. Stratified deposits of calcite along the walls of the fissures in the mortar, and as impregnations in the matrix (N+).

The formation of the secondary carbonates is attributed, mainly to the reaction between $Ca(OH)_2$ and the atmospheric CO_2.

A previous paper [8] has evidenced the presence of large concentration in anions: HCO_3^- (162 mg/l), SO_4^{2-} (~ 64 mg/l), and cations: Ca^{2+} (~ 49 mg/l), Mg^{2+} (7.1 mg/l), Na^+ (7.3 mg/l), in Arieş water (pH=7.4); these ions are responsible for the degradation process. The Arieş River pollution is caused by both mining activities in the area, as well as by the dissolution of some host rocks (carbonate rocks, andesitic rocks etc) in the neighbourhood.
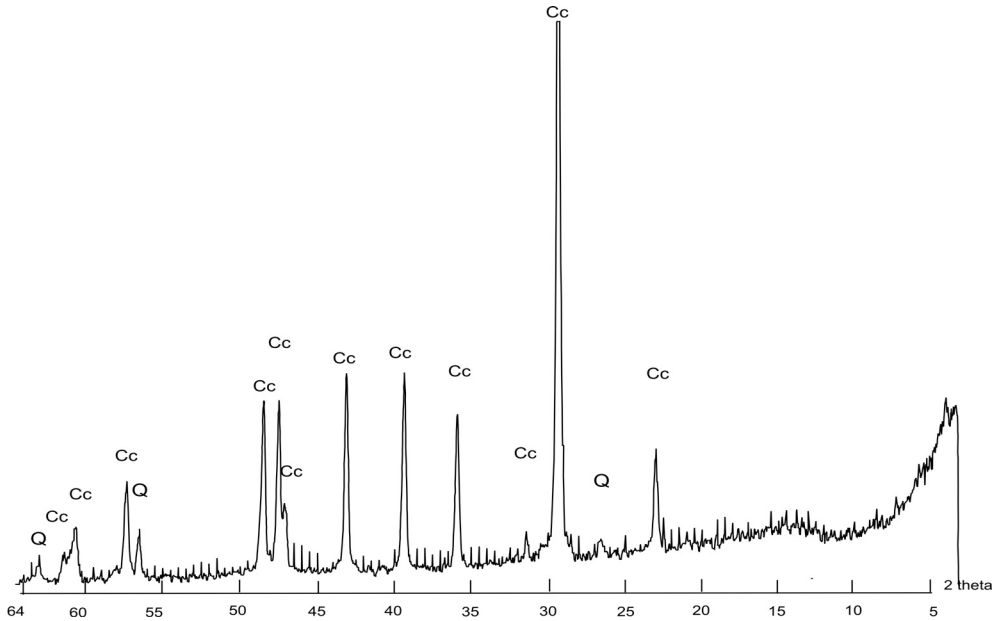
Figure 6. X-ray pattern of the carbonate crust developed along the fissures in the mortar (Cc – calcite, Q – quartz)

The sulphate attack has been evidenced during the microscopic study. Ettringite II results from this process; it is deposited in the primary pores of the mortar, where it is associated with calcite and secondary silica. Ettringite occurs as acicular crystals with random or sometimes radial orientation (Figure 7). Under polarized light it is characterized by parallel extinction, low birefringence and positive relief. Most probably, secondary ettringite forms as a product of the reaction between the calcium hydroaluminates from the cement matrix and SO_4^{2-} and Ca^{2+} present in the river water. The non-hydrated cement grains from the matrix, also gradually hydratea lead to the formation of calcium hydrosilicates and hydroaluminates, with the release of $Ca(OH)_2$. Thus, the sulphatation of hydrates represents a continuous process that follows alkali-silica reactions, as pointed out by the succession of layers in the primary pores of the mortar, images by optical microscopy.

Alkali-silica reactions (ASR) are poorly-represented in the studied samples; they have been identified only by optical microscopy, and resulted in the formation of cryptocrystalline silica deposited on the mortar pores.
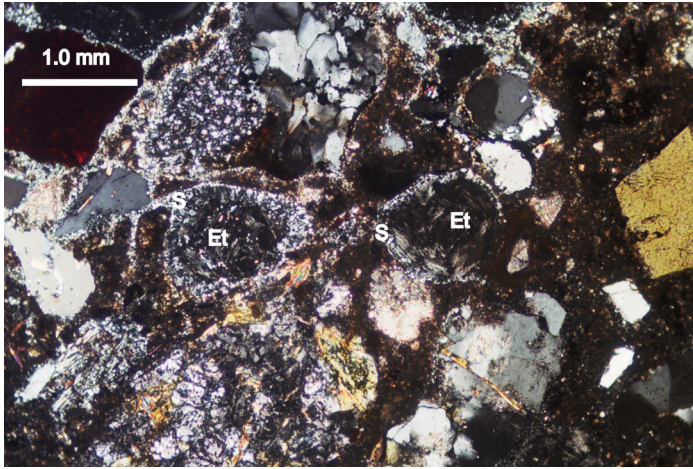
Figure 7. Acicular-fibrous crystals of ettringite (Et) in the primary pores of the matrix (N+). Cryptocrystalline silica covers the internal wall of the pores (S).

Cryptocrystalline silica represents the first product of the alteration process; under polarized light it shows low birefringence and relief (Figure 7). It forms by crystallization of silica gels present in mortar due to the interaction between alkalies from cement and the various species of active silica of the aggregate. The resulted gels have migrated from the mortar matrix towards the pores and fissures where they have gradually crystallized.
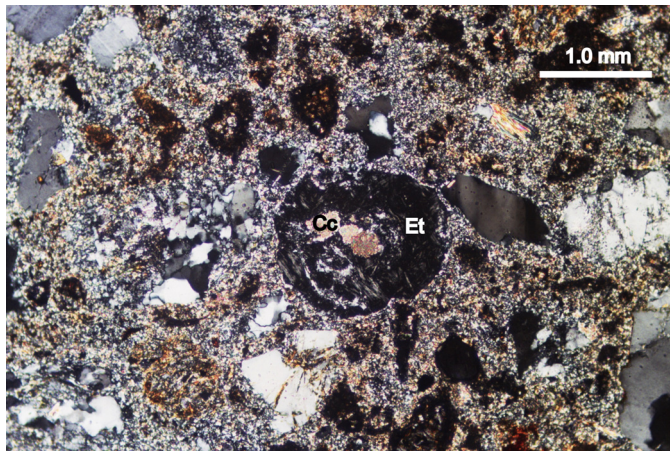
Figure 8. Pore in the mortar matrix filled by ettringite (Et) and calcite (Cc) in the central area (N+).

The spatial relationships between the alteration phases precipitated in the primary pores of the concrete have allowed the recognition of the temporal stages. Thus, the presence of the cryptocrystalline secondary silica (Figure 7) on the walls of the primary pores, points that it is the first product of alteration processes. It was followed by the ettringite II, which frequently fills completely the pores. Sometimes, the calcite resulted by carbonation appear as the latter filling of the central part of the pores (Figure 8). This succession indicated that carbonation followed the alkali-silica reactions and the sulphate attack.

CONCLUSIONS

The fissures produced within the concrete structure and the finishing mortar mainly resulted via frost-thaw cycles; additional to the primary porosity, they represented the access pathways for infiltration fluids. These fluids contain various ions from the Arieş River and the precipitation waters, as well as from the matrix of the mortar. Both CO_2 from the atmosphere and dissolved in the water, and SO_4^{2-}, Na^+ and Ca^{2+} ions contributed to the debut and progress of degradation processes (carbonation, sulphate attack, and alkali-silica reactions). The presence of SO_4^{2-} and Ca^{2+} in the mortar leads to the formation of ettringite II.

The original deposition of silica gels inside the pores suggests that the first reaction taking place in the concrete was between the silica in the aggregates and the alkalies from the matrix and from the infiltration waters. The silica gels are partly crystallized and they build-up the first (most internal) layer lining the pores. The high amounts of SO_4^{2-} and Ca^{2+} from the river waters as well as the retarded hydration of cement some compounds have facilitated the formation of secondary ettringite that represents the second layer within the pores.

The high concentration of $HCO3^-$ points to relatively lower amounts of aggressive CO_2, thus to its delayed reaction with $Ca(OH)_2$ resulting in the formation of $CaCO_3$ (calcite) consisting the last product precipitated within the pores.

The intense carbonation at the surface and in the fissures of the mortar suggest a strong diffusion of $Ca(OH)_2$ through the fissures and its reaction with atmospheric CO_2 during drying-wetting cycles.

The following time succession for the formation of secondary products could be documented: cryptocrystalline silica resulted by crystallization of silica gels is deposited along the internal walls of the voids, as a result of the first degradation process (alkali-silica reactions). This is followed by sulphate attack with the formation of ettringite II; the youngest stage was represented by carbonation. This precipitation succession is particular for

the specific *in situ* microenvironmental conditions. In the case of the dam from Buru, the pollution degree of waters from Arieş River plays a dominant role in the succession of formation of secondary minerals. This pattern may differ in case of subaerial exposure, when the interaction with infiltration fluids containing dissolved ions is an intermittent process [3].

EXPERIMENTAL SECTION

Analytical methods. Several investigation methods were used complementary in the view of establishing the structural, textural and mineralogical characteristics of the mortar, as well as of the secondary minerals resulted by degradation processes. Macroscopic observations concerned the dam under study, which were used for selective sampling (mortar and material from the white efflorescences) in the view of laboratory study. These samples were cut into thin sections (25-30 microns) used for microscopic investigations. The study of the thin sections evidenced spatial relationships between the products of the various degradation processes, thus allowing a chronology of the deposition of neoformed (secondary) minerals to be established. These studies were carried out by optical microscopy under polarized light (Nikon Eclipse E 2000 microscope), under crossed (N+) or parallel (1N) nicols. The identification of secondary mineral species was additionally based on the results of X-ray diffraction investigation performed by using Dron 3 diffractometer with Cu anticathode in the $5 – 64^o$ 2θ interval.

ACKNOWLEDGEMENTS

REFERENCES

1. Ian Sims, *Proceedings of Challenges of concrete construction. Repair, rejuvenation and enhancement of concrete, Thomas Telford, London*, **2002**, 11.
2. M. Muntean, N. Noica, L. Radu, I. Ropotă, A. Ionescu, O. Muntean, *Romanian Journal of Materials*, **2008,** *38(4)*, 284.
3. N. Har, R. Bindiu, M. Gorea, M. Benea, *Romanian Journal of Materials*, **2007,** *37(3)*, 228.
4. W. Michael, Della M. Roy Grutzeck, "Portland Cement Mineralogy", Hutchinson Ross Publishing Company, **1981,** chapter II.

5. G. Macleod, A.J. Hall, E.A. Fallick, *Mineralogical Magazine*, **1990,** *54*, 637.
6. I. Teoreanu, "Basis of inorganic binder technology", Didactical and Pedagogical Publishing House, Bucharest, **1993,** chapter V.
7. S.V. Harutyunyan, S.A. Abovyan, J.M.P. Monteiro, P.V. Mkrtchyan, K.M. Balyan, P.A. Aivazyan, *J. Am.Ceram. Soc*., **2003**, *86(12)*, 2162.
8. F.L. Forray, D.K. Hallbauer, *Environmental Geology*, **2000**, *39(12)*, 1372.